



ENHANCEMENT OF THE REMOVAL OF CADMIUM(II) FROM WATER RESOURCES BY 2,5-HEXANEDIONE BIS(SALICYLOYLHYDRAZONE) USING FLOTATION TECHNIQUE

Bakir Jeragh^{[a]*} and Ahmed A. El-Asmy^[a]

Keywords: Cd(II) removal; 2,5-hexanedione bis(salicyloylhydrazone); natural water; flotation; spectrophotometry

The removal of Cd(II) is improved using 2,5-hexanedione bis(salicyloylhydrazone) (HDSH) as complexing agent, and oleic acid (HOL) as collector by flotation method. The optimum conditions are: pH ~ 5; Cd(II) = 2×10^{-4} mol L⁻¹, surfactant = 1×10^{-3} mol L⁻¹ and HDSH = 1×10^{-4} mol L⁻¹; ionic strength [different concentrations of NaCl, KCl, KNO₃ and CaCl₂]; temperature [25±2 °C] and shaking time [3 min] were optimized. The effect of added ions (Na⁺, K⁺, Ca²⁺, Mg²⁺, Mn²⁺, Co²⁺, Ni²⁺, Cu²⁺, Zn²⁺, Hg²⁺, Al³⁺, Cl⁻, SO₄²⁻, NO₃⁻, ClO₄⁻, H₂PO₄⁻ and CH₃COO⁻ ions) was investigated on the recovery of Cd(II). The Cd(II)-HDSH complex was floated quantitatively (~100 %) under the recommended conditions. The proposed procedure was satisfactorily applied to the analysis of Cd(II) in natural [Nile, Sea, underground and lake] waters. The solid complex formed between HDSH and Cd(II) was characterized to have the formula [Cd₂(HDSH-4H)(H₂O)₄].

*Corresponding Author

E-Mail: bakir.jeragh@ku.edu.kw

[a]Chemistry Department, Faculty of Science, Kuwait University, Kuwait, P.O.Box 5969, Safat 1360, Kuwait

Experimental

Apparatus

The flotation cell used had a 15 mm inner diameter and 290 mm long. The pH was measured using Hanna Instruments 8519 pH meter provided with a glass electrode. The IR spectra were recorded on a Mattson 5000 FT-IR Spectrophotometer using KBr disc. The Cd(II) concentration in the mother liquor, after flotation, was determined using a Perkin-Elmer Atomic Absorption Spectrophotometer.

Reagents

The reagents and solvents were of analytical grade and were used as supplied. Second distilled water was used for washing and dilutions. The glassware was cleaned by washing with water. Oleic acid (HOL) was used directly as received. Its stock solution, 6.36×10^{-2} mol L⁻¹, was prepared from food grade with specific gravity 0.895 (J. T. Baker Chemical Co.) by dispersing 20 ml in 1 L kerosene. Cd(II) stock solution, 1×10^{-2} mol L⁻¹, was prepared by dissolving the requisite amount of Cd(NO₃)₂·2H₂O in 1:1 (v/v) ethanol / water and standardized complexometrically with EDTA. HCl and/or NaOH were used for adjusting the pH.

Preparation of HDSH and its Cd(II) complex

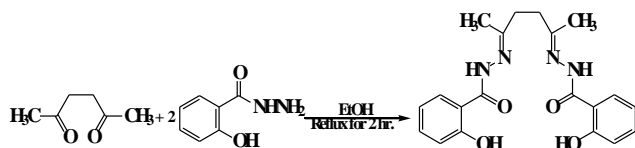
The complexing agent, HDSH, was synthesized as previously reported²⁶ and shown in Scheme 1.

Introduction

The industrial effluents alter the flow of materials and introduce chemicals to the environment. The rate increases as a result of urbanization. Most of the effluents contain heavy metals which have major hazards because of their toxicity to human beings.¹

Numerous techniques for the separation of metal ions have been reported.²⁻⁵ However, most of these suffer from lengthy separation, limitation of the volume sample, time consuming, multistage, lower enrichment factor and consumption of harmful organic solvents. These problems have been overcome using flotation^{2,3,5} which received attention due to simplicity, rapidity, economy, good separation efficiency (>95 %) for small impurity agents in the concentration range (10^{-6} – 10^{-2} mol L⁻¹) and a large applications for species having different nature and structure, flexibility and friability of equipment.⁶ The flotation is incorporated as a clean technology for wastewater treatment.⁷ So, it is chosen for the removal methods.⁸⁻¹²

Although a number of reagents are reasonable for flotation^{2,13-18} or spectrophotometric determination^{13,19-25} of metal ions, the method has not been used to analyze Cd(II) with HDSH. Therefore, the present work was undertaken to enhance the Cd(II) removal from natural waters using HDSH as a new complexing agent.



Scheme 1. Preparation reaction of HDSH

The Cd(II) complex was prepared by heating HDSH (0.7 g, 2 mmol) in 30 ml ethanol and $\text{CdCl}_2 \cdot 2\text{H}_2\text{O}$ (0.876 g, 4 mmol) in 20 ml ethanol on a water bath for 4 h. The precipitate was filtered off, washed with diethyl ether and finally dried in a vacuum desiccator over anhydrous CaCl_2 . Elemental analysis: $[\text{Cd}_2(\text{HDSH}-4\text{H})(\text{H}_2\text{O})_4]$ [Calcd. (Found)] C=35.47 (35.30); H=4.17 (3.58); N=8.26 (7.48). IR bands (cm^{-1}): 3554; 1635; 1608; 1075; 426 for the stretching vibrations of H_2O , C=O, C=N, N-N and Cd-N, respectively. ^1H NMR signals (ppm): 12.480; 7.945-7.041; 1.990; 3.362 for OH, CH_{ph}; CH₂ and CH₃, respectively.

In the IR spectrum of $[\text{Cd}_2(\text{HDSH}-4\text{H})(\text{H}_2\text{O})_4]$, the $\nu(\text{OH})$ and $\delta(\text{OH})$ bands disappeared indicating the deprotonation of the phenolic OH and its participation in bonding. The disappearance of (C=O) and (NH) bands indicated the enolization of CONH and its participation in coordination. It is evident from the appearance of new bands at 1531-1577 and 1223-1258 cm^{-1} due to $\nu(\text{C}=\text{N}^*)$ and $\nu(\text{C}-\text{O})$ vibrations. The bands at 3292, 930 and 600 cm^{-1} in $[\text{Cd}_2(\text{HDSH}-4\text{H})(\text{H}_2\text{O})_4]$ are attributed to $\nu(\text{OH})$, $\rho_r(\text{H}_2\text{O})$ and $\rho_w(\text{H}_2\text{O})$ of coordinated water.²⁶

Procedures

Flotation

A solution containing 2×10^{-4} mol L^{-1} Cd(II) was mixed with HDSH (1×10^{-4} mol L^{-1}) and 5 ml double distilled water. The pH was adjusted at ≈ 5 . The solution was then transferred quantitatively to the flotation cell and made up to 10 ml with double distilled water. The cell was shaken well for few seconds to ensure complete complexation. To this solution, 3 ml of 1×10^{-3} mol L^{-1} HOL were added and the cell was then inverted upside down many times. After complete separation, the scum containing Cd(II)-HDSH complex was separated, eluted with 5 ml of 4 M HCl, diluted to 10 ml in a volumetric flask and subjected to AAS determination. The floatability ($F\%$) of the analyte was calculated by:

$$F\% = \frac{C_i - C_f}{C_i} \times 100$$

where C_i and C_f are the initial and final concentrations of Cd(II) in the mother liquor, respectively.

Temperature

To study the effect of temperature on the flotation efficiency, two flotation cells were prepared: one containing the solution of Cd(II) and HDSH and the second containing the surfactant. The two were either heated or cooled to the same temperature. The surfactant solution was quickly poured into the solution of the investigated ion (inside a cell

jacketed with 1 cm thick fiberglass insulation) at zero time. The mixture was then floated under the same conditions.

Application

Natural water samples

The water samples were obtained from the Mediterranean Sea, Nile, tap, underground and lake. Each of pre-filtered water sample was poured into a beaker and 8 ml of concentrated HNO_3 and 3 ml of H_2O_2 (30 %) were added for complete decomposition of the organic matter. The sample, while stirring, was evaporated to one-tenth volume. After adjusting the sample pH to the desired value, the flotation and spectrophotometric determination were performed according to the recommended procedure.

Results and Discussion

Flotation process

To study the optimum conditions for maximum flotation of Cd(II), different factors were investigated.

pH

The pH, which is highly significant as it affects the metal-ligand interaction, was optimized first. The experiments using 1×10^{-4} mol L^{-1} HDSH and 1×10^{-3} mol L^{-1} of HOL surfactant were carried out to evaluate the optimum pH giving maximum flotation of 2×10^{-4} mol L^{-1} of Cd(II). The data graphically represented in Fig. 1 showed that the efficiency of flotation increases gradually with pH, reaching maximum ($\sim 100\%$) at 4.5-5.5 and then starting to decrease.

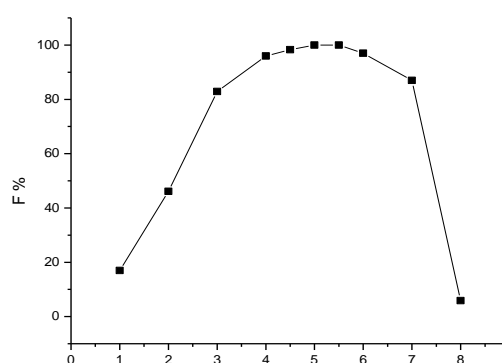


Figure 1. Flotation efficiency of 2×10^{-4} mol L^{-1} Cd(II) with pH using 1×10^{-4} mol L^{-1} HDSH and 1×10^{-3} mol L^{-1} HOL.

At pH 4.5-5.5, Cd(II)-HDSH being hydrophobic by combination with undissociated HOL begins to dissociate at $\text{pH} \geq 5.2$, through hydrogen bonding or chemically with OL^- . The hydrophobic particulates are floated to the solution surface by air bubbles. At $\text{pH} > 7$, the floatability diminishes due to the solubility of the formed precipitate or the oleic acid may give a white turbidity of sodium oleate dispersed in the bulk of the floating medium. Therefore, $\text{pH} \sim 5$ was chosen for further experiments.

Oleic acid concentration

Experiments were conducted to float Cd(II) with HOL only, but the efficiency was found ~60 %. Therefore, other experiments were carried out to find the most suitable concentration of HOL for removing 2×10^{-4} mol L⁻¹ Cd(II) at pH ~5 using 1×10^{-4} mol L⁻¹ HDSH. The floatability reached ~100% when HOL concentration was 1.5×10^{-3} mol L⁻¹; below this concentration, the flotation decreased due to the presence of insufficient amount of HOL required for complete flotation. At higher concentration, the decrease in the removal may be attributed to the changes of precipitate state.²⁹ The lower flotation at high HOL concentration may be due to the formation of a hydrate micelle coating on the solid surface.²⁹ As a result, the hydrophobicity of the surface was not suitable for flotation.¹¹ Therefore, HOL concentration must be 1×10^{-3} mol L⁻¹. The data are presented in Fig. 2.

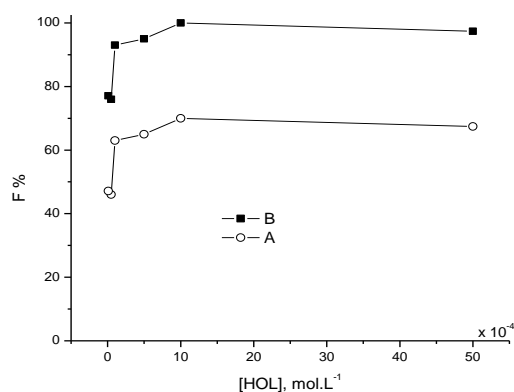


Figure 2. Floatability of 5×10^{-5} mol L⁻¹ Cd(II) versus [HOL] at pH ~5 in absence (A) and presence (B) of 1×10^{-4} mol L⁻¹ HDSH.

HDSH concentration

The variation in the concentration of HDSH at pH ~5 showed that, the floatability of Cd(II) increased abruptly and reached its maximum percentage (~100 %) at M:L ratio of 1:1. Excess HDSH had no effect facilitating the separation of Cd(II) from unknown matrices [10^{-4} mol L⁻¹ HDSH was used in all subsequent experiments.

Cd(II) concentration

The use of different concentrations of Cd(II) at HDSH = 1×10^{-4} mol L⁻¹ and HOL = 1×10^{-3} mol L⁻¹ and pH ~5 showed that the maximum floatation efficiency (~100%) of Cd(II) remained constant whenever the ratio of Cd(II) to HDSH is 1:1, 1:2, 1:3. etc. The decrease in flotation at higher concentrations of Cd(II) is attributed to the insufficient amount of HDSH to bind all Cd(II) ions existing in solution.

Reaction temperature

The variation of temperature in the range 5-90 °C had no marked effect on the floatation efficiency of Cd(II) ($[Cd^{2+}] =$

2×10^{-4} , $[HDSH] = 1 \times 10^{-4}$ and $[HOL] = 1 \times 10^{-3}$ mol L⁻¹ and pH ~5). Accordingly, all experiments (unless otherwise stated) were carried out at room temperature (25 ± 2 °C).

Stirring time

The influence of stirring time showed that a maximum floatation (~100%) was attained after 3 min of shaking indicating that the flotation-separation is not time consuming.

Ionic strength

Table 1 summarizes the effect of ionic strength varied with different salts that are usually present in natural water samples. It is to be noted that the ionic strength of the medium had no marked effect on the flotation process.

Table 1. Effect of ionic strength on the floatability of 2×10^{-4} mol L⁻¹ Cd(II) using 1×10^{-4} mol L⁻¹ HDSH and 1×10^{-3} mol L⁻¹ HOL at pH ~5.

Salt	Concentration, mol L ⁻¹	F %
KCl	0.01	99.8
	0.10	99.5
NaCl	0.01	100.0
	0.10	99.9
KNO ₃	0.01	99.7
	0.10	99.7
CaCl ₂	0.01	99.7
	0.10	99.5

Effect of cations and anions

The effect of some cations and anions which are normally present in fresh and saline waters was investigated to assess the applicability of the proposed method to recover Cd(II) added to water samples. The tolerable amounts of each ion (presented as ion: Cd ratio) are summarized in Table 2. Inspection of the data shows that the investigated cations and anions did not interfere. Some ions (Hg^{2+} , CO_3^{2-} and $H_2PO_4^-$) can interfere at concentration more than the recommended in Table 2. This interference could be removed by increasing the concentration of HDSH in experiments required higher concentration of HDSH.

Water samples

Various water samples were selected to provide a wide variety of sample matrices characterized by different types of interferences. The samples were pretreated as described previously. To 10 ml aliquots of the investigated water sample, 2.5 or 5 mg L⁻¹ Cd(II) was added after adjusting the pH to ~5. The data are presented in Table 3 and are satisfactory over than 95%.

Table 2. Effect of some cations and anions on the flotation of $[Cd^{2+}] = 2 \times 10^{-4}$, $[HDSH] = 1 \times 10^{-4}$, $[HOL] = 1 \times 10^{-3}$ mol L⁻¹ and pH ~5.

Cations	Cation/Cd(II) ratio	F %	Anion	Cation/Cd(II) ratio	F %
Na ⁺	8000	100.0	Cl ⁻	4000	100.0
K ⁺	8000	100.0	SO ₄ ²⁻	5000	100.0
Co ²⁺	2000	100.0	NO ₃ ⁻	3000	99.7
Ni ²⁺	2100	99.5	CH ₃ COO ⁻	1200	99.2
Cu ²⁺	1700	98.5			
Zn ²⁺	400	99.2			

Table 3. Recovery (R %) of Cd(II) added to 10 ml of water samples containing $[HDSH] = 1 \times 10^{-4}$ and $[HOL] = 1 \times 10^{-3}$ mol L⁻¹ at pH ~5.

Water source	Cd(II) mg L ⁻¹		R %
	Added	found	
Tap	2.5	2.46	98.4
	5.0	4.97	99.4
Nile	2.5	2.48	99.2
	5.0	4.85	97.0
Sea	2.5	2.49	96.0
	5.0	4.97	99.4
Underground	2.5	2.45	98.0
	5.0	4.92	98.4
Lake	2.5	2.40	96.0
	5.0	4.77	95.4

Effect of foreign ions

To assess the usefulness of the proposed method, the effect of the investigated diverse ions on Cd(II) analysis was studied (Table 2). The interfering cations were added as chlorides while the anions as sodium salts. The tolerance of the method with respect to foreign ions was investigated with solutions containing 5.59 mg L⁻¹ Cd(II) and various amounts of foreign ions. The tolerance criterion for a given ion was taken as the deviation of the absorbance by more than ~2% from the value expected for the system Cd(II)-HDSH.

Inspection of the data shows that most of the investigated ions at high ion: analyte ratio did not interfere. However, Al(III), Ba(II), Cu(II), citrate and bicarbonate ions interfere when added with more than 2 folds of Cd(II) [not cited in Table 2]. The interferences could be overcome by adding excess HDSH. EDTA interfered seriously which may be attributed to a competition between EDTA and HDSH for chelation with Cd(II).

Cause of Flotation

The flotation process is attributed to the coordination of HDSH that acts as a bidentate ligand coordinating through the C=N and C-O groups. The IR spectrum of the scum solid has no absorption bands corresponding to oleic acid. HOL may bind with $[Cd_2(HDSH-4H)(H_2O)_4]$ giving hydrophobic aggregates that floats on the solution surface by air bubbles.

Acknowledgment

This work was supported financially by the research sector, Kuwait University (project No. SC06/12). The authors acknowledge this support and all service labs.

References

- ¹Igwe, J. C., Abia, A. A., *African J. Biotechnol.*, **2006**, 5, 1167-1179.
- ²Karimi, H., Ghaedi, M., Shokrollahi, A., Rajabi, H., Soylak, M., Karimi, B., *J. Hazard. Mater.*, **2008**, 152, 248-252.
- ³El-Menshawly, A. M., Kenawy, I. M., El-Asmy, A. A. *J. Hazard. Mater.*, **2010**, 173, 523-527.
- ⁴Mortada, W. I., Hassanien, M. M., El-Asmy, A. A., *J. Trace Elem. Med. Biol.*, **2013**, 27, 267-272.
- ⁵Ghazy, S. E., El-Shazly, R. M., El-Shahawi, M. S., Al-Hazmi, G. A. A., El-Asmy A. A., *J. Iran. Chem. Soc.*, **2006**, 3, 140-150.
- ⁶Stoica, L., Dinculescu, M., Plapcianu, C. G., *Water Res.*, **1998**, 32, 3021-3030.
- ⁷Rubio, J., Souza, M. L., Smith, R. W., *Minerals Eng.*, **2002**, 15, 139-155.
- ⁸Doyle, F. M., *Int. J. Miner. Process.*, **2003**, 72, 387-399.
- ⁹Lazaridis, N. K., Peleka, E. N., Karapantsios, Th. D., Matis, K.A., *Hydrometallurgy*, **2004**, 74, 149-156.
- ¹⁰Doyle, F. M., Liu, Z. *J. Colloid Interface Sci.*, **2003**, 258, 396-403.
- ¹¹Saad, E., El-Shahawi, M., Mansour, R. A., El-Asmy, A. A., *Talanta*, **2008**, 76, 1041-1046.
- ¹²El-Asmy, A. A., Yousef, W. M., Akl, M. A., *Eur. J. Chem.*, **2010**, 1(3), 169-174.
- ¹³El-Menshawly, A. M., Salama, A., El-Asmy, A. A., *CJASS*, **2008**, 53(5), 206-213.
- ¹⁴Kim, Y., Kim, K., Lee, C., *Bull. Korean Chem. Soc.*, **1999**, 20, 431-435.
- ¹⁵El-Asmy, A. A., Al-Gammal, O. A., Saleh, H., *Spectrochim. Acta, Part A*, **2008**, 71, 39-44.
- ¹⁶Tavallali, H., Lalehparvar, S., Nekoei, A., Niknam, K., *J. Chinese Chem. Soc.*, **2011**, 58, 199-206.
- ¹⁷Ulewicz, M., Walkowiak, W., Jang, Y., Kim, J. S., Bartsch, R. A., *Anal. Chem.*, **2003**, 75, 2276-2279.
- ¹⁸Sasaki, T., Moshizuki, K., Ishitawa, S., *Bull. Chem. Soc. Jpn.*, **1982**, 55, 3717.
- ¹⁹Markzenko, Z., *Separation and Spectrophotometric Determination of Elements*, Harwood, Chi Chester (1986) 327.

- ²⁰Abu-Baker, M. S., Sedaira, H., Hashem, E. Y., *Talanta*, **1994**, *41*, 1669-1674.
- ²¹Malik, A. H., Rao, A. L. J., *Talanta*, **1997**, *44*, 177.
- ²²Kara, D., Alkan, M.M., *Talanta*, **2001**, *55*, 415-423.
- ²³ Hashem, E. Y., Abu-Baker, M. S., Hussain, S. M., *Spectrochim. Acta*, part A, **2003**, *56*, 761-769.
- ²⁴Zaijun, L., You, F., Zhongyun, L., Jian, T., *Talanta*, **2004**, *36*, 647-651.
- ²⁵Tarafder, P. K., Thakur, R., *Microchem. J.*, **2005**, *80*, 39-43.
- ²⁶El-Asmy, A. A., Al-Abdeen, A. Z., Abo El-Maaty, W. M., Mostafa, M. M., *J. Spectrochim. Acta Part A*, **2010**, *75*, 1516-1522.

Received: 24.11.2013.

Accepted: 09.01.2014.



USE OF ZIGBEE DEVICE MODULES IN CORROSION MONITORING

S. Santhana Prabha,^[a] R .Joseph Rathish,^[b] R. Dorothy,^[b] R .M. Joany^[c] and Susai Rajendran^{[d]*}

Keywords: ZigBee devices; corrosion monitoring; corrosion fatigue; strain in concrete structures; linear polarization resistance sensor

ZigBee-style networks began to be conceived around 1999, when many installers realized that both [Wi-Fi](#) and [Bluetooth](#) were going to be unsuitable for some industrial applications. In particular, many engineers saw a need for self-organizing ad-hoc digital radio networks. The real need for mesh has been cast in doubt since that, in particular as mesh is largely absent in the market. ZigBee protocols are intended for embedded applications requiring low data rates and low power consumption. The resulting network will use very small amounts of power — individual devices must have a battery life of at least two years to pass ZigBee certification. Typical application areas include: automation, advanced temperature control, safety and security, wireless sensor networks, industrial control-embedded sensing. ZigBee devices find applications in corrosion monitoring also such as corrosion fatigue, strain in concrete structures and linear polarization resistance sensors.

* Corresponding Authors

E-Mail: srmjoany@sify.com

[a] TCS, Chennai, India

[b] PSNA College of Engineering and Technoloy, Dindigul, India

[c] Sathyabama University, Chennai, India.

[d] Corrosion Research Centre, RVS School of Engineering and Technology, Dindigul-624005, India.

Introduction

ZigBee is a specification for a suite of high level communication protocols using small, low-power digital based on an IEEE 802 standard for personal area networks. ZigBee devices are often used in mesh form to transmit data over longer distances, passing data through intermediate devices to reach more distant ones. This allows ZigBee networks to be formed ad-hoc, with no centralized control or high-power transmitter/receiver able to reach all of the devices. Any ZigBee device can be tasked with running the network. ZigBee network can cover a range of 10- 100 metres. The size of a ZigBee device is compared with that of a €1 coin in Figure 1.

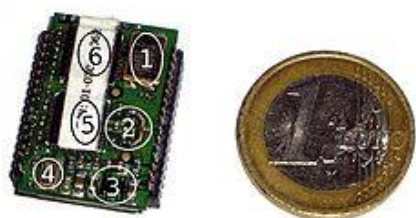


Figure 1. A ZigBee module beside a €1 coin.

ZigBee is targeted at applications that require a low data rate, long battery life, and secure networking. ZigBee has a defined rate of 250 kbit s⁻¹, best suited for periodic or intermittent data or a single signal transmission from a sensor or input device. Applications include wireless light switches, electrical meters with in-home-displays, traffic management systems, and other consumer and industrial

equipment that requires short-range wireless transfer of data at relatively low rates. The technology defined by the ZigBee specification is intended to be simpler and less expensive than other WPANs, such as Bluetooth or Wi-Fi.

The name ZigBee refers to the waggle dance of honey bees after their return to the beehive.

ZigBee protocols are intended for embedded applications requiring low data and low power consumption. The resulting network will use very small amounts of power—individual devices must have a battery life of at least two years to pass ZigBee certification.

Specification

The specification of a ZigBee device is shown in Figure 2.

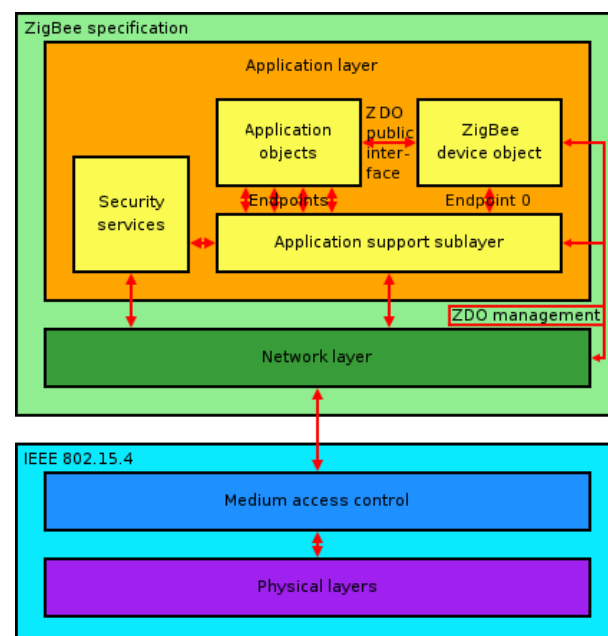


Figure 2. ZigBee specification

ZigBee is a low-cost, low-power, wireless mesh network standard. The low cost allows the technology to be widely deployed in wireless control and monitoring applications. Low power-usage allows longer life with smaller batteries. Mesh networking provides high reliability and more extensive range. ZigBee chip vendors typically sell integrated radios and microcontrollers with between 60 KB and 256 KB flash memory.

ZigBee operates in the industrial, scientific and medical (ISM) radio bands; 868 MHz in Europe, 915 MHz in the USA and Australia and 2.4 GHz in most jurisdictions worldwide. Data transmission rates vary from 20 to 250 kilobits/second.

The ZigBee network layer natively supports both star and tree typical networks, and generic mesh networks. Every network must have one coordinator device, tasked with its creation, the control of its parameters and basic maintenance. Within star networks, the coordinator must be the central node. Both trees and meshes allows the use of ZigBee routers to extend communication at the network level.

Difference between Zigbee and Bluetooth



Zigbee vs Bluetooth

There is a lot in common between Zigbee and Bluetooth, like both operating in the same frequency band of 2.4 GHz and belonging to the same wireless private area network (IEEE 802.15). But even if this is the case, they are not exactly competing technologies. Also, there is a multitude of differences between the two wireless technologies for 'personal area networks' both application and technical. Both technologies aim towards a different set of devices and applications and different means of designing for those applications.

The major differences between ZigBee and Bluetooth are summarized below.

1. Zigbee aims at automation whereas Bluetooth aims at connectivity of mobile devices in close proximity.
2. Zigbee uses low data rates, low power consumption on small packet devices while blue tooth uses higher data rates, higher power consumption on large packet devices.
3. Zigbee networks support longer range devices and more in number compared to Bluetooth networks whose range is small, for example between mobile phone and a laptop or desktop or a printer and a PC.
4. Given Zigbee's almost instant network join times (30 milliseconds) it is more suitable for critical applications while Bluetooth's longer join time is detrimental (3 seconds).
5. Bluetooth has a protocol stack size of 250 Kilo bytes and 28K bytes for Zigbee.

Uses of ZigBee devices

Recently ZigBee devices have been used in various fields¹⁻²¹ including wireless communication technologies,¹ automation,² framework for physiological parameters monitoring,³ networks for vehicular communication,⁵ electronic devices as thermostats,⁷ and wireless technologies for patient monitoring in the operating room and intensive care unit.²⁰ ZigBee devices are used in corrosion monitoring systems also.

Greenhouse environment wireless monitoring system²²

In the greenhouse environmental monitoring, the wired sensor networks have some problems, for example, complex wiring, inflexible sensor location, cable aging and corrosion and so on. To solve the above problems, **ZigBee** technology is used to build a wireless sensor network for monitoring temperature, humidity, light intensity, carbon dioxide concentration. And each node is low-power design. Based on the Modbus protocol, RS-485 bus has been built to achieve the communication between a number of greenhouse sensor networks and upper computer (PC). The system has advantages such as flexible sensors placement, low power consumption, easy installation maintenance and expansion, low cost, strong practicability.

Structural Health Monitoring (SHM) system²³

Analatom is developing a Structural Health Monitoring (SHM) system which provides both corrosion and strain measurements. This combination of data provides critical assessment of structural health, leading to prediction of failure. The SHM system's sensors can be permanently installed in high value structures, such as buildings, bridges, or aircraft, and are connected to data acquisition nodes where initial processing is performed. From the nodes, processed data is transmitted using a ZigBee/IEEE 802.15.4 compliant low-power, self-organizing, self-healing wireless network to a central PC hub for analysis and interpretation. Analatom's Linear Polarization Resistance (LPR) corrosion sensors have been installed on a mock-up bridge cable at Columbia University as part of a large project on development of a corrosion monitoring system for main cables of suspension bridges. The sensors were placed inside a full-scale mock-up suspension bridge cable located in an environmentally controlled chamber subjected to accelerated corrosion conditions for one year. The LPR sensors recorded corrosion rate measurement at 8 different locations inside the cable showing excellent agreement with temperature measurements.

Structural Health Monitoring by using corrosion degradation AI modeling²⁴

Analatom Inc. is developing a Structural Health Monitoring system using its proprietary Linear Polarization Resistance corrosion sensors combined with a TI MSP430 microprocessor for lower weight, lower power, higher sensitivity, and lower cost than conventional sensor systems. The system provides both strain and corrosion measurements in a package a few mils thick. This combination of data can provide critical assessments of

structural health, leading to prediction of failure. The MEMS sensors are permanently installed on a high-valued structure, such as a building, bridge or aircraft, and are connected to a data acquisition node. Data transmission and downloading will use a ZigBee wireless chip, a self-organizing network that has low power requirements. The sensor network provides a low-cost, non-intrusive way to detect failures, or to signal ahead of time that preventative maintenance needs to be undertaken to prevent more expensive replacement in the future. Corrosion Health Monitoring Systems and Prognostics are key elements in assuring the performance and reliability of high value, critical structures. Analatom has developed a multiplexed system that obtains data from a variety of sensors with real-time intelligent algorithms to detect, monitor and predict corrosion rates. Second generation Neural Networks have shown that total state event-shifts within non-linear systems can now be modeled, wherein concurrent, multiple and often interacting sensor signal signatures enhance and amplify this modeling process such that hidden interactions and element dependencies are clarified and understandable. Analatom has developed such a second generation Neural Network architecture whereby multiple and multi-layered element interactions can be evaluated, grouped and monitored. This enhancement now enables CBM monitoring and tracking to reflect local regions of negative impact which arise from multiple and interacting states of degradation.

Wireless sensors for corrosion health management²⁵

Analatom Inc. is developing the Structural Health Monitoring (SHM) system using its Linear Polarization Resistance (LPR) corrosion sensors combined with a Texas Instruments MSP430 microprocessor for lower weight, lower power, higher sensitivity, and lower cost than conventional sensor systems. The system provides both strain and corrosion measurements in a package a few mils thick. This combination of data provides critical assessment of structural health, leading to prediction of failure. The MEMS sensors are permanently installed in a high valued structure, such as a building, bridge or aircraft, and are connected to a data acquisition node. Data transmission and downloading uses a Max Stream ZigBee/IEEE 802.15.4 compliant chip for a wireless, self-organizing network that has low power requirements. The sensor network provides a low-cost, non-intrusive way to detect failures, or to signal ahead of time that preventative maintenance needs to be undertaken to prevent future more expensive replacement. Analatom, Inc. has developed the basic technology for a Portable Maintenance Support Tool (PMST). The device is unique and novel in that it uses a Micro Controller Unit in a handheld device to perform data analysis whilst maintaining a link with a Personal Computer based database for further support. The handheld prototype with a Liquid Crystal Display (LED) touch screen GUI takes readings from a variety of sensors and transfers the data wirelessly to a central PC hub. The handheld unit using the downloaded data from the sensor network can then provide a graphic display and additionally transfer those data to a workstation for further data analysis. Analatom, Inc. builds on its corrosion system platform (sensors, data acquisition unit, data storage) to develop a multiplexed system to obtain data from a variety of sensors, while further developing real time intelligent algorithms to monitor corrosion rates.

Piezoelectric layer (PZT layer) used in the structural health monitoring for aircraft structures²⁶

The signal of the piezoelectric layer (PZT layer) used in the structural health monitoring for aircraft structures is easily effected by radiation and crosstalk. On the principle of electromagnetic interference, the PZT layer signal is researched and some related coupling parameters are obtained. Based on the research, reasonable parameters to reduce interference were designed and a kind of anti-interference PZT layer is developed. The results of the experiments demonstrate the effectiveness of the anti-interference performance of the designed PZT layer. It can be well used for damage detection. In the same test condition, the magnitude of the crosstalk decreases to 10 percent of the original one and the SNR of fixed frequency interference is improved by 3.16 times when the optimized piezoelectric layer was used.

Detection of fatigue cracks under cyclic loads and corrosive service environments²⁷

Monitoring the continued health of aircraft subsystems and identifying problems before they affect airworthiness has been a long-term goal of the aviation industry. Because in-service conditions and failure modes experienced by structures are generally complex and unknown, conservative calendar-based or usage-based scheduled maintenance practices are overly time-consuming, labor-intensive and expensive. Metal structures such as helicopters and other transportation systems are likely to develop fatigue cracks under cyclic loads and corrosive service environments. Early detection of cracks is a key element to prevent catastrophic failure and prolong structural life. Furthermore, as structures age, maintenance service frequency and costs increase while performance and availability decrease. Current non-destructive inspection (NDI) techniques that can potentially be used for this purpose typically involve complex, time-intensive procedures, which are labor-intensive and expensive. Most techniques require access to the damaged area on at least one side, and sometimes on both sides. This can be very difficult for monitoring of certain inaccessible regions. In those cases, inspection may require removal of access panels or even structural disassembly. Once access has been obtained, automated inspection techniques likely will not be practical due to the bulk of the required equipment. Results obtained from these techniques may also be sensitive to the sweep speed, tool orientation, and downward pressure. This can be especially problematic for hand-held inspection tools where none of these parameters is mechanically controlled. As a result, data can vary drastically from one inspection to the next, from one technician to the next, and even from one sweep to the next. Structural health monitoring (SHM) offers the promise of a paradigm shift from schedule-driven maintenance to condition-based maintenance (CBM) of assets. Sensors embedded permanently in aircraft safety critical structures that can monitor damage can provide for improved reliability and streamlining of aircraft maintenance. Early detection of damage such as fatigue crack initiation can improve personnel safety and prolong service life. Kumar et al., has explained the testing of an acousto-ultrasonic piezoelectric sensor based structural health monitoring system for real-time monitoring of fatigue cracks and disbonds in bonded repairs. The system utilizes a

network of distributed miniature piezoelectric sensors/actuators embedded on a thin dielectric carrier film, to query, monitor and evaluate the condition of a structure. The sensor layers are extremely flexible and can be integrated with any type of metal or composite structure. Diagnostic signals obtained from a structure during structural monitoring are processed by a portable diagnostic unit. With appropriate diagnostic software, the signals can be analyzed to ascertain the integrity of the structure being monitored. Details on the system, its integration and examples of detection of fatigue crack and disbond growth and quantification for bonded repairs has been reported.

Accelerated corrosion test predictions using linear polarization resistance sensors with neural networks²⁸

Coates et al.²⁸ have interpreted accelerated corrosion data with specific application towards the implementation of a successful Condition Based Maintenance (CBM) program. The objectives of this work are twofold, to investigate the efficacy of specific Linear Polarization Resistance sensors, and to develop a greater understanding of interpretation of accelerated corrosion testing. Linear Polarization Resistance sensors are used to retrieve corrosion data of 1100 Aluminum and 1010 steel using accelerated corrosion tests. The accelerated tests are performed for which the times of exposure are 48 hours and 96 hours. Data from Linear Polarization Resistance sensors is compared with physical observations of metal corrosion. Preliminary tests indicate that the LPR sensor resistance varies appropriately with the corrosion rating and humidity. Quantitative standards are achieved using the ASTM G34 corrosion rating. An Artificial Neural Network (ANN) algorithm is developed in MATLAB to test the consistency and efficacy of the LPR sensors. The Neural Network proposed for this study uses twelve inputs, one hidden layer consisting of 32 neurons, and two outputs; it adapts its weight functions using the back propagation algorithm. The output parameters are the ASTM G34 corrosion rating and material loss rate. The network provides results within 13 % of experimental values for corrosion rate and accurately predicts the corrosion rating. The corrosion rate predicted by LPR data is higher than experimental results as well as the ANN values, however the difference can be accounted for by the inherent assumptions in the electrochemical methods adopted.

Environmental testing of wireless sensor system for structural health monitoring of civil infrastructure²⁹

Fuchs et al.²⁹ have investigated the environmental testing of Wireless Intelligent Sensor and Actuator Network (WISAN) currently under development at Clarkson University for the use of long- structural health monitoring of civil infrastructure. The wireless sensor nodes will undergo controlled mechanical vibration and environmental testing in the laboratory. A temperature chamber will be used to perform temperature cycle tests on the sensor nodes. The temperature chamber will also house a small shaker capable of introducing mechanical loading under the controlled temperature cycle tests. At low temperatures, the resistance of the electronics processing and storage characteristics will be studied. Also, the testing will look at volume expansion and degradation of characteristics due to freezing, degradation of functions and performance, and

mechanical characteristics caused by contraction. At high temperatures, temperature-related changes in sensor nodes due to excessively high temperatures will be investigated. Also studied will be the effects of temperature cycles, including the thermal stresses induced in the nodes and housing and the distortion caused due to expansion and contraction, fatigue, cracks, and changes in electrical characteristics due to mechanical displacement. And finally, mechanical vibration loading will be introduced to the WISAN sensor nodes. Mechanical looseness, fatigue destruction, wire disconnection, damage due to harmonic vibration, defective socket contact, joint wear, destruction due to harmonics, lead breakage, occurrence of noise and abnormal vibration, cracking will be monitored. The eventual goal of the tests is to verify WISAN's performance under anticipated field conditions in which the sensors will be deployed.

Corrosion enhanced capacitive strain gauge³⁰

Jamshidi et al. have proposed a silicon carbide passivity capacitive strain sensor which continuously and accurately measures strain in corrosive ambient and operates up to 370 °C in air. The analytical model is of low-mechanical noise, high-resolution and high-gain capacitive SiC coated sensor. The gauge is fabricated using silicon-on- insulator and coated with a thin (60 nm) pinhole-free 3C-SiC layer. The integrity of the passivation layer is tested using a hot KOH bath followed by SEM inspection which shows no defects or damage. A localized-heating, high-temperature testing setup has been built using an infra-red lamp to heat the gauge up to 370 °C while maintaining the electronics at significantly reduced temperatures. Experimental results show the strain gauge successfully continues to operate at 370 °C.

High sensitivity oxide based strain gauges and pressure sensors³¹

Strain gauges and pressure sensors are necessary tools for automotive, aerospace and biomedical monitoring applications. Of the various types of material, which can be used in their fabrication, oxides allow a degree of flexibility in their design. Furthermore, these devices are more rugged and cost effective than semiconductor sensors and have a higher sensitivity than metal-foil gauges. Arshak et al., have developed thin and thick film sensors based on oxides such as V₂O₅, CeO₂, Bi₂O₃, In₂O₃, RuO₂, TiO₂, MgO and Nb₂O₅. The devices are evaluated in terms of their sensitivity or gauge factor, linearity, hysteresis and long term stability. Furthermore, different device configurations, planar and sandwich are compared. It is found that the devices presented in this work have sensitivity comparable to that of semiconductor gauges, with good long-term stability. This is particularly true of the sandwich devices. It is observed that oxide based strain gauges may offer an alternative to existing commercial gauges, for example, in applications involving load cells, torque wrenches and limb implants.

Measurement of strain in concrete structure³²

A new strain measurement using wireless telemetry technique in civil engineering applications is proposed. The technique makes use of a transponder together with a strain

gauge. The transponder is powered by the inductive coupling method which eliminates the need for expensive cable runs in the concrete for conventional strain measurement. The measured strain data is digitized and sent back to the PC-controlled reader using Frequency Shift Keying (FSK) technique at two discrete frequencies of 134.2 kHz and 123.2 kHz. A prototype was built using commercial micro power CMOS ICs to verify its functionality. Measurements from the prototype have achieved 100 cm reading range without any trimming on the capacitors in the resonance circuit.

Corrosion fatigue machine³³

Berchem and Hocking have designed a new and simple displacement-controlled high-cycle fatigue and corrosion fatigue machine. The new design allows the simultaneous testing of more than one test specimen. Stress amplitudes and mean stresses can be selected individually; the frequency however is the same for each test specimen.

Conclusion

ZigBee is a low-cost, low-power, wireless mesh network standard. The low cost allows the technology to be widely deployed in wireless control and monitoring applications. Low power-usage allows longer life with smaller batteries. Mesh networking provides high reliability and more extensive range.

ZigBee devices can be used in automation, advanced temperature control, safety and security, wireless sensor networks industrial control, embedded sensing, medical data collection, and corrosion monitoring devices.

Acknowledgement

The authors are thankful to their respective managements.

References

- ¹Kulatunga, N. A., Navaratne, S., Dole, J., Liyanagedera, C., Martin, T. 2012 *IEEE Innovative Smart Grid Technol. - Asia, ISGT Asia 2012*, Art. no. 6303188, **2012**.
- ²Ahmad, S., *Proc. 2011 Int. Conf. Emerging Trends Networks Comp. Comm., ETNCC2011*, Art. no. 5958516, **2011**.
- ³Mahajan, N., Reddy, K. T. V., *Proc. Int. Conf. Workshop Emerging Trends Technol., 2011, ICWET 2011*, **2011**, 1306.
- ⁴Wu, C.-H., Wu, C.-H., Hong, Z.-W., Huang, K.-S. *J. Conver. Inform. Tech.*, **2011**, 6(2), 329.
- ⁵Chumkamon, S., Tuvaphanthaphiphat, P., Keeratiwintakorn, P. *ECTI-CON 2010 - The 2010 ECTI Int. Conf. Electr. Engg./Electronics, Computer, Telecommun. Inform. Technol.*, Art. no. 5491415, **2010**, 603.
- ⁶Chang, C.-S., Tan, T.-H., Chen, Y.-F., Huang, Y.-F., Lee, M.-H., Hsu, J.-C., Chen, H.-C. *Lecture Notes Comp. Sci.* 6165 LNCS, **2010**, 201.
- ⁷Starsinic, M. 2010 *Long Island Systems, Appl. Technol. Conf., LISAT 10*, Art. no. 5478336, **2010**.
- ⁸Li, C., Zhang, J. *IFCSTA 2009 Proc. - 2009 Int. Forum Computer Sci.-Technol. Appl.* 1, Art. no. 5385074, **2009**, 298.
- ⁹Fang, A., Xu, X., Yang, W., Zhang, L., *Proc. 2009 Pacific-Asia Conf. Circuits, Commun. System, PACCS 2009*, Art. no. 5232292, **2009**, 81.
- ¹⁰Yuce, M. R., *Recent Pat. Electr. Engg.*, **2009**, 2(2), 115.
- ¹¹Taylor, C., Dajani, L. *1st Int. Conf. Pervasive Technol. Related Assist. Environ., PETRA 2008*, Art. no. 43, **2008**.
- ¹²Bellido Outeiriño, F. J., Flores Arias, J. M., Real Calvo, R., Torres Roldán, M. 2008 *1st Conf. IT Revolutions*, Art. no. 5075048, **2008**.
- ¹³Yadav, A., Bhoyar, M., Joshi, C.V., *Proc. 2008 Int. Conf. Wireless Networks, ICWN 2008*, **2008**, 759.
- ¹⁴Sherman, M., Mody, A. N., Martinez, R., Rodriguez, C., Reddy, R., *IEEE Commun. Mag.*, **2008**, 46(7), 72.
- ¹⁵Yang, W., Li, M., Wang, X. *Nongye Gongcheng Xuebao*, **2008**, 24(5), 297.
- ¹⁶Kawamoto, R., Emori, T., Sakata, S., Yuasa, K., Furuhashi, K., Hara, S. 2007 *1st Int. Global Inform. Infrastruct. Symp., GIIS 2007 - "Closing the Digital Divide"*, Art. no. 4404170, **2007**, 73.
- ¹⁷Cheng, J. J.-Y., Hung, M.-H., Chang, J.-W. 2007 *IEEE Int. Conf. Networking, Sensing, Control, ICNSC'07*, Art. no. 4239113, **2007**, 895.
- ¹⁸Ng, H. S., Sim, M. L., Tan, C. M., Wong, C. C., *BT Technol. J.*, **2006**, 24(2), 130.
- ¹⁹Lopez-Villegas, J. M. *Proc. SPIE - Int. Soc. Optic. Engg.*, 5837 PART I, Art. no. 46, **2005**, 404.
- ²⁰Paksunemi, M., Sorvoja, H., Alasaarela, E., Myllylä, R., *Proc. Ann. Int. Conf. IEEE Engg. Med. Biol.*, Vol. 7, Art. no. 1615645, **2005**, 5182.
- ²¹Arvind, D. K., Wong, K. J. 2004 *IEEE, Proc. Int. Symp. Consumer Electronics - Proceedings*, **2004**, 219.
- ²²Wang, H., Dong, X.-R., Ma, Y.-Z., Yang, X.-W., Liu, F.-N. *Lect. Notes Electr. Engg.*, 132 LNEE, **2011**, 1, 579.
- ²³Clements, R., Darr, D., Morse, J., Laskowski, B. C., Betti, R., Ooi, T. K., Corder, A., *Structural Health Monit. 2011: Condition-Based Maintenance Intelligent Struct. - Proc. 8th Int. Workshop Struct. Health Monit.*, **2011**, 2, 1855.
- ²⁴Kwan, K., Morse, J., Laskowski, B.C., *Proc. 4th Eur. Workshop Struct. Health Monit.*, **2008**, 551-559.
- ²⁵Kwan, K., Caldwell, B., Morse, J., O'Day, J., Laskowski, B. C., Ooi, T.K., Corder, A., *Adv. Mater. Res*, **2008**, 38, 123-131.
- ²⁶Shi, X.-L., Yuan, S.-F., Qiu, L. *Acta. Mater. Sin.*, **2012**, 33(5), 457.
- ²⁷Kumar, A., Roach, D., Beard, S., Qing, X., Hannum, R., *Proc. SPIE - Int. Soc. Optical Engg.*, 6179, Art. no. 61790M, **2006**.
- ²⁸Coates, C. W., Olanubi, O. O., Sokoloski, R. M., Singleton, J. D., *Coll. Techn. Papers - IAA/ASME/ASCE/AHS/ASC Struct., Structural Dynamics Mater. Conf.*, **2004**, 5, 3434.
- ²⁹Fuchs, M.P., Janoyan, K.D., Sazonov, E.S., Krishnamurthy, V., Jha, R., Cross, K., *Proc. SPIE - Int. Soc. Optical Engg.*, 6174 I, Art. no. 6 17405, **2006**.
- ³⁰Jamshidi, B., Azevedo, R.G., Wijesundara, M.B.J., Pisano, A.P. *Proc. IEEE Sensors*, Art. no. 4388522, **2007**, 804-807.
- ³¹Arshak, K., Morris, D., Arshak, A., Korostynska, O., *J. Mater. Sci.: Mater. Electron.*, **2006**, 17(9), 767.
- ³²Chuah, Y. T., Chan, P.K., Siek, L., *Int. Symp., IC Technol., Systems Appl.*, **2001**, 9, 438.
- ³³Berchem, K., Hocking, M. G., *Meas. Sci. Technol.*, Art. no. N05, **2006**, 17(10), 60.

Received: 10.12.2013.

Accepted: 09.01.2014.



STRUCTURAL ANALYSIS OF (2E)-3-[4-(1H-BENZIMIDAZOL-2-YLMETHOXY)PHENYL]-1-(4-CHLOROPHENYL)PROP-2-EN-1-ONE

Ratika Sharma,^[a] S. Samshuddin,^{[b],[c]} B. Narayana,^[b] Vivek V. Gupta,^[a] Rajni Kant^{[a]*}

Keywords: Benzimidazole; crystal structure; Direct method; intramolecular hydrogen bond;

The title compound, C₂₃H₁₆N₂O₂Cl crystallizes in the triclinic space group P-1 with unit cell parameters $a=7.1747(7)$, $b=9.5663(7)$, $c=13.8456(11)$ Å, $\alpha=97.174(6)$, $\beta=97.910(7)$, $\gamma=98.781(7)$, $Z=2$. The benzimidazol ring is almost perpendicular to the chlorophenyl ring with dihedral angle 88.1(8)°. There are no significant interaction between the molecules except weak C-H-O intramolecular hydrogen bonding. In the benzimidazole ring the five and six membered rings are almost planar with very small deviation. Packing diagram of the given crystal system represent the layer arrangement of the molecules and within the layer the pair of the molecules are reversibly oriented along the b-axis.

* Corresponding Authors

Fax: +91 191 243 2051

E-Mail: rkvk.paper11@gmail.com

[a] Department of Physics and Electronics, Jammu University, Jammu Tawi-180 006.

[b] Department of Studies in Chemistry, Mangalore University, Mangalagangothri-574 199, India.

[c] Department of P.G. Studies in Chemistry, Alva's College, Moodbidri – 574 227, India.

Introduction

Various substituted imidazol derivatives have been found to possess a significant biological exhibition such as anti-helminthic, analgesic, antibacterial, antifungal and antiviral.¹ Benzimidazole, in an extension of the well-elaborated imidazole system. These are basically synthesized by the fusion of benzene ring and imidazole ring. Benzimidazole derivatives play important role in medical field with so many pharmacological activities such as anti-diabetic and anti-cancer activities.^{2,3,4} They have also showed moderate activity against fungi⁵. Extensive biochemical and pharmacological studies have confirmed that its derivatives are effective against various strains of microorganism⁶.

The synthesis of novel benzimidazole derivatives remains a main focus of medicinal research. The benzimidazole ring system and its related compounds play an important role in pharmaceutical and agricultural fields due to their broad spectrum of biological activities.^{7,8} Benzimidazoles are also useful as insecticides, acaricides, nematocides, herbicides and other plant-protective agents in the field of pest control.⁹ In addition, benzimidazole derivatives have played a crucial role in the theoretical development of heterocyclic chemistry and are also used extensively in organic synthesis.

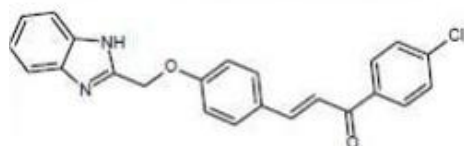
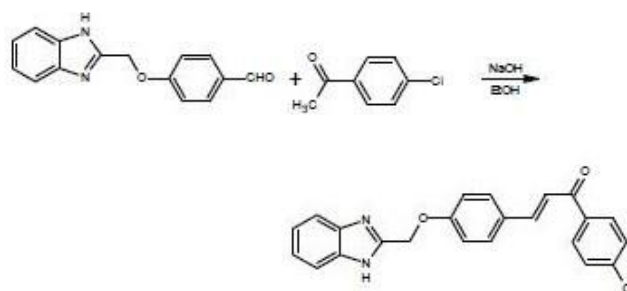


Figure 1. Structure of title compound

Experimental

Synthesis

A mixture of a 4-(1H-benzimidazol-2-ylmethoxy) benzaldehyde (2.52g, 0.01 mol) and *p*-chloroacetophenone (1.4 g, 0.01 mol) in 50 mL ethanolic sodium hydroxide was stirred at 5-10 °C for 3 h, then maintained at room temperature for 24 h and poured into ice cold water. The precipitate that appeared after neutralization with dil. HCl was filtered off and recrystallized from 1,4-dioxane. The single crystals were grown from DMF by slow evaporation method and yield of the compound was 64 %. (m.p. 481 K) . A schematic reaction scheme is shown below.



Scheme 1

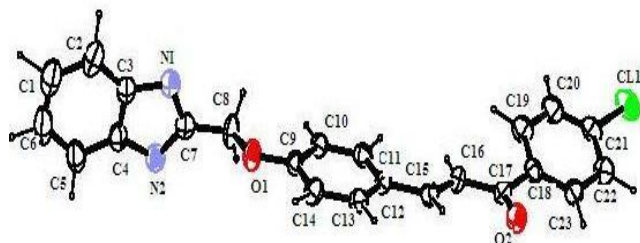
X-Ray Structure determination

X-ray intensity data of 6305 reflections (of which 3603 unique) were collected at 293(2) K on *X'calibur* CCD area-detector diffractometer equipped with graphite monochromated MoK α radiation ($\lambda=0.71073$ Å). The crystal used for data collection was of dimensions 0.30 X 0.20 X 0.20 mm. The intensities were measured by ω scan mode for θ ranges 3.73 to 27.34°. 1984 reflections were treated as observed ($I>2\sigma(I)$). Data were corrected for Lorentz and polarization factors. The structure was solved by direct methods using SHELXS97.¹⁰

Table 1. Crystal data and other experimental details

CCDC Number	975115
Crystal description	Block
Crystal size	0.30 x 0.20 x 0.20 mm
Empirical formula	C ₂₃ H ₁₆ N ₂ O ₂ Cl
Formula weight	387.83
Radiation, Wavelength	Mo K α , 0.71073 Å
Unit cell dimensions	$a = 7.1747(7)$, $b = 9.5663(7)$, $c = 13.8456(11)$ Å, $\alpha = 97.174(6)^\circ$, $\beta = 97.910(7)^\circ$, $\gamma = 98.781(7)^\circ$
Crystal system, space group	Triclinic, P-1
Unit cell volume	919.83 Å ³
No. of molecules per unit cell, Z	2
Absorption coefficient	0.230 mm ⁻¹
$F(000)$	402
θ range for entire data collection	$3.44 < \theta < 26.00$
Reflections collected / unique	6305 / 3603
Reflections observed $I > 2\sigma(I)$	1984
Range of indices	$h = -8$ to 8 , $k = -11$ to 11 , $l = -16$ to 17
No. of parameters refined	317
Final R -factor	0.0528
$wR(F^2)$	0.0939
R_{int}	0.0327
R_{sigma}	0.0911
Goodness-of-fit	0.961
$(\Delta/\sigma)_{max}$	0.001
Final residual electron density	$-0.233 < \Delta\rho < 0.045$ eÅ ⁻³

All non-hydrogen atoms of the molecule were located in the best E-map. Full-matrix least-squares refinement was carried out using SHELXL97.¹⁰ All the hydrogen atoms are located on a difference electron density map and their positional and isotropic thermal parameters were included in the refinement. The final refinement cycles converged to an $R = 0.0591$ and $wR(F^2) = 0.1341$ for the observed 2024 reflections. Residual electron densities ranged from -0.326 to 0.427 eÅ⁻³. Atomic scattering factors were taken from International Tables for X-ray Crystallography (1992, Vol. C, Tables 4.2.6.8 and 6.1.1.4). The crystallographic data are summarized in Table 1.

**Figure 2.** ORTEP view of the molecule with displacement ellipsoids drawn at the 40 % probability level. H-atoms are shown as small sphere of arbitrary radii.

Selected bond lengths, bond angles and torsion angles are given in Table 2. Geometry of intra- molecular hydrogen bonds is given in Table 3. An ORTEP¹¹ view of the title

compound with atomic labeling is shown in Fig.2. The geometry of the molecule was calculated using the PLATON¹² and PARST software.¹³

Table 2. Selected bond lengths (Å) and bond angles (°) for non hydrogen atoms (e.s.d.'s are given in parentheses)

Bond distances		Bond angles	
Cl1- C20	1.728(3)	O2-C17-C16	120.9(3)
N1- C7	1.364(3)	O2-C17-C99	119.3(2)
N1- C3	1.388(3)	O1-C9-C10	115.02
N2- C4	1.388(3)	O1-C9-C14	125.0(2)
N2- C7	1.313(3)	N1-C7-C3	105.1(2)
		N1-C7-C8	121.6(3)
		N2-C7-N1	115.0(3)
		N2-C7-C8	123.4(3)

Results and Discussion

In the title compound, C₂₃H₁₆N₂O₂Cl the dihedral angle between the benzimidazole ring and phenyl ring is 76.13(8)° and the benzimidazol ring is almost perpendicular to the chlorophenyl ring with dihedral angle 88.1(8)°. In the benzimidazole the five and six membered rings are twisted from each other with dihedral angle 2.02(8)° comparable with the related structures.¹⁴ In (Figure 2), all bond lengths and angles are normal and comparable with those reported for related compounds.^{15,16} The Cl-C bond distance in chloro-benzene ring is normal and comparable with the related structures.^{17,18}

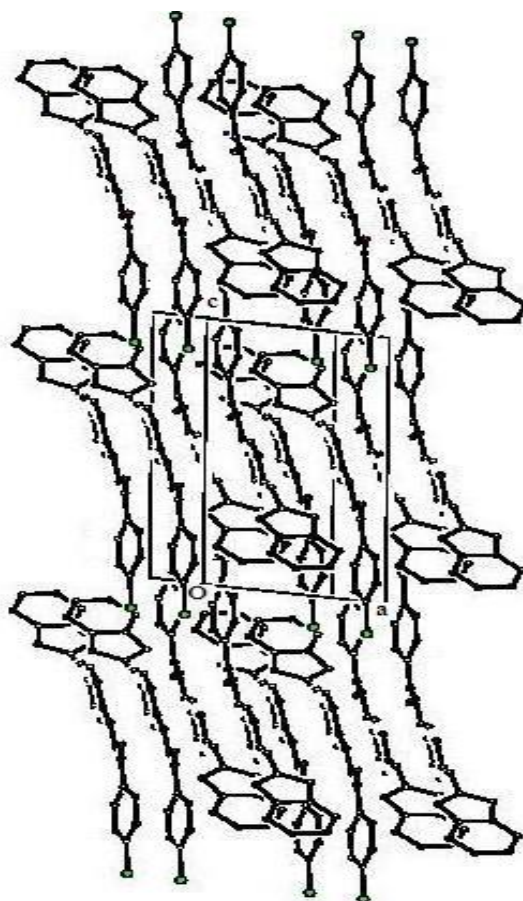
**Figure 3.** Packing diagram viewed down the b-axis

Table 3 Geometry of intramolecular hydrogen bonds

D-H...A	D-H, Å	H...A, Å	D...A, Å	∠[D-H...A, °]
C15- H11...O2	0.95(2)	2.44(2)	2.79(3)	102
C18- H16...O2	0.94(3)	2.49(3)	2.77(4)	98

The packing diagram of the molecules (Figure 3) represent the systemic arrangement of the molecules within the unit cell. Molecules are arranged to form layers along the b-axis and the pairs of the molecules are reversibly oriented from each other.

Acknowledgements

One of the authors (Rajni Kant) acknowledges the Department of Science & Technology for single crystal X-ray diffractometer as a National Facility under Project No. SR/S2/CMP-47/2003.BN and SS thank Mangalore University for the research facilities.

References

- ¹Shalini, K., Kumar, N., Sharma, P. K., 2011 *Biointerface Res. Appl. Chem.*, **2011**, 1, 184.
- ²Ramanpreet, W., Md., H., Syeda F. N., Khalid, I., HS., L., *IJRPC*, 2011, 1(3), 2231.
- ³Kubo, K., Oda, K., Kaneko, T., Satoh, H., Nohara, A., *Chem Pharm Bull.*, **1990**, 38(10), 2853.
- ⁴Uchida, M., Chihiro, M., Morita, S., Yamashita, H., Yamasaki, K., Kanbe, T., Yabuuchi, Y., Nakagawz, K., *Chem Pharm Bull.*, **1990**, 38(6), 1575.
- ⁵Ansari, K. F., Lal, C., *J. Med. Chem.*, **2009**, 44, 4028.
- ⁶Göker, H., Kus, C., Boykin, D.W., Yildiz, S., Altanlar, N., *Bioorg Med Chem.*, **2002**, 10, 2589.
- ⁷Pujar, M. A., Bharamgoudar, T. D., Sathyanarayana, D. N., *Transition Met. Chem.*, **1988**, 13, 423.
- ⁸Bouwman, E., Driessen, W. L., Reedijk, J., *Coord. Chem. Rev.*, **1990**, 104, 143172.
- ⁹Madkour, H. M. F., Farag, A. A., Ramses, S. S. & Ibrahiem, N. A. *A. Phosphorus, Sulfur Silicon*, **2006**, 181, 255.
- ¹⁰Sheldrick, G. M., *Acta Cryst.*, **2008**, A64, 112.
- ¹¹Farrugia, L. J., *J. Appl. Cryst.*, **1999**, 32, 837.
- ¹²Spek, A. L. *Acta Cryst.*, **2009**, D65, 148.
- ¹³Nardelli, M., *J. Appl. Cryst.*, **1995**, 28, 659.
- ¹⁴Haridharan, N., Ramkumar, V., *Acta Cryst.*, **2013**, E69, 0818.
- ¹⁵Ouzidan, Y., Kandri Rodi, Y., Jasinski, J. P., Butcher, R. J., Golen, J. A., El Ammari, L., *Acta Cryst.*, **2011**, E67, o1091.
- ¹⁶Kandri Rodi, R. Y., Ouazzani C. F., Essassi, E. M., Luis, S. V., Bolte, M., El Ammari, L., *Acta Cryst.*, **2011**, E67, o3234.
- ¹⁷Sukumar, N., Ponnuswamy, M. N., Thenmozhiyal, Jeyaraman, J. C., *J. Crystall. Spectros. Res.*, **1993**, 23, 871.
- ¹⁸Sugumar, P., Kavalvizhi, R., Ponnuswamy, M. N., *Acta Cryst.*, **2013**, E69, o1239.

Received: 26.12.2013.

Accepted: 09.01.2014.



INVESTIGATION OF THE ADSORPTION PROCESSES BY RADIO-SPECTROSCOPIC METHOD

Marsagishvili T.,^[a] Chagelishvili V.,^[a] Machavariani M.^[a] and Pradeep K. Sharma^[b]

Keywords: Electrochemical system; radio-waves; electromagnetic radiation; nonlinear phenomenon; aliphatic alcohols; adsorption.

The processes of electromagnetic radiation of radio-waves range in electrochemical systems are the matter of consideration in the present study. Two potentials, constant potential and low variable potential (with amplitude of 10 mV) are applied simultaneously in these systems to the metal-solution interface. The aim of the present work is: investigation of the adsorption processes in electrochemical systems by radio-spectroscopic method. The adsorption processes of the organic molecules are of great importance for creation of optochemotronic sensors, for electrochemiluminescence and various other processes. The analytical expressions for coordinates and rate of particles in such system are received. Moreover, expressions for vector-potential of the electromagnetic radiation of the system, which is connected with this motion, are also considered. The main outcome is existence of nonlinear, quadratic dependence between the signal of the electromagnetic radiation of the radio-wave range U and amplitude of a variable potential E , which is applied to the interface. The same dependence exist in electrochemical systems, where there is no current. Obtained theoretical results are used for the analysis of the experimental data, which was received for adsorption-desorption of aliphatic alcohols. Although there is no charge transfer between the alcohol molecules and electrode during the adsorption, quadratic dependence between U and E is investigated for all peaks on desorption SHS(second harmonic signal) - curves of butanol-1, butanol-2, hexanol, pentanol and isoamyl molecules on mercury electrode. For different concentrations of alcohols, different frequencies and values of the amplitude of variable potential were applied. Experimental results confirm the accuracy of proposed theoretical model.

* Corresponding Authors

E-Mail: tamaz.marsagishvili@gmail.com

[a] Iv. Javakhishvili Tbilisi State University, R. Agladze Institute of Inorganic Chemistry and Electrochemistry; 11, Mindeli str., Tbilisi, 0186, Georgia

[b] J.N.V. University, Jodhpur, Rajasthan, India, IN-342005

Introduction

The new method based on recording of the electromagnetic radiation in radio-wave frequency band has been in practice by electrochemical systems researches since last 10 to 15 years.¹⁻¹⁰ This method allows to record electromagnetic radiation connected to adsorption - desorption processes by removal so-called SHS, E (signal of the second harmonic, potential) curves. The peaks located at the left on these curves and on the right of significance of the potential are well selected when the maximum on the curve C , E (differential capacity, potential) is reached for the same process. It is possible to find out the detailed description of a method and obtained results in the work done by the previous workers.^{2,3,9} Fundamentals of the classical theory generated by an electrochemical system of oscillations with the double frequency $2\omega_0$, when an external variable signal of ω_0 frequency acts on a system may also be find in these reports.^{11,12} The base of the working mechanism of such nonlinear electrochemical generator is essentially nonlinear form of volt-ampere curve. At the same time it is important that a charge transfer from discharged (regenerated) or adsorbed (desorbed) particle on an electrode (from an electrode) in an electrochemical system takes place. In the reports^{3,9,10} desorption process was investigated by the registration method of the second harmonic signal (SHS). The measurements were conducted

on frequency 800 Hz, when the system is acted by a variable signal with frequency 400 Hz, and amplitude 50 mV. Measurements of dependence of differential capacity from a potential were conducted simultaneously. As it was indicated in this work on a curve SHS, E the minimum near to a maximum of desorption peak of a curve SHS, E is observed. At the Left and to the right of this minimum on a curve SHS, E , the left and right peaks are observed. In reports^{3,9,10} the correlation between $\partial C/\partial E$, E and SHS, E curves for an adsorption of a number of organic substances was investigated, though it was indicated¹⁰, that this correlation is sometimes disturbed. In article⁷ the model description for electromagnetic radiation of an electrochemical system is represented when an adsorption on a mercury electrode of various organic substances from aqueous and non-aqueous solutions takes place. It was shown, that during the simultaneous registration of electromagnetic radiation in one system, SHS and C method of a measurement of SHS most accurate and informative. It allows extract parameters of a double electrical layer, which cannot be defined by other methods. In article¹⁸ the experimental data obtained by SHS method for process of desorption of aliphatic alcohols (butanol and hexanol) on a mercury electrode are indicated. For these systems it is supposed, that during the adsorption and desorption process the charge transfer from a particle on the electrode and on the other hand does not take place. Nevertheless, this system is investigated experimentally just by a SHS method. It means that when there is no charge transfer between a particle and electrode this method also can successfully be applied, and it is more informative, as it was presumed.

In earlier reports^{13,14} we were depend upon separate mechanisms, which explain electromagnetic radiation of a range of radio-waves in non-stationary, heterogeneous, in

particular, electrochemical systems. Unfortunately, the phenomena connected with a radiation of the electromagnetic waves of a range of radio-waves, has rather complicated in nature. The full theoretical analysis of all processes causing in the issue to this radiation does not always manage to be finished in analytical form. Because of this, it is important that the experimental study of such systems would be conducted in broader band of parameters describing an electrochemical system.

Presently it is possible today to propose a number of the theoretical approaches for the description of the phenomenon of electromagnetic radiation in electrochemical systems, especially in the most interesting part of experimentally obtained outcomes¹⁸ in the field of the nonlinear phenomena.

Theoretical part

For mathematical description of electromagnetic phenomenon in electrochemical system we'll use method of temporal Green functions at finite temperature.

We will describe liquid phase by polarization operator:¹⁵

$$\vec{P}(\vec{r}, t)$$

In this case electrolyte can be described in linear approximation by one-particle retarded Green's function when finite temperatures:

$$G_k^R(\vec{r}, \vec{r}', t, t') = -\frac{i}{\hbar} \theta(t-t') \left\langle \left[P_1(\vec{r}, t) P_k(\vec{r}', t') \right] \right\rangle_0 \quad (1)$$

where angular brackets mean quantum-statistical averaging, $\theta(t-t')=1$, for $t-t'>0$; $\theta(t-t')=0$, for $t-t'<0$. For homogeneous isotropic systems (in volume of electrolyte) this Green's function can be easily connected with complex dielectric permeability of electrolyte:

$$\varepsilon = 1 + 4\pi G^R \quad (2)$$

Homogeneity and isotropy of medium near the electrode is disturbed and dependence between G^R and ε has much more complicated character.^{16,17}

In the existing approach it is possible to take into account effects of a frequent and space dispersion of a liquid phase within the framework of various models. We shall use an approximation of separation of dependence on space and temporary coordinates for Green function:

$$G_k^R(\vec{r}, \vec{r}', \omega) = G_k^R(\vec{r}, \vec{r}') G^R(\omega) \quad (3)$$

As to dependence of G from ω , formally it would be possible to determine this dependence on the base of experimental data in absorption spectra of a system in corresponding region of frequencies. For determination of the form of function

$$G(\vec{r}, \vec{r}')$$

the conduction of complicated quantum mechanical calculations is necessary. Instead of it is possible to simulate this function by various damping oscillating functions. The corresponding parameters (characteristic size of damping and period of oscillations) for these models can be determined, for example, by free energies of solvation. If in a system round positive ions in first solvated shell the dipole molecules of a solvent of one type would only be collected, the characteristic size for polarization oscillations would be approximately equal to a diameter of a molecule of a solvent. Unfortunately, in our case the picture is more complicated and it is possible to consider this parameter only as observable fact.

We shall imply, that solvated particle moves in a liquid phase and radiates an electromagnetic field. Effective mass, charge and size of this particle will be determined by corresponding approximate parameters.

When making concrete calculations it is possible to use some models for a Green function describing a liquid phase (for simplicity we shall reduce functions in $\varphi\zeta$ representation):

$$G_{\text{bp}}(\vec{r}, \vec{r}') = -\frac{C_0}{4\pi} \delta(\vec{r} - \vec{r}') \quad (4)$$

$$G_{\text{pp}}^{(\lambda)}(\vec{r}, \vec{r}') = -\frac{C_0}{32\pi^2 \lambda^3} e^{-\frac{(\vec{r} - \vec{r}')^2}{\lambda}} \quad (5)$$

$$G_{\text{pp}}^{(\lambda)}(\vec{r}, \vec{r}') = -\frac{C_0}{32\pi^2} v(v^2 - 3\lambda^2) e^{-v\sqrt{(\vec{r} - \vec{r}')^2}} \cos\left(\gamma\sqrt{(\vec{r} - \vec{r}')^2}\right) \quad (6)$$

where C_0 is constant connected with the dielectric properties of the system, λ and v are parameters.

Depending on an electrode potential the distribution of different charged particles will vary in liquid phase. Dependence of concentration, as function of a distance from an electrode, we shall describe by model damping functions.

In connection with a strain of solvate shell of the charged particles near to a surface of the electrode, in accordance with growth of the electrode potential, the distance from the particle up to the surface of the electrode decreases.

We consider a system, in which two potentials are enclosed in the interface: constant (E) and variable (with amplitude E_{V1} and frequency ω_0).

In researched region of frequencies we can register electromagnetic radiation connected with non-uniform translation movement of the charged solvated particles. The equation of motion for these particles we shall present as¹³:

$$m \frac{d\vec{v}(\vec{r}, t)}{dt} = q\vec{D}(\vec{r}, t) - \kappa\vec{v}(\vec{r}, t) \quad (7)$$

where
 $\vec{v}(\vec{r}, t)$ is rate of the particle in point r and time point t ,
 m is mass of this particle,
 q is charge,
 κ is factor of friction for the electrolyte,
 D is induction of an electromagnetic field applied at the interface.

The corresponding potential has a form:

$$\begin{aligned} E_z(z') &= E(z') + E_{V1}(z') \cos(\omega t) \\ E_x + E_y &= 0 \end{aligned} \quad (8)$$

For plane-parallel electrodes the solution of the equation (7) results in following expressions for coordinates and velocity of a particle:

$$\begin{aligned} z' &= z'_0 + qD(z') \left[\frac{\kappa}{m\tau} + e^{-\frac{\kappa}{m\tau}} - 1 \right] + \\ &+ q \frac{D_{V1}(z')}{\frac{\kappa^2}{m\tau^2} + \omega_0^2} \left[\frac{\kappa}{m\omega_0} \sin(\omega_0 t) - \cos(\omega_0 t) + e^{-\frac{\kappa}{m\tau}} \right] \\ x' &= x'_0; y' = y'_0 \end{aligned} \quad (9)$$

$$\begin{aligned} \frac{dz'}{dt} &= q \frac{\kappa}{m\tau} D(z') \left(1 - e^{-\frac{\kappa}{m\tau}} \right) + \\ &+ q \frac{D_{V1}(z')}{\frac{\kappa^2}{m\tau^2} + \omega_0^2} \left[\frac{\kappa}{m} \cos(\omega_0 t) - \omega_0 \sin(\omega_0 t) + \frac{\kappa}{m} e^{-\frac{\kappa}{m\tau}} \right] \end{aligned} \quad (10)$$

$$\frac{dx}{dt} = 0, \quad \frac{dy}{dt} = 0.$$

where z is direction perpendicular to a surface of the electrode.

As approaching a surface of an electrode the part of particles passes in an adsorbed condition, at that time the redistribution of an electronic density on a particle takes place. Under an action of an external variable field the particle makes non-uniform movement near to an adsorbed condition and as the corollary radiates an electromagnetic field. The expression for vector potential of this field has a form (see article¹³):

$$\begin{aligned} A_z(x, y, z, \omega) &= \frac{q}{c} \int dz' S_\varepsilon(z') \Phi(z') \varepsilon(\omega) \left\{ \frac{\kappa}{m} I(z') \left[\frac{1}{\gamma - i\omega} - \right. \right. \\ &\left. \left. \frac{1}{\frac{\kappa}{m} - i\omega} \right] + \frac{I_{V1}(z')}{\frac{\kappa^2}{m\tau^2} + \omega_0^2} \left[\frac{\kappa}{m\omega_0^2} \frac{\gamma - i\omega}{(\gamma - i\omega)^2} + \right. \right. \\ &\left. \left. \frac{\omega_0^2}{\omega_0^2 + (\gamma - i\omega)^2} - \frac{\kappa}{m} \frac{1}{\frac{\kappa}{m} - i\omega} \right] \right\} \\ &\gamma \rightarrow 0 \end{aligned} \quad (11)$$

where ε is dielectric permeability of an electrolyte on frequency ω , I and I_{V1} are electric field strengths of constant and variable components.

The approximation of particles when an adsorption takes place corresponds to emerging of peak on a capacity curve as function of parameters describing a field of an electrode. The corresponding radiation of electromagnetic waves (SHS) will depend on ω .

In accordance with growth of negative significance of an electrode potential, desorption of adsorbed particles takes place. Redistribution of an electron density and change of the charge density on a particle takes place at the moment of desorption. The expression for a vector potential will look like similar to the equation (11), with corresponding boundary conditions. One peak on a curve of capacity and two peaks on a curve of electromagnetic radiation as function of potential corresponds to each adsorption - desorption process in this case. The directed movement of charged particles under the influence of an external field results in modification of current, flowing through a system. This modification can be connected with three processes:

1. Electron transfer from a particle to an electrode and vica versa;
2. Relaxation process connected with transition of charged particles;
3. Transition of the charged particles under the influence of an external field, rate of which is determined by the Eqn. (10).

In case, when redistribution of the charge density between particles and electrode takes place throughout particle motion, the density is determined by the following equation (for brevity this ratio and number of others are added in operator form):

$$\begin{aligned} \rho(\omega_h) &= -G_p(\omega_h) I(\omega_h) \\ \omega_h &= 2\pi kT; \quad n=0, \pm 1, \pm 2 \end{aligned} \quad (12)$$

where k is Boltzmann's constant, ρ is modification of an electron density under the influence of an external field, $G_{pp}(\omega_h)$ is Fourier representation of a temperature Green function of operators ρ and p .

Micro-currents which appear in the described system have the form:

$$\vec{i}(\omega) = \int \rho(\vec{r}, \omega) \vec{v}(\vec{r}, \omega) d\vec{r} \quad (13)$$

where, ρ is charge density of a particle, v is rate of particle's motion. The equation of motion for a particle differs from the equation (7) and takes the form:

$$m \frac{d\vec{v}(\vec{r}, t)}{dt} = q(t) D(\vec{r}, t) - \kappa \vec{v}(\vec{r}, t) \quad (7a)$$

where $q(t)$ is charge on the particle at the moment.

In frames of a simple model, when the particles move perpendicularly to an electrode surface (10), the expression for micro-currents takes a form:

$$i(\omega) = P(\omega) + M(\omega) E_{V1} + N(\omega) E_{V1}^2 \quad (14)$$

where $P(\omega)$, $M(\omega)$ and $N(\omega)$ are the coefficients.

In case when an electron transfer from a particle on an electrode does not take place, dependence of micro-currents on quadrate of voltage amplitude of an external variable field is also possible (polarization of any chemical bond of a particle is enough for this). The dipole moment induced under an action of an external field is equal:

$$\delta d = \alpha E_{V1} \quad (15)$$

where α is polarizability of molecules along this chemical bond.

If length of a dipole moment is equal to 1, then for micro-currents we shall receive expression similar to the equation (13), where the density of a charge ρ can be received from the following expression:

$$\rho = \frac{\alpha}{l} E_{V1} \quad (16)$$

In a general form the coefficients $P(\omega)$, $M(\omega)$ and $N(\omega)$ have a rather complicated form. However, for the double frequency $\omega = 2\omega_n$ the form of factors $P(\omega)$, $M(\omega)$ and $N(\omega)$ essentially becomes simpler. The expression for a signal of the second harmonics, which can be registered in a system, contains square-law dependence on amplitude E_{V1} :

$$U(2\omega) = \frac{1}{2} L \frac{m \alpha}{\kappa l} \frac{\varepsilon(2\omega)}{R(2\omega)} E_{V1}^2 \quad (17)$$

where $R(2\omega_n)$ is resistance of a measuring circuit, L - factor connected to geometry of electrodes and parameters of a space dispersion of a dielectric permeability of the electrolyte.

In works^{11,12} is shown, that when sinusoidal variable voltage of ω frequency is applied on an electrode, except of variable current of ω frequency a constant component of the current and second harmonic - component of the current with 2ω frequency arises in an electrochemical circuit. The emerging of these additional components is connected with the nonlinear and asymmetrical form of dependence of a current from an overstress.

The work of such "nonlinear" electrochemical generator has a quantum character. Expression for secondary harmonic's voltage includes such characteristics of an electrochemical system as: factor of friction of an electrolyte near to a electrode's surface, significance of a dielectric permeability at the frequency of a secondary harmonic, effective length of the dipole of some chemical bond of adsorbed-desorbed particle, polarization of which ensures "work" of this nonlinear generator.

Results and Discussions

In work¹⁸ the outcomes of an experimental research of desorption process of aliphatic spirits butanol-1 and hexanol-1 on a mercury electrode obtained by SHS method are represented. In same work the data for dependence of a differential capacity of an electrode potential is given.

As can be seen from the experimental data, given in work¹⁸, the adsorption - desorption process is accompanied by two peaks of electromagnetic radiation: the "left" peak, maximum of which is on the left side of a potential of a maximum of capacity peak (see Fig.3b, 4b in work¹⁸) and "right" peak, maximum of which is on the right side of maximum potential.

For butanol-1 (when the concentration is 0.47 mol L⁻¹) and hexanol-1 (when the concentration is 0.015-0.030 mol L⁻¹) for left and right peaks the dependence of an electromagnetic signal $U(\omega)$ from quadrate of amplitude of variable component E_{V1} of an electrode's field is well visible. So that, the signal of the second harmonic of electromagnetic radiation will be square-law function of a voltage amplitude of a variable component of a field applied to an interface:

$$U(\omega) = C(\omega) E_{V1}^2 \quad (18)$$

During adsorption process the molecule of spirit comes nearer to a surface of an electrode, and molecules of water - move away from a surface of an electrode. Redistribution of a density of a charge on OH groups at this time takes place.

Table 1. Experimental significances of voltage difference corresponding to microcurrents.

Alcohol	Concentration, mol L ⁻¹	<i>E</i> , mV	Left peak frequency, kHz			Right peak frequency, kHz		
			1.3	12.6	125.6	1.3	12.6	125.6
Butanol-1	0.07	5	40.0	35.7	26.4	8.2	7.9	5.3
		10	157.9	142.9	116.4	31.4	28.6	26.4
		15	364.3	321.4	264.3	72.9	82.1	64.3
	0.5	5	89.3	85.7	80.1	54.3	52.1	47.1
		10	350.0	335.7	300.0	217.9	214.3	185.7
		15	821.4	792.9	714.3	492.9	458.1	428.6
	0.7	5	95.0	102.1	85.0	71.4	75.0	57.5
		10	378.6	364.3	328.6	264.3	235.7	219.6
		15	878.6	842.9	721.4	635.7	642.9	478.6
Butanol-2	0.07	5	40.0	35.7		7.5	5.7	
		10	158.6	144.3		24.3	22.9	
		15	364.3	321.4	235.7	57.1	46.4	31.4
	0.5	5	94.3	88.6	85.7	46.1	45.0	42.1
		10	360.7	350.0	322.0	194.3	178.6	165.7
		15	821.4	821.4	720.0	425.0	414.4	364.3
	0.7	5	96.4	94.3	84.3	52.1	51.4	43.9
		10	457.1	364.3	324.3	235.7	207.1	182.1
		15	871.4	842.5	828.6	471.4	457.1	432.1
Hexanol	0.03	5	173.6	123.6	75.0	137.9	93.6	42.9
		10	721.4	485.7	285.7	564.3	350.0	173.6
		15	1592.9	1085.7	714.3	1264.3	821.4	382.1
Pentanol	0.1	5	131.4	120.0	89.29	93.6	84.3	55.0
		10	514.3	464.3	350.0	353.6	314.3	217.9
		15	1150.0	1050.0	785.0	800.0	750.0	496.4
Isoamyl alcohol	0.1	5	119.3	104.3	82.1	78.6	67.9	42.9
		10	457.1	407.1	303.6	292.9	242.9	167.9
		15	1050.0	950.0	721.4	700.0	571.4	385.7

The implications of $C(\omega)$, which are obtained with the help of formula (18) for left and right peaks of electromagnetic radiation (on SHS, E - curves) are given in the Table 1. As may be seen from this table, for both spirits the dependence of $U(\omega)$ from $E_{V1}(\omega)$ with a good exactness is described by the formula (18). For amplitudes of 2.5 and 10 mV we receive implications of $C(\omega)$ coefficient, distinguished from average value (at given ω frequency and concentration of spirit) less than on 10 % (except for one experiment for hexanol at frequency 1.3 kHz and concentration 0.03 mol L⁻¹, where the deviation reaches 17 %).

Thus, the registration of an electromagnetic signal reveals the interesting phenomenon in electrochemical systems - nonlinear dependence between a variable potential, influencing a system, and corresponding response when charge transfer between an adsorbed particle and electrode does not take place.

The square-law dependence between a registered signal of electromagnetic radiation and amplitude of the variable potential, applied to a system, takes a place both for left, and for right peaks of SHS, E - curves. Heights of right and left peaks are different, because during desorption the redistribution of an electronic density takes place in a system, that in its turn induces both modification of a particle's rate, and redistribution of a charge on OH groups of spirit and water molecules.

As the analysis of the experimental data shows, the left peak of micro-current for butanol-2, as a rule, exceeds by intensity the corresponding peak for butanol, when for right peaks the intensity for butanol is always lower. It may be assumed, that the left peak of radiation is determined by the motion of electrolyte molecules and the right one by motion of alcohol molecules principally.

The values of $C(\omega)$ coefficient (in μV^{-1}) for different systems at low concentrations are given in the Tables 2-7.

Table 2. The values of $C(\omega)$ coefficient (in μV^{-1}) for ethylene glycol containing 0.01 M NaCl at 25 °C

	Frequency, 20 Hz				Frequency, 200 Hz			
	E=10 mV		E=20 mV		E=10 mV		E=20 mV	
	E, mV	$C(\omega)$	E, mV	$C(\omega)$	E, mV	$C(\omega)$	E, mV	$C(\omega)$
min	1450	13.1	1450	15.0	1450	12.1	1430	12.1
max	1250	19.1	1250	19.9	1200	15.3	1100	17.0
min	800	8.0	870	1.35	870	1.5	900	4.0
max	660	17.6	670	17.1	670	15.7	850	26.5
min	540	0.9	540	1.75	540	1.9	750	12.0
max	430	39.0	400	4.1	430	30.0	650	17.2
min	380	4.9	380	7.4	390	9.6	390	87.5
max	270	318.0	270	313	290	228	290	275

Table 3. The values of $C(\omega)$ coefficient (in μV^{-1}) for ethylene glycol containing 0.1 M NaCl at 25 °C

	Frequency, 20 Hz				Frequency, 200 Hz			
	E=10 mV		E=20 mV		E=10 mV		E=20 mV	
	E, mV	$C(\omega)$	E, mV	$C(\omega)$	E, mV	$C(\omega)$	E, mV	$C(\omega)$
min	1400	13.6	1400	12.0	1400	9.7	1450	14.0
max	1100	19.5	1140	19.9	1200	11.1	1140	18.0
min	830	4.7	830	4.3	820	0.3	820	0.5
max	300	204	250	247.5	300	194	300	198

Table 4. The values of $C(\omega)$ coefficient (in μV^{-1}) for ethylene glycol containing 0.01 M KCl at 25 °C

	Frequency, 20 Hz				Frequency, 200 Hz			
	E=10 mV		E=20 mV		E=10 mV		E=20 mV	
	E, mV	$C(\omega)$	E, mV	$C(\omega)$	E, mV	$C(\omega)$	E, mV	$C(\omega)$
min	875	0.5	870	0.7	850	4.1	860	1.9
max	660	17.7	650	18.1	650	16.9	660	16.5
min	530	3.0	540	2.55	520	1.6	530	1.8
max	430	42.0	420	42.3	420	35.4	430	34.65
max	380	3.0	380	2.8	380	2.0	380	8.65
min	265	311.0	260	272.0	300	239	280	229.5

Table 5. The values of $C(\omega)$ coefficient (in μV^{-1}) for ethylene glycol containing 0.1 M KCl at 25 °C

	Frequency, 20 Hz				Frequency, 200 Hz			
	E=10 mV		E=20 mV		E=10 mV		E=20 mV	
	E, mV	$C(\omega)$	E, mV	$C(\omega)$	E, mV	$C(\omega)$	E, mV	$C(\omega)$
min	825	1.1	825	1.0	800	3.0	800	2.8
max	300	214.0	300	212.0	300	197.0	300	187.5

Table 6. The values of $C(\omega)$ coefficient (in μV^{-1}) for ethylene glycol containing 0.01 M CsCl at 25 °C

	Frequency, 20 Hz				Frequency, 200 Hz			
	E=10 mV		E=20 mV		E=10 mV		E=20 mV	
	E, mV	$C(\omega)$	E, mV	$C(\omega)$	E, mV	$C(\omega)$	E, mV	$C(\omega)$
max	1300	56.9	1300	57.0	1300	43.2	1300	38.3
min	850	2.3	830	0.8	820	1.9	820	1.8
max	660	17.0	640	16.8	640	14.7	640	13.0
min	540	2.1	540	2.4	520	3.6	520	1.45
max	425	44.0	430	44.5	430	34.0	430	28.0
min	380	5.0	400	32.6	380	3.3	380	5.5

Table 7. The values of $C(\omega)$ coefficient (in μV^{-1}) for ethylene glycol containing 0.1 M CsCl at 25 °C

	Frequency, 20 Hz				Frequency, 200 Hz			
	E=10 mV		E=20 mV		E=10 mV		E=20 mV	
	E, mV	C(ω)	E, mV	C(ω)	E, mV	C(ω)	E, mV	C(ω)
max	1250	58.5	1250	57.0	1260	51.7	1250	50.6
min	800	1.3	800	1.75	780	0.9	790	0.7
max	300	194.0	300	191.0	300	177.0	290	174.0
min	100	220.0	200	170.0	200	101.3	150	148.0

Conclusions

Theoretical model, which shows the existence of nonlinear, quadratic dependence between the signal of electromagnetic radiation of radio-wave range U and amplitude of variable potential E , which is applied to the interface is proposed. The same dependence exist in electrochemical systems, where is no current. Experimental results confirm the accuracy of proposed theoretical model.

As the analysis of the tables with experimental data reveals, that the quantity of peaks of second harmonic signal increases, with a decrease in concentration of solution. Which mean, that the registration of the radiation, induced by other chemical bonds, or perhaps ions pairs, which can be formed in given system, is possible at low concentrations? It can be observed from the Tables 2-7 also, that mass and size of the cation (K, Na, Cs) does not have influence at the value of the radiated signal. At the same time decrease of concentration leads to increase of the signal (Tables 2-7). This can be explained by increase of friction coefficient κ with decrease of the concentration.

References

- ¹Khatiashvili, N. G., Proc. Conf. «Physical properties of the mineral systems of the earth's interior», Prague, 1985.
- ²Khatiashvili, N. G., Japaridze, J. I., Chagelishvili, V. A. *Elektrokimiya*, **1984**, 20, 1402.
- ³Chagelishvili, V. A., Khatiashvili, N. G., Japaridze, J. I. *Elektrokimiya*, **1986**, 22, 70-73.
- ⁴Khatiashvili, N. G., Perelman, M. E., Phys. Earth Planet. Interiors, **1989**, 57, 169-177.
- ⁵Khatiashvili, N. G., Perelman, M. E., Bull. Acad. Sci. Georgia, **1988**, 129, 81-84.
- ⁶Khatiashvili, N. G., Perelman, M. E., X. Jubilee All-Union Symp. Mechanoemiss. Mechanochem. Solid State. Rostov na Donu, **1986**.
- ⁷Japaridze, J. I., Damaskin, B. B., Khokhashvili, M. O., Chagelishvili, V. A., Russ. J. Electrochem., **1997**, 33.
- ⁸Khatiashvili, N. G., Electrochemical radiation during destruction of rocks and crystals. Metsniereba: Tbilisi, **1990**.
- ⁹Chagelishvili, V. A., Khokhashvili, M. O., Japaridze, J. I., *Elektrokimiya*, **1987**, 23, 1660-1663.
- ¹⁰Damaskin, B. B., Japaridze, J. I., Khokhashvili, M. O. *Elektrokimiya*, **1989**, 25, 979-981.
- ¹¹Damaskin, B. B., *Principles of contemporary methods of studying of electrochemical reactions*. Publishing house of Moscow State University: Moscow, **1965**.
- ¹²Damaskin, B. B., Petrii, O. A., Introduction to electrochemical kinetics. Publishing house «High school»: Moscow, **1975**.
- ¹³Marsagishvili, T. A., Tatishvili, G. D., Poverkhnost., **1993**, 5, 9.
- ¹⁴Marsagishvili, T. A., Tatishvili, G. D., Russ. J. Electrochem., **1993**, 29, 1278.
- ¹⁵Dogonadze, R. R., Kuznetsov, A. M., Summary of science and Technics. Physical chemistry. Kinetics. VINITI: Moscow, **1973**, 2.
- ¹⁶Platzman, F., Wolff, P., Waves and interactions in plasma of solid state. Mir: Moscow, **1975**.
- ¹⁷Dogonadze, R. R., Marsagishvili, T. A. The chemical physics of solvation.. Part A. Elsevier: Amsterdam, **1985**.
- ¹⁸Japaridze, J. I., Chagelishvili, V. A., Khokhashvili, M. O., Chankashvili, M. V., Lochoshvili, D. M., Russ. J. Elektrochem., **1999**, 35, 1278.

Received: 11.01.2014.

Accepted: 17.01.2014.



SYNTHESIS AND X-RAY STRUCTURE OF 2-AMINO-4-(4-FLUOROPHENYL)-7,7-DIMETHYL-5-OXO-5,6,7,8-TETRAHYDRO-4H-CHROMENE-3-CARBONITRILE

Dalbir Kour,^[a] D. R. Patil,^[b] Madhukar B. Deshmukh,^[b] Vivek K. Gupta^[a] and Rajni Kant^{[a]*}

Keywords: Crystal structure; direct methods; conformations; C-H...O, N-H...N and N-H...O intra- and intermolecular interactions; crystallographic dimers; substituted tetrahydro-4H-chromene-3-carbonitrile

The title compound, 2-amino-4-(4-fluorophenyl)-7,7-dimethyl-5-oxo-5,6,7,8-tetrahydro-4H-chromene-3-carbonitrile (C₂₁H₂₄FN₃O₃), crystallizes in the monoclinic space group C2/c with unit cell parameters: a=31.342(3), b= 9.3481(9), c= 15.9051(11) Å, β= 118.687(9)°, Z = 8. The crystal structure was solved by direct methods and refined by full-matrix least-squares procedures to a final R-value of 0.0588 for 2776 observed reflections. The fused cyclohexene and pyran rings adopt sofa and boat conformations, respectively. The four essentially planar atoms (C1/C2/C5/C6) of pyran ring (maximum deviation = 0.0878 Å for C2) form a dihedral angle of 87.85(7)° with the benzene ring and is almost coplanar with the mean plane of the cyclohexene ring [dihedral angle = 7.23(7)°]. In the crystal, molecules are connected into inversion dimers via pairs of N-H...N hydrogen bonds and these dimers are further linked by N-H...O hydrogen bonds into a two-dimensional network.

* Corresponding Authors

Fax: +91 191 243 2051

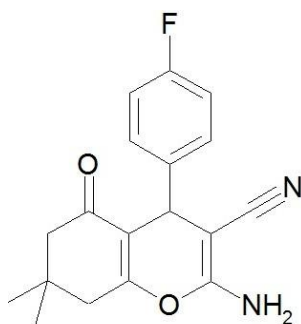
E-Mail: rkvk.paper11@gmail.com

[a] X-ray Crystallography Laboratory, Post-Graduate Department of Physics & Electronics, University of Jammu, Jammu Tawi - 180 006, India.

[b] Department of Chemistry, Shivaji University, Kolhapur - 416 004 (MS), India.

Introduction

In recent years, polyfunctionalized 4H-pyrans and their derivatives have been the subject of significant interest for the synthetic community and have been widely recognized as versatile scaffolds with diverse biological activities.¹⁻⁴ These are often used in cosmetics, pigments and are utilized as potentially biodegradable agrochemicals.^{5,6} 4H-Pyran derivatives are also potential calcium channel antagonists⁷ which are structurally similar to biologically active 1,4-dihydropyridines. Furthermore, these compounds can be employed as pigments, photoactive materials and used as biodegradable agrochemicals.⁸ Hence, investigation of the structural features of biologically relevant tetrahydrobenzo[b]pyran derivatives is of both scientific and practical interest. The present investigation is a continuation of our work⁹ that includes synthesis and structural studies of a polyfunctionalized substituted pyran derivative (**1**).



Scheme 1. Structure of the compound **1**.

Experimental

Synthesis

In a 50 ml round bottom flask charged with 1mmole of dimedone, 1 mmole of 4-fluorobenzaldehyde and 1 mmol of malononitrile. Then 5 ml of aqueous ethanol (1:1) and 25 mol % of NH₄Cl was added and the reaction mixture stirred at 30-45 min. at 50-55 °C. The reaction was monitored by TLC. After completion of reaction, the reaction mixture poured on crushed ice and stir well. The solid precipitated was filtered and recrystallized in ethanol to afford pure product. M.P.: 205-207 °C, Yield: 84 %. ¹H NMR (300 MHz, DMSO-d₆): δ 1.26(s, 3H, CH₃), 1.35(s, 3H, CH₃), 2.38-2.46(m, 2H, CH₂), 2.71(s, 2H, CH₂), 4.57(s, 1H, CH), 6.18-6.23(d, 2H, NH₂), 7.17-7.23(m, 2H, Ar-H), 7.42-7.47(m, 2H, Ar-H).

Crystal structure determination and refinement

The X-ray intensity data of a well defined crystal (0.30 x 0.20 x 0.10 mm) were collected at room temperature (293 K) by using a CCD area-detector diffractometer (*X'calibur system – Oxford diffraction, 2010*) which is equipped with graphite monochromated MoKα radiation (λ=0.71073 Å). The cell dimensions were determined by the least-squares fit of angular settings of 2901 reflections in the θ range 3.85 to 28.27°. A total number of 8432 reflections were collected of which 2776 reflections were treated as observed (*I* > 2σ(*I*)). Data were corrected for Lorentz, polarization and absorption factors.

The structure was solved by direct methods using SHELXS97.¹⁰ All non-hydrogen atoms of the molecule were located from the E-map. Full-matrix least-squares refinement was carried out by using SHELXL97 software.¹⁰ The geometry of the molecule is determined by PLATON.¹¹ All the hydrogen atoms were positioned geometrically and were treated as riding on their parent C/N atoms, with C-H distances of 0.93–0.98 Å and N-H distance of 0.88-0.89 Å;

and with $U_{\text{iso}}(\text{H}) = 1.2U_{\text{eq}}(\text{C/N})$, except for the methyl groups where $U_{\text{iso}}(\text{H}) = 1.5U_{\text{eq}}(\text{C})$. The final refinement cycles yielded an R-factor of 0.0588 ($wR(F^2)=0.1424$) for the observed data. The residual electron density ranges from -0.253 to $0.191 \text{ e}\text{\AA}^{-3}$.

Atomic scattering factors were taken from International Tables for X-ray Crystallography (1992, Vol. C, Tables 4.2.6.8 and 6.1.1.4). The crystallographic data are summarized in Table 1. CCDC-963179 contains the supplementary crystallographic data for this paper.

Results and discussion

An ORTEP view of the title compound with atomic labeling is shown in Figure 1.¹² In the crystal structure, it is observed that structure unit contains a substituted 5,6,7,8-tetrahydro-4H-chromene, a benzene ring and a DMF solvent.

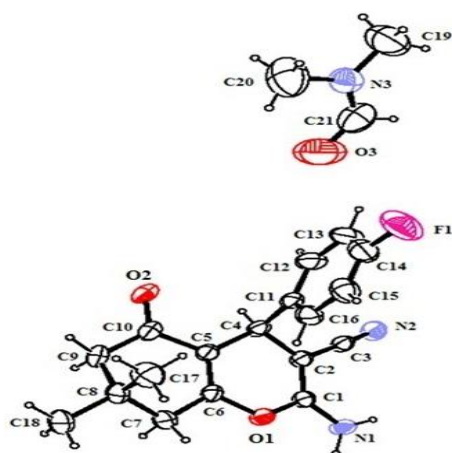


Figure 1. ORTEP view of the molecule with displacement ellipsoids drawn at the 50 % probability level. H atoms are shown as small spheres of arbitrary radii.

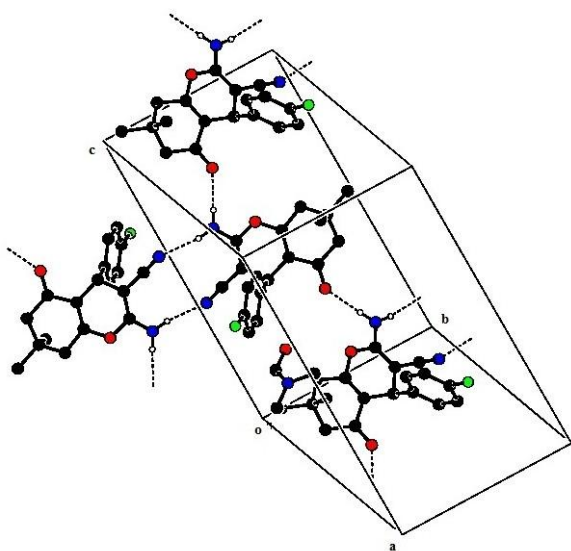


Figure 2. The packing arrangement of molecules in the unit cell box. The dashed lines show intermolecular N-H...O and N-H...N hydrogen bonds.

Table 1. Crystal data and other experimental details for **1**.

CCDC	963179
Crystal description	White block
Crystal size	0.30 x 0.20 x 0.10
Empirical Formula	$\text{C}_{21}\text{H}_{24}\text{FN}_3\text{O}_3$
Formula weight (g mol^{-1})	385.43
Radiation, Wavelength (\AA)	Mo $K\alpha$, 0.71073
Unit cell dimensions	$a = 31.342(3)$, $b = 9.3481(9)$, $c = 15.9051(11) \text{ \AA}$, $\beta = 118.687(9)^\circ$
Crystal system, Space group	monoclinic, $C 2/c$
Unit cell volume (\AA^3)	4088.0(6)
No. of molecules per unit cell, Z	8
No. of parameters refined	265
Absorption coefficient (mm^{-1})	0.091
$F(000)$	816
θ range for entire data collection ($^\circ$)	$3.87 < \theta < 26.00$
Limiting indices	$-38 \leq h \leq 38$, $-11 \leq k \leq 10$, $-18 \leq l \leq 19$
Reflections collected / unique	8432/3998
Reflections observed ($I > 2\sigma(I)$)	2776
Final R-factor	0.0588
$wR(F^2)$	0.1424
R_{int}	0.0478
R_{sigma}	0.0532
Goodness-of-fit	1.016
$(\Delta/\sigma)_{\text{max}}$	0.001
Final residual electron density ($\text{e}\text{\AA}^{-3}$)	$-0.253 < \Delta\rho < 0.191$

The geometry of the molecule was calculated using the PLATON¹¹ and PARST¹³ software. All bond lengths and angles are normal and correspond to those observed in related structures^{14,15} (Table 2).

Table 2. Selected bond lengths (\AA) and angles ($^\circ$) for non hydrogen atoms (e.s.d.'s are given in parentheses) for **1**.

Bond lengths		Bond angles	
F1- C14	1.359(3)	C1- O1- C6	118.9(1)
O1- C1	1.371(2)	N1- C1- C2	128.0(2)
O1- C6	1.380(2)	N1- C1- O1	110.6(2)
O2- C10	1.227(2)	C2- C1- O1	121.4(2)
N1- C1	1.332(3)	N2- C3- C2	177.8(2)
N2- C3	1.144(3)	C5- C6- O1	122.7(2)
O3- C21	1.246(4)	O1- C6- C7	111.4(2)
N3- C21	1.307(4)	O2- C10- C5	119.9(2)
N3- C20	1.427(4)	O2- C10- C9	122.1(2)
N3- C19	1.427(4)	C13- C14- F1	118.8(3)
		F1- C14- C15	118.8(3)
		C21- N3- C20	122.3(3)
		C21- N3- C19	119.5(3)
		C20- N3- C19	118.1(3)
		O3- C21- N3	123.5(4)

The cyclohexene ring (C5/C6/C7/C8/C9/C10) and pyran ring (O1/C1/C2/C4/C5/C6) exhibit *sofa* and *boat* conformations, respectively, with asymmetry parameters ($\Delta\text{Cs}(\text{C5})=9.236$ and $\Delta\text{Cs}(\text{C4})=2.453$, $\Delta\text{Cs}(\text{C5-C6})=10.94$).¹⁶

Table 3. Geometry of intra- and intermolecular hydrogen bonds for **1**.

D-H...A	D-H (Å)	H...A (Å)	D...A (Å)	θ [D-H...A(°)]	Symmetry code
C19-H19C...O3	0.96	2.295	2.704	105	
N1-H11...N2	0.89	2.502	2.898	170(3)	-x,-y,-z+1
N1-H22...O2	0.88	2.049	2.934	178	x,-y+1,+z+1/2

The four essentially planar atoms (C1/C2/C5/C6) of pyran ring (maximum deviation=0.0878 Å for C2) form a dihedral angle of 87.85(7)° with the benzene ring and is almost coplanar with the mean plane of the cyclohexene ring [dihedral angle=7.23(7)°]. The nitrile group is typical [N≡C=1.144(3) Å] and the double bonds C10=O2 and C21=O3 are confirmed by their respective distances of 1.227(2) and 1.246 (4) Å. These distances are larger than the standard value for carbonyl group [1.192 Å] and this lengthening could be due to the strong intermolecular interactions.

Both H-atoms of the NH₂ group are involved in the formation of N1-H22...O2 and N1-H11...N2 intermolecular hydrogen bonds. In the crystal, molecules are connected into dimers via N1-H11...N2 hydrogen bonds generating an R₂² (12) graph-set motif¹⁷ and these dimers are further connected by N1-H22...O2 (Table 3) hydrogen bonds into a two-dimensional network (Fig. 2).

Acknowledgements

One of the authors (Rajni Kant) acknowledges the Department of Science & Technology for single crystal X-ray diffractometer as a National Facility under Project No. SR/S2/CMP-47/2003.

References

- ¹Zamocka, J., Misikova, E., Durinda, J., *J. Prep.*, **1991**, 46, 610.
- ²Wang, J. L., Liu, D., Zhang, Z. J., Shan, S., Han, X., Srinivasula, S. M., Croce, C. M., Alnemri, E. S., Huang, Z., *Proc. Natl. Acad. Sci. USA*, **2000**, 97, 7124.
- ³Hatakeyama, S., Ochi, N., Numata, H., Takano, S., *J. Chem. Soc. Chem. Commun.*, **1988**, 17, 1202.
- ⁴González, R., Martín, N., Seoane, C., Marco, J. L., Albert, A., Cano, F. H., *Tetrahedron Lett.*, **1992**, 33, 3809.
- ⁵Morinaka, Y., Takahashi, K., *Japanese Patent JP52017498*, **1977**.
- ⁶Hafez, E. A. A., Elnagdi, M. H., Elagamey, A. G. A., El-Taweel, F. M. A. A., *Heterocycles*, **1987**, 26, 903.
- ⁷Sua 'rez, M., Salfra 'n, E., Verdecia, Y., Ochoa, E., Alba, L., Martín, N., Martínez, R., Quinteiro, M., Seoane, C., Novoa, H., Blaton, N., Peeters, O. M., De Ranter, C., *Tetrahedron*, **2002**, 58, 953.
- ⁸Fotouhi, L., Heravi, M. M., Fatehi, A., Bakhtiari, K., *Tetrahedron Lett.*, **2007**, 48, 5379.
- ⁹Kant, R., Gupta, V. K., Kapoor, K., Patil, D. R., Chandam, D. R., Deshmukh, M. B., *Acta Cryst.*, **2013**, E69, o417.
- ¹⁰Sheldrick, G. M., *Acta Cryst.*, **2008**, A64, 112.
- ¹¹Spek, A. L., *Acta Cryst.*, **2009**, D65, 148.
- ¹²Farrugia, L. J., *J. Appl. Cryst.*, **2012**, 45, 849.
- ¹³Nardelli, M., *J. Appl. Cryst.*, **1995**, 28, 659.
- ¹⁴Wang, X., *Acta Cryst.*, **2011**, E67, o832.
- ¹⁵Anthal, S., Brahmachari, G., Laskar, S., Banerjee, B., Kant, R., Gupta, V. K., *Acta Cryst.*, **2012**, E68, o2592.
- ¹⁶Duax, W.L., Norton, D. A., *Atlas of Steroid Structures*, New York: Plenum Press, **1975**, 1.
- ¹⁷Bernstein, J., Davis, R. E., Shimon, L., Chang, N. -L., *Angew. Chem. Int. Ed. Engl.*, **1995**, 34, 1555.

Received: 26.12.2013.
Accepted: 19.01.2014.



THERMOCHEMISTRY OF OZONIDES DECOMPOSITION

Franco Cataldo^{[a]*}**Keywords:** Ozonides; Thermochemical Calculations; Group Increments; Decomposition Enthalpy

Little is known about ozonides and their decomposition notwithstanding the growing interest for these compounds in medicinal chemistry or as intermediates in chemical synthesis. Using the Van Krevelen's group increment approach we have calculated the theoretical decomposition enthalpies of a series of olefins ozonation products adopting the simple assumption that the ozonides decompose into aldehydes and carboxylic acids but also by-products of ozonation like polyozonides, bis-peroxides and polycarbonyloxide decompose into the same products. It was found that all the homologous series of 1-olefin ozonides decompose with a $\Delta H_{\text{dec}} = -267 \text{ kJ mol}^{-1}$ and considering the other by-products the decomposition range of the entire crude ozonation mixture of 1-olefins is given by $\Delta H_{\text{dec}} = -272 \pm 20 \text{ kJ mol}^{-1}$. For the homologous series of symmetrical olefins of the type R-CH=CH-R the canonical ozonides with 1,2,4-trioxolane ring decompose with $\Delta H_{\text{dec}} = -298 \text{ kJ mol}^{-1}$ while considering the other by-products the decomposition range of the entire crude ozonation mixture of symmetric olefins is given by $\Delta H_{\text{dec}} = -288 \pm 10 \text{ kJ mol}^{-1}$. Asymmetric olefins of the type R-CH=CH-R' with $\text{R} \neq \text{R'}$ can be represented by the monounsaturated fatty acids series or by the methyl and the ethyl esters of fatty acids. Also for this homologous series the canonical ozonides with 1,2,4-trioxolane ring decompose with $\Delta H_{\text{dec}} = -298 \text{ kJ mol}^{-1}$ while considering the other by-products the decomposition range of the entire crude ozonation mixture of symmetric olefins is given by $\Delta H_{\text{dec}} = -288 \pm 10 \text{ kJ mol}^{-1}$.

* Corresponding Authors

E-Mail: franco.cataldo@fastwebnet.it

[a] Actinium Chemical Research srl, Via Casilina, 1626A, 00133 Rome, Italy

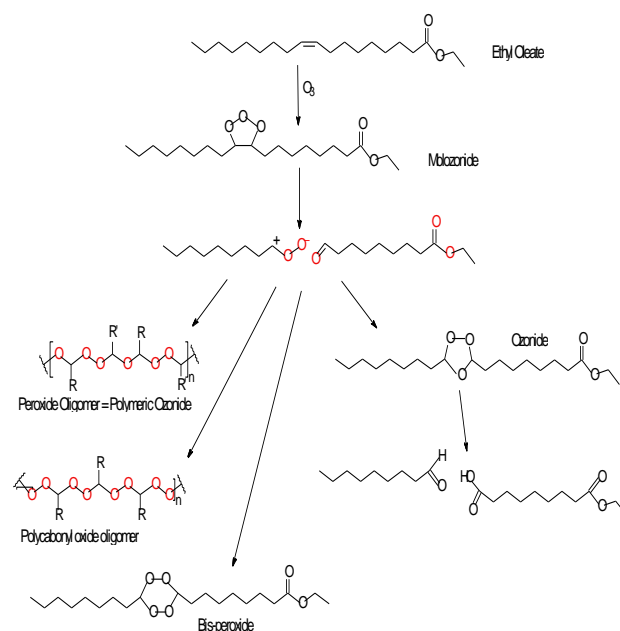
Introduction

Previously¹ we have shown that the decomposition enthalpy of ethyl oleate ozonide can be predicted by a simple thermochemical estimation using the group increment approach proposed by Van Krevelen² and integrated with that of Benson.³

The first calculation was the determination of the enthalpy of formation (ΔH_f°) of the ozonide in the 1,2,4-trioxolane form (in an hypothetical gas phase) under standard conditions of temperature and pressure (25 °C and 1 bar). It was made by using the group increment values proposed by Van Krevelen² and using a group increment of $-114.1 \text{ kJ mol}^{-1}$ for the peroxide group of the 1,2,4-trioxolane ring, which was determined in the previous work from various sources and considerations.¹ The ether group of the 1,2,4-trioxolane ring has the canonical Van Krevelen's value of -120 kJ mol^{-1} .¹ A similar calculation is performed on the ΔH_f° of the classical decomposition product of ozonide i.e. aldehydes and carboxylic acids using again the group increment approach. The thermal decomposition of fatty acids ozonides was investigated for the first time by Privett and Nickell.⁴ The accepted mechanism of the ozonide thermal decomposition involves the homolytic cleavage of O-O bond, which is also considered to be the rate-determining step leading to aldehydes, carboxylic acid and other minor products. The difference between the ΔH_f° of the decomposition products of the ozonide and the formation enthalpy of the latter gives the reaction enthalpy ΔH_R° which corresponds to the decomposition enthalpy ($\Delta H_{\text{dec}}^\circ$) of the ozonide.

This paper is an extension of our thermochemical calculation approach to a series of other olefins determining again the $\Delta H_{\text{dec}}^\circ$ of the resulting ozonides.

The 1,2,3-trioxolane adduct formed in the early stages of olefin ozonolysis rearranges not only into the canonical ozonide with 1,2,3-trioxolane ring but may give other side products like polymeric ozonide, polycarbonyl oxide oligomer and bis-peroxides as shown in Scheme 1. In this paper we show through calculations that the presence of these side products have a minimal effect on the decomposition enthalpy of the ozonide because the decomposition of the side products lead to $\Delta H_{\text{dec}}^\circ$ values analogous to those found for the canonical ozonides.

**Scheme 1.** General ozonolysis reaction products of ethyl oleate

The interest in the thermochemistry of ozonides is primarily linked to the possibility to monitor the progress of an ozonation reaction simply by measuring the decomposition enthalpy of the ozonized reaction mixture as shown recently in the case of the ozonolysis of ethyl oleate.¹

The ozonolysis reaction is of great importance in the industry for example for the preparation of vanillin from isoeugenol and azelaic acid from oleic acid but also a number of other organic and inorganic compounds.⁵ Emerging fields of ozone applications regard drug synthesis,⁶ ozonolysis of terpenes^{7,8} and ozonolysis of vegetable oils.^{1,9-15} The latter topic is attracting a growing attention because it was discovered that the ozonides of vegetable oils have interesting germicidal and fungicidal properties and are being used as ingredients in pharmaceutical and cosmetic formulations.⁹⁻¹⁵ Even wound healing effects were attributed to ozonated vegetable oils and were proposed as ointments for the treatment of burns.¹⁴ Stable ozonides were also found to display interesting anti-malarial activity.¹⁶⁻²² Based on these current and potential applications of ozonides, it is interesting to explore more in detail their thermochemistry focused more on the stability of the ozonide, its thermal decomposition path. The present work is a continuation of our earlier work on the same subject.¹

Results and Discussion

Thermochemistry of 1-alkene ozonides decomposition

The calculations of the enthalpy of formation of a series of 1-alkene ozonides were made according to the Van Krevelen procedure² using a group increment of $-114.1 \text{ kJ mol}^{-1}$ for the peroxide group of the 1,2,4-trioxolane ring and adopting the canonical value of $-120.0 \text{ kJ mol}^{-1}$ for the ether group of the same ring.¹ The calculations have also considered the ring correction for the five membered 1,2,4-trioxolane group which is $+20 \text{ kJ mol}^{-1}$.²

The results of thermochemical calculations are reported in Table 1. According to the Criegee mechanism,²³ a series of expected products from the rearrangement of the molozonide or unstable primary ozonide, are shown in Scheme 1. However, terminal alkenes give little or no cross-ozonide formation.²³ Consequently, the main product of ozonization of terminal olefins is necessarily the asymmetric ozonide [A] shown in Fig.1, while the symmetric structure [B] of the cross-ozonide is not formed or may be present in small amounts. Similarly, the cross-ozonide [C] is as well not formed from the ozonolysis of terminal olefins.²³

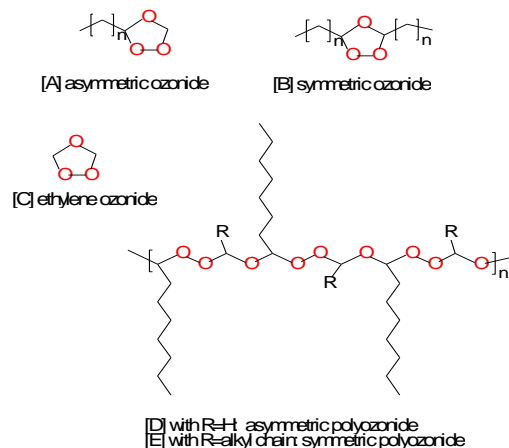


Figure 1. Ozonides formed from terminal olefins after the molozonide rearrangement. The main product is structure [A].

The ozonolysis of alkenes leads inevitably to the formation of polyozonides with structure [D] and [E] (Fig.1) as side or main reaction products in many cases.²³⁻²⁷ The polyozonide structure is analogous to the structure of the canonical ozonide but instead of being cyclic it is a straight chain and the resulting oligomer may be linear or even cyclic and may be asymmetric [D] and symmetric [E] reflecting the structure of the canonical ozonide in straight chain. In the case of terminal olefins ozonation, the main products are the asymmetric ozonide [A] and its linear oligomer [D]. The enthalpy of formations of the cross-ozonide with symmetric structure [B] and the corresponding polyozonide [E] are also given in Table 1.

Table 1. Enthalpy of formation of 1-olefin ozonides (kJ mol^{-1})

Parent olefin	Asymmetric and symmetric ozonides and polyozonides (Fig.1)			
	[D]	[A]	[E]	[B]
Ethylene	-278.1	-258.1	-278.1	-258.1
Propene	-304.8	-284.8	-331.5	-311.5
1-Butene	-326.8	-306.8	-375.5	-355.5
1-Pentene	-348.8	-328.8	-419.5	-399.5
1-Hexene	-370.8	-350.8	-463.5	-443.5
1-Heptene	-392.8	-372.8	-507.5	-487.5
1-Octene	-414.8	-394.8	-551.5	-531.5
1-Nonene	-436.8	-416.8	-595.5	-575.5
1-Decene	-458.8	-438.8	-639.5	-619.5
1-Undecene	-480.8	-460.8	-683.5	-663.5
1-Dodecene	-502.8	-482.8	-727.5	-707.5
1-Tridecene	-524.8	-504.8	-771.5	-751.5
1-Tetradecene	-546.8	-526.8	-815.5	-795.5
1-Pentadecene	-568.8	-548.8	-859.5	-839.5
1-Hexadecene	-590.8	-570.8	-903.5	-883.5
1-Heptadecene	-612.8	-592.8	-947.5	-927.5
1-Octadecene	-634.8	-614.8	-991.5	-971.5

In our calculation, we estimate the difference in the formation enthalpy between the asymmetric ozonide [A] and its straight chain oligomer [D] by considering $+20 \text{ kJ mol}^{-1}$ as correction for 5 ring for the ozonide [A]. In this way, the formation enthalpy of [A] is systematically higher by 20 kJ mol^{-1} than the formation enthalpy of the corresponding polyozonide [D] and the same applies for the cross-ozonide [B] toward the corresponding polyozonide [E] (see Table 1).

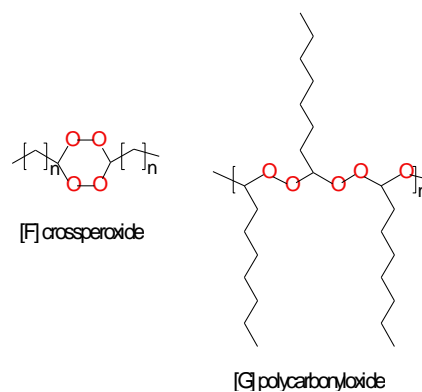


Figure 2. Other products formed in terminal olefin ozonolysis reactions

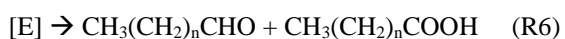
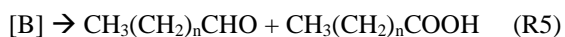
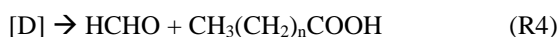
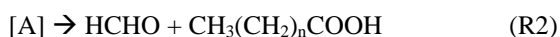
The reason why the asymmetric ozonide [A] (and its oligomer [D]) is by far the main ozonolysis product of terminal olefins is due to the fact that the molozonide of any 1-alkene decomposes into two fragments, the most alkylated being under the form of carbonyl oxide while the less alkylated fragment gives the aldehyde.²³ Since the carbonyl oxide of the type $\text{CH}_3\text{-(CH}_2\text{)}_n\text{-CH}^+\text{-O-O}^-$ is the main fragment of molozonide decomposition, in addition to the regular ozonide with asymmetric structure [A], it can also give a series of other products shown in Fig. 2 and consisting of the bis-peroxide with structure [F] and the polycarbonyl oxide oligomer with structure [G].²³⁻²⁵

In Table 2 are reported the enthalpy of formation of a series of bis-peroxides derived from terminal olefins. In this case the difference in the enthalpy of formations between the cyclic structure [F] and the straight chain of the polycarbonyl oxide structure [G] is only -3 kJ mol^{-1} for the former, so that it is assumed that the free energy of formation of [F] is practically identical to that of [G].

Table 2. Enthalpy of formation (kJ mol^{-1}) of aldehydes and carboxylic acid derived from the decomposition of ozonides; enthalpy of formation of cyclic peroxide [F] and [G] of Fig. 2

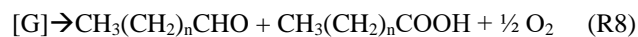
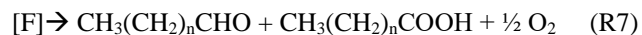
Parent Olefin	Products		
	Aldehyde	Carboxylic acid	[F] and [G]
Ethylene	-118	-381	-275.2
Propene	-171	-439	-317.8
1-Butene	-193	-461	-361.8
1-Pentene	-215	-483	-405.8
1-Hexene	-237	-505	-449.8
1-Heptene	-259	-527	-493.8
1-Octene	-281	-549	-537.8
1-Nonene	-303	-571	-581.8
1-Decene	-325	-593	-625.8
1-Undecene	-347	-615	-669.8
1-Dodecene	-369	-637	-713.8
1-Tridecene	-391	-659	-757.8
1-Tetradecene	-413	-681	-801.8
1-Pentadecene	-435	-703	-845.8
1-Hexadecene	-457	-725	-889.8
1-Heptadecene	-479	-747	-933.8
1-Octadecene	-501	-769	-977.8

Having determined the enthalpy of formation of all key ozonolysis products of terminal olefins and reasonably assuming that their thermal decomposition leads in any case to the formation of aldehydes and carboxylic acids, we have also calculated the enthalpy of formation of the expected aldehydes and carboxylic acids from the decomposition of the ozonides of terminal olefins according to the general scheme:



The enthalpy of formation of the corresponding acids and aldehydes are reported in Table 2.

Furthermore, also the bis-peroxide [F] and the polycarbonyl oxide [G] decompose in a similar way:



Using the calculated enthalpies of formation reported in Table 1 and 2, we have calculated the enthalpies of reactions R1-R8 which are the theoretical decomposition enthalpies of the ozonides and the ozonolysis products and are reported in Table 3.

The calculations show that for any terminal olefin ozonide with structure [A], irrespective of its alkyl chain length, the decomposition enthalpy according to R1 and R2 is approximately -270 kJ mol^{-1} (see Table 4). The corresponding decomposition enthalpy of the polyozonides with structure [D] and with reaction paths R3 and R4 is about -250 kJ mol^{-1} .

Table 3. Enthalpy of reaction for the decomposition of ozonides and peroxides considered in the text.

Reaction	kJ mol^{-1}
R1	-267.2
R2	-272.2
R3	-247.2
R4	-252.2
R5	-298.5(*)
R6	-278.5(*)
R7	-292.2
R8	-295.2

(*) Calculated but not occurring

Although the formation of symmetric ozonide [B] and the corresponding polyozonide [E] is not expected in terminal olefins, their calculated decomposition enthalpies according to R5 and R6 are $-298.5 \text{ kJ mol}^{-1}$ and $-278.5 \text{ kJ mol}^{-1}$ respectively. Instead, the formation of the bis-peroxide [F] and the corresponding polycarbonyl oxide [G] are, at least, expected as side products in the ozonation of terminal olefins and their decomposition enthalpy according to R7 and R8 are respectively $-292.2 \text{ kJ mol}^{-1}$ and $-295.2 \text{ kJ mol}^{-1}$ once again irrespective of the length of the side alkyl chain of the ozonide (see Table 4).

The conclusion from these thermochemical estimations is that any ozonide from a terminal olefin should decompose with a release of energy comprised from a minimum of -295 kJ mol^{-1} to a maximum of -250 kJ mol^{-1} depending on the proportion of canonical ozonide [A] or polyozonide [D] present in the reaction mixture and the bis-peroxide [F] or the polycarbonyl oxide [G] eventually present.

This is a very important result because it shows that both terminal olefin ozonides and regular ozonides or the corresponding polyozonides have the same decomposition enthalpy. The decomposition enthalpy can increase if there is the formation of the bis-peroxide [F] and the polycarbonyl oxide [G]. For 1-decene some authors^{26,27} have shown that the ozonide [A] yield is about 55% at room temperature the remaining 45% can be described as a mixture of [D], [F] and [G].

Table 4. Calculated decomposition enthalpy of a series of 1-alkene ozonides expressed in kJ mol⁻¹ and in J g⁻¹

Alkene	Molecular weight		Average ΔH_{dec} value		Upper limit	
	Olefine	Ozonide	kJ mol ⁻¹	J g ⁻¹	kJ mol ⁻¹	J g ⁻¹
Propene	42.08	90.08	-270	-2997	-295	-3275
1-Butene	56.11	104.11	-270	-2594	-295	-2834
1-Pentene	70.14	118.14	-270	-2286	-295	-2497
1-Hexene	84.16	132.16	-270	-2043	-295	-2232
1-Heptene	98.19	146.19	-270	-1847	-295	-2018
1-Octene	112.22	160.22	-270	-1685	-295	-1841
1-Nonene	126.24	174.24	-270	-1550	-295	-1693
1-Decene	140.27	188.27	-270	-1434	-295	-1567
1-Undecene	154.30	202.30	-270	-1335	-295	-1458
1-Dodecene	168.32	216.32	-270	-1248	-295	-1364
1-Tridecene	182.35	230.35	-270	-1172	-295	-1281
1-Tetradecene	196.38	244.38	-270	-1105	-295	-1207
1-Pentadecene	210.41	258.41	-270	-1045	-295	-1142
1-Hexadecene	224.43	272.43	-270	-991	-295	-1083
1-Heptadecene	238.46	286.46	-270	-943	-295	-1030
1-Octadecene	252.49	300.49	-270	-899	-295	-982
1-Nonadecene	266.51	314.51	-270	-859	-295	-938
1-Eicosene	280.54	328.54	-270	-822	-295	-898
1-Heneicosene	294.57	342.57	-270	-788	-295	-861
1-Docosene	308.59	356.59	-270	-757	-295	-827
1-Tricosene	322.62	370.62	-270	-729	-295	-796
1-Tetracosene	336.65	384.65	-270	-702	-295	-767

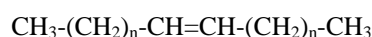
Thus, the decomposition enthalpy of 1-decene ozonide, intended as crude mixture, should be expected to have a minimum value at -295 kJ mol⁻¹, while the decomposition enthalpy of the pure ozonide [A] marks the average temperature limit, i.e. -270 kJ mol⁻¹ (which is indeed the approximate average between the lower limit of -295 kJ mol⁻¹ and the upper limit of -250 kJ mol⁻¹).

This result represents a correction of our earlier estimation which suggested a higher decomposition enthalpy for 1-decene ozonide because of a mistake.¹ Furthermore, the decomposition enthalpy of 1-decene ozonide measured by Anachkov et al.²⁸ as 349 kJ mol⁻¹ appears considerably higher than the expected value from those reported in the present work.

Although the Table 4 shows that the decomposition enthalpy of 1-alkene ozonides is constant when reported in kJ mol⁻¹, it is not constant if it is expressed as J/g because the decomposition enthalpy is smaller for compounds having higher molecular weight. This could seem obvious but since the decomposition enthalpy is measured by DSC and automatically expressed in J/g, the Table 4 could be used for the immediate judgement of the results and for the quick conversion from J g⁻¹ to kJ mol⁻¹.

Thermochemistry of symmetric alkene ozonides decomposition

The enthalpies of formation of the ozonides of symmetrical alkenes having the general structure as shown below,



were similarly obtained through the Van Krevelen group increment approach.²

Table 5. Calculated enthalpies of formation of a series of symmetric alkene ozonides, polyozonides, bis-peroxides and aldehydes and carboxylic acids derived from the decomposition reaction of the ozonides (in kJ mol⁻¹)

Alkene	Polyozonide	Ring ozonide	Aldehyde	Carboxylic acid	Cyclic bisperoxide
2-Butene	-331	-311	-171	-439	-326
3-Hexene	-375	-355	-193	-461	-370
4-Octene	-419	-399	-215	-483	-414
5-Decene	-463	-443	-237	-505	-458
6-Dodecene	-507	-487	-259	-527	-502
7-Tetradecene	-551	-531	-281	-549	-546
8-Hexadecene	-595	-575	-303	-571	-590
9-Octadecene	-639	-619	-325	-593	-634
10-Eicosene	-683	-663	-347	-615	-678

The enthalpies of formation of the resulting ozonides, the polyozonides and the cyclic bis-peroxide or the linear polycarbonyloxide are reported in Table 5. In this table, are also reported the formation enthalpies of the expected products derived from the decomposition of the ozonides and the decomposition of the bis-peroxides of these series to the corresponding aldehydes and carboxylic acids.

It is interesting to note that the symmetric olefins give cross-ozonides having the same structure as the canonical ozonides. This simplifies greatly the complexity of the possible reaction products between ozone and the olefin after the Criegee rearrangement.

Indeed symmetric olefins were used to study another curious phenomenon of the structure of ozonides which may occur in cis and trans form.^{29,30}

Unfortunately the group increment approach in thermochemical calculations is not enough refined to be able to distinguish between the cis and trans isomers of ozonides. Another interesting general result in the ozonation of symmetric olefins is the fact that the ozonation of a cis olefin leads predominantly to a cis ozonide and viceversa.^{29,30} We cannot go through the subtle reasons for these results which are in any case explained well in ref.,²³ and involve the stereospecific 1,3 dipolar cycloaddition of ozone to a double bond.

Another aspect of the symmetric olefin ozonation is the ozonide yield. Cis-olefins give systematically a significantly higher canonical ozonide yield (as total sum of cis and trans ozonide) than the trans olefins. At higher olefin concentration in the reaction mixture the typical ozonide yield is 66% in the ozonation of a cis-olefin and only 33% in the ozonation of the trans-olefin. These yields can be increased respectively to 95% and 65% if the ozonation is conducted at high dilution in an inert solvent like pentane.^{29,30} The effect of dilution on the yield is an important point. The dilution minimizes the formation of polyozonides and polycarbonyloxides and increases the yield of regular (canonical) ozonide. Conversely, at high olefin concentration the formation of the polyozonides and polycarbonyloxides is favoured especially if the starting substrate is the trans-olefin.^{29,30}

In Table 6 are reported the calculation results regarding the decomposition enthalpy of the ozonides of symmetric olefins. Also in this case the canonical ozonide releases the largest amount of decomposition energy i.e. -298 kJ mol^{-1} followed by the decomposition enthalpy of the bis-peroxide or polycarbonyl oxide at -284 kJ mol^{-1} and, finally by the polyozonide at -278 kJ mol^{-1} . It is interesting to note that the decomposition enthalpy of the four main ozonolysis products are spread into a narrow region of $-288 \pm 10 \text{ kJ mol}^{-1}$ while in the case of terminal olefin ozonides the range was $-272 \pm 22 \text{ kJ mol}^{-1}$.

These theoretical calculations are of practical importance in predicting the decomposition enthalpies of the mixtures of crude ozonation products derived from the ozonolysis of olefins and in showing that the ozonide decomposition enthalpy is the same for a selected homologous series if expressed in kJ mol^{-1} .

The decomposition of the ozonides of unsaturated fatty acids esters

The purpose of this study is to predict the decomposition enthalpy of oleic acid ethyl ester and to compare the resulting value with the decomposition enthalpy of ozonides of all other unsaturated fatty acids ethyl ester. Furthermore, the theoretical values of the decomposition enthalpy are compared with the experimental values. Although a series of unsaturated fatty acids are listed in Table 7, we focus our attention to the oleic acid ethyl ester.

The calculated enthalpy of formation of ethyl oleate ozonide (Fig. 3 structure H) is $-998.5 \text{ kJ mol}^{-1}$.¹ If a $+20 \text{ kJ mol}^{-1}$ is taken as the correction for the ozonide ring,² then the mentioned value is more correctly attributable to the ethyl oleate polymeric ozonide (Fig. 3 structure I), while for the canonical ozonide the enthalpy of formation is $-978.5 \text{ kJ mol}^{-1}$.

Table 6. Calculated decomposition enthalpies of symmetrical olefins ozonides type R-CH=CH-R

Compound	Decomposition enthalpy, kJ mol^{-1}		
	canonical ozonide	polyozonide	cyclic peroxide
2-Butene	-298,5	-278,5	-284,4
3-Hexene	-298,5	-278,5	-284,4
4-Octene	-298,5	-278,5	-284,4
5-Decene	-298,5	-278,5	-284,4
6-Dodecene	-298,5	-278,5	-284,4
7-Tetradecene	-298,5	-278,5	-284,4
8-Hexadecene	-298,5	-278,5	-284,4
9-Octadecene	-298,5	-278,5	-284,4
10-Eicosene	-298,5	-278,5	-284,4

Table 7. A series of unsaturated fatty acids

Trivial name	Systematic name	Mw
Palmitoleic acid	Z-9-Hexadecenoic acid	254,408
Vaccenic acid	(E-11)-Octadecenoic acid	282,461
Paulinic acid	(Z-13)-Eicosenoic acid	310,51
Oleic acid	(Z-9)-Octadecenoic acid	282,46
Elaidic acid	(E-9)-Octadecenoic acid	282,46
Gondoic acid	(Z-11)-Eicosenoic acid	310,51
Erucic acid	(Z-13)-Docosenoic acid	338,57
Nervonic acid	(Z-15)-Tetracosenoic acid	366,62

The enthalpies of formation of a series of other products, which can be formed from the ozonolysis of ethyl oleate based on the Criegee mechanism, are reported in Table 8 wherein the decomposition enthalpies are also listed in the last column. The chemical structures of these products are illustrated in Fig. 3. In our simplified model we have assumed that the thermal decomposition of the ozonides leads to the formation of a mixtures of carboxylic acid and aldehyde as already discussed in the previous sections for other simpler olefins. Knowing the enthalpies of formation of these acids and aldehydes it is possible to predict the decomposition enthalpy of the given ozonide to the carboxylic acid and aldehyde derivatives.

The case of ethyl oleate ozonolysis is the most complex among those examined in the present work since the olefin is asymmetric and consequently it can give a rich mixture of ozonolysis products ranging from canonical ozonide, cross-ozonide, polyozonides, symmetric and asymmetric bis-peroxide and symmetric/asymmetric polycarbonyl oxide (see Fig. 3).

Table 8. Calculated enthalpies of formation of ethyl oleate ozonides, polyozonides and bis-peroxide and the resulting calculated decomposition enthalpy (all values in kJ mol^{-1}); the structures are reported in Fig. 3.

Compound	ΔH_f°	ΔH_{dec}
Canonical ozonide [H]	-978,5	-298,5
Polyozonide [I]	-998,5	-278,5
Canonical bis-peroxide [J]	-992,6	-284,4
Alkyl-Alkyl cross-ozonide [K]	-619,5	-298,5
Alkyl-Alkyl cross-polyozonide [L]	-639,5	-278,5
Alkyl-Alkyl bis-peroxide [M]	-633,6	-284,4
Ester-Ester cross-ozonide [N]	-1337,5	-298,5
Ester-Ester polyozonide [O]	-1357,5	-278,5
Ester-Ester bis-peroxide [P]	-1351,6	-284,4

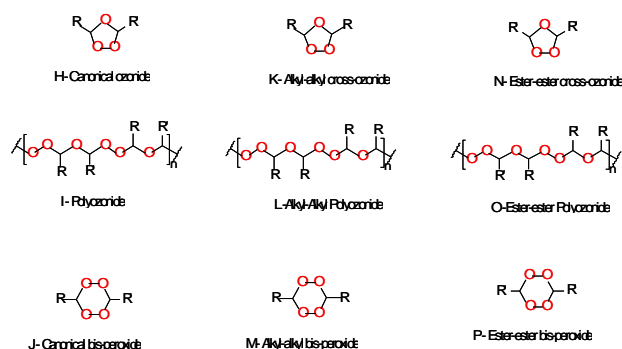


Figure 3. Products derived from the ozonation of ethyl oleate or other fatty acids esters

It is interesting to note that all the calculated values of decomposition enthalpy for any considered ozonolysis intermediate are between -278.5 to -298.5 kJ mol $^{-1}$. This result is very important because it shows that any ozonation product of an asymmetric olefin like ethyl oleate will decompose with the release of approximately the same amount of energy. This implies that for the study of the decomposition of ozonides of asymmetric olefins there is no need to isolate the single canonical ozonide [H] and then study its own decomposition. Instead, it is sufficient to study the decomposition of the crude ozonation mixture without caring about the exact proportion of the various possible components ([H-P] of Fig. 3) because the amount of heat released will be necessarily inside the range lying between -278.5 to -298.5 kJ mol $^{-1}$ assuming that the decomposition products are a mixture of aldehydes and carboxylic acids.

The values for the decomposition of ethyl oleate ozonide, Table 8, are applicable to all the homologous series of asymmetric olefins (Table 7) either as ethyl ester or as methyl ester or as a free fatty acid.

Although in theoretical calculation we considered all the possible reaction products in the ozonolysis of ethyl oleate (Fig. 3), the experimental reality is less complex.³¹⁻³³ First, the cleavage of the ozonolysis products of oleic acid are essentially azelaic acid, azelaic semialdehyde, pelargonaldehyde and pelargonic acid.³¹ Second, the ozonation of methyl oleate or other unsaturated fatty acids give high yields of canonical ozonide [H] of Fig. 3 especially if the reaction is conducted under dilution of an inert solvent like pentane.^{32,33} Of course the lack of dilution will favour the formation of other by-products like for example the cross-ozonides [K] and [N] of Fig. 3. The ozonation of methyl oleate or the ozonation of the trans isomer methyl elaidate give identical mixtures of cis and trans canonical ozonides [H].^{32,33} Our calculations are not refined enough to permit a distinction between cis and trans isomers of ozonides. Another important experimental fact is that the high yield of canonical ozonide [H] is also favoured when starting with a cis olefin like methyl oleate or ethyl oleate.^{32,33} The trans-olefin isomer like methyl elaidate and ethyl elaidate tend to give lower yield of canonical ozonide [H] of Fig.3 favouring other products including the polyozonide [I] of Fig. 3.^{32,33}

Indeed, in our earlier study on the decomposition of ethyl oleate ozonide (crude mixture) we measured a $\Delta H_{\text{dec}} = -243$

kJ mol $^{-1}$ while the calculated theoretical threshold is -278.5 kJ mol $^{-1}$.¹ Further work is in progress in this field and it can be anticipated that with further experimental refinements the decomposition enthalpy of ethyl oleate ozonide matches the theoretical calculation range for ΔH_{dec} .³⁴

Conclusions

With group increment calculation approach is shown that all the homologous series of terminal 1-olefin ozonation products decompose releasing an enthalpy of -272 ± 22 kJ mol $^{-1}$. The upper limit of the decomposition enthalpy is released by the decomposition of the bisperoxide structure [F] and polycarbonyloxide structure [G] of Fig. 2 with $\Delta H_{\text{dec}} = -295$ kJ mol $^{-1}$. The canonical ozonide [A] of Fig. 1 shows an average $\Delta H_{\text{dec}} = -270$ kJ mol $^{-1}$. In the ozonation of terminal olefin the latter compound is known to be preponderant. Finally, the polyozonide [D] of Fig. 2 decomposition represents the lower limit with $\Delta H_{\text{dec}} = -250$ kJ mol $^{-1}$.

The ozonation products of symmetrical olefins decompose releasing -288 ± 10 kJ mol $^{-1}$. The canonical ozonide (which is always preponderant as ozonation product and under certain reaction conditions the unique compound) shows a $\Delta H_{\text{dec}} = -298$ kJ mol $^{-1}$. The bis-peroxide and polycarbonyloxide show a $\Delta H_{\text{dec}} = -284$ kJ mol $^{-1}$ and finally the corresponding polyozonide decomposes with a $\Delta H_{\text{dec}} = -278$ kJ mol $^{-1}$.

Monounsaturated fatty acids and fatty acid esters represent a case of asymmetrical olefin with two different substituents R and R' attached to the double bonds (see Fig. 3). Also here, the analysis of all the possible ozonation products and their decomposition (see Fig. 3) leads to the conclusion that $\Delta H_{\text{dec}} = -288 \pm 10$ kJ mol $^{-1}$ with the lower limit of -298 kJ mol $^{-1}$ represented by the decomposition of the canonical ozonide [H] and cross-ozonides [K] and [N] which should be also the preponderant structures. The intermediate decomposition value is represented by the decomposition of bis-peroxide and polycarbonyloxide (structures [J], [M] and [P] of Fig. 3). The upper limit is represented by the polyozonide decomposition (structures [I], [L] and [O] of Fig. 3) with $\Delta H_{\text{dec}} = -278$ kJ mol $^{-1}$.

References

- Cataldo, F. *Chem. Phys. Lipids* **2013**, 175-176, 41.
- Van Krevelen, D. W. **1990**. *Properties of Polymers. Their Correlation with Chemical Structure; Their Numerical Estimation and Prediction from Additive Group Contributions*. Elsevier, Amsterdam, Chapter 20.
- Benson, S. W. *Thermochemical Kinetics* 2nd ed. Wiley, New York, **1976**, 266.
- Privett, O. S., Nickell, E. C., *J. Am. Oil Chem. Soc.*, **1966**, 43, 393.
- Rakovsky, S., Zaikov, G. E., *Kinetics and Mechanism of Ozone Reactions with Organic and Polymeric Compounds in Liquid Phase*. **1998**, Nova Science Publishers Inc. New York.
- Van Ornum, S. G., Champeau R. M., Pariza, R., *Chem. Rev.*, **2006**, 106, 2990.
- Stolle, A., *Eur. J. Org. Chem.*, **2013**, 2265.

- ⁸Cataldo, F., Ursini, O., Lilla, E., Angelini, G., *Ozone Sci. Eng.*, **2010**, 32, 274.
- ⁹Lezcano, I., Nuñez, N., Espino, M. Gómez, M., *Ozone Sci. Eng.*, **2000**, 22, 207.
- ¹⁰Fernández Torres, I., Curtiellas Piñol, V., Sánchez Urrutia, E., Gómez Regueiferos, M., *Ozone Sci. Eng.*, **2006**, 28, 187.
- ¹¹Díaz, M. F., Gavín, J. A., Gómez, M., Curtielles, V., Hernández, F., *Ozone Sci. Eng.*, **2006**, 28, 59.
- ¹²Menéndez, S., Re, I., Falcón, I., Argote, M. B., Méndez, I., Fernández, D., Elías-Calle, B., Valero, M., *Int. J. Ozone Therapy*, **2008**, 8, 25.
- ¹³Hernández, F., Hernández, F., Zamora, Z., Díaz, M., Ancheta, O., Rodríguez, S., Torres, D., *Exp. Parasitology*, **2009**, 121, 208.
- ¹⁴Sakazaki, F., Kataoka, H., Okuno, T., Ueno, H., Semma, M., Ichikawa, A., Nakamuro, K., *Ozone Sci. Eng.*, **2007**, 29, 503.
- ¹⁵Skalska, K., Ledakowicz, S., Perkowski, J., Sencio, B., *Ozone Sci. Eng.*, **2009**, 31, 232-237.
- ¹⁶Almeida Barbosa, L. C., Cutler, D., Mann, J., Kirby, G. C., Warhurst, D. C., *J. Chem. Soc. Perkin Trans. I*, **1992**, 3251.
- ¹⁷Wang, X., Dong, Y., Wittlin, S., Charman, S.A., Chiu, F. C., Chollet, J., Katneni, K., Mannila, J., Morizzi, J., Ryan, E., Scheurer, C., Steuten, J., Santo-Tomas, J., Snyder, C., Vennerstrom, J. L., *J. Med. Chem.*, **2013**, 56, 2547.
- ¹⁸Kumar, N., Sharma, M., Rawat, D. S., *Curr. Med. Chem.*, **2011**, 18, 3889.
- ¹⁹Wang, X., White, K. L., Wittlin, S., Zhou, L., Vennerstrom, J. L., *Proc. Natl. Acad. Sci. U.S.A.*, **2011**, 108, 4400.
- ²⁰Dong, Y., Wittlin, S., Sriraghavan, K., Chollet, J., Charman, S. A., Charman, W. N., Scheurer, C., Urwyler, H., Santo Tomas, J., Snyder, C., Morizzi, J., Koltun, M., Creek, D., Matile, H., Wang, X., Padmanilayam, M., Dorn, A., Brun, R., Vennerstrom, J.L. *J. Med. Chem.* **2010**, 53, 481.
- ²¹Zhou, L., Alker, A., Ruf, A., Wang, X., Chiu, F.C., Morizzi, J., Charman, S. A., Charman, W. N., Scheurer, C., Wittlin, S., Dong Y., Hunziker D., Vennerstrom J.L. *Bioorg. Med. Chem. Lett.* **2008**, 18,1555.
- ²²Vennerstrom, J. L., Fu, H. N., Ellis, W. Y., Ager, A.L. Jr, Wood, J. K., Andersen, S. L., Gerena, L., Milhous, W. K., *J. Med. Chem.* **1992**, 35, 3023.
- ²³Smith, M. B., March, J. *Advanced Organic Chemistry* 5th Ed. J. Wiley & Sons Inc., New York, **2001**, 1522-1525.
- ²⁴Razumovskii, S. D., Zaikov, G. E., *Ozone and its Reactions with Organic Compounds*, **1984**, Elsevier, Amsterdam.
- ²⁵Bailey, P. S. *Ozonation in Organic Chemistry. Volume 1: Olefinic Compounds*, **1978**, Academic Press, New York.
- ²⁶Greenwood, F. L., Rubinstein, H., *J. Org. Chem.*, **1967**, 32, 3369.
- ²⁷Diaper, D. G. M., *Can. J. Chem.*, **1968**, 46, 3095.
- ²⁸Anachkov, M. P., Rakovsky, S. K., Fotty, R. K., Stoyanov, A. K., *Thermochim. Acta*, **1994**, 237, 213.
- ²⁹Murray, R. W., Youssefyeh, R. D., Williams, G. J., *Tetrahedron* **1968**, 24, 4337.
- ³⁰Murray, R. D., Williams, G. J., *Adv. Chem. Ser.*, **1968**, 77, 32.
- ³¹Pryde, E. H., Anders, D. E., Teeter, H. M., Cowan, J. C., *J. Org. Chem.* **1960**, 25, 618.
- ³²Privett, O. S., Nickell, E. C., *J. Lipid Res.*, **1963**, 4, 208.
- ³³Nickell, E. C., Albi, M., Privett, O. S., *Chem. Phys. Lipids* **1976**, 17, 378.
- ³⁴Cataldo, F., *Paper in preparation*.

Received: 14.12.2013.

Accepted: 20.01.2014.



SHAPE EVOLUTION OF STRONTIUM CARBONATE ARCHITECTURES USING NATURAL GUMS AS CRYSTAL GROWTH MODIFIERS

B. Sreedhar,^{[a,]*}, M. Sulochana,^[b] Ch. Satya Vani,^[c] D. Keerthi Devi,^[a] and N. V. Subba Naidu^{[b]*}

Keywords: Keywords: natural gums; screw capped; self assembly; architectures; SrCO₃

Strontium carbonate architectures assembled from nanorods are successfully synthesized at room temperature and screw capped method at 100 °C. Our experiments show that the protocol followed for the synthesis of SrCO₃ as well as the concentration of various gums used, play an important role in the size and morphology of SrCO₃. Here in, we obtained aragonite type nanorod aggregates with unusual morphologies via transformation of metal carbonates at different conditions using natural gums as additives. A rational mechanism based on the oriented self-assembly of SrCO₃ nuclei is proposed for the formed architectures. The crystals undergo an interesting morphology changes and have been well characterized by X-ray diffraction (XRD), Scanning Electron Microscopy (SEM), Transmission Electron Microscopy (TEM), Thermogravimetric Analysis (TGA) and Fourier Transform Infrared spectroscopy (FT-IR) techniques. This method is simple, low-cost and environmentally friendly route for the synthesis of SrCO₃ architectures with altogether different morphologies.

*Corresponding Authors

Fax: +91-40-27160921

E-Mail: sreedharb@iict.res.in

- [a] Inorganic and Physical Chemistry Division, Indian Institute of Chemical Technology (Council of Scientific and Industrial Research), Hyderabad, Andhra Pradesh, 500607, India
- [b] Department of Chemistry, Sri Venkateswara University, Tirupati, Andhra Pradesh, 517 502, India Chapters

morphological controlled synthesis of BaCO₃ and SrCO₃, ZnO nanostructures, in the present work we describe our observations of the use of various other gums - Gum Karaya (GK), Gum Kondagagu (GKG), Gum Olibinum (GO) and Gum Tiruman (GT) on the morphology-controlled biomimetic synthesis of SrCO₃ architectures.

Introduction

Biom mineralization processes to synthesize hierarchical inorganic crystals or hybrid inorganic-organic materials with controlled size and morphology have attracted considerable attention in recent years owing to the importance of such materials in various fields such as medicine, ceramics, catalysis and cosmetics ¹. Fundamental understanding of the formation mechanism and tuning of facile, mild and effective reaction conditions for the synthesis of such materials still remains a great challenge in nanoscience and nanotechnology. Although great progress has been achieved on the synthetic strategies used to date such as co-precipitation, chemical vapor deposition (CVD), hydrothermal route and reverse micelle method, they usually require catalysts, expensive and even toxic templates or surfactants, high temperature, and a series of complicated procedures, thus, suffer from developing tunable protocols to prepare well-defined hierarchical morphology and special architecture forms. Low temperature, surfactant-free, solution-phase chemical fabricating procedure that is environmentally benign and user-friendly still remains a challenge - a struggling task for the synthesis and architecture control of hierarchical nanostructures at room temperature. Use of natural gums – biocompatible and biodegradable materials for bio-inspired morphogenesis strategies is looked as a viable alternative to expensive organic ligands and additives. In continuation of our recent research activities on the use of Gum Acacia (GA) – that is proved to be a very good reducing agent for the reduction of Ag, Pd and Pt, and as a crystal growth modifier for

It is important to select suitable surfactant molecules that act as templates or shape controllers, directing the formation of a structure toward a desired target arrangement – a process of synthesizing inorganic minerals that is controlled by biomolecules or polymers. Biom mineralization of SrCO₃ complex structures can be easily generated by using natural gums as structure directing agents in ambient and low temperature precipitation experiments in the mineralization process. Strontium carbonate is itself an important raw material in modern electronic industry.² Furthermore, strontium carbonate has only one crystal-phase, so it has been widely studied as a model system for bio-crystallization.³⁻⁸ Therefore, controlled synthesis of SrCO₃ crystals has attracted much interest. In order to obtain SrCO₃ hierarchical superstructures, many additives, as crystal growth modifiers and superstructure-directing reagents, have already been attempted to mimic biom mineralization. Strontium carbonate is a very important reagent and has attracted intensive attention because of its interesting additional applications in industry and many other fields: as a constituent of ferrite magnets for small direct current motors, as an additive in the production of glass for color television tubes,⁹ production of iridescent and specialty glasses, chemiluminescence sensors, pigments, driers, paints, pyrotechnics,¹⁰⁻¹⁴ strontium metal and other strontium compounds.¹⁰ Very recently, Shi et al. reported the synthesis of SrCO₃ nanowires and their catalytic activity to ethanol with reaction temperature.¹⁴ Different fabrication methods for the synthesis of SrCO₃ such as self-assembled monolayers,¹⁵⁻¹⁸ ion entrapment method,⁷ hydrothermal method,^{19,20} microemulsion mediated solvothermal method,²¹ homogeneous precipitation by enzyme-catalyzed reaction,²² biological synthesis using the fungus fusarium oxysporum²³ have been reported. SrCO₃ nanostructures with

various morphologies, such as nanowires, nanorods, sphere like and ellipsoid-like particles, were successfully synthesized by a microemulsion-mediated solvothermal method. Du et al²⁴ reported the synthesis of SrCO₃ mesoporous spheres using 1,1,3,3-tetramethylguanidinium lactate as additive. However, there are no reports found in literature on the synthesis of SrCO₃ with different sizes and morphologies by employing natural gums, as controlling the morphology- and size-directing reagent.

Natural gums mainly consist of three fractions (1) Highly branched polysaccharide consisting of galactose backbone with linked branches of D-galactose, L-arabinose, L-rhamnose, which terminate in D-glucuronic acid and 4-O-methyl-D-glucuronic acid. (2) Arabinogalactan-protein complex (GAGP-GA glycoprotein) in which arabinogalactan chains is covalently linked to a protein chain through serine and hydroxyproline groups. (3) Glycoprotein having the highest protein content (~50 wt. %). Gum Karaya (GK) is a vegetable gum produced as an exudate by trees of the genus *Sterculia* and chemically it is an acid polysaccharide. Gum Kondagogu (GKG) is the dried exudates obtained from tree *Cochlospermum gossypium* which belongs to the family Bixaceae and is a hydrophilic biopolymer. Gum Olibanum (GO) is the dried, gummy exudation obtained from various species of Burseraceae trees and is available in small tears or lumps of white-yellowish or yellow-reddish in colour. Gum Tiruman (GT) or Indian gum is a non-starch polysaccharide. In all these gums, the functional group (-OH) present in arabinose and rhamnose and (-COOH) of glucuronic acids play a crucial role in the growth and formation metal carbonates whereas the proteinaceous core with amino acids stabilize the formed metal carbonates.²⁵ It not only acts as a stabilizer,²⁶ but also acts as surfactant and templating agent for which the functional group moieties (-OH, COOH and -NH₂) have been found to play a key role in mimicking the biomineralization process. The crystallization involves the formation of different hierarchical structures like rice grain, doughnut shaped, flower shaped, hexagonal rods and cross shaped which have never been seen before in natural biominerals. Proteins and polysaccharides with complicated patterns of various functional groups in natural gums selectively adsorb on to the metal ion thereby hindering the crystal growth, followed by the mesoscale self-assembly of nanometer-scale building block into hierarchical superstructures.²⁷⁻³² The key reaction of CO₂ with Sr²⁺ ions entrapped within the natural gums leads to the growth of beautiful structures of strontianite nanocrystalline, such an aggregated morphology not normally observed using other surfaces as templates.

Recent work carried out in our group showed that natural gum, Gum acacia (GA) could exert a strong influence on external morphology and/or crystalline structure of barium carbonate³³ and strontium carbonate.³⁴ It was found that different shapes of BaCO₃ and SrCO₃ particles could be successfully obtained. In order to investigate the availability and functionality of other natural gums - Gum Karaya (GK), Gum Kondagogu (GKG), Gum Olibanum (GO) and Gum Tiruman (GT) on the morphological control of other crystals, further studies needed to be conducted.

In the present investigation, rod-, shuttle-like, peanut, bouquet and sphere-like SrCO₃ architectures were achieved by tuning the reaction conditions. This work may provide

new insights into the morphological control of SrCO₃ particles and the controllable synthesis of other novel inorganic material using natural gums. The objective of the current study was thus to evaluate the ability of different gums to inhibit crystal growth of a model compound comparing the different gums at the same molar ratio in different reaction conditions. However, to the best of our knowledge, controlled synthesis of SrCO₃ architectures using natural gums has not been achieved to date.

Experimental Section

Materials and SrCO₃ synthesis

Ammonium carbonate (NH₄)₂CO₃ and strontium chloride (SrCl₂) were of analytical grade and used without further purification. Double distilled water was used in all experiments. In a typical experiment, at room temperature, 0.2662 g (1 mM) of SrCl₂ was taken along with different proportions of homogenized natural gums (0.5 % and 1.0 %) in different 25 ml glass beakers. They were dissolved in 20 ml distilled water and the mixed solution was stirred thoroughly with the help of magnetic stirrer. Then NaHCO₃ (2 mM; 2 ml) solution is added by continuous stirring and kept for 24 h at room temperature. After 24 h, the crystals formed were filtered washed several times with distilled water and dried at room temperature. A similar solution was prepared and heated to 100 °C and kept at this temperature for a fixed time (5 h) by refluxion in tightly fixed screw cap. After 5 h reaction time the screw cap tubes were allowed to cool to 50 °C and maintained at that temperature for about 15 h before being allowed to cool slowly to ambient temperature over 3 to 4 h. The product was separated from the solution by centrifugation, washed with absolute ethanol three times and dried in vacuum. The sizes and morphologies of the as-synthesized crystals have been well characterized by X-ray diffraction (XRD), Scanning Electron Microscopy (SEM), Transmission Electron Microscopy (TEM), Thermogravimetric analysis (TGA) and Fourier Transform Infrared spectroscopy (FT-IR) techniques.

Characterization

X-ray diffraction measurements of the strontium carbonate architectures were recorded on Rigaku diffractometer (Cu radiation, $\lambda = 0.1546$ nm) running at 40 kV and 40 mA (Tokyo, Japan). FT-IR spectra of SrCO₃ structures were recorded with a Thermo Nicolet Nexus (Washington, USA) 670 spectrophotometer. The morphology, microstructure and composition of the samples were examined by scanning electron microscopy (FEI Quanta 200 FEG). The crystals were collected on a round cover glass (1.2 cm), washed with deionised water and dried in a desiccator at room temperature. The cover glass was then mounted on a SEM stub and coated with gold for SEM analysis. Thermogravimetric Analysis (TGA) was carried out on a TGA/SDTA Mettler Toledo 851^e system using open alumina crucibles containing samples weighing about 8–10 mg with a linear heating rate of 10 Kmin⁻¹ in nitrogen atmosphere (flow rate 30 mL min⁻¹). The morphology, size, and shape distribution of the synthesized SrCO₃ nanostructures were observed on TECNAI FE12 TEM instrument operating at 120 kV using SIS imaging software.

The particles were dispersed in methanol and a drop of it was placed on formvar-coated copper grid followed by air drying. The diffraction patterns were recorded at selected area to determine the crystal structure and phases of crystals at 660 mm camera length.

Results and Discussion

Structural characterization of SrCO_3 architectures

The phase composition and phase structure of the SrCO_3 architectures obtained with various gums - gum karaya (GK), gum kondagagu (GKG), gum olibinum (GO) and gum tiruman (GT) at two different gum concentrations (0.5 % and 1.0 %) in screw capped and room temperature methods were examined by XRD. Since all the different shapes have same composition, XRD patterns of the as-synthesized materials without gum and with 1 % gum concentration of the various gums at 100 °C by screw capped method are only shown in Figure 1.

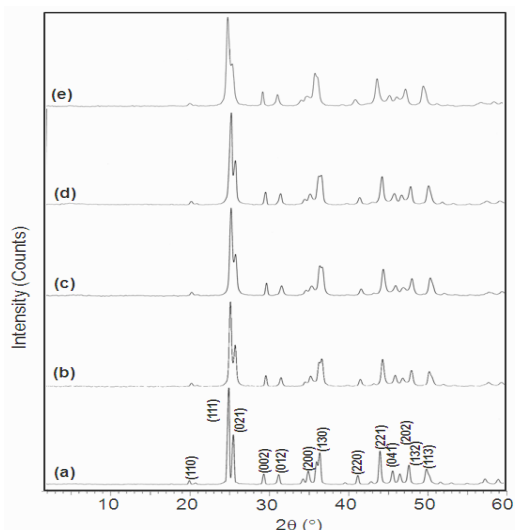


Figure 1. XRD patterns of as synthesized SrCO_3 hierarchical architectures obtained without gum (a), with 1% GK (b), 1 % GKG (c), 1 % GO (d), and 1 % GT (e) in pressure vial at 100 °C for 5 h.

As strontium carbonate is a single-phase crystal, it could be seen that XRD patterns of SrCO_3 prepared with different gums have the same diffraction pattern and all the peaks could be perfectly indexed to a pure orthorhombic structure of strontium carbonate (space group $\text{Pmcn} \{62\}$) of SrCO_3 with lattice constants $a = 5.107 \text{ \AA}$, $b = 8.414 \text{ \AA}$, and $c = 6.029 \text{ \AA}$ (JCPDS card no.05-418) and no characteristic peaks from other impurities have been detected indicating that the as-synthesized products have high phase purity. The XRD patterns of SrCO_3 presented in Figure. 1 exhibit peaks characteristic of scattering angles (2θ) at 20.3, 25.1, 25.8, 29.5, 31.2, 35.1, 36.5, 41.2, 44.0, 45.5, 46.3, 47.7 and 50.1 corresponding to the following diffraction peaks with (hkl) indices (110), (111), (021), (002), (012), (200), (130), (220), (221), (041), (202), (132), and (113) crystallographic planes, respectively similar to pure orthorhombic strontionite [JCPDS-05-418]. It may also be seen that the peak (111) is the strongest, suggesting that SrCO_3 crystals obtained at both room temperature and screw capped methods, grow mainly

along with the (111) phase. The strong and sharp diffraction peaks in Figure 1 indicate that the as obtained SrCO_3 hierarchical architectures are principally crystalline. The absence of some diffraction peaks in Figure 1b-e, when compared to the XRD pattern of SrCO_3 crystals obtained without gum (Figure 1a) is due the presence of gum on the crystal faces, resulting into the formation of an organic-inorganic hybrid material that is in consonance with the observations in TGA analysis.

Effect of additives on the morphology and size of SrCO_3

The SEM micrographs at both lower and higher molar ratio (0.5 % and 1 %) of different natural gums in ambient and screw capped method have been characterized. Figures 2 and 4 show low magnification SEM micrographs of SrCO_3 particles obtained from aqueous solution in the absence and presence of different gums namely, gum karaya (GK), gum kondagagu (GKG), gum olibinum (GO), gum tiruman (GT) synthesized at room temperature and screw capped method at 100 °C. As can be seen from Fig. 2, in the absence of gum, the as-obtained particles appeared bundle-like dendrimers consisting of many small SrCO_3 needles aligned radially towards both ends. Flower-like and bouquet like morphologies of SrCO_3 nanostructures are seen with gum karaya (GK) and gum kondagagu (GKG). Peanut like morphologies are observed commonly in both gum olibinum (GO) and gum tiruman (GT). At higher magnification (Figure 3 and Figure 5) nanocrystals self assembled into interesting morphologies can be clearly seen.

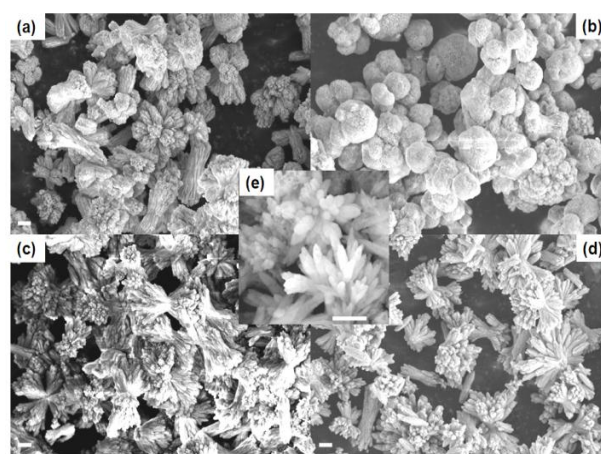


Figure 2. Low magnification SEM images of as synthesized SrCO_3 hierarchical architectures obtained with 1 % GK (a), 1 % GKG (b), 1 % GO (c), with 1 % GT (d), and without gum (e) at room temperature. Scale bar measures 1 μm .

To know the influence of concentration of the various gums on the morphology and size of the products, separate experiments were carried out using 0.5 and 1.0 % gums. Except for a small decrease in the size of the nanostructures, no significant change in the morphology of the synthesized SrCO_3 architectures were identified by changing the concentration of the various gums. This behavior can be attributed due to the effective passivation of the surfaces and suppression of the growth of the nanoparticles through strong interactions with the particles via their main functional molecular groups of gums namely, hydroxyl groups and carboxylic groups. Further observation shows that there exist many fragments ruptured at the middle parts

of the bundles. Therefore, it could be inferred that the middle parts of the bundles are more fragile than their radial branches. When 0.5 % of the various gums were added into the reaction mixture, the morphology of SrCO_3 particles formed showed a significant difference, when compared to the above mentioned bundle like dendrimers formed in the absence of gum.

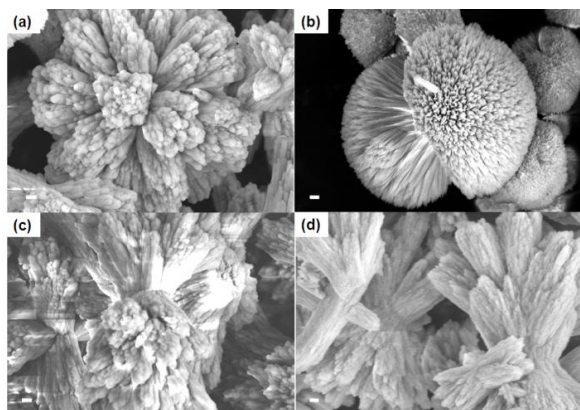


Figure 3. High magnification SEM images of as synthesized SrCO_3 hierarchical architectures obtained with 1 % GK (a), 1 % GKG (b), 1 % GO (c), and 1 % GT (d) at room temperature. Scale bar measures 200 nm.

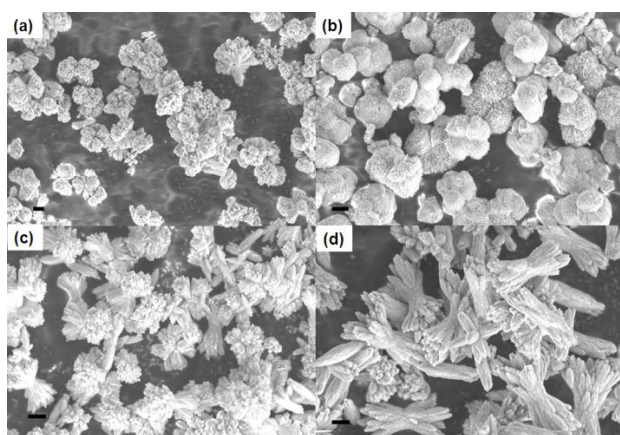


Figure 4. Low magnification SEM images of as synthesized SrCO_3 hierarchical architectures obtained with 1 % GK (a), 1 % GKG (b), 1 % GO (c), and 1 % GT (d) in pressure vial for 5 h. Scale bar measure 1 μm .

The morphology of as synthesized particles with the various gums are more homogenous whatever may be the shape or size they are appearing in and the flower like particles with branches consist of self assembled nanoparticles. Further, on increasing the concentration of the gum (1.0 %), the shape of the formed architectures though remained same showed a decrease in size and depended on the gum used for the synthesis. Significant decrease in size was observed with GK that can be attributed due to the selective oriented adsorption of GK on crystal faces along the growth direction of the needle like branches and due to steric inhibition limits the growth of the needles. At higher concentration of GK (1.0 %), the ends of the dumbbell ends tend to become large and the part that undergoes quenching self-assemble to form of flower like structure with nanocrystals. But in GKG, when the concentration is raised to 1.0 %, like shape with nanocrystals were obtained. As can be seen in Figure 3b, the formation of the nanostructure starts from the centre and then the crystals start to assemble on either direction with the ends of the bouquet having a

larger semi circular morphology. In the case of both GO and GT, the structures formed appear more or less similar in morphology - peanut like structures consisting of aggregated nanocrystals. These peanut like structures appear to be overlapping to form flower like structures with GT (Figure 3d).

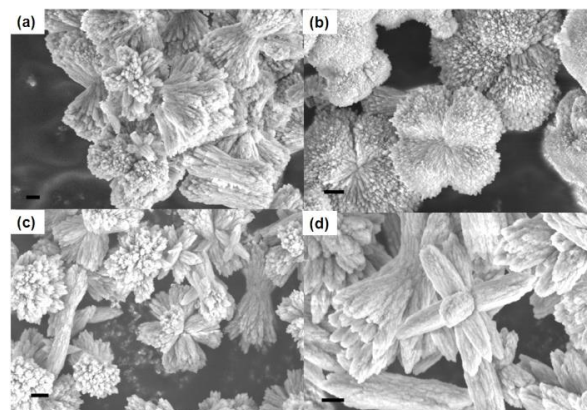


Figure 5. High magnification SEM images of as synthesized SrCO_3 hierarchical architectures obtained with 1 % GK (a), 1 % GKG (b), 1 % GO (c), and 1 % GT (d) in pressure vial for 5 h. Scale bar measure 500 nm.

The morphology and structure of the as-formed SrCO_3 architectures was further confirmed by TEM and the images are shown in Figure 6. As can be seen in Figure 6 individual architectures consisting of nanorods with perfect bouquet, flower like and pea nut like assembly, in accordance to the observations from SEM.

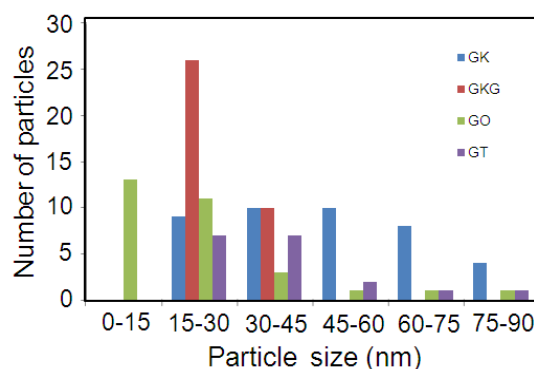
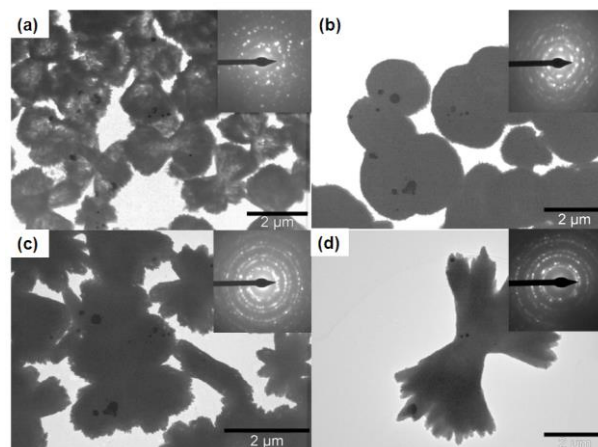


Figure 6. TEM images of as synthesized SrCO_3 hierarchical architectures obtained with 1 % GK (a), 1 % GKG (b), 1 % GO (c), 1 % GT (d) gums in pressure vial for 5h with the respective SAED pattern (inset) and particle size distribution (e).

As we have not observed SrCO_3 as discrete nanorods even at room temperature or in screw capped reaction of 5 h, it clearly indicates that these architectures are actually integrated and are not just aggregations of nanorods into different shapes. The size of the as obtained nanoparticles in screw capped method show a significant dependence on the gums used i.e., for GK 17 - 78 nm, GKG 20 - 38 nm, GO 9 - 58 nm and GT 25 - 57 nm as shown in the particles size distribution figure in Figure 6e. The corresponding selected area electron diffraction patterns for all the as-synthesized SrCO_3 from various gums show clear diffraction spots, reiterating the crystalline nature of the formed nanostructures. Both the XRD and SAED analysis indicate that the anisotropic growth of these architectures is along (111) direction.

FTIR analysis

To identify the growth mechanism and the effect of the different gums on SrCO_3 architectures, the samples were analysed by FT-IR spectroscopy.

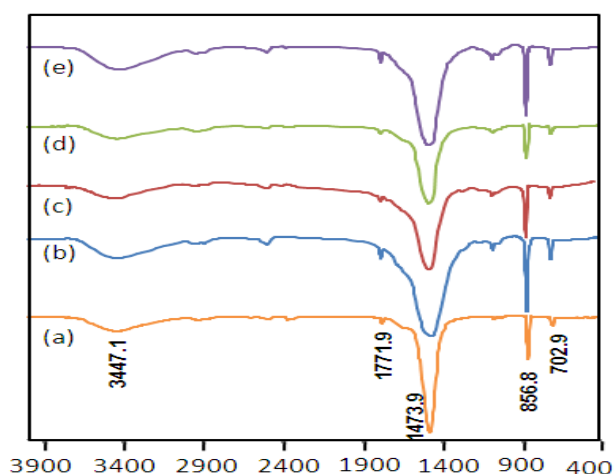


Figure 7. FT-IR spectra of as synthesized SrCO_3 hierarchical architectures obtained without gum (a), with 1 % GK (b), 1 % GKG (c), 1 % GO (d), and 1 % GT(e) at room temperature.

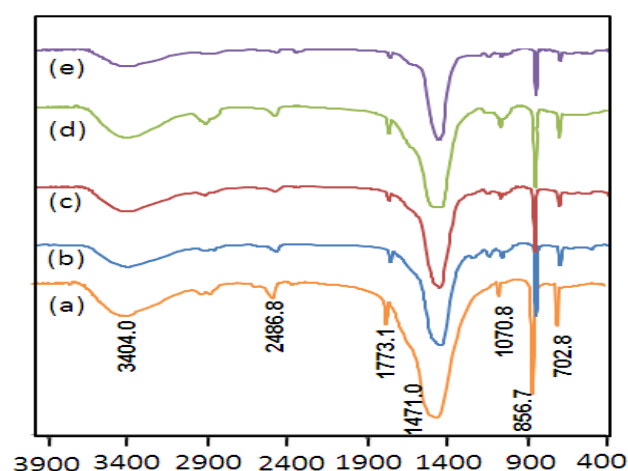


Figure 8. FT-IR spectra of as synthesized SrCO_3 hierarchical architectures obtained without gum (a), with 1 % GK (b), 1 % GKG (c), 1 % GO (d), and 1 % GT(e) in pressure vial at 100 °C for 5 h.

The sharp peaks at 856.8, 702.9 cm^{-1} (Figure 7), 856.7, 702.8 cm^{-1} (Figure 8) are due to the in-plane and out-plane bending of CO_3^{2-} group. The IR bands at 1473.9 and 1471.0 cm^{-1} (Figure 7, 8) correspond to the asymmetric stretching mode of C-O bond while the weak band at 1070 cm^{-1} is attributed to the symmetric C-O stretching vibration. The band at 3447 and 3404 cm^{-1} can be attributed to OH stretching vibration due to hydrogen bonding and/or N-H stretching of the $-\text{NH}_2$ group from the functional groups present in additives. The characterized peaks at 1070, 856, 1473 and 702 cm^{-1} of SrCO_3 crystal correspond to the ν_1 , ν_2 , ν_3 and ν_4 vibration modes, respectively and at 1771.9 and 1773.1 cm^{-1} belongs to the C=O stretching vibration of carboxyl groups.

The FTIR results indicate that all the gums used in this study get adsorbed on the crystal faces during the mineralization process that directs the self-assembling of nanocrystals resulting in interesting architectures and form organic-inorganic hybrid materials.

Thermogravimetric studies

Thermogravimetric analysis helps us to understand the decomposition steps more precisely as we can know the evolved gas fragments as a function of temperature or time. As representative systems, the TG/DTG thermograms of SrCO_3 synthesized with GK, GKG, GO and GT at 100 °C in screw capped reaction are shown in Figure 9a, b, c, d, respectively.

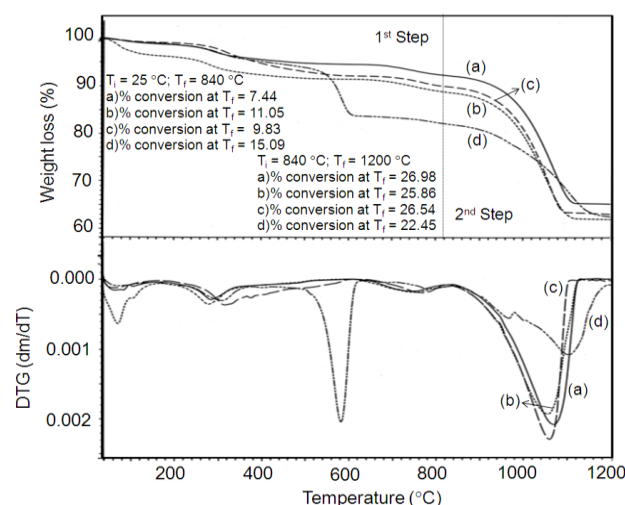


Figure 9. TGA-DTG thermograms of as-synthesized SrCO_3 hierarchical architectures obtained with 1 % GK (a), 1 % GKG(b), 1 % GO (c), and 1 % GT (d) in pressure vial at 100 °C for 5 h.

TGA profile of SrCO_3 structures synthesized without gum³⁷ shows a single step decomposition in the range 850–1050 °C. The corresponding mass loss was quite similar to the theoretical value of the mass loss of the above decomposition (29.81 %) and almost the same with that occurred for the thermal decomposition of the high pure SrCO_3 phase between 900–1150 °C.³⁵ Figure 8 represents the TG-DTG thermograms of SrCO_3 with various gums. The first step in the temperature range between 25–840 °C is due to the decomposition of the various gums in the as-synthesized SrCO_3 nanostructures. Similar decomposition

profile was observed in SrCO_3 nanocrystallites synthesized using GA that was ascribed due to the evolution of CO_2 (mass fragment 44 a.m.u, from the decomposition of –COOH functional groups in GA) from GA component in the inorganic and organic hybrid SrCO_3 nanocrystallites.³⁷ The second step in the temperature range 840-1200 °C can be attributed mainly due to the decomposition of SrCO_3 nanocrystallites into SrO and CO_2 . The corresponding mass losses were found to be 26.98 % (GK), 25.86 % (GKG) 26.54 % (GO), and 22.45 % (GT) that correspond to 29.1 %, 29.0 %, 29.4 %, and 26.4 % respectively of CO_2 from the SrCO_3 nanostructures and that are close to the theoretical value of the mass loss ~ 30 % of the high pure SrCO_3 phase between 900–1150 °C. The decrease in the amount of decomposition for the SrCO_3 nanostructures when GT is used as the additive may be due to the incomplete decomposition of the sample till 1200 °C. The temperature of maximum decomposition of SrCO_3 is found to be 1070, 1052, 1060 and 1105 °C for GK, GKG, GO, and GT, respectively. This variation in the temperature can be ascribed to the size effect of the nanoparticles existing within the nanocrystallites of the formed inorganic-organic hybrid materials.

Conclusions

In summary, uniform hierarchical SrCO_3 architectures in the form of bouquet, peanut, and flower like morphologies were efficiently obtained by using natural gums as crystal growth modifiers at room temperature and screw capped methods at 100 °C which are confirmed by SEM and TEM micrographs. The crystalline nature and spectral features of strontium carbonate is confirmed by XRD and SAED pattern and FTIR, respectively. TGA study confirms that the as synthesized SrCO_3 nanocrystallites using various gums are having both inorganic and organic components resulting into the formation of inorganic-organic hybrid materials. It can be concluded that the whole growth process of SrCO_3 was affected by the additive and the reaction conditions. This simple protocol emphasizes that it is possible to fabricate the different morphologies and sizes of SrCO_3 particles with self assembly hierarchical architectures assisted by natural gums as additives and can be used in many potential applications.

Acknowledgements

MS and NVSN thank DICT for giving opportunity to carry out a part of the present work at CSIR-IICT, Hyderabad, India.

References

- Braun, P. V., Osenar, P., and Stupp, S. I., *Nature* **1996**, 380, 325.
- Omata, K., Nukui, N., Hottai, T., Showa, Y., and Yamada, M., *Catal. Commun.*, **2004**, 5(12), 755.
- Kuthar, J., Nells, G., Seshadri, R., Schaub, M., Butt, H. J., and Tremel, W., *Chem. Eur. J.* **1998**, 4(9), 1834.
- Kuthar, J., Seshadri, R., Nells, G., Assenmacher, W., Butt, H. J., Mader, W., and Tremel, W., *Chem. Mater.*, **1999**, 11(5), 1317.
- Kuthar, J., Bartz, M., Seshadri, R., Vaughan, G. B. M., and Tremel, W. J., *Mater. Chem.*, **2001**, 11(2), 503.
- Sastry, M., Kumar, A., Damle, C., Sainkar, S. R., Bhagwat, M., and Ramaswamy, V., *Cryst. Eng. Commun.*, **2001**, 3(21), 81.
- Rautaray, D., Sainkar, S. R., and Sastry, M., *Langmuir*, **2003**, 19(3), 888.
- Qi, L., Xi, K., and Ma, J., *Acta Chimica Sinica*, **2003**, 61(1), 126.
- Bastow, T. J., *Chem. Phys. Lett.* **2002**, 354(1-2), 156–159.
- Zeller, A. F., *Chem. Tech.*, **1981**, 19, 762.
- Griffiths, J., *Ind. Miner.*, **1985**, 218, 21.
- Erdemoglu, M., and Canbazoglu, M., *Hydrometallurgy*, **1998**, 49(1-2), 135.
- Owusu, G., and Litz, J. E., *Hydrometallurgy*, **2000**, 57(1), 23.
- Shi, J. J., Li, J. J., Zhu, Y. F., Wei, F., and Zhang, X. R., *Anal. Chim. Acta*, **2002**, 466(1), 69.
- Aizenberg, J., Black, A. J., and Whitesides, G. M., *J. Am. Chem. Soc.*, **1999**, 121(18), 4500.
- Küther, J., Bartz, M., Seshadri, R., Vaughan, G. B. M., and Tremela, W., *J. Mater. Chem.*, **2001**, 11(2), 503.
- Kuthar, J., Nelles, G., Seshadri, R., Schaub, M., Butt, H. J., and Tremel, W., *Chem. Eur. J.*, **1998**, 4(9), 1834.
- Kuthar, J., Seshadri, R., and Tremel, W., *Angew. Chem., Int. Ed.*, **1998**, 37(21), 3044.
- Li, S. Z., Zhang, H., Xu, J., Yang, D. R., *Mater. Lett.*, **2005**, 59, 420.
- Huang, Q., Gao, L., Cai, Y., and Aldinger, F., *Chem. Lett.*, **2004**, 33(3), 290.
- Cao, M. H., Wu, X. L., He, X. Y., and Hu, C. W., *Langmuir*, **2005**, 21(13), 6093.
- Sondi, I., and Matijevic, E., *Chem. Mater.*, **2003**, 15(6), 1322.
- Rautaray, D., Sanyal, A., Adyanthaya, S. D., Ahmad, A., and Sastry, M., *Langmuir*, **2004**, 20(16), 6827.
- Du, J. M., Liu, Z. M., Li, Z. H., Han, B. X., Huang, Y., and Zhang, J. L., *Micro. Meso. Mater.*, **2005**, 83(1-3), 145.
- Devi, D. K., Pratap, S. V., Haritha, R., Sivudu, K. S., Radhika, P., and Sreedhar, B., *J. Appl. Polym. Sci.*, **2011**, 121(3), 1765.
- Sreedhar, B., Reddy, P. S., and Devi, D. K., *J. Org. Chem.*, **2009**, 74(22), 8806.
- Yu, S. H., and Colfen, H., *J. Mater. Chem.*, **2004**, 14(14), 2124.
- Colfen, H., and Antonietti, M., *Langmuir*, **1998**, 14(3), 582.
- Sommerdijk, N. A. J. M., *Chem. Rev.* **2008**, 108(11), 4499.
- Colfen, H., *Macromol. Rapid Commun.*, **2001**, 22(4), 219.
- Qi, L. M., Colfen, H., Antonietti, M., Li, M., Hopwood, J. D., Ashley, A. J., and Mann, S., *Chem. Eur. J.*, **2001**, 7(16), 3526.
- Qi, L. M., Colfen, H., Antonietti, M., *Angew. Chem. Int. Ed.*, **2000**, 39(3), 604.
- Sreedhar, B., Satya Vani, Ch., Keerthi Devi, D., Sreeram, V., Basaveswara Rao, M. V., Rambabu, C., *Am. J. Mater. Sci.* **2012**, 2(5), 142.
- Sreedhar, B., Satya Vani, Ch., Keerthi Devi, D., and Basaveswara Rao, M. V., Rambabu, C., and Saratchandra Babu, M., *Cryst. Res. Technol.*, **2011**, 46(5), 485.
- Liu, X., Peng, X., Xie, W., Wei, Q., *Chin. J. Mater. Res.*, **2005**, 19, 287.

Received: 24.12.2014.

Accepted: 20.01.2014.



THE EFFECT OF pH ON BIOACCUMULATION OF Cd, Hg AND Pb BY WATER HYACINTH

M. Sjahrul

Keywords: Water hyacinth, heavy metals, cadmium, lead, mercury, binding of metals, bioaccumulation

Water hyacinth grows and multiplies rapidly in the water contaminated by heavy metals such as Cd, Hg, and Pb. The water hyacinth was planted in Long Ashton media at varying pH, concentrations of Cd, Hg, and Pb and planting time. The roots adsorbed more Cd, Hg and Pb than the stalks and leaves. The maximum absorption was found at pH 5.0 and the minimum at pH 7.0. The higher the metal concentration in the media and longer the planting time, the absorption of the metal ion increased considerably. It was concluded that the acidity level of media could be an indicator of the absorption of Cd, Hg, and Pb metals by the water hyacinth.

Corresponding Authors

E-Mail: eddievedder_jie@yahoo.com

[a] Department of Inorganic Chemistry, Faculty of Mathematics and Natural Sciences, University of Hasanuddin, Makassar, Indonesia Author Address line 1

Introduction

One way of removing heavy metals existing in aquatic environments is to use aquatic plants which absorb heavy metals.¹ Some metal ions have a strong affinity towards amino groups and sulfhydryl groups.² These type of metals definitely react with these groups present in enzymes and form chelates with organic molecules. The stability of these type of divalent metal chelates generally correlates with electronegativity of the metals, e.g.: Hg > Pb > Cu.³ Through this stability trend, metals that released into the water can substitute the other metal that have been bound to the sediment and other particles in the water.⁴

It has been reported that water hyacinth can absorb a variety of heavy metals from water and can be used to reduce the burden of heavy metal pollution. It was found that 1 ha of water hyacinth can absorb 1012.5 ; 132.5 ; 867 g of Cd, Hg , Ni respectively day⁻¹ when the metals were present alone in the water. When all of the three metals were present together then 1 ha of water hyacinth can consecutively absorb Cd, Hg, Ni in amount as much as 922.5; 1410; 262.5 g day⁻¹.⁵ In the presence of 3-10 mg of Cd as cadmium nitrate L⁻¹, the precipitation of Cd could be observed in hypodermal tissues and epidermal cells in 24 h.⁵ It was found that the absorption of Pb increases with increasing Pb concentration in growing media; 100 mg of Pb L⁻¹ does not have any detrimental effect on growth.⁷ Besides cadmium and lead, other very toxic metals such as mercury can also be bound by water hyacinth,^{5,8} thus water hyacinth can be used as bioaccumulator for toxic heavy metals.⁹ Water hyacinth is able to stimulate these metals biological collection at a high concentration of the plant in the medium solution.^{2,3} This ability of water hyacinth to absorb and accumulate heavy metals Cd , Pb and Hg is caused by lots of great space in the protoplasm of the cells (vacuolization) which contain a lot of amino acids and other compounds that have chelating functions.

Material and methods

Hyacinth samples were taken two days before planting in the growing media solution. Water hyacinth having 4 leafs with an average height of 16-20 cm and the average weight of 30-35 grams were selected. Samples were then taken to greenhouse for growing in a Long Ashton solution. The water hyacinth were planted in the vase containing Long Ashton solution media at different pH values and at random planting time. The harvested water hyacinth was dried digested in a Kjeldahl flask with concentrated HNO₃, H₂SO₄, and HClO₄. The heavy metal contents were analyzed with using a Philips PU9100X atomic spectrophotometer. Lead(II) nitrate, cadmium chloride and mercury(II) nitrate solutions (each 1000 ppm) were used as reference solutions.

Result and Discussion

The results indicated that the amount of Cd absorbed by the root, stem and leaves (kg⁻¹ relates to dry weight) of the plant in the solution at pH 6 was 2, 5 and 8 mg L⁻¹ concentration after 1, 3, 6, 10, 15 and 20 days. The amount absorbed showed a higher linear correlation with the initial concentration of Cd in the solution than with the number of days. Similar trends were obtained with Hg and Pb as well.

At 8 mg L⁻¹ Cd concentration the average bioaccumulation of Cd (2313.0 mg kg⁻¹) was higher than that at 5 and 2 mg L⁻¹ (838.7 and 432.6 mg kg⁻¹) doses respectively. The average concentration of Cd in the root was (2083.0 mg kg⁻¹) which was higher than that in the stem and leaf 306.2 mg kg⁻¹. The accumulation rates during the first ten days were higher than during the second 10 days (between the 10-20 days).

The bioaccumulation rate of Cd if the solution contained exclusively Cd ions was found to be significantly different than that in the case of mixtures of heavy metals (Cd + Pb, Cd + Hg, and Cd + Pb + Hg). The highest Cd bioaccumulation was found in the case of exclusively Cd-ion containing solution.

The bioaccumulation of metals (Cd, Hg and Pb) showed better non-linear correlation with the pH (between 4 and 7) than with the time (1-20 days) at 5 mg L⁻¹ Cd, Hg or Pb concentrations) in the root, stem and leaves as well.

The average absorption of Cd concentration was found to be 1492.5 mg kg⁻¹ in the root. This was found to be more than that in the stem 318.1 mg kg⁻¹. The highest Cd content found in the root was 3339.6 mg kg⁻¹ and the lowest values were 962.0 and 66.4 mg kg⁻¹ in the stem and leaves, respectively.

The effect of pH on the bioaccumulation of Cd was significant ($P < 0.0001$), the average values were found to be 950.0, 817.8 and 674.6 mg kg⁻¹ at pH 4.0, 6.0 and 7.0, respectively. The differences might be the consequence of the differences in the released OH ions at certain sites in the root.

Conclusion

The sorption of Cd, Hg and Pb by the water hyacinth plant increases with the increasing concentrations of the heavy metal ions between 1 and 8 ppm during growing. The optimal pH to bioaccumulate Cd, Hg and Pb is around pH=5.0. The rate of bioaccumulation increases in the first 20 days of growing water hyacinth for all three toxic metals. The heavy metals (Cd, Hg and Pb) accumulated in higher amount in roots than in stem or leaves.

References

- ¹O'Keefe, D. H., Hardy, K. J. and Rao, R. A., *Env. Poll., Ser. A.*, **1984**, 133-147.
- ²Saeni, M. S., *Kimia Lingkungan*. Depdikbud, Dirjen PendidikanTinggi, Pusat Antar Universitas Ilmu Hayat, IPB, Bogor, 1989.
- ³Bowen, H. J. M., *Trace Elements in Biochemistry*, Academic Press Inc, London, 1966.
- ⁴Hutzinger, O., *Environmental Chemistry*, Springer Verlag Berlin Heidelberg, New York, 1980.
- ⁵Buddhari, W., Virabalin., R., Aikamphon, K., *Int. Conf. Water Hyacinth Hyderabad, India*, **1984**, 379-386.
- ⁶Gopal, B., *Water Hyacinth*, Elsevier Tokyo, **1987**.
- ⁷Widyanto, L., *Widyapura*, **1977**, 1(5-6), 64-69.
- ⁸Muramoto, S., Okie, Y., *Bull. Environ. Contam. Toxicol*, **1983**, 30.
- ⁹Wolverton, B. C., McDonald, R. C., *J. Water Pollut. Control Fed.*, 1979, 51, 305-313.

Received: 18.12.2013.

Accepted: 22.12.2014.



REMOVAL OF FLUORIDE FROM DRINKING WATER BY QUARTERNARY AMINATED RESINS FROM SAW-DUST

Anurag Choudhary,^[a] P. T. S. R. K. Prasad Rao,^[b] Shobha Sharma^[a] and Vinita Sharma^[a]

Keywords: Fluoride, removal, resins, saw-dust, water analysis, drinking water purification

Safe drinking water is a severe problem in many parts of the various countries including India a fast developing country. Authors have used some low-cost materials and their products as one of the best adsorbents for the removal of fluoride from water mainly used for drinking and other domestic purposes. Results are appreciable to be applied in large scale purposes.

* Corresponding Authors

Fax:

E-Mail:

[a] a - Department of Chemistry, J.N.V. University, Jodhpur-342001, INDIA

[b] PG Department of Chemistry, P.B.Siddharth College of Arts & Science, VIJAYWADA-520 010 INDIA.

Introduction

Fluoride has been recognized as an essential component in human diet. Skeletal and dental problems can be prevented by maintaining fluoride concentration of one ppm in dietary intake, however long term consumption of water having high fluoride concentrations lead to bone diseases such as osteofluorosis and systemic fluorosis, which is an endemic problem¹ in many countries, the matter has been reviewed by Susheela.² Cases of endemic fluorosis have been reported from all places of world, particularly China, Japan, Thailand, Persian Gulf, Saudi Arabia, Europe, USA, Canada, Argentina and African Countries² In India cattle and human fluorosis was detected in 1930 and 1937³, respectively, the population of 50 % districts of more than fifteen states are affected by high fluoride concentration in drinking water. Severely affected states are Andhra Pradesh, Uttar Pradesh, Tamil Nadu & Rajasthan. The fluoride level in the ground water used for drinking purposes in Thar and Aravali regions of Rajasthan, has been found as 12-90 ppm and 1.44-28.1 ppm respectively.⁴⁻⁶

Several defluoridation methods based on the adsorption, precipitation & ion exchange has been developed during last four decades, however none of these could solve this problem at a completely acceptable level.⁷ The materials used include lime & related compounds,⁵⁻⁷ trivalent metal oxides, hydroxides & carbonates,^{8,9} activated alumina,¹⁰ activated carbon and ion exchangers¹¹ etc. Attempt has also been made to tackle this problem by Government agencies, NGO's, medical experts, Center of Community Economics and Development Consultant Society, Department of Science and Technology etc.¹² Rajasthan Government had a program to transfer and propagate a domestic defluoridation technology called Nalgonda Technique (NA) in selected villages.¹³ A more recent process of defluoridation is KRASS, which is said to be simpler and effective, however the claims have not been substantiated.¹⁴

Nalgonda Technique involves direct addition of known quantities of lime and alum depending upon the $[F^-]$ in water, unfortunately the technology is not very successful because of the difficulties in controlling the dose of alum and the lack of awareness among people. The process is suitable only for water having $[F^-] < 10$ ppm. The defluoridation by activated alumina (AA) has been studied at length by Bulusu and Nawlakhe.¹⁰ $[F^-]$ less than 1 ppm can be achieved easily by using AA as an adsorbent, however it has certain operational, control and maintenance problems, the important one is the clogging of bed. In the KRASS process, water containing high $[F^-]$ was passed through a PVC column of 64-122 cm in length & 5-6 cm in dia., filled with a low cost material under patent. The column after exhaustion is regenerated with 10% alum solution.

The residual $[Al^{+3}]$ in water treated by NA, AA and KRASS methods was found 2.01-6.46, 0.1-0.3 and 0.1-0.15 ppm respectively. Aluminium is a neurotoxin and its concentration as low as 0.08 ppm in drinking water is reported to have caused Alzheimer's disease,¹⁵ thus generation of residual $[Al^{+3}]$ by these treatments may initiate a secondary toxicity problem, greatest drawback of these processes. In the present communication the efforts have been made to remove $[F^-]$ from water by aluminium free material, quaternary aminised saw dust (SD) derivatives

Experimental Section

Materials

All the reagents and chemicals used in this study are commercially available and are of high purity AR grade.

A 100 m mol L⁻¹ stock solution of $[F^-]$ was prepared by dissolving sodium fluoride in de-ionized water. These solutions were further diluted to suitable concentrations as & when required. The pH of solutions was adjusted by adding dilute HCl or NaOH solution.

AIMIL make MK II model spectrophotometer and Naina make pH meter model 303 with combined glass electrode were used for measuring residual $[F^-]$ & pH measurement respectively.

Table 1. Physical properties of SD derivatives

S.No	Derivatives	Particles		Degree of substitution	Water retain, g g ⁻¹	Salt splitting capacity, meqv g ⁻¹	Weak acid exchange capacity , meqv g ⁻¹
		amount , %	size, mesh				
1	TMAHP- SD	60	>100	0.25	2.52	0.66+0.03	0.25+0.05
		40	60-100				
2	TMAHP- SD	60	>100	0.24	2.64	0.58+0.02	0.25+0.03
		40	60-100				
3	TMAHP- SD	60	40-60	0.21	2.10	0.46+0.03	0.20+0.03
		40	>60				
Stability: 6-8 weeks at pH 3- 10; Swelling in water: slightly.							

Table 2. Freundlich constants for the adsorption of fluoride ion on SD derivatives*

Adsorbent	Freundlich constants					
	Average k_d	K	n	SD	R^2	r
TMAHP- SD	2132+50	3.459×10^{-3}	2.52	1.06×10^{-2}	0.99	0.99
TEAHP-SD	1583+70	2.887×10^{-3}	2.60	2.15×10^{-2}	0.99	0.97
DEAE-SD	0782	2.286×10^{-3}	3.10	0.86×10^{-2}	0.98	0.99

([F⁻]=0.02 g dm⁻³, Time of contact =30 min, Adsorbent amount = 0.15 g, Temperature = 30 °C, Volume = 0.1 dm³, pH=8)

The adsorbents used in this study are saw dust derivatives, namely quaternary aminised trimethylamino-hydroxypropyl-, triethylamino-hydroxypropyl- and diethylaminoethyl-sawdust referred onward as TMAHP-, TEAHP- & DEAE-SD, respectively. These were prepared as described earlier. The physical properties of SD derivatives viz. degree of substitution, particle size, water regain, salt splitting capacity, exchange capacity, swelling and stability were evaluated by known methods. These are reported in Table 1.

Distribution Coefficients

The uptake of fluoride on the derivatives was estimated in terms of distribution coefficient, K_d . The derivatives (0.02-0.4 g) were stirred with 100 ml of 0.02 g dm⁻³ aqueous solution at pH 7-8, until complete equilibrium was obtained. The adsorbent was then removed by filtration through glass wool and the residual [F⁻] in the solution was computed spectrophotometrically, from the linear optical density (OD) vs concentration curves by measuring OD at the max absorbance region of the complex¹⁸. The K_d values were evaluated using the formula¹⁹:

$$K_d = \frac{(100-x)V}{xm}$$

where

V is the volume of solution in ml,

m is the weight of the adsorbent in grams and

x is the % of [F⁻] remaining in the solution.

Batch Adsorption Study

Adsorption experiments were performed by agitating 0.02- 0.2 g of SD derivatives with 100 ml aq. soln. of fluoride, 0.02 dm⁻³ in skew cap jars. The agitation was continued for 30 min. at ambient temperature (30 + 0.02 °C).

The initial pH of the solution was adjusted by adding requisite amounts of acid or alkali solution. The equilibrated solutions were centrifuged for 10 min at 10,000 RPM in T 24 model (GDR) centrifuge and analyzed for the residual [F⁻].

Results and Discussions

The efficiency of SD derivatives for the removal of F⁻ from water was evaluated by calculating the K_d values for fluoride ion at pH 8. The results (Table 2) show that all the SD derivatives have good affinity for fluoride ion and the order of adsorption for the fluoride ion towards the derivatives is – TMAHP-SD > DEAE-SD > TEAHP-SD

The results also indicate, that the K_d values increase with the decrease in pH of the solution, which may be attributed to the neutralization of surface negative charge of SD derivatives¹⁷

Adsorption Isotherms

Adsorption isotherms (AI) for fluoride ions in water on SD derivatives, when the system is in equilibrium were found regular, positive and convex to the concentration axis followed by a plateau and another rise and formation of plateau. The sharp rise of isotherms in the initial stages of low equilibrium concentration indicates that there are plenty of readily available sites for fluoride ion. Eventually a plateau is reached in all the three cases, this indicates that the saturation of adsorbent surface at this stage. Further rise in the adsorption isotherms and the formation of another plateau probably indicates mono dispersity of adsorption accompanied by the formation of small sized ionic micelles on the surface. A similar behavior has been observed in the adsorption of merocynine over silver halides.^{20, 21}

Table 3. Effect of pH on K_d and removal of fluoride (in %) by SD derivatives*

S.No.	pH	Fluoride removal in % and K_d values					
		TMAHP-SD		TEAHP-SD		DEAE-SD	
		% [F ⁻]	K_d	% [F ⁻]	K_d	% [F ⁻]	K_d
1	3	81	2842	76	2111	61	1043
2	4	72	1714	66	1294	55	815
3	5	66	1294	60	1000	49	640
4	8	61	1043	51	694	45	545
5	9	54	783	47	591	41	463

An average of three sets. [F⁻]=0.02 g dm⁻³; Time of contact=30 min; Adsorbent amount=0.15 g; Temperature = 30 °C; Volume = 0.1 dm³

Table 4. Effect of Adsorbent dose on K_d and removal of F⁻ (in %) by SD-derivatives*

Amount of adsorbent	TMAHP-SD		TEAHP-SD		DEAE-SD	
	% [F ⁻]	K_d	% [F ⁻]	K_d	% [F ⁻]	K_d
0.04	33	1203	30	1071	29	996
0.08	41	868	41	851	40	833
0.12	50	833	48	833	43	769
0.16	65	1135	58	845	51	680
0.20	74	1385	65	928	66	949
Average K_d		1126		976		918

An average of three sets. [F⁻] = 0.02 g dm⁻³; Time of contact = 30 min; pH = 8; Temperature =30 °C; Volume = 0.1 dm³; λ_{\max} = 570 nm

Table 5. Effect of time on K_d and removal of F⁻ (in %) by SD-derivatives*

Time, min	TMAHP-SD		TEAHP-SD		DEAE-SD	
	% [F ⁻]	K_d	% [F ⁻]	K_d	% [F ⁻]	K_d
30	61.0	1043	51	694	45	545
60	62.5	1110	56	883	48	615
90	65.0	1238	58	920	52	722
120	68.0	1417	60	1000	54	783

An average of three sets. [F⁻] = 0.02 g dm⁻³; pH = 8; Temperature =30 °C; Volume = 0.1 dm³; λ_{\max} = 570 nm; Adsorbent amount = 0.15 g

The experimental data was analyzed in the light of Freundlich²², Langmuir²³ and BET²⁴ equations to predict the nature of adsorption. The A I do not strictly follow any one model, however at low concentrations of fluoride ion (1-10 ppm) as are generally available in the drinking waters, the Freundlich model is obeyed. The plots of log C_e against log x/m were found linear yielding an intercept on the ordinate. The Freundlich constants K and $1/n$ were calculated from the intercept and slope of these curves using computerized LRG program and reported in Table 2. The Freundlich constant K is a measure of capacity of the adsorbent while n denotes the intensity of adsorption, a value of n between 1 and 10 is considered to be a favorable adsorption. The adsorption capacity was found maximum for TMAHP-SD. The extent of adsorption, n , was found in the range of 2.52 to 3.1, which is quite satisfactory.

Effect of pH

The effect of pH on the adsorption of F⁻ on to SD derivatives was studied at pH 3, 4, 5, 8 and 9. The % removal of fluoride ion at different pH is given in Table 3. It was observed that the adsorption occurred in the entire range of pH studied, however the uptake of F⁻ increased with the decreasing pH of the solution. The pH of the solution reportedly affect the surface charge of SD derivatives, the

decrease in pH helps in neutralizing the negative charge of SD derivatives and permit the easier movement of fluoride ion in the vicinity of the Vander-Waal's forces, thereby increasing the % removal of fluoride ion at lower pH.

Effect of Adsorbent Dosage

Table 4 shows the amount of fluoride removed as a function of adsorbent dosage at pH 8 and 0.02 g dm⁻³ of initial [F⁻] and at 30 °C. Adsorbent dosage was varied from 0.02 to 0.4 g per 100 ml and equilibrated for 30 min. From the results, it is evident that optimum dosage of adsorbent per 100 ml required for the maximum removal of fluoride is 0.1 g. It is interesting to note that the same dose of other adsorbents exhibit comparatively low fluoride removal capacity.

Effect of Time

The effect of contact time on the adsorption of fluoride on SD derivatives was studied at pH 3. The results (Table 5) show that 85 to 90 % adsorption takes place in 30 min and for the remaining 10 to 15 % at least 90-120 min are required.

Table 6. Effect of temperature on K_d and removal of F^- (in %) by SD-derivatives*

Temperature, °C	K_d		
	TMAHP-SD	TEAHP-SD	DEAE-SD
25	984	661	462
30	1044	694	545
40	1354	1059	771
50	1698	1445	1047
Slope	-2172.4+/-156	-2993.0+/-47	-3170.6+/-28
R	0.994	0.999	0.999
$\Delta S^* \text{ J mol}^{-1}$	-136+/-2.80	-117+/-0.84	-115+/-0.51
$\Delta G^* \text{ kJ mol}^{-1}$	56.03+/-0.68	56.95+/-0.20	57.84+/-0.12
$\Delta H, \text{ kJ mol}^{-1}$	15.55+/-0.87	22.37+/-0.26	23.64+/-0.16

An average of three sets. $[F^-] = 0.02 \text{ g dm}^{-3}$; Time of contact = 30 min; pH = 8; Volume = 0.1 dm^3 ; $\lambda_{\text{max}} = 570 \text{ nm}$; Adsorbent amount = 0.15 g

Table 7. Effect of nature and concentration of surfactants on the removal of fluoride by TMAHP-SD

Fluoride removal in % in the presence of Arkoline surfactants			
Concentration	SPW	N-65	HCS
0.05	60	61	63
0.10	57	60	65
0.15	54	61	68
0.20	50	60	71
0.25	42	60	74
0.30	38	60	71

An average of three sets.; $[F^-] = 0.02 \text{ g dm}^{-3}$; Adsorbent = 0.15 g; pH = 8; Time of contact = 30 min; Volume = 0.1 dm^3 ; Temperature = 30°C .

Table 8. Effect of added ions on the removal of fluoride (in %) by TMAHP-SD

Concn., g dm^{-3}	Cl^-	NO_3^-	SO_4^{2-}	HCO_3^-
0.01	60.0	60.0	60.0	58.0
0.02	61.5	61.0	59.0	56.5
0.03	60.5	60.5	60.0	55.0
0.04	60.0	61.5	60.5	54.0
0.05	61.5	61.0	61.5	52.0

An average of three sets; $[F^-] = 0.02 \text{ g dm}^{-3}$; ime of contact=30 min; pH = 8; Volume = 0.1 dm^3 ; Adsorbent = 0.15 g; $\lambda_{\text{max}} = 5$;

Effect of Temperature

The effect of temperature on the % removal of fluoride ion by starch derivatives was investigated at 30, 40 and 50°C keeping all other parameters constant, these results are summarized in Table 6. The % uptake is highly dependent on $[F^-]$ in solution and increase with the increase in temperature, indicating that the process of adsorption is endothermic in nature.

Effect of Surfactants

The effect of nature and concentration of added surfactants on the adsorption of fluoride ion on the SD derivatives was investigated at room temperature. The

results in Table 7 show that the surfactants have a little effect on the adsorption of fluoride ion on the derivatives. The % removal of fluoride ion increased with the increase in added cationic surfactants concentration and decreased with the increasing [anionic surfactant], nonionic surfactants however have no effect. It appears that cationic surfactants neutralize some negatively charged sites of the adsorbent resulting in the improved migration of F^- on the SD derivative. The decreased adsorption by anionic surfactants may be attributed to the competitive adsorption of fluoride ion and the surfactants.

Effect of Added Co-ions

The effect of added co-ions e.g. Cl^- , SO_4^{2-} , NO_3^- and HCO_3^- on the % removal of fluoride ion was investigated with TMAHP-SD. The results (Table 8) indicate that the addition of co-ions in the range investigated has no appreciable effect, however the increase in $[\text{HCO}_3^-]$ slightly decrease the adsorption efficiency. This may be due to the competitive rate of adsorption of fluoride and bicarbonate ions. The observation is in accordance with the studies on activated alumina and magnesnia.

The Mechanism of Adsorption

The mechanism of adsorption may be considered as a mixed effect of classical as well as of chromatographic adsorption. The introduction of glycedyl trialkyl ammonium groups in the SD derivatives imparts it a strongly cationic anion exchanger's character.²⁵ At lower pH, these exist in chloride form, the higher exchange capacity of these forms are well documented. Initially all the Cl^- ions of the TMAHP-SD are exchanged by F^- ions with the formation of first plateau, after the saturation point is reached i.e. the capacity of ion exchanger is exhausted the F^- ions are held by hydrogen bonding and weak VanderWaal's forces showing the rise in adsorption isotherm and the formation of another plateau.



where R_1 stands for cross linked cellulose (SD) and R for methyl or ethyl groups.

Saw-Dust is basically a wood cellulose which acquires a negative surface charge by virtue of primary hydroxyls on each D-glucopyranose units. The alkaline treatment of cellulose (SD), during the introduction of quaternary ammonium group, causes degradation of about 2 % with the loosening of the structure and the introduction of some acidic sites which do contribute to negative charge.²⁶ In acidic media the primary hydroxyls on the D-glucopyranose units may get protonated acquiring a partial positive charge which helps the fluoride ions to move in the vicinity of the SD molecule where hydrogen bonding comes into play and the fluoride ion is held by hydrogen bonding, resulting in the increased adsorption after exhausting the anion exchange capacity. It is the reason why the SD derivatives can not be completely regenerated.

Conclusion

The present study demonstrates that the cationic SD derivatives have potential to remove fluoride from drinking water without any other toxic affect. The study has following salient features:

The up take of fluoride ion is rapid in initial stages and decreases gradually while approaching equilibrium.

The major part of total adsorption, nearly 80 % of uptake at equilibrium takes in less than 30 minutes.

The up take of fluoride ion is significantly dependent on the pH of water, increases with the decrease in pH of water.

The up take of fluoride ion by SD derivatives is also influenced by the presence of surfactants. The up take of fluoride ion increases with the increase in [cationic surfactant], and decreases with the increase in [anionic surfactant], nonionic surfactants have no effect.

The material after the use can be burnt, thus pose no waste disposal problem.

References

- ¹Dean, H. T., Arnold, F. A. Jr. and Evolve, E., *Publ. Health Rep.*, **1942**, 57, 115.
- ²Susheela, A. K., *Proc. Rome Symp.*, **1994**, IAHS Publ. No. 233.
- ³Shortt, H. E., Robert, G. R., Bernard, T. W. and Nayyar, A. S. M., *Indian J. Med. Res.*, **1937**, 25, 553.
- ⁴Choubisa, S. L., Choubisa, D. K., Joshi, S. C. and Choubisa L., *Fluoride*, **1997**, 30, 223.
- ⁵Gupta, S. C., Rathor, G. S. and Doshi, C. S., *Indian J. Environ. HLTH*, **1993**, 35, 97.
- ⁶Choubisa, S. L., Choubisa L. and Choubisa, D. K., *Indian J. Environ. Health*, **2001**, 43, 177.
- ⁷Sujana, M. G., Thakur, R. S., Das S. N. and Rao, S.B., *Asian J. Chem.*, **1997**, 9, 561.
- ⁸Tokunaga, S., Haron, M. J., Wasay, S. A., Wong, K. F., Laosangthum, K. and Uchimi, *Int. J. Environ. Stud.*, **1995**, 48, 17.
- ⁹Bulusu, K. R. and Nawlakhe, W. G., *Indian J. Environ Health* **1988**, 30, 262.
- ¹⁰Bulusu, K. R. and Nawlakhe, *Indian J. Environ. Health*, **1990**, 32, 197.
- ¹¹Bhatt, D. B., Bhatt, P. R., Prasad, H. H., Popat, K. M. and Anand, P. S., *Indian J. Chem. Technol.*, **2004**, 11, 299 and references therein.
- ¹²Nawlakhe, W. G., Kulkarni, D. N., Pathak, B. N. and Bulusu, K. R., *Indian J. Environ. Health*, **1975**, 17, 26.
- ¹³Kumar, N., *Yojana*, **1999**, 6, 45.
- ¹⁴Gupta, K. R., Gupta, S. K. and Gupta, A. B., *Water Sci. Techn.* **1999**, 40, 167.
- ¹⁵Davidson, A. M., Walker, G. S., Oli, H. and Lewins, A. M., *The Lancet*, **1982**, 785.
- ¹⁶Prakash A. and Prasadrao P. T. S. R. K., *Chem Environ. Res.*, **2006**, 15, 27.
- ¹⁷Prakash, A. and Solanki, S., *Res. Ind.*, **1993**, 38, 35.
- ¹⁸*Standards methods for the examination of water and waste water*, **1975**, APHA, AWWA, WPCF, Wshington DC 2005.
- ¹⁹Srivastava, S. K., Bhattacharjee, G., Tyagi, R., Pant, N. and Pal, N., *Environ. Technol. Lett.*, **1988**, 9, 1173.
- ²⁰Gills, C. H. and MacEvan, T. H., *J. Chem. Soc.*, **1960**, 3973.
- ²¹Gills, C. H., Easton, I. A. and Mackay, G., *J. Chem. Soc.*, **1964**, 4495.
- ²²Freundlich, H., *Colloidal and Capillary Chemistry*, **1928**, Methuen, London.
- ²³Langmuir, I., *J. Am. Chem. Soc.*, **1918**, 40, 1361.
- ²⁴Brunauer, S., Emmet, P. H. and Teller, E., *J. Am. Chem. Soc.*, **1938**, 60, 309.
- ²⁵*Durolite Ion Exchange Manual 1960*, Western Division of Diamond Alkali Company, Red Wood City, California USA.
- ²⁶Young, R. A. and Liss, L., *Cellul. Chem. Technol.*, **1985**, 24, 273.

Received: 22.12.2013.

Accepted: 23.01.2014.



HYBRID ALUMINUM MATRIX COMPOSITES PREPARED BY SPARK PLASMA SINTERING (SPS)

Zoltán Károly,^{[a]*} Csaba Balázsi,^[b] Katalin Balázsi,^[c] Attila Petrik,^[b] János Lábár,^[b] and Ayaj Dhar^[d]

Keywords: Sintering; Al matrix composites; Graphene; Spark plasma sintering (SPS)

Aluminum Matrix composites have been intensively investigated over a long time due to their unique combination of beneficial properties including low density, high strength to weight ratio, increased hardness, advantageous tribology, corrosion resistance, etc. In the present work we studied the combined effect of various reinforcing phases including Al_2O_3 , SiC , Si_3N_4 and graphene on the aluminum matrix. The composites were fabricated by powder metallurgical method, in which the powder blend was rapidly sintered by spark plasma sintering. The main conclusion was that hybrid composite can perform better only if the development of porosity is eliminated by improving the wettability of the reinforcing particles.

* Corresponding Authors

E-Mail: karoly.zoltan@ttk.mta.hu

- [a] Institute of Materials and Environmental Chemistry, Research Centre for Natural Sciences HAS, Budapest, H-1025, Hungary
- [b] Bay Zoltán Nonprofit Ltd. for Applied Research, H-1116 Budapest, Hungary
- [c] Institute for Technical Physics and Material Science, Research Centre for Natural Sciences HAS, Budapest, H-1025, Hungary
- [d] CSIR-National Physical Laboratory, New Delhi 110 012, India

Introduction

Aluminum alloys has long been investigated for structural purposes. Their beneficial properties including low density, high thermal conductivity, high strength, corrosion resistance and toughness can be harnessed especially in the automotive and aeronautics industry due to the substantial weight reduction. The main obstacle of their tribological application is the low hardness and poor wear behavior. There are two main approaches to overcome these problems: (i) reducing the grain size of the metal matrix, (ii) or as more widespread method is the incorporation of hard reinforcing phases such as particles, whiskers or fibers into the aluminum matrix. The aluminum matrix composites with ceramic particles and fibers exhibited improved properties over monolithic aluminum alloys in terms of strength, wear resistance and yield. For reinforcing phase Si_3N_4 , Al_2O_3 , SiC , B_4C , TiC and graphite particles are most frequently used.¹ The commonly used micronized reinforcing phases, however, considerably decrease the ductility of the matrix. It was found that strength can be increased without the decrease in the ductility in case of nanosized reinforcing phases.² Moreover, at the same volume ratio higher strengthening is achieved than micrometer counterparts.³ The big challenge for nanosized reinforcing particles is their homogeneous dispersion within the matrix.

The effect of the various reinforcing phases has been widely studied, however, recent studies have focused on hybrid reinforcing when several type of reinforcing phases are incorporated in the matrix. In this way strength, young modulus and as well as reduction in the thermal expansion could be improved even more.⁴ An interesting approach of

hybrid reinforcing is the dispersion of graphite particles beyond hard ceramic particles. The graphite particles improve the malleability of the matrix, while other valuable properties can be retained. This approach is especially advantageous in tribological applications as the graphite increases the resistance to seizure, while the composite has substantial strength due to other reinforcing phases.⁵⁻⁶

Substitution of graphite with graphene is also very promising. Beyond excellent electric, thermal and optical properties, graphene possesses outstanding mechanical properties, too. The flawless graphene is currently the strongest material with a Young modulus (E) of 0.5-1 TPa and tensile strength (σ_{int}) of 130 GPa.⁷ There have been several trials to harness these properties in various composites incorporating 0.5-3 wt. % graphene. True graphene is currently prepared by epitaxial growing or other time-consuming and costly method with low production rate. It is much easier to prepare so-called multilayer graphene nanosheets (MLG) that consist of several or even several tens of graphene layers. These MLG are available as powder and their incorporation in the matrix is reported to improve the overall mechanical properties also.⁸⁻⁹

In the present work we investigated hybrid aluminum composites, in which beyond ceramic particles multilayer graphene nanosheets were also added. As a comparison, purely ceramic reinforced composites were also examined.

The two most widespread methods of composite production are the powder metallurgy and the casting (pressure and mixture casting). During production of ceramic reinforced aluminum composites homogenous dispersion of the reinforcing additives in the matrix is a significant unresolved problem. Nanosized ceramic particles are rather difficult to disperse in the aluminum matrix for two reasons: 1) the high viscosity of the molten aluminum; 2) the bad wettability of the ceramic by the aluminum melt. Mechanical mixing usually applied in case of micrometer sized powders is not suitable for nanosized counterparts because of the high surface to volume ratio that give rise to rapid agglomeration. One approach to circumvent this problem is the high energy milling during powder metallurgy.

Spark plasma sintering, a recently developed method has been increasingly applied both in powder metallurgy and in ceramic preparation as well.¹⁰ Main advantage of this method over others is the much faster sintering at lower temperatures that makes possible to avoid the harmful grain coarsening and the unwanted reactions among the different phases.¹¹ The characteristics of this technology are the fast heating rate, the effective size reduction and the clean grain surface due to the plethora of microdischarges among the grains.

Experimental

The starting powders used in these experiments were aluminum, SiC, Si₃N₄, Al₂O₃ and graphene. Major characteristics (particle size, phase composition, etc.) of starting materials are listed in Table 1. Multilayer graphene (MLG) was prepared by milling synthetic graphite (Aldrich) in ethanol using a highly efficient attritor mill (Union Process, type 01-HD/HDDM) equipped with zirconia agitator delta discs and zirconia grinding media in a 750 ml silicon nitride tank. The milling process has been performed with high rotation speed, 4000 rpm until 10 h. The milled product was dried and sieved with a filter with a mesh size of 325. According to analysis the mean thickness of the crystallites was 13.7 nm, which is equivalent to ca.40 graphene layers.¹²

The aluminum was mixed with various reinforcing phases in different proportions. In the present work three of such composite compositions are discussed. The compositions of these experiments are as follows:

Exp. 1.: 70 wt.% Al + 30 wt.% Al₂O₃

Exp. 2.: 50 wt.% Al + 15 wt.% Al₂O₃+ 35 wt.% SiC

Exp. 3.: 30 wt.% Al + 50 wt.% Al₂O₃+ 10 wt.% SiC + 5 wt.% Si₃N₄ + 5 wt.% graphene

The powders were mixed and homogenized also in an attritor mill in ethanol at 600 rpm until 1 h.

The obtained mixtures were then sintered to discs of 2 cm in diameter by spark plasma sintering machine (HD P5, FCT GmbH). A chamber pressure of 1 mbar was maintained during consolidation. The powders were uniaxially compressed throughout the sintering process with 50 MPa. Sintering was performed for 10 minutes at 600 °C using 100 °C heating rate. Temperature was continuously measured by thermocouples inserted to the graphite die. Linear reduction of the powder compacts was monitored on line by measuring the relative displacement of the graphite punch.

The density of the sintered materials was measured by Archimedes method. The hardness was measured using Vickers indentation method at loads of 3 N. Scanning electron microscopy (LEO 1540 XB FESEM) was used for the characterization of the obtained microstructure. Phase analysis of powders and sintered discs was performed by X-ray powder diffraction (XRD, Philips PW 1050) using Cu K α radiation.

Table 1. Main characteristics of the starting materials

Precursors	Source	Powder particle size, μm	Impurities (wt.%)
Aluminum		1-3	Fe+Si<0.2
Al ₂ O ₃	ALMATIS, CT 3000LS SG	0.5	< 0.2
SiC	H.C. Stark, Grade UF-25	0.4	O ₂ – 1.8
Si ₃ N ₄	UBE America Inc., SN-ESP	0.5	O ₂ - 2 C – 0.2

Results

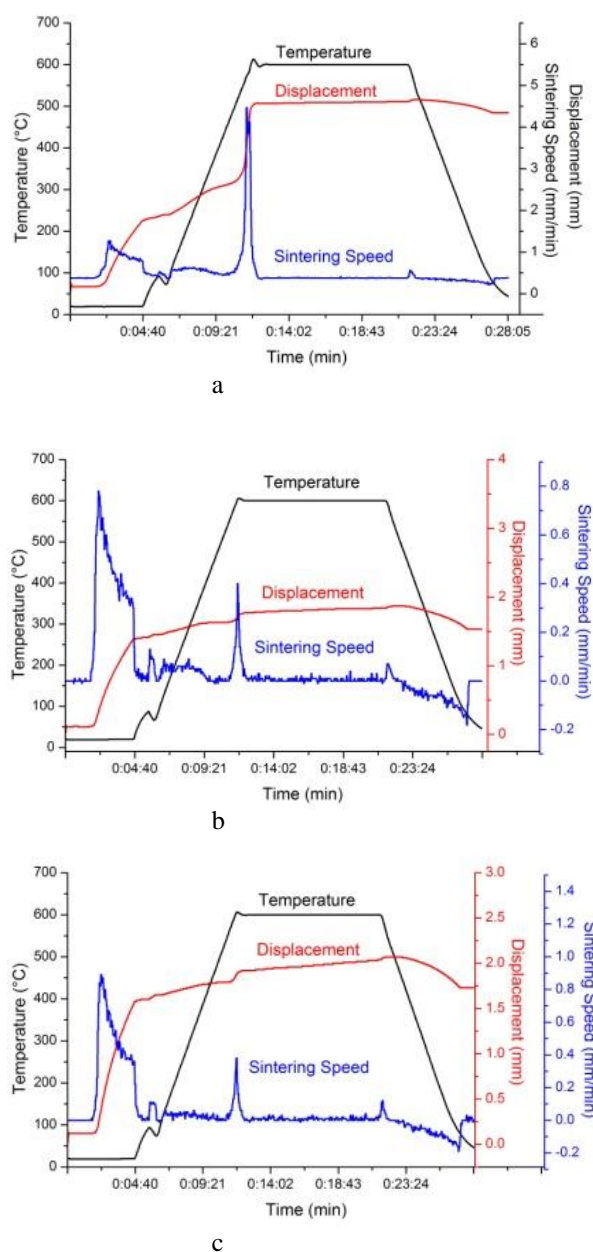
Figure 1.a-c show the sintering curves employed in the particular experiments including the temperature, the shrinkage as well as the rate of shrinkage as the function of the treatment time. The first peak of rate of shrinkage corresponds to the compaction of the powder on the effect of the applied compressive force. The peak around at 600 °C indicates, however, the starting of sintering. The highest overall shrinkage was observed in Experiment 1. This could be predicted taking into account the considerably high aluminum content of its starting composition. After 10 min of sintering further reduction could not be observed, while in the case of the other Experiments it seemingly did not finish that implies an incomplete sintering. It is confirmed by density values listed in Table 2. In Experiment 1 we achieved a 94 % theoretical density after consolidation, while that remained much smaller in the other experiments. The smaller theoretical density is in line with the findings³ that increasing proportion of ceramic particles raise the porosity and the much less values of the obtained density agree with the theoretical ones. This is because the compressibility of the hard ceramic particles in a ductile matrix becomes difficult. The situation gets worse in case of nanosized reinforcing particles. The nanosized particles tend to agglomerate and create a network. It is interesting that usually higher density can be achieved using micronsized reinforcing particles because of their better compressibility and their smaller surface to volume ratio. Graphite as solid lubricant is considered to promote the relative motion and arrangement of the particles in the matrix material resulting in higher density.⁶ Accordingly, in Experiment 3 containing graphene the apparent density became higher, however, in respect of theoretical density it gave a similar result as Experiment 2. It is probably due to the high content of reinforcing particles that surpass the aluminum matrix. The applied ceramic particles in all experiments were generally high in the hope that their effect on strength improvement would gradually increase with the proportion. Strength increasing mechanisms involve the increase in hardness due to grain refinement (Hall-Petch relationship), the hindering effect of the particles on dislocation motion as well as the accumulation of dislocations due to the different thermal expansion of the ceramic particles and the matrix material.³

Table 2. Density and hardness values of particular experiments

Experimental mixtures	Obtained density, g·cm ⁻³	Theoretical density, %	Micro-hardness, GPa
No.1. 70 wt.% Al + 30 wt.% Al ₂ O ₃	2.98	94	1.81
No.2. 50 wt.% Al + 15 wt.% Al ₂ O ₃ + 35 wt.% SiC	1.98	65	0.25
No.3. 30 wt.% Al + 50 wt.% Al ₂ O ₃ + 10 wt.% SiC + 5 wt.% Si ₃ N ₄ + 5 wt.% graphene	2.10	63	0.43

There is a great variation in microhardness values among samples of the particular experiments (Table 2). One suggests that with increasing proportion of ceramic particles hardness should be increased, too. In contrast, the highest value for hardness was obtained for the sample that contained reinforcing phases at the lowest proportion. The considerably smaller hardness of the other two experiments was probably due to the increased porosity. The increased hardness in experiment 3 compared to the 2nd one can most probably be attributed to the higher ceramic content of the former. Yet, it was not as high as expected because of the co-existence of higher porosity. The increased porosity could also be attributed to the addition of SiC particles, the poor wettability of which resulted in pores at the particle-matrix interphase as well as lead to low interphase bonding between Al and SiC. Further problem may occur for SiC reinforced Al composites that SiC particles may react with the aluminum at the interphases to form Al₄C₃ and Si phases along the grain boundary as well as that the surface of the aluminum grains could be covered with thin oxide film that prevent strong bond formation between SiC and aluminum. In either case degradation in the mechanical properties can occur. There are several ways to overcome these problems including the deposition of the SiC particles with thin films possessing good wettability to the alumina melt [13] or alloying the aluminum with Si and Mg [2, 11]. As Al₄C₃ could not be detected by XRD analysis, it suggests that during the short time of sintering the above mentioned reaction could not take place.

Figures 2.a-c show scanning micrographs of the starting powder mixtures, while Figures 3.a-c compare the fractured surface of the sintered samples. Analyzing the microstructure, SEM images show a considerable difference in the size of the grains of the aluminum matrix and those of the reinforcing particles. It can be also observed that the reinforcing particles remained agglomerated and did not create a homogenous dispersion in the matrix in spite of the intensive milling. This favors a pattern, in which the reinforcing phases situate around the Al grains creating a quasi coherent network.

**Figure 1a-1c.** Sintering curves of experiments 1-3 (a-c)

The images made of the fractured surface of the composite did not reveal the particular pores, but it can be perceived that fracture occurred along the grain boundaries of the additive particles protruding the surface that confirms the poor wettability of the nonmetallic phases.

Conclusions

Aluminum matrix composites were prepared using various ceramic particles and graphene as reinforcing phases by powder metallurgical method applying novel spark plasma synthesis. The characteristic of the starting material is the nanometer sized reinforcing phases as well as their relatively higher proportions (30-70 wt%) in the matrix. Due to the generally lower temperature and time duration of SPS sintering we managed to avoid the reactions between different phases at the interphase to form Al₄C₃ that would be a detrimental effect on the mechanical properties.

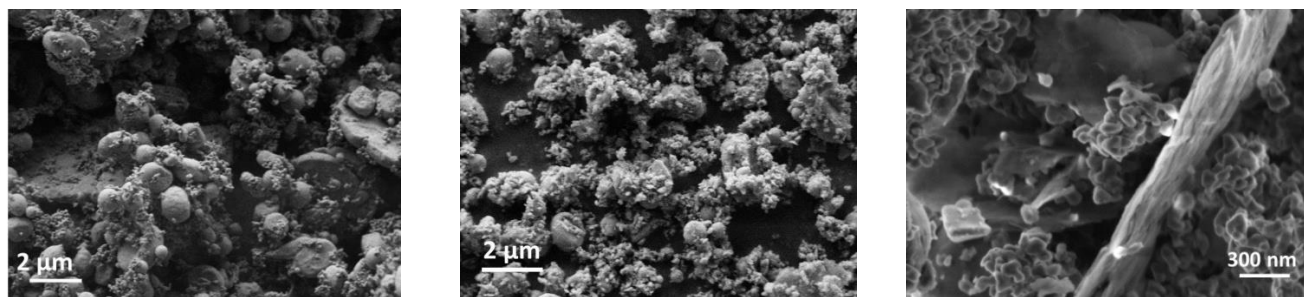


Figure 2a-2c. SEM images of the starting mixture of the particular experiments

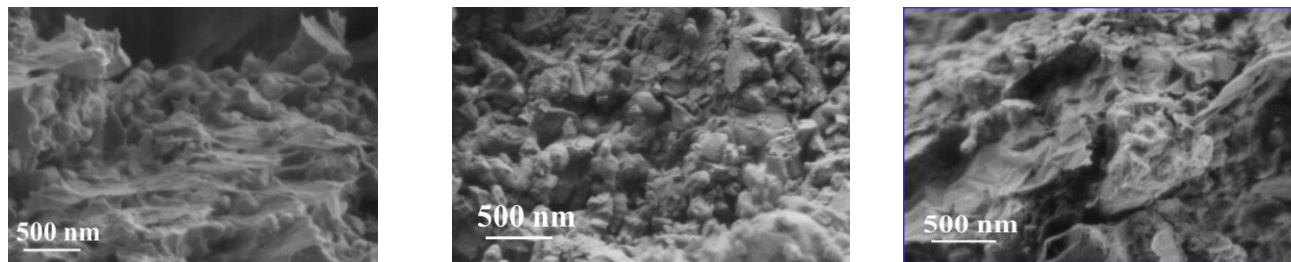


Figure 3a-3c. SEM images of the fractured surface of sintered discs prepared in the particular experiments

Dense composite with improved hardness, however, could be achieved having the reinforcing phases in the lowest (30 wt. %) proportion in the matrix. Increasing the reinforcing phases the porosity also increased considerably decreasing the hardness. Therefore, it is reasonable to avoid the incorporation of reinforcing particles in higher amount in the matrix or their surface must be deposited previously with a thin film creating good wettability to aluminum. Further research will be conducted in this direction.

Acknowledgements

This work was supported by the National Office for Research and Technology (NKTH) (Project No: REG-KM-09-1-2009-0005). The authors acknowledge the Hungarian-Indian co-operation R&D&I framework program TET_09_IN_DST (ALNANO09)

References

- ¹Mahdavi, S., Akhlaghi, F., *Tribol. Lett.*, **2011**, *44*, 1.
- ²Mazahery, A. and Shabani, M. O., *Strength of Materials*, **2012**, *44*.

- ³Dash, K., Chaira, D., Ray, B. C., *Mater. Res. Bull.*, **2013**, *48*, 2535.
- ⁴Show, B. K., Mondal, D. K., Biswas, K., Maity, J., *Mater. Sci. Eng. A*, **2013**, *579*, 136.
- ⁵Ravindran, P., Manisekar, K., Vinoth Kumar, S., Rathika, P., *Mater. Design*, **2013**, *51*, 448.
- ⁶Mahdavi, S., Akhlaghi, F., *J. Mater. Sci.*, **2011**, *46*, 7883.
- ⁷Lee, Ch., Wei, X., Kysar, J. W., Hone, J., *Science*, **2008**, *321*, 385.
- ⁸Porwala, H., Tatarkoc, P., Grasso, S., Khaliqa, J., Dlouhý, I., Reece, M. J., *Carbon*, **2013**, *64*, 359.
- ⁹Jian L., Haixue, Y., Kyle, J., *Ceram. Int.*, **2013**, *39*, 6215.
- ¹⁰Mizuuchi, K., Inoue, K., Agari, Y., Nagaoka, T., Sugiooka, M., Tanaka, M., Takeuchi, T., Tani, J., Kawahara, M., Makino, Y., Ito, M., *Composites: Part B*, **2012**, *43*, 2012.
- ¹¹Bhushan, R. K., Kumar, S., Das, S., *Int. J. Adv. Manuf. Technol.*, **2013**, *65*, 611.
- ¹²Kun P., Wéber F., Balázs, C., *Centr. Eur. J. Chem.*, **2011**, *9*, 47.
- ¹³Kretz F., Gácsi Z., Kovács J., Pieczonka T., *Surf. Coat Technol.*, **2004**, *180–181*, 575.

Received: 10.01.2014.

Accepted: 24.01.2014.



SYNTHESIS AND CRYSTAL STRUCTURE OF 4-(DIPHENYLMETHYL)-1-METHYLPIPERAZIN-1-IUM PICRATE

Sumati Anthal^[a], B. Nasrin^[b], B. Narayana^[b], B. K. Sarojini^[c], Vivek K. Gupta^[a] and Rajni Kant^{[a]*}

Keywords: 4-(Diphenylmethyl)-1-methylpiperazin-1-ium picrate; crystal structure; direct methods; N-H...O hydrogen bonding.

The title compound, 4-(diphenylmethyl)-1-methylpiperazin-1-ium picrate, C₁₈H₂₃N₂C₆H₂N₃O₇ crystallizes in the monoclinic space group P2₁/c with unit cell parameters: $a=9.8141(6)$, $b=12.6772(6)$, $c=19.9860(12)$ Å, $\beta=100.318(6)^\circ$, $Z=4$. The crystal structure was solved by direct methods and refined by full-matrix least-squares procedures to a final R -value of 0.0516 for 2703 observed reflections. The piperazine ring adopts a chair conformation and two benzene rings makes a dihedral angle of $75.17(8)^\circ$ with each other. The crystal packing is stabilized by intermolecular N-H...O and C-H...O interactions. π - π interactions have also been observed.

* Corresponding Authors

Fax: +91 191 243 2051

E-Mail: rkvk.paper11@gmail.com

[a] X-ray Crystallography Laboratory, Post-Graduate Department of Physics & Electronics, University of Jammu, Jammu Tawi - 180 006, India

[b] Department of Studies in Chemistry, Mangalore University, Mangalagangothri-574 199, India

[c] Department of Studies in Chemistry-Industrial Chemistry Section, Mangalore University, Mangalagangothri-574 199, India

Experimental Methods

Synthesis

Cyclizine (0.26 g, 0.001 mol) and picric acid (0.29 g, 0.001 mol) were dissolved in 30 ml acetonitrile and stirred over a hot magnetic stirrer for few minutes. The resulting solution was allowed to cool slowly at room temperature. Single X-ray quality crystals of the title compound appeared after few days. (M.P.: 445-447 K).

Introduction

Cyclizine is a piperazine derivative with antihistamine properties. It is an ideal antiemetic agent and possesses anticholinergic activity. It is useful for the prevention and treatment of travel sickness, post operative vomiting, drug induced nausea and for the symptomatic relief of vertigo.¹ In addition to the antihistamine effects, these H₁-receptor antagonists show pharmacological properties such as anti-inflammatory, anti-allergic and antiplatelet activities.²

The crystal structures of some related compounds viz., cinnarizinium dipicrate,³ cyclizine hydrochloride,⁴ imipraminium picrate,⁵ nevirapinium picrate,⁶ pefloxacin picrate,⁷ 1-methylpiperazine-1,4-diium picrate⁸ have been reported. In continuation of our work on the picrates of pharmaceutical compounds, this paper reports the crystal structure of title compound (1).

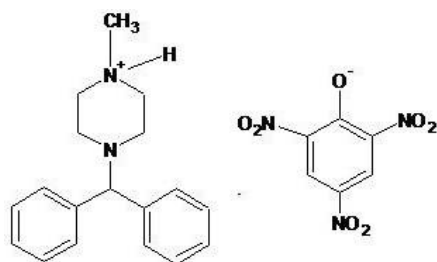


Figure 1. Chemical structure of the title compound

X-ray Data Collection, Crystal Structure Determination and Refinement

The X-ray intensity data of a well defined crystal (0.30 x 0.20 x 0.20 mm) were collected at room temperature (293 K) by using *X'calibur* CCD area-detector diffractometer which is equipped with graphite monochromated MoK α radiation ($\lambda=0.71073$ Å). The cell dimensions were determined by the least-squares fit of angular settings of 2354 reflections in the θ range 3.87 to 28.17°. A total number of 9897 reflections were collected of which 4789 reflections were unique. The intensities were measured by ω scan mode for θ ranges 3.59 to 26.00°. 2703 reflections were treated as observed ($I > 2\sigma(I)$). Data were corrected for Lorentz, polarization and absorption factors.

The structure was solved by direct methods using SHELXS97.⁹ All non-hydrogen atoms of the molecule were located from the best E-map. Full-matrix least-squares refinement was carried out by using SHELXL97 software.⁹ All the hydrogen atoms (except N1 H atom) were geometrically fixed and allowed to ride on the corresponding non-H atoms with C-H distances of 0.93-0.99 Å and with $U_{iso}(H) = 1.2U_{eq}(C)$, except for the methyl groups where $U_{iso}(H) = 1.5U_{eq}(C)$. The final refinement cycles yielded an R -factor of 0.0516 ($wR(F^2) = 0.1057$) for the observed data. The residual electron density ranges from -0.182 to 0.157 eÅ⁻³. Atomic scattering factors were taken from International Tables for X-ray Crystallography (1992, Vol. C, Tables 4.2.6.8 and 6.1.1.4).

Table 1. Crystallographic data and other experimental details of (1).

CCDC deposition no.	975380
Crystal description	Yellow block
Chemical Formula	$C_{18}H_{23}N_2 \cdot C_6H_2N_3O_7$
Molecular weight, g mol ⁻¹	495.49
Cell parameters	
<i>a</i> , Å	9.8141(6)
<i>b</i> , Å	12.6772(6)
<i>c</i> , Å	19.9860(12)
β , deg	100.318(6)
Unit cell volume, Å ³	2446.4(2)
Crystal system	Monoclinic
Space group	P 2 ₁ /c
Temperature, K	293(2)
Number of molecules per unit cell,	4
Radiation	MoK α ,
Wavelength, Å	0.71073
<i>F</i> (000)	1040
θ range for entire data collection	3.59< θ <26.00
Range of indices	$-12 \leq h \leq 11$ $15 \leq k \leq 13$ $-24 \leq l \leq 17$
Number of measured reflections	9897
Number of unique reflections	4789
Number of observed reflections	2703
Number of parameters refined	330
Restraints	0
Refinement method	Full-matrix least squares on <i>F</i> ²
Final <i>R</i> -factor	0.0516
<i>wR</i> ² (<i>F</i> ²)	0.1057
Weight	$1/[\sigma^2(F_o^2) + (0.1079P)^2 + 0.1143]$, where $P = [F_o^2 + 2F_c^2]/3$
Goof(<i>S</i>) on (<i>F</i> ²)	1.000
Final residual electron density, Å ³	-0.182< $\Delta\rho$ <0.157
(Δ/σ) _{max} in the final cycle	0.001 (for <i>z</i> H1)
Scan mode	ω

CCDC-975380 contains the supplementary crystallographic data for this structure. These data can be obtained free of charge from The Cambridge Crystallographic Data Centre via www.ccdc.cam.ac.uk/data_request/cif.

Results and Discussion

An ORTEP view of the title compound with atomic labeling is shown in Figure 2.¹⁰ The geometry of the molecule was calculated using the PLATON¹¹ and PARST¹² software. Crystal data, along with data collection and structure refinement details are summarized in Table 1. Selected bond lengths and angles are given in Table 2, while hydrogen bonds are presented in Table 3.

The overall molecular geometry of the title compound, including bond distances¹³ has a normal range. In the title molecule, piperazine ring adopts a chair conformation with best mirror plane passing through the atoms N1 and N4 and best two fold rotational axis bisecting the bonds N1-C2 with asymmetry parameter [$\Delta C_s(N1)=0.64$ and $\Delta C_2(N1-C2)=2.98$].¹⁴ The dihedral angle between the six membered rings (C8-C13) and (C14-C19) is 75.17(8)°. Within the benzene ring of the 2,4,6-trinitrophenolate, the C-C-C bond angles of the three nitro-connected C-atoms are 123.3(3)°, 121.2(2)° and 125.3(2)°, and are a little larger than the remaining three C-C-C bond angles.

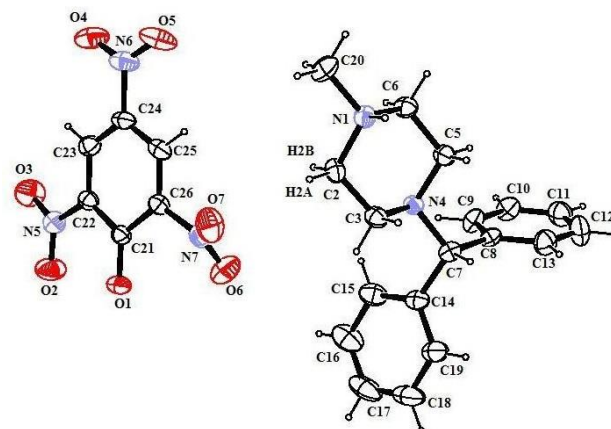
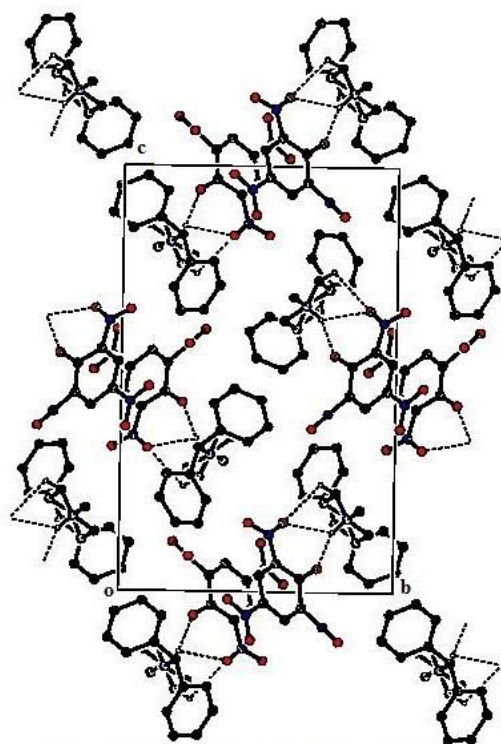
**Figure 2.** ORTEP view of the molecule with displacement ellipsoids drawn at the 50 % probability level. H atoms are shown as small spheres of arbitrary radii.**Figure 3.** The crystal packing view down the a-axis is shown.

Table 2. Selected bond lengths (Å) and angles (°) for (1).

Bond lengths, Å		Bond angles, °			
N5-C22	1.442(3)	O2-N5-C22	120.0(2)	O5-N6-O4	124.5(2)
N4-C5	1.460(2)	C5-N4-C3	107.9(1)	N4-C3-C2	111.3(2)
N4-C3	1.465(3)	C5-N4-C7	111.6(2)	C25-C26-N7	117.2(2)
N4-C7	1.477(3)	C3-N4-C7	110.7(1)	C21-C26-N7	117.5(2)
C21-O1	1.245(2)	O1-C21-C26	121.9(2)	N1-C6-C5	110.8(2)
N5-O2	1.214(2)	O1-C21-C22	126.4(2)	N4-C7-C8	111.5(2)
N5-O3	1.214(2)	O2-N5-O3	121.3(2)	N4-C7-C14	110.2(2)
N1-C20	1.488(3)	O3-N5-C22	118.7(2)	O5-N6-C24	117.4(3)
N1-C2	1.488(3)	C20-N1-C2	111.7(2)	O4-N6-C24	118.2(3)
N1-C6	1.488(3)	C20-N1-C6	111.9(2)	C23-C24-C25	121.2(2)
C26-N7	1.461(3)	C2-N1-C6	109.9(26)	C23-C24-N6	119.3(2)
N6-O5	1.222(3)	N1-C2-C3	110.2(2)	C25-C24-N6	119.4(2)
N6-O4	1.229(3)	N4-C5-C6	110.1(2)	O7-N7-O6	123.1(3)
N6-C24	1.460(3)	C23-C22-N5	116.2(2)	O7-N7-O6	123.1(3)
N7-O7	1.208(3)	C21-C22-N5	120.4(2)	O6-N7-C26	117.3(2)
N7-O6	1.217(3)				

Table 3. Hydrogen bonding parameters (Å, °) for (I).

H-Bonds	D-H, Å	H...A, Å	D...A, Å	D-H ...A, °	Symmetry Code
C2-H2A...O3	0.97	2.41	3.339(3)	161	
N1-H1...O1	0.94(2)	1.83(2)	2.709(3)	153(2)	x, -y+1/2, z+1/2
N1-H1...O2	0.94(2)	2.35(2)	3.031(3)	129(2)	x, -y+1/2, z+1/2
C2-H2B...O2	0.97	2.59	3.078(3)	111	x, -y+1/2, z+1/2

In the crystal structure of the title compound, intermolecular N-H...O and C-H...O hydrogen bonds link the methylpiperazinium unit with 2,4,6-trinitrophenolate unit.

In addition to these interactions, the crystal structure contains a π - π stacking interaction between the rings (C21-C26) at (-x, 1-y, -z) with [centroid-centroid separation = 3.650(1) Å, interplanar spacing = 3.461 Å, centroid shift = 1.348 (2) Å]. A packing view of the molecules in the unit cell viewed down the a-axis is shown (see Figure 3).

The intermolecular hydrogen bonds are responsible for the formation of hydrogen bonded network thus, providing more stability to the molecules in the unit cell. The three dimensional framework is further stabilized by π - π interactions between the rings (C21-C26). The summary of intra- and intermolecular N-H...O, C-H...O hydrogen bonds is given (see Table 3).

Acknowledgements

One of the authors (Rajni Kant) acknowledges the Department of Science and Technology for single crystal X-ray diffractometer as a National Facility under Project No. SR/S2/CMP-47/2003. BN thanks UGC for financial assistance through BSR one time grant for the purchase of chemicals. BN thanks Mangalore University for research facilities.

References

- ¹Tehseen, A., Mumtaz, A., Asrar, A. K., Islam, U. K., *Proc. Pakistan Acad. Sci.*, **2004**, 41, 21.
- ²Abbas, A., Mohsen, K., Shahnaz, C., Babak, N., *Iranian J. Pharm. Res.*, **2012**, 11, 1027.
- ³Jasinski, J. P., Butcher, R. J., Siddegowda, M. S., Yathirajan, H. S., Chidan, C. S. K., *Acta Cryst.*, **2011**, E67, o500.
- ⁴Bertolasi, V., Borea, P. A., Gilli, G., Sacerdoti, M., *Acta Cryst.*, **1980**, B36, 1975.
- ⁵Harrison, W. T. A., Bindya, S., Ashok, M. A., Yathirajan, H. S., Narayana, B., *Acta Cryst.*, **2007**, E63, o3143.
- ⁶Harrison, W. T. A., Sreevidya, T. V., Narayana, B., Sarojini, B. K., Yathirajan, H. S., *Acta Cryst.*, **2007**, E63, o3871.
- ⁷Fun, H. K., Hemamalini, M., Shetty, D. N., Narayana, B., Yathirajan, H. S., *Acta Cryst.*, **2010**, E66, o714.
- ⁸Dutkiewicz, G., Samshuddin, S., Narayana, B., Yathirajan, H. S., Kubicki, M., *Acta Cryst.*, **2011**, E67, o390.
- ⁹Sheldrick, G. M., *Acta Cryst.*, **2008**, A64, 112.
- ¹⁰Farrugia, L. J., *J. Appl. Cryst.*, **2012**, 45, 849.
- ¹¹Spek, A. L., *Acta Cryst.*, **2009**, D65, 148.
- ¹²Nardelli, M., *J. Appl. Cryst.*, **1995**, 28, 659.
- ¹³Allen, F. H., Kennard, O., Watson, D. G., Brammer, L., Orpen, A. G., Taylor, R. *J. Chem. Soc. Perkin Trans. 2*, **1987**, S1-19.
- ¹⁴Duax, W. L., Norton, D. A., *Atlas of Steroid Structures*, New York: Plenum Press, **1975**, 1.

Received: 28.12.2013

Accepted: 30.01.2014.



OCCURRENCE AND DISTRIBUTION OF STAPHYLOCOCCUS AUREUS AND COLIFORM BACTERIA IN THE INNER GULF OF THAILAND

Phawadee Buathong^[a], Wannisa Leelaruji^[a], Pramot Sojisuporn^[b], Gullaya Wattayakorn^[b],
and Warawut Chulalaksananukul^{[c],[d],[e]*}

Keywords: *Staphylococcus aureus*, coliform, Gulf of Thailand, flood.

Global warming is a phenomenon that causes many environmental issues, including the frequency of heat waves, severity of storm surges, changes in rain pattern, flooding, and coastal erosion. In Thailand, the worst flooding in 2011 has imposed more impacts to the environment, human life and socioeconomic activities. The exceeding amount of floodwater was drained into the adjoining Gulf of Thailand in order to solve the flooding problem. As a result, the inner Gulf of Thailand was affected by the high volume of floodwater together with pathogenic bacteria such as *Staphylococcus aureus* and coliform bacteria which are generally used as indicators of a number of other bacteria. The results from this study revealed that total coliforms had higher spread rate toward the west coast of the inner Gulf, while *S. aureus* was found to be highest at the central part of the inner Gulf of Thailand. In general, the highest abundance of both the examined groups was observed during November 2011 after the high rainfall (flood) event.

*** Corresponding Authors**

E-Mail: warawut.c@chula.ac.th

- [a] Program in Biotechnology, Faculty of Science, Chulalongkorn University, Bangkok 10330, Thailand.
- [b] Department of Marine Science, Faculty of Science, Chulalongkorn University, Bangkok 10330, Thailand.
- [c] Biofuels by Biocatalysts Research Unit, Chulalongkorn University, Bangkok 10330, Thailand.
- [d] Department of Botany, Faculty of Science, Chulalongkorn University, Bangkok 10330, Thailand.
- [e] Aquatic Resources Research Institute, Chulalongkorn University, Bangkok 10330, Thailand.

Introduction

Global warming is caused mostly by increasing concentrations of greenhouse gases in the atmosphere. It is causing climate patterns to change and causes many environmental issues around the world. Important effects due to climate change are the frequency of heat waves, severity of storm surges, more intense droughts, and floods. In addition, sea-level rise is projected to accelerate during the 21st century, with dramatic impacts in low-lying regions where subsidence and erosion problems already exist. These factors also affect the flow of matter, as well as changes in the volume of sediments and nutrients being swept out to the coastal seas, and will affect biological, physical and chemical components of water through different paths thus enhancing the risk of waterborne diseases. Climate change has almost certainly had an impact on Thailand. The coastal area of Thailand is already experiencing the impacts of global climate change, as manifested by the frequency and severity of tropical storms, floods, and coastal erosion over the last several decades. Climate change is causing the rising of sea temperatures and acidity of seawater affecting marine life and coastal aquaculture. It is a threat to food security, public health and the occupation of the coastal communities¹.

During the flood season in 2011, Thailand witnessed its worst flooding in many years. Heavy rain combined with multiple tropical storms throughout the extended rainy season played a large part in the extensive flooding. The average precipitation of the Chaophraya watershed area from May to October 2011 was the highest in history, which was 143 % of the average rainy season rainfall of regular years. Some 66 of Thailand's 77 provinces were reportedly affected by severe, record-high flooding, including the Bangkok metropolitan area and its surrounding areas¹. This big flood impacted also the local sewage systems leading to a release of untreated water into the river, posing a severe danger for health. Lower water quality drained from floodwater into rivers and the Gulf of Thailand has been observed by the Pollution Control Department as well as researchers from various universities¹. From this incident, the Gulf of Thailand which had been affected by the high volume of floodwater could also be contaminated by some pathogenic bacteria such as *Staphylococcus aureus*, coliform bacteria and *Vibrio* spp. which may impose some impacts on marine life and adversely affect the economy of the country.

Coliform bacteria are organisms that are present in the environment and in the faeces of all warm-blooded animals and humans, which are a commonly used as bacterial indicator of sanitary quality of foods and water. Coliforms can be found in the aquatic environment, in soil and on vegetation; they are universally present in large numbers in the faeces of warm-blooded animals. Most coliform bacteria are non-pathogenic microorganisms (non-pathogen), but the amount of coliform bacteria (coliform bacteria count) used as indicators of food sanitation and water. Coliform bacteria that found in food and water indicate the impurity and unhygienic and can be indicates that the water is contaminated with germs².

Staphylococcus is the microbes in the Family Micrococcaceae which are Gram-positive staining with their primary habitat in the skin, glands and mucous membranes of warm-blooded animals including humans. It has a round shape and arrangement is similar to grapes. Anyway, it can be found as single cells, in pairs or short chains. Their colonies have smooth rounded edges and have cream, yellow, orange colour. *S. aureus* survive well in the environment and may also be isolated from a range of sources that come into contact with man and animals. The optimum temperature range is 30 to 37 °C, pH 4.0-10.0 and tolerate to salt at 18-20 %. *S. aureus* were classified as "Facultative anaerobe" and can produce eight types of enterotoxin toxin; A, B, C1, C2, C3, D, E and H, which are the most common for food poisoning is A and D. The toxins are heat resistant and may not be destroyed even boiling for half an hour. It's heat resistant is up to 121°C for 15 minutes, this toxin can be dissolved in water and salt solution. *S. aureus* can produce the toxin at 37 °C better than at 25 and 10 °C respectively. It also tolerate to gamma radiation that dose permitted for food as well².

Goodwin et al. (2012)³ studied the spread of *S. aureus* in seawater and beaches in Southern California. Most of *S. aureus* were found in the water samples (59 %, $n = 328$) and in the sand (53 %, $n = 358$). The cultures were found to be correlated with other variables such as location, temperature and the number of people swimming in that particular area. Viau et al. (2011)⁴ studied bacterial pathogens in coastal waters of Hawaii in order to understand the distribution of five species of pathogenic bacteria, including *Salmonella*, *Campylobacter*, *S. aureus*, *Vibrio vulnificus* and *Vibrio parahaemolyticus* by collect water samples from 22 rivers in O'ahu coastal area. Total five species of pathogenic bacteria were found. *Vibrio* is bacteria Genus that are very important in medical, there are four species; *V. cholerae*, *V. parahaemolyticus*, *V. vulnificus* and *V. alginolyticus*. The two species that was commonly found in Thailand are *V. parahaemolyticus* and *V. cholerae*. *V. cholerae* is the cause of cholera and *V. parahaemolyticus* is the cause of food poisoning⁵. *V. parahaemolyticus* outbreaks have increased in the recent 10-20 years, mainly caused by the consumption of raw or uncooked seafood which has reported an outbreak of diarrhoea in several countries including the U.S.A, China, Japan and Korea. This bacterium is pathogenic in humans which are distributed in the tropical ocean and coastal environment⁶, because it has the ability to tolerate saline water and was isolated from marine sediment, oysters, crabs, lobsters, squid, shrimp and many other species of fish⁷.

In Thailand, the Office of Water Quality Management, Pollution Control Department conducted the analysis of microbial quality in coastal water collected along the coasts during 2005 to 2012, and found that the levels of bacterial species increased significantly during such period. It was suggested that such bacteria may be transported with the floodwaters which had been accelerated discharges into the sea. However, there have been few studies on human pathogenic bacteria in seawater from the Gulf of Thailand to date. Hence, the present study aims to investigate the occurrence and distribution of *Staphylococcus aureus* and coliform bacteria in seawater samples from 20 stations in the inner Gulf of Thailand after the big flood in October 2011.

Materials and Methods

Research area

The site of this study is the innermost area of the Upper Gulf of Thailand (inner Gulf), located at 12°40'–13°36'N and 99°57'–101°00'E (Fig. 1). The inner Gulf is roughly rectangular in shape, about 100 km long and 100 km wide, with an average depth of 15 m. It is the catchment basin of four large rivers on the northern side and two on the western coast. Among them, the Chaophraya River has the biggest volume, with the average runoff per year of 13.22×10^3 MCM. The Gulf is surrounded by highly populated areas and some heavily polluting industries. Some untreated effluents have been discharged from industrial sites into the small tributaries that feed into the inner Gulf. In addition, domestic wastewater generated by residents in and around the area is discharged into open ditches, which ultimately draining into the inner Gulf⁸.

Sampling stations and sample collection

Two sampling events were conducted during November 2011(after the big flood event) and February 2012. During each event, seawater samples were collected from the 20 sampling stations in the inner Gulf of Thailand (Fig. 1), at a depth of 1 m from the sea surface in order to avoid contamination from surface micro-layer. The samples were collected into pre-sterilized bottles (100 ml) fitted with tight screw caps. Care was taken to avoid accidental contamination of the water during collection and transportation to the laboratory for analysis. Physical-chemical parameters, including salinity (*S*), temperature (*T*), pH, and dissolved oxygen (*DO*) were measured using a multi-parameter probe (YSI model 650-01m environmental monitoring systems; YSI, Yellow Springs, OH). These parameters were measured *in-situ* in the surface water of the sea where bacterial pathogens were sampled. Total suspended solids (TSS) were analysed in the laboratory by the standard method.

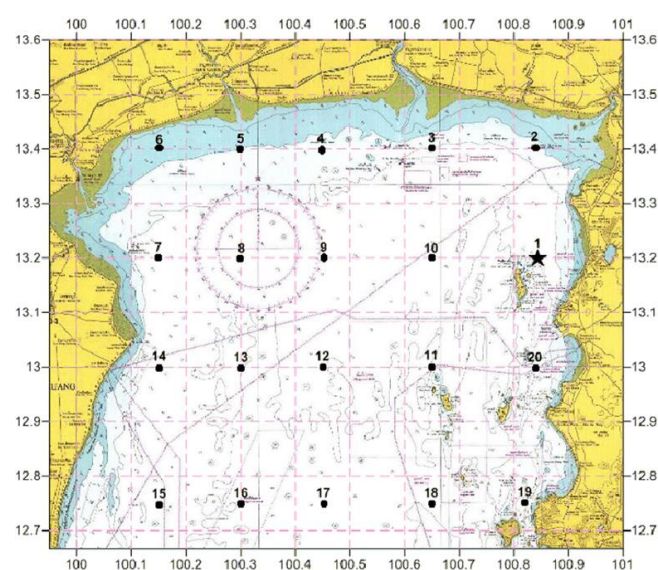


Figure. 1. Map showing sampling stations in the study area of the inner Gulf of Thailand.

Table 1. Mean±sd and range of the measured physico-chemical parameters of seawater in the study area

Parameters	Salinity, ‰	Temperature, °C	pH	Dissolved oxygen, mg L ⁻¹	Total suspended solids, mg L ⁻¹
November 2011					
Mean±s.d	29.7±4.1	29.7±1.6	8.3±0.1	5.7±1.3	71.3±11.6
Range	20.6-33.8	27.7-33.2	8.1-8.5	3.4-8.8	65.0-109.0
February 2012					
Mean±s.d.	30.9±3.7	28.3±1.0	8.2±0.2	5.0±0.8	78.1±29.7
Range	21.6-34.1	26.3-30.1	8.0-8.5	4.1-7.2	55.0-141.0

Bacteriological analysis

Water samples were analysed for pathogenic bacteria by using Petrifilms (3M, St. Paul, MN). The cultures were incubated at 37 °C for 24 hours, then colonies count was carried out as colonies forming unit (CFU) as follows:

Staphylococcus aureus detection

Staphylococcus aureus was detected and enumerated from surface water samples by pipetting 1 ml sample into the central part of the Petrifilm, which was slowly closed with another film and then placed the pressing sheet on the 3M Petrifilm STX and using index finger pressed them firmly until the sample was spread all over the foam. The films were left to become harden by 1-2 minutes then incubated at 37 °C for 24 hours. The counts were recorded and reported in colony forming units (CFU mL⁻¹).

Total coliform bacteria detection

Total coliform bacteria was detected and enumerated from surface water samples by pipetting 1 ml sample into the central part of the Petrifilm, which was slowly closed with another film and then placed the pressing sheet on the 3M Petrifilm EC and using index finger pressed them firmly until the sample was spread all over the foam. The films were left to become harden by 1-2 minutes then incubated at 37 °C for 24 hours. The counts were recorded and reported in colony forming units (CFU mL⁻¹).

Statistical analyses

Parameters for correlation analysis included *S*, *T*, *DO*, *TSS*, and log-transformed concentrations of *Staphylococcus aureus* and coliform bacteria. Multiple regression analyses were done using Pearson's correlations between *Staphylococcus aureus* and coliform bacteria dataset and *T*, *S*, or *S* and *T* combined. Correlations were considered significant at $p \leq 0.05$.

Results and Discussion

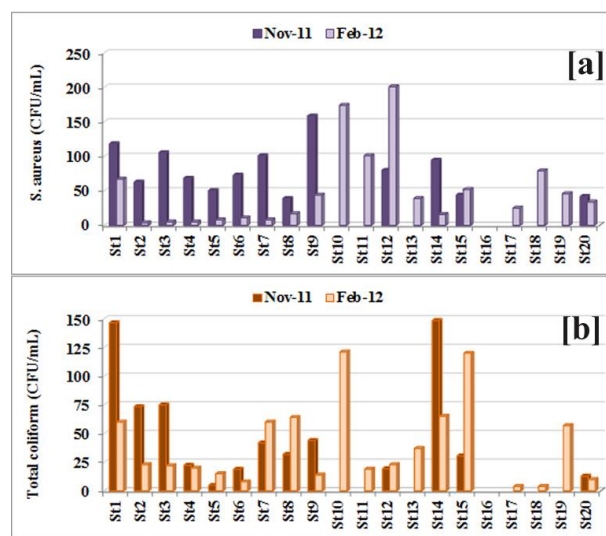
Physico-chemical parameters of seawater

Table 1 shows the results of mean values and ranges of physico-chemical characteristics of the seawater in the inner Gulf of Thailand during the two sampling periods. The water temperature during sample collections varied from 27.7 °C to 33.2 °C in November 2011 and from 26.3 °C to

30.1 °C in February 2012. pH of water varied between 8.0 to 8.5, *DO* varied from 3.4 to 8.8 mg L⁻¹ and salinity from 20.6 to 34.1‰. Comparatively salinity was higher in February 2012 than in November 2011. Total suspended solids concentration varied from 55.0 to 141.0 mg L⁻¹ and higher concentrations recorded in February 2012.

Bacterial pathogens

The abundance of *Staphylococcus aureus* and total coliform in water samples during the two sampling periods is presented in Fig. 2. During the investigated periods, *Staphylococcus aureus* varied from 39 to 159 CFU mL⁻¹ in November 2011 and from 4 to 201 CFU mL⁻¹ in February 2012; while total coliform varied from 5 to 149 CFU mL⁻¹ in November 2011 and from 4 to 121 CFU mL⁻¹ in February 2012. In general, the over all mean counts of both *Staphylococcus aureus* and total coliform were comparatively higher in November 2011 than in February 2012.

**Figure 2.** Abundance of *S. aureus* (a) and coliform bacteria (b) in samples from the inner Gulf of Thailand

The distribution patterns of *Staphylococcus aureus* and total coliform during the two sampling periods are depicted in Fig. 3. The density of *S. aureus* was found to be highest at the central part of the inner Gulf in both sampling events (Fig. 3a). Increasing levels of *S. aureus* in the water in November 2011 may be attributed to post-flood contamination. Floodwater can introduce a number of organisms that can be harmful when they produce other bio-hazardous materials.

Table 2. Correlations of *Staphylococcus aureus* and coliform bacteria with environmental parameters during the two sampling periods

	<i>Staphylococcus aureus</i>			Total coliform		
	<i>R</i>	<i>n</i>	<i>p</i>	<i>R</i>	<i>n</i>	<i>P</i>
November 2011						
<i>S</i> , ‰	0.016	13	0.612	0.074	13	0.211
<i>T</i> , °C	0.019	13	0.781	0.043	13	0.727
<i>DO</i> , mg L ⁻¹	0.018	13	0.787	-0.011	13	0.930
<i>TSS</i> , mg L ⁻¹	-0.005	13	0.395	-0.018	13	0.127
February 2012						
<i>S</i> , ‰	0.125	19	0.042*	-0.043	19	0.520
<i>T</i> , °C	-0.098	19	0.500	0.109	19	0.521
<i>DO</i> , mg L ⁻¹	0.469	19	0.045*	-0.353	19	0.177
<i>TSS</i> , mg L ⁻¹	-0.005	19	0.385	-0.003	19	0.676

R: Pearson product-moment correlation coefficients for log-transformed *Staphylococcus aureus* (in CFU mL⁻¹) and total coliform (in CFU mL⁻¹); *n*: number of samples; *p*: significance, with $p \leq 0.05$ considered significant (*); *S*: salinity, *T*: temperature, *DO*: dissolved oxygen, *TSS*: total suspended solids

Coliform bacteria have been used to evaluate the general quality of water. In November 2011, the total coliform had higher spread rate along the west coast between Cha-am and Huahin; as well as along the east coast between the Bangpakong estuary and Sattahip. In February 2012, it was found that the concentration of total coliform was less abundance and concentrated mostly along the east coast of the inner Gulf (Fig. 3b). The adverse effect of the marine environment on coliforms is manifested by decreased survival of coliform bacteria. When they enter the sea, enteric bacteria are subjected to simultaneous stresses whose impact on cell metabolism will lead to either their maintenance or their decay in marine environments. However, high levels of total coliforms do not necessarily relate specifically to faecal pollution, but to the bacterial loading of enteric within the water system.

Temperature and salinity are often the most important environmental factors controlling bacterial abundance in estuarine and marine waters. Correlations between total coliform bacteria and environmental parameters during both sampling periods however, were not significant ($p \geq 0.05$, Table 2). On the other hand, significant and positive correlations were found between *Staphylococcus aureus* abundance and salinity and dissolved oxygen in the February 2012 sampling period. The lack of a relationship in November 2011 may be due to the extreme climate event.

This comparative assessment of distribution and abundance of human pathogenic bacteria is helpful to infer that the Gulf of Thailand has experienced the impacts of sewage outfalls and extreme climate events. In the future, as the dataset expands and as more storms are characterized, it will be possible to conduct further analyses that will increase the usefulness of the observed relationships. The observations from this study are useful for managing effluent outfalls into coastal ecosystems. Every effort leading to the reduction in pollution indicating bacteria and microbes of human health concern has to be promoted and implemented.

Acknowledgments

This research was partially supported by the Higher Education Research Promotion and National Research University Project of Thailand, Office of the Higher Education Commission (CC1030A) and the Integrated Innovation Academic Center: IIAC Chulalongkorn University Centenary Academic Development Project (CU56-CC06). We thank Dr. Sompop Rungsupa and the crew of the R/V Chulavijai for their help in the field.

References

- ¹World Bank, *Thai Flood 2011: Rapid Assessment for Resilient Recovery and Reconstruction Planning*, **2012**, 377.
- ²Abou-Elala, S., Kamel, M. M., Fawzy, M. E., *Desalination*, **2010**, 250, 1-5.
- ³Goodwin, K., McNay, M., Cao, Y., Ebentier, D., Madison, M., Griffith, J., *Water Res.*, **2012**, 46, 4195-4207.

Figure 3. Areal distribution of *S. aureus* (a) and total coliform (b) in the study area

Correlation of environmental variables and bacterial population

The correlation among the bacterial population and environmental variables is presented in Table 2.

- ⁴Viau, E., *Water Res.*, **2011**, 45, 3279-3290.
- ⁵Mohammed, R., *Marine Pollut. Bull.*, **2012**, 64, 1201-1209.
- ⁶Shen, X., Cai, Y., Liu, C., Liu, W., Hui, Y., Su, Y., *Int. J. Food Microbiol.*, **2009**, 136, 129-132.
- ⁷Slonczewski, J., Foster, J., *Microbiology An Evolving Science*, 1st ed. United States of America: W.W. Norton & Company, Inc., **2009**.
- ⁸Wattayakorn, G., "Environmental Issues in the Gulf of Thailand", In: E. Wolanski (ed.), *The Environment in Asia Pacific Harbours*, Springer, Netherland, **2005**, 497.
- ⁹Wikipedia, *Coliform bacteria* [online], Available from: http://en.wikipedia.org/wiki/Coliform_bacteria, **2013**, 18 Jan.
- ¹⁰Wikipedia, *Staphylococcus aureus* [online], Available from: http://en.wikipedia.org/wiki/Staphylococcus_aureus, **2013**, 18 Jan.
- ¹¹Wikipedia, *Vibrio* [online], Available from: <http://en.wikipedia.org/wiki/Vibrio>, **2013**, 18 Jan.
- ¹²Joseph, S. W., Colwell, R. R., Kaper, J. B., *Crit. Rev. Microbiol.*, **1982**, 10, 77-124.
- ¹³Hamzah, A., Kipli, S. H., Ismail, S. R., Una, R., Sarmani, S., *Microbiological Study in Coastal Water of Port Dickson, Malaysia. Sains Malaysiana*. **2011**, 40(2), 93-99.
- ¹⁴Elmir, S. M., Wright, M. E., Abdelzaher, A., Solo-Gabriele, H. M., Fleming, L. E., Miller, G., Rybolowik, M., Shih, M. P., Pillai, S. P., Cooper, J. A., Quay, E., *Water Res.*, **2007**, 41(1), 3-10.
- ¹⁵Solic, M., Krstulovic, N., *Marine Pollut. Bull.* **1992**, 24(8), 411-416.
- ¹⁶U.S. EPA (United States Environmental Protection Agency), *Ambient water quality criteria for bacteria EPA/440/5-84-002*, U.S. Environmental Protection Agency, Office of Water, Regulations and Standards, Criteria and Standards Division, Washington, D.C., **1986**.
- ¹⁷Thompson, F. L., Tetsuya, I., Swings, J., *Microbiol. Mol. Biol. R.*, **2004**, 68, 403-431.
- ¹⁸Noriega-Orozco, L., Acedo-Félix, E., Higuera-Ciapa, I., Jiménez-Flores, R., Cano, R., *Rev. Latinoam. Microbiol.*, **2007**, 49, 60-67.
- ¹⁹Fujino, T., Okuno, D., Nakada, A., Aoyama, A., Fukay, K., Mukay, T., *Med. J. Osaka Univ.*, **1953**, 4, 299-304.
- ²⁰Martinez-Urtaza, J., Bowers, J. C., Trinanès, J., DePaola, A., *Food Res. Int.*, **2010**, 43, 1780-1790.
- ²¹EEC Council Directive of 8 Dec 1975 concerning the quality of bathing water (76/160/EEC), *Offic. J. Eur. Commun.*, L/031, **1976**, 1-7.

Received: 02.01.2014.

Accepted: 01.02.2014.



STUDIES ON ANTIBACTERIAL AND ANTICANCER ACTIVITY OF *NERIUM OLEANDER* EXTRACTS

Omar Hamad Shehab Al- Obaidi

Keywords: *Nerium oleander*; antibacterial and anticancer activity; extraction; isolation; aqueous extract; alcoholic extract; hexane extract.

The active substances such as volatile oils (11.1 %) and tannins (39.2 %) from *Nerium oleander* plant (*Nerium oleander*) is reported. Some mineral elements such as sodium (107 ppm), calcium (96 ppm) and potassium (73 ppm) were found in the *Nerium oleander* seeds. The anti-bacterial activity of extracts from *Nerium oleander* showed the ability of inhibition in pathogenic bacteria *Escherichia Coli* and *Aurous Staphylococcus* for all different extracts by vary inhibition diameters for different active substances, concentrations and bacteria. The effect of *Nerium oleander* extracts (after the chemical assay) on the growth of (L₂₀B) cell line was studied using *in vitro* system and compared with anticancer drug cisplatin (cis-Pt) as a positive control. The cancer cells were treated with different concentrations of the extract for each of the three treatments. The cytotoxic activity was tested by inhibition rate as parameter. The results showed significant differences ($P<0.05$). There was strong correlation between the three treatments and the different concentrations in comparison with cisplatin.

Corresponding Authors

E-Mail:

[a] Department, Women Education College, Al-Anbar University, Anbar, Iraq

Introduction

Nerium oleander,¹ toxic in all its parts, is an evergreen shrub or small tree in the dogbane family *Apocynaceae*. It is the only species currently classified in the genus *Nerium*. It is most commonly known as oleander, from its superficial resemblance to the unrelated olive *Olea*. It is so widely cultivated that no precise region of origin has been identified, though southwest Asia has been suggested. The ancient city of Volubilis in Morocco may have taken its name from the Berber name oualilt for the flower.² Oleander is one of the most poisonous of commonly grown garden plants.



Figure 1. *Nerium oleander* plant

Oleander shrub, Morocco *N. oleander* is either native or naturalized to a broad area from Mauritania, Morocco, and Portugal eastward through the Mediterranean region and the Sahara (where it is only found sporadically), to the Arabian peninsula, southern Asia, and as far East as Yunnan in southern parts of China.³ It typically occurs around dry stream beds.

Bud of a white-flowered cultivar is an ornamental gardening. Oleander grows well in warm subtropical regions, where it is extensively used as an ornamental plant in landscapes, in parks, and along roadsides. It is drought-tolerant and will tolerate occasional light frost down to 10 °C (50 °F).⁴ It is commonly used in landscaping freeway medians in California, Texas and other mild-winter states in the Continental United States because it is upright in habit and easily maintained. Its toxicity renders it deer-resistant. It is tolerant of poor soils and drought. Oleander can also be grown in cooler climates in greenhouses and conservatories, or as indoor plants that can be kept outside in the summer. Oleander flowers are showy and fragrant and are grown for these reasons. Over 400 cultivars have been named, with several additional flower colours not found in wild plants having been selected, including red, purple, pink, and orange; white and a variety of pinks are the most common. Many cultivars also have double flowers. Young plants grow best in spaces where they do not have to compete with other plants for nutrients.

Nerium oleander has historically been considered a poisonous plant because some of its compounds may exhibit toxicity, especially to animals, when consumed in high amounts. Among these compounds are oleandrin and oleandrigenin, known as cardiac glycosides, which are known to have a narrow therapeutic index and can be toxic when ingested.

Toxicity studies of animals administered oleander extract concluded that rodents and birds were observed to be relatively insensitive to oleander cardiac glycosides.⁵ Other mammals, however, such as dogs and humans, are relatively sensitive to the effects of cardiac glycosides and the clinical manifestations of "glycoside intoxication".⁶

However, despite the common "poisonous" designation of this plant, very few toxic events in humans have been reported. According to the Toxic Exposure Surveillance System (TESS) in 2002 there were 847 human exposures to oleander reported to poison centers in the United States.⁷

Despite this exposure level, from 1985 through 2005, only three deaths were reported. One cited death was apparently due to the ingestion of oleander leaves by a diabetic man.⁸ His blood indicated a total blood concentration of cardiac glycosides of approximately $20 \mu\text{g L}^{-1}$ which is well above the reported fatal level. Another study reported on the death of a woman who self-administered "an undefined oleander extract" both orally and rectally and her oleandrin tissue levels were 10 to $39 \mu\text{g g}^{-1}$ which were in the high range of reported levels at autopsy.⁹ And, finally, one study reported the death of a woman who ingested oleander 'tea'.¹⁰ Few other details were provided.

In contrast to consumption of these undefined oleander derived materials, there is no toxicity or deaths reported from topical administration or contact with *Nerium oleander* or specific products derived from them. In reviewing oleander toxicity Lanford and Boor¹¹ concluded that, except for children who might be at greater risk, "the human mortality associated with oleander ingestion is generally very low, even in cases of moderate intentional consumption (suicide attempts)".¹¹

Toxicity studies that have been conducted in dogs and rodents administered oleander extracts by intramuscular (IM) injection indicated that on an equivalent weight basis, doses of an oleander extract with glycosides ten times in excess of those likely to be administered therapeutically to humans are still safe and without any "severe toxicity observed".¹²

Experimentals

(Cisplatin) (10 mg in 20 ml solution) was provided by Ebew (Austria).

Nerium oleander was obtained from the local market. It was grounded and kept at a laboratory temperature until used, The aqueous extract was prepared by placing 40 g of *Nerium oleander* powder in the conical flask containing 200 mL of distilled water and stirred with magnetic blender for 30 minutes and then centrifuged for 15 minutes. The solution was kept in an electric furnace at 35°C until we get the extract and from it we prepared the solutions with 5, 10, 15, 20 and 25 % concentration.

Alcohol extract was obtained by putting 50 g of *Nerium oleander* powder in a extraction unit (Soxhlet) and 350 ml of 80 % ethanol was added and heated to 40°C and then the extract was extracted by using vacuum rotary evaporator over a period of 12 h. also at 35°C ¹³ after that by the same way aqueous extract solutions prepared.¹⁴

The percentage of oil in the seeds, based on the Association of Official Analytical Chemists (AOAC) method¹⁵ was estimated from the extract extracted with hexane. The volatile oils were extracted from the ether extract from which the solvent was separated.

Tannins were isolated from *Nerium oleander* by adding 75 ml of distilled water to 0.5 g of *Nerium oleander* powder The mixture put in boiled water bath for 30 minutes, then the mixture run in centrifuge at 200 cycle\minutes for a

period of 20 minutes .The solution transfer to flask 100 ml and complete the volume to the mark with distilled water then added to the mixture 20 ml of 4 % lead acetate with shaking then continued and filtered. The sludge dried at 70°C in electric furnace.¹⁶

Ash content was estimated by taking 2 g of *Nerium oleander* powder and burning it in an oven at 550°C , The ash so obtained was collected and weighed.

The percentage of moisture was estimated from 2 g of *Nerium oleander* powder which was heated to 60°C for a period of 24 hours in an electric furnace. The heated material after cooled and weighed to estimate the loss in weight.

The pH of the solution, obtained from blending 10 grams of *Nerium oleander* powder with 100 ml of distilled water and stirring the mixture using a magnetic stirrer for 10 minutes, was measured using a pH -Meter.

The presence of semi-alkaloids, carbohydrates, saponin, flavonoids, lipids, proteins, and tannins were also detected.^{17,18} The results are given in Table 1.

Study the activity against pathogenic bacteria

Agar-well diffusion method, suggested by Kirby Baauer,¹⁹ was used to measure the sensitivity of *Escherichia Coli* and *Staphylococcus aureus* bacteria (isolated and diagnosed in culture laboratory in children's hospital in Ramadi). The Mueller Hinton agar was also used to test the sensitivity of bacteria towards the extract from *Nerium oleander*. The dishes were placed in incubator at 37°C for 24 hours and inhibition diameter was measured (Inhibition Zone)¹⁹ in each hole by ruler.

Preparation of standard solutions of isolated substances from *Nerium oleander*

A series of different extracts solutions have been prepared for concentrations of (5 %, 10 %, 15 %, 20 % and 25 %) mg mL^{-1} .

Study of cytotoxic effect on cancer cell line

One type of cancer cell lines (L₂₀B) were used to study the impact of the extracts from *Nerium oleander* on the growth of cells in laboratory.

All solutions are prepared at the same center and culturing tissues were studied in vitro under optimum conditions by the same center. The growth media used in tissue culture technique was MEM (Minimum Essential Media) was provided by Fetal Calf Serum 10 % to form a confluent monolayer, then subculture to discard the previous growth medium and the cell washed with sterilized phosphate buffer solution (PBS) by autoclave at 121°C for 15 min and addition 2-3 min and moving the culture flask kindness. The trypsin-versene solution to discard and cells incubated at 37°C until the cell separation from ground flask, added new growth media and redistribution of cells at the microtiter and incubated at 37°C .²⁰

Statistical Analysis

Data were analyzed by analysis of variance ANOVA. Investigation of differences between cis-platin and the relation with other groups by using the statistical program (SPSS) within significant level ($P < 0.05$).²¹

Result and discussion

The results of the phytochemical (screening of plant materials) studies of the *Nerium oleander* are presented in Table 1.

Table 1. Results of the statements chemical substances effective in *Nerium oleander*

Active Compounds	Reagents	Indicators	Results
Alkaloids	Draggendorff	orange	+
Tannins	Ferric chloride, Lead acetate	greenish blue soln. gelatinous ppt.	+
Intense tannins	Lead acetate	light brown ppt.	+
Flavonoids	aq. NH_3	yellow soln.	+
Amino acids	Alnhidran	purple	+
Phenols	potassium ferrocyanide	greensh – blue ppt.	-
Resins	hydrochloric acid	turbid	+
Terpenoids	Salkowski	dark red	-
Saponins	mercury chloride	white ppt.	+
Carbo- hydrates	α -naphthol	purple	+
Loco antho- cyanidine	hydrochloric acid	red ppt.	+
Steroids	The same of terpenoids reagent after one day	bluish solution	+
Glycosides	Benedict	red ppt.	+

(+) and (-) indicate the positive and negative tests, respectively.

Figure 1 and Table 2 show the percentage of the active contents, tannins and volatile oils isolated from *Nerium oleander*.

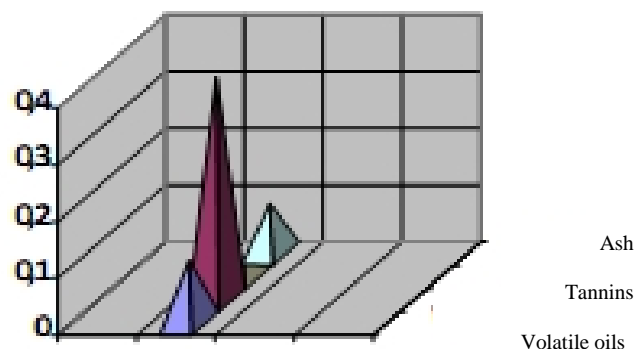


Figure 2. The percentage amounts of extracted materials

The percentage depends on several factors, including climatic conditions and different seasons of the year as the high temperature leads to the loss of more water, and that the decline reduces the loss of water from the plant.¹⁶

$$\text{Total carbohydrates} = 100 - (\% \text{ moisture} + \% \text{ crude protein} + \% \text{ crude fat} + \% \text{ ash content})$$

The sum of percentages of proteins and carbohydrates is about 91.1 %, which is consistent with the calculated ratios published in previous paper.²²

Table 2. Percentage of active combatants in *Nerium oleander*

Active combatants	Percentage, %
Volatile oils	11.1
Tannins	39.2
Moisture	2.1
Ash	8.8
PH	6.0

Nerium oleander contains sodium is 107 ppm, calcium and potassium are 96 and 73 ppm, respectively, all are important functional and metabolic metals for human body.²¹

Table 3 shows the anti-bacterial activity of *Nerium oleander* extracts towards pathogenic *Escherichia Coli* and *Aurous Staphylococcus* bacteria. The water extracts showed higher activity at 25 mg mL^{-1} , the inhibition diameter was 22 mm for *Aurous Staphylococcus* and 19 mm for *Escherichia Coli*.

The inhibition action of alcohol extract is due to the presence of flavonoids, tannins, and some of phenolic compounds which have a biological influence on many bacteria races due to the presence of hydroxyl groups which have the ability to form hydrogen bonds with hydroxyl group in these compounds and water molecules in bacterial cell. Since the water is 90 % of weight and therefore it will disables dynamic actions in bacterial cell.²³ The phenolic compounds have the ability to coagulate the bacterial cell proteins and destroy enzymes involved in the manufacture of necessary amino acids to increase cell division.²⁴

Table 3. Effect of aqueous extract of *Nerium oleander* in different concentrations on growth of pathogenetic bacterial races

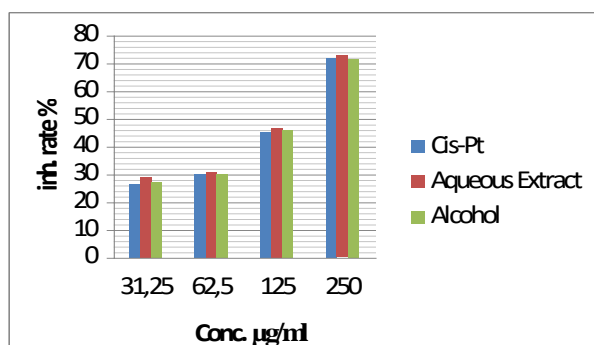
Conc. in mg mL ⁻¹	Inhibition diameter, mm	
	<i>Staphylococcus aureus</i>	<i>Escherichia Coli</i>
25	22	19
20	17	13
10	14	11
10	11	9
5	9	8

Study of Cytotoxic Effect

Cancer cell lines were used to study the effect of *Nerium oleander* extracts on the growth of cells in laboratory to know the efficiency of extracts as anti-tumors. cancer cell line type mice transformed cell line (L₂₀B) used with different concentrations comparable with anticancer drug cisplatin as a positive control after 72 h exposure time.

We calculate the proportion of cell numbers under the optimal conditions for growth in the absence of extracts, so that the output is the control group. Extracts were added to study its effects on cell growth in selected lines.

Extracts were divided into three groups, first one included a hot water extract, second was hot alcoholic extract and the third had cis-Pt. The result were statistically analyzed by ANOVA. The results demonstrated the impact of compounds on cell number ratio when using cell line (L₂₀B). It is clear that hot alcoholic extract have the greatest influence on the proportion of growth cell number and the effect was significant ($P < 0.05$). This result is compared with published literature.²⁵ The effect of aqueous extract was also significant ($P < 0.05$) but the percentage of inhibition - as in the Figure 3 was less than alcoholic extract (Table 4, Figure 3).

**Figure 3.** The comparison of inhibition rates between three treatments with cis-Pt drug in cell line L₂₀B

References

- ¹*Nerium oleander* L. "Germplasm Resources Information Network". United States Department of Agriculture, 1998.
- ²Bingtao, L., Antony, J., Leeuwenberg, M. and Middleton, D. J., "Nerium oleander L.", Flora of China. Harvard University, 2009.
- ³INCHEM *Nerium oleander* L. (PIM 366). International Programme on Chemical Safety: INCHEM, 2005.

Table 4. Inhibition effect of extract and cis-Pt on cancer line (L₂₀B) with different concentrations after 72 h exposure time.

Treatment conc. µg mL ⁻¹	Inhibition rates, %		
	cis-Pt	Aqueous extract	Alcohol extract
31.25	26.55	28.98	27.10
62.5	29.95	30.88	30.09
125	45.10	46.65	45.99
250	71.97	72.76	71.45

- ⁴Huxley, A., "The New Horticultural Society Dictionary of Gardening", vol. 3. London, MacMillan, 1992.
- ⁵Szabuniewicz, M., Schwartz, W. L., McCrady, J. D., Russell, L. H., Camp, B. J., *Southwestern Vet.*, **1972**, 25(2), 105-114.
- ⁶Szabuniewicz, M., McCrady, J. D. and Camp, B. J., *Arch. Int. Pharmacodyn. Therapy*, **1971**, 189, 12-21.
- ⁷Watson, W. A., Toby, L., Litovitz, G., Rodgers, C., Klein-Schwartz, W., Reid, N., Youniss, J., *Am. J. Emergency Med.*, **2003**, 23(5), 589-666.
- ⁸Wasfi, I. A., Zorob, O., Al-Katheeri, N. A., Al-Awadhi, A. M., *Forensic Sci. Int.*, **2008**, 179(2-3), 31-36.
- ⁹Blum, L. M., Reiders, F., *J. Anal. Toxicol.*, **1987**, 11(5), 219-221.
- ¹⁰Haynes, B. E., Bessen, H. A., Wightman, W. D., *Ann. Emerg. Med.*, **1985**, 14(4), 350-353.
- ¹¹Langford, S. D., Boor, P. J., *Toxicology*, **1996**, 109(1), 1-13.
- ¹²Newman, R. A., Yang, P., Pawlus, A. D., Block, K. I., *Molecular Interventions*, **2008**, 8(1), 36-49.
- ¹³Harborne, T. B., "Phytochemical methods". Halasted Press. John Wiley & Sons, New York., **1973**, 178.
- ¹⁴Ba-Angood, S. A., Ermel, K. and Schmutterer, H., "J. Natural Appl. Sci.", **1996**, 1, 13-25.
- ¹⁵Association of Official Analytical Chemists AOAC. *Official Method of Analysis*, 13th ed. Washington, DC, **1989**, 13(4-5), 245-252.
- ¹⁶Francis, G., Kerem, Z., Makkar, H. P. S. and Becker, K., *Brit. J. Nutrition*, **2002**, 88, 587-605.
- ¹⁷Pavia, D. L., Lampman, G. M. and Kriz, G. S., *Org. Chem. Mason.*, **2004**, 53, 653.
- ¹⁸Vandpitte, J., Engback, K., Piot, P. and Henck, C. C., "Basic laboratory procedures in clinical bacteriology" WHO, Geneva, **1991**, 78-110.
- ¹⁹Freshney, R. I., "Cultured of Animal Cells: A manual for Basic Techniques", Inc. Publication, New York, **2000**, 64-69.
- ²⁰Al-Mohammed, N., Al-Rawi, T., Younis, K. M., Al-Morani, W. K., "Principles of Statistics", Al-Mousl Univ., **1986**, 7, 50-52.
- ²¹Herrera, E., Barbas, C., *J. Physiol. Biochem.*, **2001**, 57(2), 43-56.
- ²²Gaw, A., Murphy, M. J., Cowan, R. A., O'Reilly, D. S. J., Stewart, M. J., Shepherd, J., "An illustrated colour text clinical biochemistry", 2nd ed., UK, **1999**, 106-114.
- ²³Grimshaw, J., "Deposides, Hydrolysable Tannins, Lignans, Lignin and Humic Acid". Amsterdam: Elsevier Science Publishing Co. **1976**, Vol. 111, Part D, 92-102.
- ²⁴Yin, F., Giuliano A. E., Van Herle, A. J., *Thyroid Apr.*, **1999**, 9(4), 369-76.
- ²⁵Jing, Y., Waxman, S., *Anticancer Res.*, **1995**, 15(4), 1147-52.

Received: 09.01.2014.

Accepted: 01.02.2014.



CRYSTAL STRUCTURES OF 1-BENZOYL-2-HYDROXY-7-METHOXYNAPHTHALENE ANALOGUES: DIMERIC FEATURES OF THE MOLECULAR PACKING

Akiko Okamoto^[a], Atsushi Nagasawa^[a], and Noriyuki Yonezawa^[a]

Keywords: Intra- and intermolecular hydrogen bonds, Dimeric aggregates, Molecular packing

Molecular alignments of 1-aryl-2-hydroxy-7-methoxynaphthalene analogues are classified into two groups, i.e., molecular stacking standing one behind another and dimeric aggregates. In single molecular structures, the 1-aryl-2-hydroxy-7-methoxynaphthalene analogues show apparently same spatial organizations. The carbonyl groups in these molecules form intramolecular O–H...O=C hydrogen bonds with the adjacent hydroxy groups, affording six-membered cyclic structures. The aryl groups constrained by the intramolecular hydrogen bonds essentially induce dimeric aggregates via formation of a pair of *intermolecular* O–H...O=C hydrogen bonds. When interactions led by the substituents of the benzene rings reduce the stability by the *intermolecular* O–H...O=C hydrogen bonds, the molecular packing should turn one-behind-one type piling.

Corresponding Authors

Phone: +81-42-388-7601

E-Mail: aokamoto@cc.tuat.ac.jp

[a] Department of Organic and Polymer Materials Chemistry,
Tokyo University of Agriculture and Technology, 2-24-16
Naka-machi, Koganei, Tokyo 184-8588, Japan

Introduction

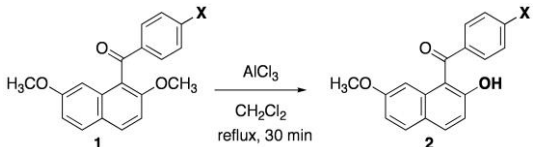
Molecules with non-coplanarly aligned aromatic rings, such as binaphthyl and biphenyl compounds, have been in the limelight because of their unique spatial shapes affording characteristic optic and electronic properties and asymmetric molecular environments. In consequence, various applications have been undertaken such as optically active polymers and catalysts, organic fluorescent dyes and light-emitting diodes, and so on.¹⁻⁵ Naphthalene compounds bearing *peri*-substituents have also received much attention as compounds of characteristic structured aromatic core for a variety of functional materials.⁶⁻⁸ Therefore, structure analyses have been actively performed.⁹⁻¹¹ Recently, we have revealed that arylation at the 1- and 8-positions of naphthalene proceeds smoothly via conventional electrophilic aromatic arylation on condition that suitable acid mediator employed.^{12,13} According to X-ray crystal structure studies, the resulting 1,8-diaroylated naphthalene derivatives, such as 1,8-dibenzoyl-2,7-dimethoxynaphthalene,¹⁴ have a non-coplanar organization of the aromatic rings. Almost all 1,8-diaroylnaphthalene compounds form the stacking structures standing one behind another in the molecular packing via intermolecular (phenyl)C–H...O=C interactions between the aryl groups of the adjacent molecules. On the other hand, the ether-cleaved 1,8-dibenzoylnaphthalene analogue, 1,8-dibenzoyl-2,7-dihydroxynaphthalene, shows dimeric aggregates composed of two types of independent molecules in the crystal.¹⁵ Inter- and intramolecular O–H...O=C hydrogen bonds between the hydroxy groups and the carbonyl ones seem to relate with the formation ability of dimeric aggregates. In this consequence, the authors have planned to clarify the dimeric feature of the molecular packing with more simplified molecules.

Herein, the X-ray crystal structure of 1-benzoyl-2-hydroxy-7-methoxynaphthalene is reported, and the structure-determining factors are discussed through comparison with the methoxy-retained analogue, 1-benzoyl-2,7-dimethoxynaphthalene. Furthermore, the stability of the molecular packing concerning dimeric feature is estimated relatively by comparing with the 1-(4-substituted benzoyl)-2-hydroxy-7-methoxynaphthalene analogues.

Results and discussion

Synthesis of 1-aryl-2-hydroxy-7-methoxynaphthalene analogues **2** were performed by reference to AlCl₃-mediated methyl ether-cleavage reaction of 1-(4-chlorobenzoyl)-2,7-dimethoxynaphthalene (**1d**) (Table 1).¹⁶ 1-Aroyl-2,7-dimethoxynaphthalenes **1** satisfactorily gave the corresponding 2-methyl ether cleaved-compounds (**2**) (entries 1, 2, and 5), with exception of a rather moderate yield of compound **2c** in the reaction of 1-(4-methoxybenzoyl)-2,7-dimethoxynaphthalene (**1c**) (entry 3). By increasing of the amount of AlCl₃ from five equimolar amounts to 7.5 equimolar amounts, the methyl ether cleavage was slightly accelerated (entry 4). AlCl₃-mediated alkyl–oxygen bond cleavage reaction presumably proceeds smoothly by the assist of the neighbouring effect of the aryl group. In the case of 1-arylnaphthalene analogue (**1c**), the oxygen atom of methoxy group in the aryl group should coordinates to AlCl₃. As a result of virtually decreased AlCl₃ around the carbonyl moiety, the ether cleavage reaction of the 1-arylnaphthalene analogue (**1c**) might be retarded.

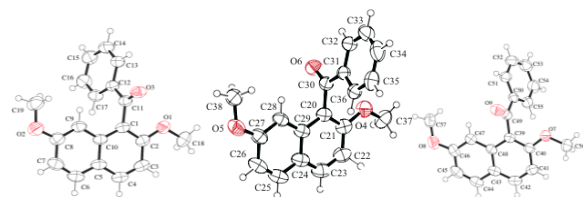
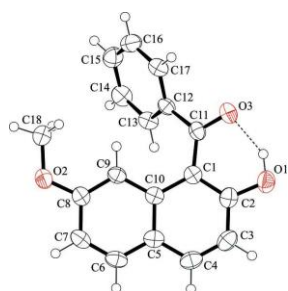
Figures 1 and 2 show crystal structures of 1-benzoyl-2,7-dimethoxynaphthalene (**1a**)¹⁷ and 1-benzoyl-2-hydroxy-7-methoxynaphthalene (**2a**).¹⁸ There are three independent molecules in the crystal of 1-arylnaphthalene **1a**. The independent molecules are labeled (A), (B), and (C). Each independent molecule has essentially the same non-coplanar conformation. The respective dihedral angles between the benzene rings and the naphthalene rings of the molecules are 75.34(7)°, 86.46(7)°, and 76.55(6)°.

Table 1. AlCl₃-mediated methyl–oxygen bond cleavage reaction of 1-aroynl-2,7-dimethoxynaphthalene (**1**)^a


Entry	Substrate (X)	Molar ratio substrate:AlCl ₃	Product (X)	Yield, % ^b
1	1a (H)	1 : 5	2a (H)	52
2	1b (CH ₃)	1 : 5	2b (CH ₃)	63
3	1c (OCH ₃)	1 : 5	2c (OCH ₃)	42
4	1c (OCH ₃)	1 : 7.5	2c (OCH ₃)	56
5	1d (Cl)	1 : 5	2d (Cl)	75

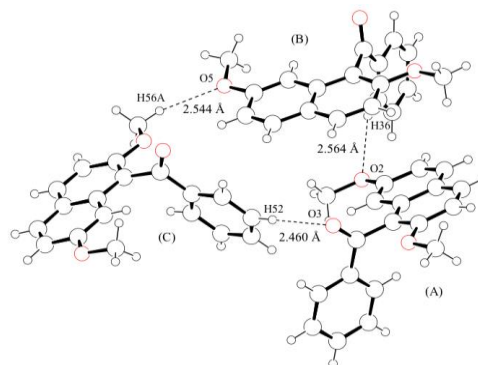
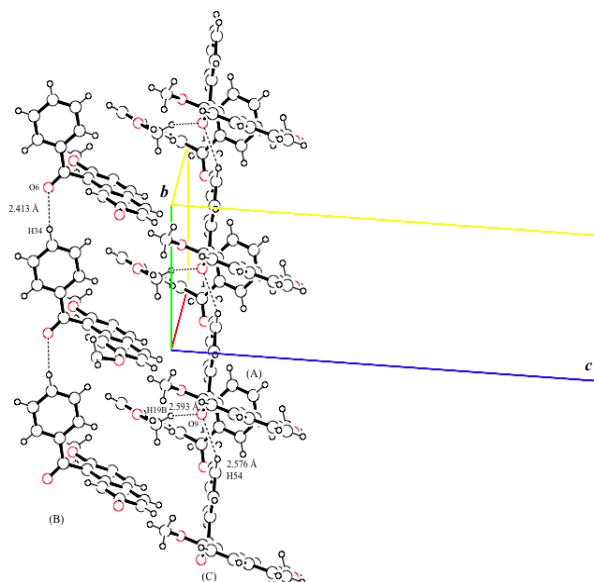
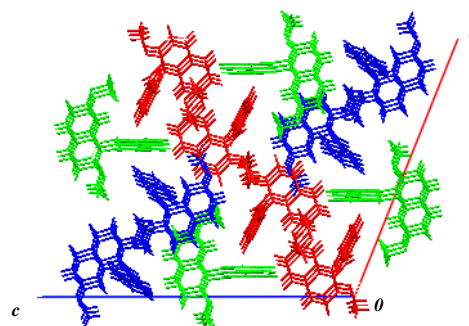
^aReaction conditions: 1-aroynl-2,7-dimethoxynaphthalene **1**, AlCl₃ [5 or 7.5 equivomolar amounts (against substrate **1**)], dichloromethane, reflux, 30 min. ^b Isolated yields.

The crystal structure is stabilized by intermolecular hydrogen bonds among three independent molecules and between same types of the independent molecules (Figure 3). Among three independent molecules, hydrogen bonds between independent molecules (A) and (B) [C36–H36...O2 = 2.564 Å], between independent molecules (B) and (C) [C56–H56A...O5 = 2.544 Å], and between independent molecules (C) and (A) [C52–H52...O3 = 2.460 Å] are observed.

**Figure 1.** Molecular structures of independent molecules (A)(left), (B)(center), and (C)(right) of 1-benzoyl-2,7-dimethoxynaphthalene (**1a**), with the atom-labeling scheme and displacement ellipsoids drawn at the 50% probability level.**Figure 2.** Molecular structure of 1-benzoyl-2-hydroxy-7-methoxynaphthalene (**2a**), with the atom-labeling scheme and displacement ellipsoids drawn at the 50% probability level.

In addition, the independent molecules (B) are connected to each other by intermolecular hydrogen bonds between the benzene ring and the carbonyl group [C34–H34...O6 = 2.413 Å]. The independent molecules (C) are also linked with intermolecular hydrogen bonds between the benzene ring and the carbonyl group [C54–H54...O9 = 2.576 Å]. The independent molecules (B) and (C) are stacked along the *b* axis and form the columnar structures, respectively. On the other hand, the independent molecules (A) have no effective interactions with themselves. They have only

weak interactions with independent molecules (C) [C19–H19...O9 = 2.593 Å] and are piled in the gap of the two different columnar structures of independent molecules (B) and (C) (Figures 4 and 5).

**Figure 3.** The intermolecular C–H...O hydrogen bonds among independent molecules (A), (B), and (C) of 1-aroynaphthalene **1a**.**Figure 4.** The partial crystal packing diagram of 1-aroynaphthalene **1a**, viewed down the *a* axis.**Figure 5.** The molecular arrangement of 1-aroynaphthalene **1a**, viewed down the *b* axis: molecules (A) (green), (B) (red), and (C) (blue).

In the molecule of 1-benzoyl-2-hydroxy-7-methoxynaphthalene (**2a**), there is an intramolecular O–

H...O=C hydrogen bond between the hydroxy group and the carbonyl one on the naphthalene ring. The angles between the C=O bond vector and the least squares planes of the naphthalene ring and the phenyl ring are 30.58(6)° and 42.82(7)°, respectively, while the dihedral angle between the naphthalene ring and the phenyl ring is 58.65(5)°. In the crystal, the molecules are connected by pairs of *intermolecular* O–H...O=C hydrogen bonds, forming centrosymmetric dimers (Figure 6). The dimeric aggregates are related to each other through four kinds of interactions: (methoxy)oxygen...carbon(methoxy) interaction along the *a* axis [$O2...C18 = 3.060(2)$ Å], (naphthalene) carbon...oxygen(carbonyl) interaction along the *b* axis [$C4...O3 = 3.036(18)$ Å], (naphthalene) carbon...hydrogen (naphthalene) along the *b* axis [$C6...H6 = 2.891$ Å], and (benzene) carbon...hydrogen (methyl) along the *c* axis [$C16...H18A = 2.88$ Å].

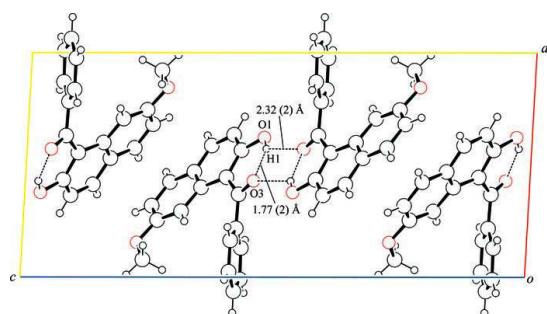


Figure 6. The partial crystal packing diagram of 1-arylnaphthalene **2a**, viewed down the *b* axis. Square-shaped cyclic O–H...O=C hydrogen bonds are shown as dashed lines.

The dihedral angle between the benzene ring and the naphthalene one of 1-benzoyl-2-hydroxy-7-methoxynaphthalene (**2a**) is smaller than that of the methoxy-retained precursor (**1a**). The data indicates that the intramolecular O–H...O=C hydrogen bond in 1-benzoyl-2-hydroxy-7-methoxynaphthalene (**2a**) determines the orientation of the aryl group and thus promotes the formation of the cyclic *intermolecular* O–H...O=C interactions involving the same donor and acceptor groups in pairs of molecules. In other words, the aryl groups without fixation are aligned in the specific orientations as represented in three independent molecules of methoxy-retained precursor **1a**.

Figure 7 shows molecular structures in the crystal of the 1-aryl-2-hydroxy-7-methoxynaphthalene analogues **2b–2d**. These analogous compounds have essentially similar spatial organizations. The nonbonding distances of 1-benzoyl-2-hydroxy-7-methoxynaphthalene **2a** and the analogues **2** are listed in Table 2 with the methoxy-retained molecule **1a**.

In a similar manner of 1-benzoyl-2-hydroxy-7-methoxynaphthalene **2a**, the analogues **2b–2d** forms intramolecular O–H...O=C hydrogen bonds between the hydroxy groups and the adjacent carbonyl groups. Furthermore, the methyl group-bearing analogue **2b**¹⁹ also form two *intermolecular* O–H...O=C hydrogen bonds affording centrosymmetric dimers as well as 1-arylnaphthalene **2a** (Figure 8). The molecular packing features C–H... π interactions involving the centroid of the C5–C10 ring (CT1) and the centroid of the C12–C17 phenyl ring (CT2). On the other hand, no dimeric pairs are

observed in the molecular packing of methoxy group-bearing analogue **2c** and chloro group-bearing one **2d**.²⁰

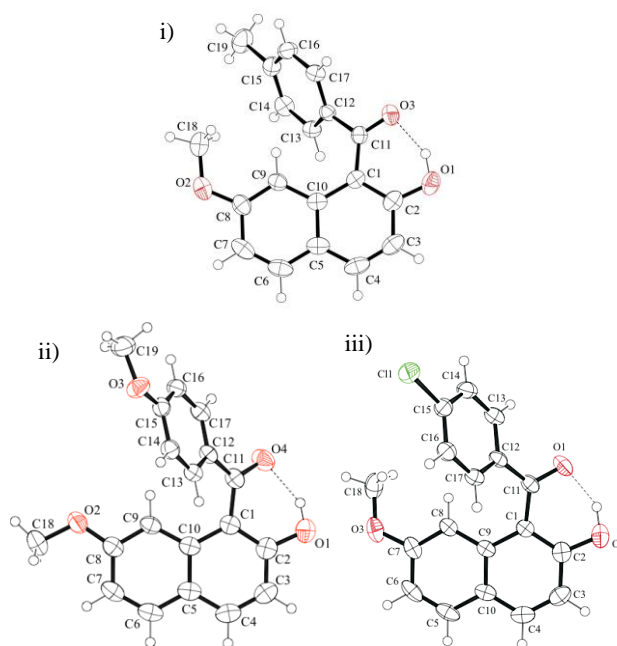


Figure 7. Molecular structures of 1-aryl-2-hydroxy-7-methoxynaphthalene analogues: i) Analogue **2b** (X= CH₃); ii) Analogue **2c** (X= OCH₃), and iii) Analogue **2d** (X= Cl), with the atom-labelling schemes and displacement ellipsoids drawn at the 50% probability level.

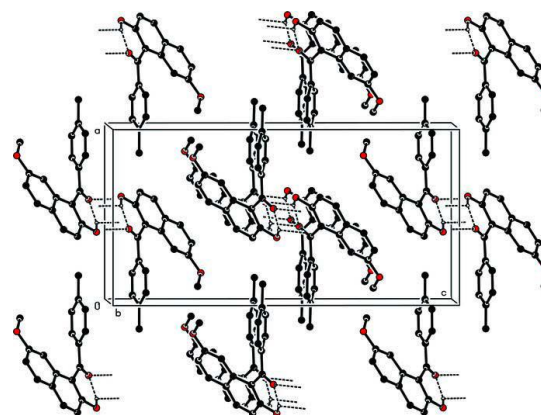


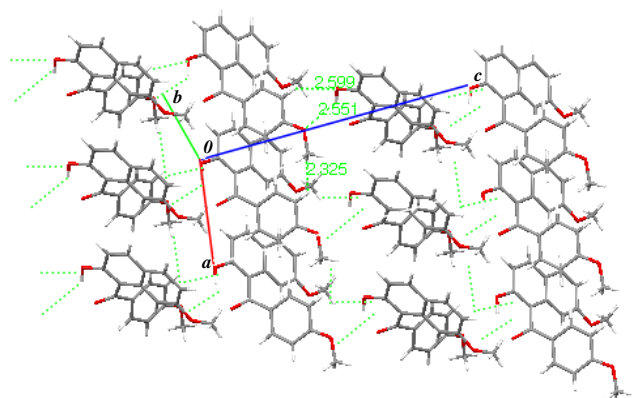
Figure 8. A crystal packing of analogue **2b** (X= CH₃), viewed down the *b* axis. Intermolecular hydrogen bonds are shown as dashed lines. H atoms not involved in hydrogen bondings have been omitted for clarity.

The methoxy group-bearing analogue forms two types of interactions such as (hydroxy)O–H...O–CH₃(4-methoxyphenyl) and (hydroxy)H–O...H–C(phenyl) in crystal (Figure 9). These interactions make infinite O...H chains along the *ac* diagonal. In the case of chloro group-bearing analogue **2d**, a three-dimensional molecular network is formed by loose van der Waals interactions such as (naphthalene)C–H...O=C and (hydroxy)H–O...H–C(phenyl). The alternate arrangement of (*R*)- and (*S*)-configured molecules makes us naturally envision that the molecules align to avoid electrostatic repulsions of Cl against Cl of the adjacent molecule (Figure 10).

Table 2. Nonbonding distances of 1-benzoyl-2,7-dimethoxynaphthalene (**1a**) and 1-aroil-2-hydroxy-7-methoxynaphthalene analogues **2**.

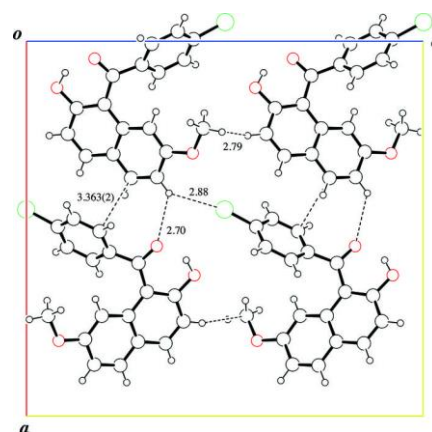
D-X...A	D-X (Å)	X...A _{intra} (Å)	X...A (Å)	D...A (Å)	D-X...A (°)
1-H-2-OCH₃ 1a					
C36-H36...O2	0.95		2.56	3.4116(18)	149
C56-H56A...O5	0.98		2.54	3.4862(19)	161
C52-H52...O3 ⁱ	0.95		2.46	3.395(2)	168
C34-H34...O6 ⁱⁱ	0.95		2.41	3.143(2)	133
C54-H54...O9 ⁱⁱⁱ	0.95		2.58	3.2451(19)	128
C19-H19B...O9 ⁱⁱⁱ	0.98		2.59	3.116(2)	113
1-H-2-OH 2a					
O1-H1...O3	0.92(2)	1.77(2)		2.5792(14)	145(2)
O1-H1...O3 ⁱ	0.92(2)		2.32(2)	3.0088(16)	132.4(18)
1-CH₃-2-OH 2b					
O1-H1...O3	0.95(2)	1.70(2)		2.5618(14)	148(2)
O1-H1...O3 ⁱ	0.95(2)		2.33(2)	3.0083(16)	128(1)
C6-H6...CT1 ⁱⁱ	0.95		2.71	3.5203(13)	144
C17-H17...CT1 ⁱⁱⁱ	0.95		2.76	3.5492(12)	141
C19-H19...CT2 ^{iv}	0.98		2.88	3.7834(16)	154
1-OCH₃-2-OH 2c					
O1-H1...O4	0.92(2)	1.79(3)		2.6193(14)	147.8(19)
O1-H1...O3 ⁱ	0.92(2)		2.55(2)	3.0924(13)	118.1(16)
C14-H14...O1 ⁱⁱ	0.95		2.599(1)	3.4118(15)	144
1-Cl-2-OH 2d					
O2-H2...O1	0.94(2)	1.71(2)		2.5573(16)	148(2)

Symmetry codes: for molecule **1**: (i) $x, y+1, z-1$, (ii) $x, y+1, z-1$, (iii) $x, y, z+1$; for molecule **2a**: (i) $-x+1, -y+1, -z+1$; for molecule **2b** (CT1 and CT2 are the centroids of the C5–C10 and C12–C17 rings, respectively): (i) $-x+1, -y+1, -z+1$, (ii) $-x+1, y-1/2, -z+1/2$, (iii) $x, y+1, z$, (iv) $-x+2, -y+1, -z+1$; For molecule **2c**: (i) $x-1/2, -y+3/2, z-1/2$; (ii) $x+1/2, -y+3/2, z+1/2$.

**Figure 9.** A crystal packing of analogue **2c** (X= OCH₃), viewed down the *a* axis. Intermolecular O...H hydrogen bonds are shown as green dashed lines.

Conclusively, the single molecular spatial organizations of 1-aroil-2-hydroxy-7-methoxynaphthalene analogues are essentially the same regardless of its substituent on the benzene ring. On the other hand, it is entirely dependent on the balance between *intermolecular* O–H...O=C hydrogen bonds and interactions of the substituents whether the molecular packing shows dimeric features or not. 1-Aroil-2-hydroxy-7-methoxynaphthalene analogues are susceptible to form a pair of *intermolecular* O–H...C=O hydrogen bonds between the hydroxy groups and the carbonyl groups.

As a result, they induce dimeric aggregates in crystal. On the other hand, the molecular packing turns one-behind-one type piling when the *intermolecular* O–H...O=C hydrogen bonds are weakened by the interactions of the substituents of the benzene rings.

**Figure 10.** A crystal packing of analogue **2d** (X=Cl), viewed down the *b* axis. Intermolecular hydrogen bonds are shown as dashed lines.

Experimental

All reagents were of commercial quality and were used as received. Solvents were dried and purified using standard techniques.

Measurements

^1H NMR spectra were recorded on a JEOL JNM-AL300 spectrometer (300 MHz) and a JEOL ECX400 spectrometer (400 MHz). Chemical shifts are expressed in ppm relative to internal standard of Me_4Si (δ 0.00). ^{13}C NMR spectra were recorded on a JEOL JNM-AL300 spectrometer (75 MHz). Chemical shifts are expressed in ppm relative to internal standard of CDCl_3 (δ 77.0). IR spectra were recorded on a JASCO FT/IR-4100 spectrometer. Elemental analyses were performed on a Yanaco CHN CORDER MT-5 analyzer. High-resolution FAB mass spectra were recorded on a JEOL MStation (MS700) ion trap mass spectrometer in positive ion mode.

X-ray Crystallography

For the crystal structure determination, the single-crystals of the compound **1** and **2** were used for data collection on a four-circle Rigaku RAXIS RAPID diffractometer (equipped with a two-dimensional area IP detector). The graphite-mono-chromated Cu K α radiation (λ = 1.54187 Å) was used for data collection. The lattice parameters were determined by the least-squares methods on the basis of all reflections with $F^2 > 2\sigma(F^2)$. The data collection and cell refinement were performed using *PROCESS-AUTO* software. The data reduction was performed using *CrystalStructure*. The structures were solved by direct methods using *SIR2004* and refined by a full-matrix least-squares procedure using the program *SHELXL97*. All H atoms were found in a difference map and were subsequently refined as riding atoms, with the aromatic C–H = 0.95 Å and methyl C–H = 0.98 Å, and with $U_{\text{iso}}(\text{H}) = 1.2U_{\text{eq}}(\text{C})$.

Synthetic procedures of 1-benzoyl-2,7-dimethoxynaphthalene (1a)

To a mixture of benzoyl chloride (8.10 mmol, 0.923 mL) and AlCl_3 (10.4 mmol, 1.38 g) in dichloromethane (19.0 mL), dichloromethane solution of 2,7-dimethoxynaphthalene (2,7-dimethoxynaphthalene/dichloromethane: 7.50 mmol, 1.37 g/19 mL) was added by portions at 0°C under nitrogen atmosphere. After the reaction mixture was stirred at 0°C for 6 h, it was poured into iced water (100 mL) and the mixture was extracted with CHCl_3 (30 mL \times 3). The combined extracts were washed with 2 M NaOH aq. and brine, and dried over anhydrous magnesium sulfate. The solvent was removed under reduced pressure to give powdery product (98 % yield). The crude product was purified by recrystallization (hexane–chloroform, isolated yield 65 %). Yellow platelet single-crystals suitable for X-ray diffraction were obtained by crystallization from hexane–dichloromethane.

1-Benzoyl-2,7-dimethoxynaphthalene (1a)

Yellow platelet (hexane/dichloromethane), Mp 358.5–362.0 K; IR (KBr): 1663, 1627 cm^{-1} ; ^1H NMR δ (300 MHz, CDCl_3): 7.84–7.89 (m, 3H), 7.72 (d, J = 8.7 Hz, 1H), 7.57 (t, J = 7.2 Hz, 1H), 7.43 (t, 2H, J = 7.8 Hz), 7.16 (d, J = 9.0 Hz,

1H), 7.01 (dd, J = 2.4, 8.7 Hz, 1H), 6.79 (d, J = 2.4 Hz, 1H), 3.78 (s, J = 8.6 Hz, 3H), 3.71 (s, 3H), ppm; ^{13}C NMR δ (75 MHz, CDCl_3): 198.07, 158.77, 154.93, 137.98, 133.31, 132.98, 130.96, 129.62, 129.44, 128.48, 124.29, 121.67, 117.01, 110.17, 102.02, 56.24, 55.09 ppm; HRMS (FAB; *m*-nitrobenzyl alcohol [*m*-NBA]) m/z : $[\text{M}+\text{H}]^+$: calcd for $\text{C}_{19}\text{H}_{17}\text{O}_3$ 293.3365, found 293.1185.

Methyl–oxygen bond cleavage of 1-benzoyl-2,7-dimethoxynaphthalene (1a)

To a solution of 1-benzoyl-2,7-dimethoxynaphthalene (**1a**, 10.0 mmol, 2.92 g) in dichloromethane (100 mL), AlCl_3 (50.0 mmol, 6.65 g) was added by portions at r.t under nitrogen atmosphere. After the reaction mixture was refluxed for 30 min, the resulting dark red solution was poured into iced-water (100 mL). The aqueous layer was extracted with chloroform (30 mL \times 3). The combined organic layers were washed with brine (30 mL \times 3), and dried over anhydrous magnesium sulfate overnight. The solvent was removed under reduced pressure to give powdery product (quant.). The crude product was purified by repeated recrystallization from hexane to give compound **2** as yellow platelets (52 %).

1-Benzoyl-2-hydroxy-7-methoxynaphthalene (2a)

Yellow platelet (hexane), Mp 371.8–372.3 K; IR (KBr): 3446, 1617, 1572, 1511, 1200 cm^{-1} ; ^1H NMR δ (300 MHz, CDCl_3): 11.64 (s, 1H), 7.85 (d, J = 9.0 Hz, 1H), 7.62 (d, J = 8.7 Hz, 1H), 7.62 (dt, J = 1.7, 7.5 Hz, 2H), 7.55 (tt, J = 1.7, 7.5 Hz, 1H), 7.43 (tt, J = 1.7, 7.5 Hz, 2H), 7.08 (d, J = 9.0 Hz, 1H), 6.89 (dd, J = 2.4, 8.7 Hz, 1H), 6.59 (d, J = 2.4 Hz, 1H), 3.27 (s, 3H) ppm; ^{13}C NMR δ (75 MHz, CDCl_3): 200.8, 162.8, 158.2, 140.8, 136.5, 134.1, 132.3, 130.1, 129.14, 128.8, 123.7, 116.5, 115.9, 113.7, 106.5, 54.5 ppm; HRMS (FAB; *m*-NBA) m/z : $[\text{M}+\text{H}]^+$: calcd for $\text{C}_{18}\text{H}_{15}\text{O}_3$ 279.1021, found 279.0999.

Other arylation and ether cleavage reactions affording **1** and **2** were undertaken by essentially the same procedure as above.

Spectral data and elemental analyses

1-(4-Methylbenzoyl)-2,7-dimethoxynaphthalene (1b)

Pale yellow powder [PTLC; hexane : AcOEt = 2:1 (w/w)], Mp 392.6–394.1 K; IR (KBr): 1656, 1627, 1604, 1512, 1251 cm^{-1} ; ^1H NMR δ (300 MHz, CDCl_3): 7.86 (1H, d, J = 9.0 Hz), 7.76 (2H, d, J = 8.1 Hz), 7.72 (1H, d, J = 8.7 Hz), 7.22 (2H, d, J = 8.1 Hz), 7.16 (1H, d, J = 8.7 Hz), 7.01 (1H, dd, J = 9.0, 2.4 Hz), 6.78 (1H, d, J = 2.4 Hz), 3.80 (3H, s), 3.71 (3H, s), 2.41 (3H, s) ppm; ^{13}C NMR δ (75 MHz, CDCl_3): 197.67, 158.71, 154.76, 144.25, 135.53, 132.98, 130.72, 129.67, 129.57, 129.23, 124.32, 122.04, 116.98, 110.23, 102.10, 56.30, 55.11, 21.69 ppm; HRMS (FAB; *m*-NBA) m/z : $[\text{M}+\text{H}]^+$: calcd for $\text{C}_{20}\text{H}_{19}\text{O}_3$ 307.1334, found 307.1302.

1-(4-Methoxybenzoyl)-2,7-dimethoxynaphthalene (1c)

Colorless platelet (methanol), Mp 368.5–368.9 K; IR (KBr): 1659, 1624, 1599, 1510, 1251 cm^{-1} ; ^1H NMR δ (300 MHz, CDCl_3): 7.83 (3H, d, J = 9.0 Hz), 7.70 (1H, d, J = 9.0 Hz), 7.15 (1H, d, J = 9.0 Hz), 7.00 (1H, dd, J = 9.0, 2.4 Hz),

6.89 (2H, d, $J = 9.0$ Hz), 6.78 (1H, d, $J = 2.4$ Hz), 3.83 (3H, s), 3.79 (3H, s), 3.70 (3H, s) ppm; ^{13}C NMR δ (75 MHz, CDCl_3): 196.54, 163.81, 158.69, 154.60, 132.98, 131.98, 131.09, 130.61, 129.56, 124.34, 122.15, 116.98, 113.73, 110.28, 102.17, 56.36, 55.41, 55.14 ppm; HRMS (FAB; *m*-NBA) m/z : $[\text{M} + \text{H}]^+$: calcd for $\text{C}_{20}\text{H}_{19}\text{O}_4$ 323.1283, found 323.1332.

1-(4-Chlorobenzoyl)-2,7-dimethoxynaphthalene (1d)

Colorless needle (hexane), Mp 394.7–395.2 K; IR (KBr): 1667, 1628, 1586, 1512 cm^{-1} ; ^1H NMR δ (300 MHz, CDCl_3): 7.87 (1H, d, $J = 9.0$ Hz), 7.78 (2H, d, $J = 8.4$ Hz), 7.72 (1H, d, $J = 9.0$ Hz), 7.39 (2H, d, $J = 8.4$ Hz), 7.16 (1H, d, $J = 9.0$ Hz), 7.02 (1H, dd, $J = 2.4, 9.0$ Hz), 6.78 (1H, d, $J = 2.4$ Hz), 3.79 (3H, s), 3.73 (3H, s) ppm; ^{13}C NMR δ (75 MHz, CDCl_3): 196.81, 158.96, 155.02, 139.71, 136.45, 132.94, 131.28, 130.87, 129.72, 128.86, 124.34, 121.06, 117.15, 110.05, 101.88, 56.239, 55.168 ppm; calcd for $\text{C}_{19}\text{H}_{15}\text{O}_3\text{Cl}$: C, 69.83%; H, 4.63%; found: C, 69.61%; H, 4.74%.

1-(4-Methylbenzoyl)-2-hydroxy-7-methoxynaphthalene (2b)

Yellow platelet (hexane), Mp 385.6–386.1 K; IR (KBr): 3443, 2929, 1620, 1561, 1514, 1233 cm^{-1} ; ^1H NMR δ (300 MHz, CDCl_3): 11.40 (s, 1H), 7.83 (d, $J = 8.9$ Hz, 1H), 7.61 (d, $J = 8.6$ Hz, 1H), 7.52 (d, $J = 7.9$ Hz, 2H), 7.22 (d, $J = 7.9$ Hz, 2H), 7.07 (d, $J = 8.9$ Hz, 1H), 6.89 (dd, $J = 2.4, 8.9$ Hz, 1H), 6.64 (d, $J = 2.4$ Hz, 1H), 3.31 (s, 3H), 2.41 (s, 3H) ppm; ^{13}C NMR δ (75 MHz, CDCl_3): 200.0, 162.3, 158.1, 143.2, 138.0, 136.1, 134.2, 130.0, 129.5, 129.3, 123.8, 116.5, 115.8, 114.0, 106.6, 54.5, 21.7 ppm; HRMS (FAB; *m*-NBA) m/z : $[\text{M} + \text{H}]^+$: calcd for $\text{C}_{19}\text{H}_{17}\text{O}_3$ 293.1178, found 293.1189.

1-(4-Methoxybenzoyl)-2-hydroxy-7-methoxynaphthalene (2c)

Yellow platelet (hexane), Mp 375.0–376.5 K; IR (KBr): 3420, 2929, 1618, 1596, 1576, 1511, 1246, 1220 cm^{-1} ; ^1H NMR δ (300 MHz, CDCl_3): 10.94 (s, 1H), 7.82 (d, $J = 8.9$ Hz, 1H), 7.67–7.61 (m, 3H), 7.07 (d, $J = 8.9$ Hz, 1H), 6.92–6.88 (m, 3H), 6.73 (d, $J = 2.4$ Hz, 1H), 3.86 (s, 3H), 3.39 (s, 3H) ppm; ^{13}C NMR δ (75 MHz, CDCl_3): 199.0, 163.4, 161.4, 158.1, 135.6, 134.2, 132.8, 132.1, 130.0, 123.8, 116.5, 115.8, 114.3, 113.9, 106.5, 55.6, 54.7 ppm; HRMS (FAB; *m*-NBA) m/z : $[\text{M} + \text{H}]^+$: calcd for $\text{C}_{19}\text{H}_{17}\text{O}_4$ 309.1127, found 309.1107.

1-(4-Chlorobenzoyl)-2-hydroxy-7-methoxynaphthalene (2d)

Yellow platelet (hexane), Mp 391–391.5 K; IR (KBr): 3434, 1623, 1583, 1513, 1214, 843 cm^{-1} ; ^1H NMR δ (300 MHz, CDCl_3): 11.35 (s, 1H), 7.85 (d, 1H, $J = 9.0$ Hz), 7.63 (d, 1H, $J = 9.0$ Hz), 7.58 (d, 2H, $J = 8.7$ Hz), 7.40 (d, 2H, $J = 8.7$ Hz), 7.07 (d, 1H, $J = 9.0$ Hz), 6.91 (dd, 1H, $J = 2.4,$

9.0 Hz), 6.58 (d, 1H, $J = 2.4$ Hz), 3.37 (s, 3H) ppm; ^{13}C NMR δ (75 MHz, CDCl_3): 199.1, 162.6, 158.2, 138.8, 138.7, 136.5, 133.8, 130.7, 130.2, 128.9, 123.7, 116.4, 115.8, 113.4, 106.5, 54.5 ppm; Anal. Calcd for $\text{C}_{18}\text{H}_{13}\text{ClO}_3$: C 69.13, H 4.19. Found: C 69.11, H 4.09.

Acknowledgement

This work was partially supported by the Ogasawara Foundation for the Promotion of Science & Engineering, Tokyo, Japan.

References

- Alfonso, I., Burguete, M. I., Galindo, F., Luis, S. V., Vigar, L., *J. Org. Chem.*, **2007**, 72, 7947.
- Zhang, F. R., Song, H. B., Zi, G. F., *Dalton Trans* **2011**, 40, 1547.
- Lackner, A. D., Samant, A. V., Toste, F. D., *J. Am. Chem. Soc.*, **2013**, 135, 14090–14093.
- Lee, Y., Lee, M., *J. Org. Chem.*, **2013**, 117, 12878–12883.
- Takashima, H., Fukuda, M., Nakagaki, F., Ogata, T., Tsukahara, K., *J. Phys. Chem. B.*, **2013**, 117, 2625–2635.
- Jiang, Y. L., Gao, X. N., Zhou, G. N., Patel, A., Javer, A., *J. Org. Chem.*, **2010**, 75, 324–333.
- Shinamura, S., Miyazaki, E., Takiyama, K., *J. Org. Chem.*, **2010**, 75, 1228–1234.
- Frischmann, P. D., Würthner, F., *Org. Lett.*, **2013**, 15, 4674–4677.
- Cohen, S., Thirumalaikumar, M., Pogodin, S., Agranat, I., *Struct. Chem.*, **2004**, 15, 339–346.
- Gore, P. H., Henrick, K., *Acta Cryst.*, **1980**, B36, 2462–2465.
- Jing, L.-H., Qin, D.-B., He, L., Gu, S.-J., Zhang, H.-X., Lei, G., *Acta Cryst.*, **2005**, E61, o3595–o3596.
- Okamoto, A., Yonezawa, N., *Chem. Lett.*, **2009**, 38, 914.
- Okamoto, A., Mitsui, R., Yonezawa, N., *Chem. Lett.*, **2011**, 40, 1283.
- Nakaema, K., Noguchi, K., Okamoto, A., Yonezawa, N., *Acta Cryst.*, **2008**, E64, o2497.
- Mohri, S., Yoshiwaka, S., Isozaki, K., Yonezawa, N., Okamoto, A., *Acta Cryst.*, **2013**, C69, 1541–1544.
- Okamoto, A., Mitsui, R., Watanabe, S., Tsubouchi, T., Yonezawa, N., *Int. J. Org. Chem.*, **2012**, 2, 194–201.
- Kato, Y., Nagasawa, A., Hijikata, D., Okamoto, A., Yonezawa, N., *Acta Cryst.*, **2010**, E66, o2659.
- Nagasawa, A., Mitsui, R., Kato, Y., Okamoto, A., Yonezawa, N., *Acta Cryst.*, **2010**, E66, o2677.
- Nagasawa, A., Mitsui, R., Okamoto, A., Yonezawa, N., *Acta Cryst.*, **2010**, E66, o2820–o2821.
- Mitsui, R., Nakaema, K., Noguchi, K., Yonezawa, N., *Acta Cryst.*, **2008**, E64, o2497.

Received: 30.12.2013.
Accepted: 02.02.2014.



POTENTIAL OF LACCASE PRODUCED FROM MICROFUNGUS *AUREOBASIDIUM PULLULANS* VAR. *MELANOGENUM* TO DEGRADE POLYCYCLIC AROMATIC HYDROCARBONS

Wannisa Leelaruji,^[a] Phawadee Buathong,^[a] Patcharaporn Kannan,^[a] Rungtiwa Piamtongkam,^[a] Suphang Chulalaksananukul,^[b] Gullaya Wattayakorn^[c] and Warawut Chulalaksananukul^{[d],[e],[f]*}

Keywords: biodegradation, laccase, lipolytic yeast, naphthalene, polycyclic aromatic hydrocarbons (PAHs).

Polycyclic aromatic hydrocarbons (PAHs) are a group of persistent organic pollutants that are resistant to degradation and can remain in the environment for a long time. PAHs are mainly produced as by-products of incomplete combustion, such as from fossil fuel burning, forest fires, coal fires or vehicle emissions. Currently, PAHs increasingly cause major environmental problems because of continuing industrial development. Biodegradation by microbes is the major natural mechanism for PAHs removal from the environment. The main objective of this research was to study the biodegradation of four types of PAHs (naphthalene, anthracene, pyrene and benzo[a]pyrene) by laccase produced from the lipolytic yeast, *Aureobasidium pullulans* var. *melanogenum*, screened from Sichang Island (Thailand). The optimal condition for growing *A. pullulans* var. *melanogenum* and its laccase production was first evaluated, and revealed that laccase production could be induced with 2 mM guaiacol and 0.5 M CuSO₄ in the yeast malt (YM) growth medium. Laccase was then lyophilized and stored in capsule form at +4 °C to maintain enzymatic activity. The subsequent ability to degrade naphthalene, anthracene, pyrene and benzo[a]pyrene was determined using high performance liquid chromatography. The results revealed that the laccase activity of one capsule (0.16 g) of lyophilized laccase was 711 U mL⁻¹ (4.4 U mg⁻¹) and could degrade a mixture of benzo[a]pyrene (37 µg mL⁻¹), anthracene (7.5 µg mL⁻¹), pyrene (99 µg mL⁻¹) and naphthalene (90 µg mL⁻¹) by 45.33, 38.16, 25.38 and 24.35 % after 48 hours incubation respectively. Furthermore, the result also revealed that laccase (5 g) from *A. pullulans* can degrade naphthalene and anthracene in soil samples by 51.34 and 85.06 % respectively, after incubation for 9 days.

* Corresponding Authors

E-Mail: warawut.c@chula.ac.th

- [a] Program in Biotechnology, Faculty of Science, Chulalongkorn University, Bangkok 10330, Thailand.
- [b] Department of Chemical Engineering, Faculty of Engineering, Mahidol University, Nakornpathom, 73170, Thailand.
- [c] Department of Marine Science, Faculty of Science, Chulalongkorn University, Bangkok, 10330, Thailand.
- [d] Biofuels by Biocatalysts Research Unit, Chulalongkorn University, Bangkok, 10330, Thailand.
- [e] Department of Botany, Faculty of Science, Chulalongkorn University, Bangkok, 10330, Thailand.
- [f] Aquatic Resources Research Institute, Chulalongkorn University, Bangkok 10330, Thailand.

Introduction

Polycyclic aromatic hydrocarbons (PAHs) are environmental pollutants in soil, water and air. They and their derivatives are widespread products of incomplete combustion of organic materials; both from natural combustion, such as forest fires, and also from anthropogenic activities.^{1,2} These compounds are a class of hazardous organic chemicals consisting of two or more fused benzene rings in linear, angular and cluster arrangements.^{3,4} Low-molecular weight PAHs (containing less than four benzene rings) are acutely toxic, which affect the reproduction and mortality of aquatic animals and most high-molecular weight PAHs (containing four or more benzene rings) are mutagenic and carcinogenic. PAHs in the soil can do harmful to people's health via food chain. Consequently, soil was contaminated by PAHs at

significance concentrations.⁵ High molecular weight PAHs are resistant to bacterial degradation in soil and sediments. This has been attributed to their limited bioavailability because of low water dissolution rates, sorption by solid matrices, and incorporation into solid particles. An investigation into the activity of microorganism with high PAH degrading capacity is, therefore, essential for an efficient bioremediation of these compounds.⁶

Biodegradation of PAHs has been performed by fungi; fungal laccases from *Trametes versicolor* and *Myceliophthora thermophila* have been shown to be able to oxidize the 12 target PAHs.³ Laccase (benzenediol: oxygen oxidoreductases), in the family of blue multi-copper oxidases⁷ is a polyphenol oxidase containing four copper atoms in its active site⁸ and is capable of oxidizing a wide range of aromatic compounds, with the concomitant reduction of molecular oxygen to water.⁷

Aureobasidium pullulans is ubiquitous, polymorphic and oligotrophic black yeast-like microfungus.⁹ It is particularly well known for its biotechnological significance as a producer of the biodegradable extra cellular polysaccharide (EPS) *pullulan* (poly- α -1,6-maltotriose).¹⁰ This yeast also produces numerous degradable enzymes; including fructofuranosidase, glucoamylase and xylanase. However, laccase produced by *A. pullulans* has not been widely recognized and studied.⁷ In this study, we conducted two experimental studies of PAHs degradation in both the test solutions and artificially contaminated soil, aiming at evaluating the potential of an enzyme, laccase, from *A. pullulans* var. *melanogenum* for degrading of PAHs.

Materials and Methods

Preparation of laccase for biodegradation of PAHs

A microfungus, *Aureobasidium pullulans*, used for the biodegradation experiments of PAHs was screened from soil from the contaminated site at Sichang Island (Chonburi, Thailand), which was used as an inoculum source in a series of microbial culture experiments at the Biofuels by Biocatalysts Research Unit, Chulalongkorn University, Thailand. The inoculum was cultured in the yeast malt (YM) broth (3 % (w/w) of 3 g yeast extract, 3 % (w/v) malt extract, 5 % (w/v) peptone, 10 % (w/v) glucose) at 30 °C for 48 h with shaking at 200 rpm in shaking incubator. This culture was then inoculated at 1 % (v/v) into laccase production medium (2 mM of guaiacol and 0.5 mM CuSO₄ in YM; LPM)¹¹. Growth of *A. pullulans* was measured by spectrophotometer over 120 h of culture in terms of the culture turbidity using the absorption at a wavelength of 600 nm, and the colony forming units (CFU mL⁻¹) were determined by spread plate technique. They were diluted to 30-300 colonies to count the number of cells. The culture of the micro-fungus was centrifuged finally at 10,000 rpm, 4°C for 15 min in a refrigerated centrifuge, and the supernatant was harvested as a crude laccase preparation, lyophilized, and stored in capsules at +4°C. In this study, we conducted the following two different experiments for degradation of PAHs with the harvested enzymes.

Experiment 1. Biodegradation of PAHs using the crude laccase prepared from *A. pullulans* colonies

One capsule of laccase (0.16 g) has 711 unit (U) mL⁻¹ of laccase activity (one unit of laccase activity was defined as the amount of enzyme catalyzing the production of 1 µM of 2,2'-azinobis-(3-ethylbenzthiazoline-6-sulfonate) per min per mL).¹² A capsule of laccase was added to a laboratory bottle containing 2 mL of water and 1 mL of PAHs mixture including benzo[a]pyrene, pyrene, anthracene, and naphthalene with the initial concentration of 37, 99, 7.5 and 90 µg mL⁻¹, respectively. Then, 1 mL of Tween 80 (5 % v/v) and 5 mL acetate buffer (100 mM, pH 4.5) were added to the mixture, and the mixture was incubated in a laboratory water bath with magnetic stirrer at 30 °C for 48 h and shaking at 150 rpm. 1 mL of the test samples were collected from the laboratory bottle every 12 h. The PAHs were then extracted from 1 mL of the test samples using 2 mL of hexane. After that, 0.75 mL of 15 % (v/v) triton X 100 was added to each of the solution, and they were shaken for 6 h at 200 rpm.¹³ The concentrations of PAHs remained in the extracts were determined with a HPLC (Shimadzu, LC-20A series) connected to an Inertsil ODS-P HP column (0.46 mm in diameter and 250 mm in length) and equipped with an UV detector. The mobile phase was an 80:20 (v/v) ratio acetonitrile:water mixture, run at a flow rate of 1.5 mL min⁻¹.

Experiment 2. Biodegradation of PAHs in soil samples using the crude laccase prepared from *A. pullulans*.

Three replicates of soil samples were collected from Sichang Island shore, Chonburi province, Thailand. The soil samples were sterilized and stored at +4°C. These soil samples (1g each) were spiked with naphthalene and

anthracene that has concentration of 4.5 and 0.25 mg mL⁻¹, respectively. 5 g of laccase (711 unit (U) mL⁻¹ of laccase activity) was added to each of these artificially PAH-contaminated soil samples. The Tween 80 and acetate buffer solutions were then added to the soil samples. Lastly, double distilled deionised water was used to make the final volume to 50 mL. Biodegradation experiments of PAHs in the slurry samples were carried out by the analytical steps as described in Experiment 1, with the incubation time of 14 days and collected sample every 2 days. The remnant concentrations of PAHs in the tested soils were determined by HPLC, using the same conditions as described in Experiment 1.

Results

Experiment 1: Biodegradation of PAHs using the crude laccase prepared from *A. pullulans* colonies

Fig. 1 shows the degradation curves of the four different PAHs carried out in the experiments. After incubation with laccase for 48 h, the concentration of PAHs were all decreased as the incubation time increased to a minimum from 24 h (benzo[a]pyrene) or 36 h (pyrene and naphthalene) onwards, except for anthracene which was not reached completion by the end of the 48 h incubation period. At 48 h, the remaining concentrations of naphthalene, anthracene, pyrene and benzo[a]pyrene were 68, 4.7, 72 and 20 µg mL⁻¹ respectively. The degradation efficiencies for benzo[a]pyrene, anthracene, pyrene and naphthalene were found to be 45.33 %, 38.16 %, 25.38 % and 24.35 % after 48 h incubation. Thus, benzo[a]pyrene was the most biodegradable PAH, followed by anthracene while pyrene and naphthalene were more recalcitrant.

Experiment 2: Biodegradation of PAHs in contaminated soil samples using the crude laccase prepared from *A. pullulans*

The results also revealed that laccase from *A. pullulans* can degrade naphthalene and anthracene in soils by 51.34 and 85.06 % respectively, after incubation for 9 days (Figs. 2 and 3).

Discussion

Experiment 1. Biodegradation of PAHs using the crude laccase prepared from *A. pullulans* colonies

The degradation of four PAHs by laccase in the present study was similar to that previously reported⁵ where laccase was shown to efficiently degrading aged anthracene, benzo[a]pyrene and benzo[a]anthracene from contaminated soil. The specificity of laccase catalysis was proposed to be related to the ionization potentials of the substrates⁵. Moreover, the laccase catalyzed oxidation process was enhanced when adding certain low molecular weight compounds as mediators, such as 2,2-azino-bis-(3-ethylbenzothiazoline-6-sulfonic acid) (ABTS). A suitable mediator would form an intermediate with high activity that could transfer electrons from oxygen molecules to the substrate and so enhance the substrate degradation¹⁴.

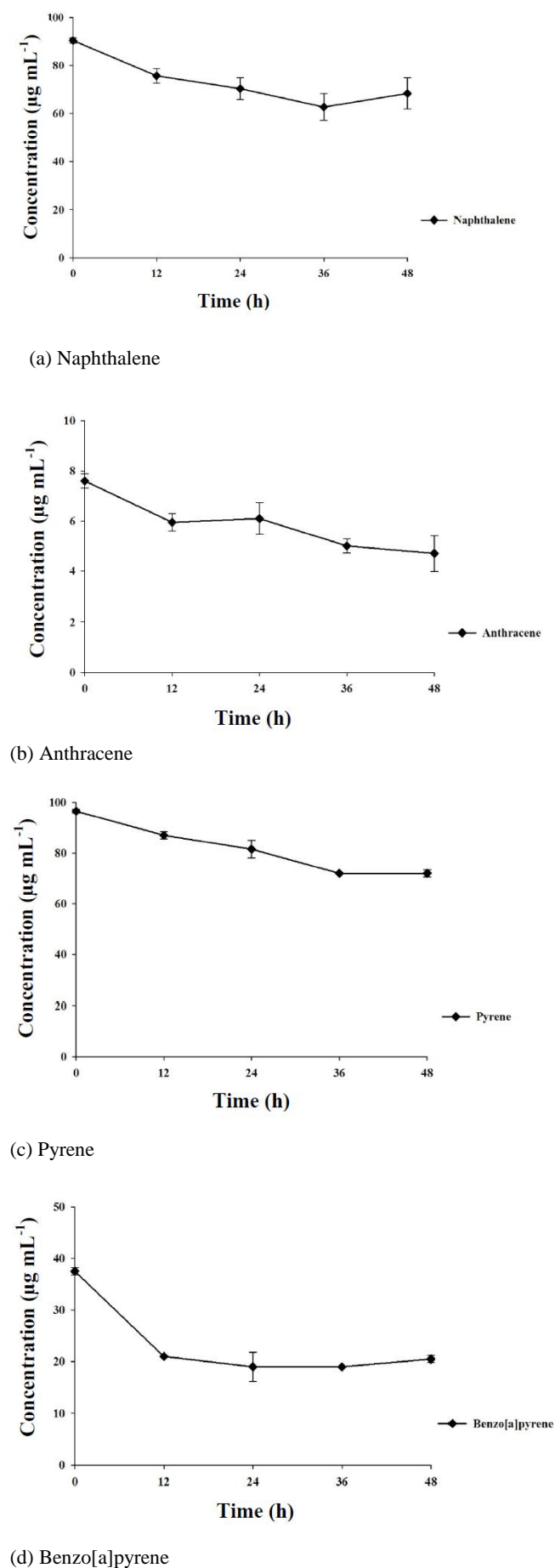


Figure 1. Biodegradation of PAHs by laccase showing the residual concentration over time

Previously, it was reported that degradation of phenanthrene with purified laccase from *T. versicolor* 951022 did not occur, but did when ABTS or 1-hydroxybenzotriazole (HBT) was added into the reaction mixture¹⁵. In the presence of 5 mM ABTS or HBT, laccase at 5 U mL⁻¹ could oxidize 40 % and 30 % of a 20 mg L⁻¹ phenanthrene solution in 2 h, respectively. In contrast, other PAHs, such as anthracene, fluorene, benzo[a]pyrene and perylene, were almost completely removed by the laccase from *T. versicolor* after the addition of HBT.

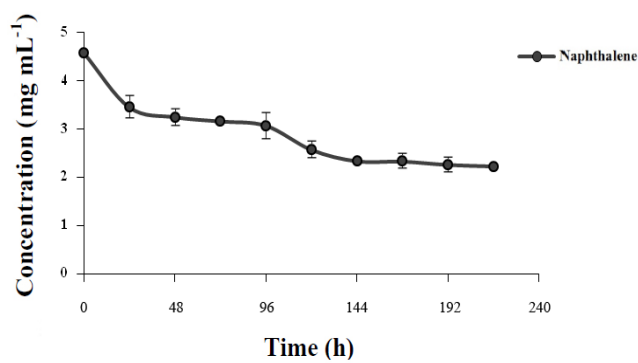


Figure 2. Changes of naphthalene concentration in the tested soil

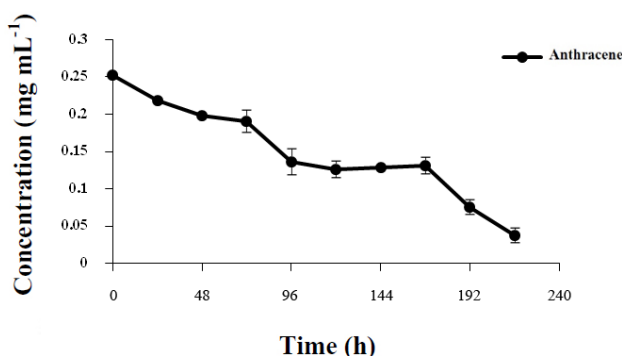


Figure 3. Changes of anthracene concentration in the tested soil

Experiment 2. Biodegradation of PAHs in contaminated soil using the crude laccase prepared from *A. pullulans*

Biodegradation of PAH-contaminated soil by laccase was performed by added 5 g of laccase into spiked soil samples from Sichang Island. This method was performed to test the influence of soil particles on biodegradability in the degradation process. It was found that the residues of naphthalene and anthracene in soil were removed by 51.34 and 85.06 % respectively after 9 days of incubation with laccase. The reasons behind this can be attributed to the absence of oxygen which can inhibit the laccase activity^{16,17} and the ability of PAHs to be bound with soil particles. Such sorbed PAHs can then be regarded as non-bioavailable and thus non-biodegradable.

In conclusion, laccase has shown the ability to degrade all four PAHs effectively, but had different specificity in degrading PAHs with different structure. Laccase showed to be more efficient in degrading ring type aromatic structure,

but was not affected by the size of the structure. This experiment was conducted in the laboratory under various controlled factors to demonstrate the potential application of laccase to be used in the treatment of PAHs. As a result, this research is particularly useful in bioremediation application to treat PAH-contaminated site in order to achieve better health and environment. However, the biotechnological applications when used to treat soil and/or underground-water which were contaminated with certain toxic compounds normally have better results when the process was carried out in the laboratory than outside the laboratory environment. Therefore, further studies should be performed to test the efficiency of enzyme laccase or whole microbial cells in degrading PAHs outside the laboratory environment with variable physical and biological factors. Moreover, these laboratory results showed a useful basis for the development of future research project aiming at directly testing these enzymatic degradation systems in a model polluted area. Such an investigation would certainly help verify whether the degradation of polycyclic aromatic hydrocarbon could be equally efficient in a representative environment.

Acknowledgments

This research is part of the project entitled “Knowledge Management for Marine Pollution Abatement and Biodiversity Conservation around Sichang and Siracha, Chonburi Province (2nd Year)” funded by The National Research Council of Thailand (NRCT). Soil samples were gifted by the Aquatic Resources Research Institute (ARRI), Sichang Island, Chulalongkorn University.

References

- ¹Lundstedt, S., *Analysis of PAHs and their transformation products in contaminated soil and remedial processes*, PhD Thesis, Department of environmental and toxicological chemistry, University of Amsterdam, The Netherlands, **2003**, 56.
- ²Mrozik, A., Piotrowska-Seget, Z., Labuzek, S., *Pol. J. Environ. Stud.*, **2003**, 12, 15 – 25.
- ³Alcalde, M., Bulter, T., Arnold, F. H., *J. Biomol. Screen*, **2002**, 7, 547 – 553.
- ⁴Juckpech, K., Pinyakong, O., Rerngsamran, P., *Sci. Asia*, **2012**, 38, 147 – 156.
- ⁵Li, X., Lin, X., Yin, R., Wu, Y., Chu, H., Zeng, J., Yang, T., *J. Health Sci.*, **2010**, 56, 534 – 540.
- ⁶Cambria, M. T., Minniti, Z., Librando, V., Cambria, A., *Appl. Biochem. Biotechnol.*, **2008**, 149, 1–8.
- ⁷Xiao, Y. Z., Hong, Y. Z., Li, J. F., Hang, J., Tong, P. G., Fang, W., Zhou, C. Z., *Appl. Genet. Mol. Biotechnol.*, **2006**, 71, 493 – 501.
- ⁸Rich, J. O., Manitchotpisit, P., Peterson, S. W., Leathers, T. D., *Rangsit J. Arts Sci.*, **2011**, 1, 41 – 47.
- ⁹Gaur, R., Singh, R., Gupta, M., Gaur, M. K., *Afr. J. Biotechnol.*, **2010**, 9, 7989 – 7997.
- ¹⁰Zalar, P., Gostinčar, C., de Hoog, G. S., Uršič, V., Sudhadham, M., Gunde-Cimerman, N., *Stud. Mycol.*, **2008**, 61, 21–38.
- ¹¹Theerachai, M., Morel, S., Guieysse, D., Remaud-Simeon, M., Chulalakasanukul, W., *Afr. J. Biotechnol.*, **2012**, 11, 1964 – 1969.
- ¹²Li, A., Zhu, Y., Xu, L., Zhu, W., Tian, X., *Afr. J. Biochem. Res.* 2, **2008**, 181-183.
- ¹³Luepromchai, E., Lertthamrongsak, W., Pinphanichakarn, P., Thaniyavarn, S., Pattaragulwanit, K., Juntongjin, K., *Songklanakarin J. Sci. Technol.*, **2007**, 29, 515 – 527.
- ¹⁴Gao, D., Liang, H., Du, L., Chen, J., *Afr. J. Biotechnol.*, **2010**, 9, 6888 – 6893.
- ¹⁵Han, M. J., Choi, H. T., Song, H. G., *J. Microbiol.*, **2004**, 42, 94 – 98.
- ¹⁶Bamforth, M. S., Singleton, L., *J. Chem. Technol. Biotechnol.*, **2005**, 80, 723–736.
- ¹⁷Waung, W. D., *Optimizing enzymatic preparation of mechanical pulp through the characterization of new laccases and non-productive interactions between enzymes and lignin*. Master Degree Thesis, Department of Chemical Engineering & Applied Chemistry, University of Toronto, Canada, **2010**, 92.

Received: 02.01.2014.

Accepted: 06.02.2014.



CHROMATOGRAPHY OF ANTICANCER DRUGS. PART 2

Tibor Cserhádi and Mária Szőgyi

Keywords: anticancer drugs; chromatography; normal and reversed phase HPLC; size exclusion and gel-permeation chromatography; ultra performance liquid chromatography; natural anticancer compounds.

Various liquid chromatographic techniques including normal phase and reversed phase liquid chromatography (HPLC, RP-HPLC), ultra performance liquid chromatography (UPLC), size exclusion chromatography (SEC), and gel permeation chromatography (GPC) applied for the separation and quantitative determination of synthetic anticancer drugs and natural anticancer compounds are reviewed.

Corresponding Authors

E-Mail: szogyim t-online.hu

[a] Research Center for Natural Sciences, Hungarian Academy of Sciences, Budapest, Hungary

Introduction

Various liquid chromatographic techniques have been extensively applied not only for the separation and quantitative determination of synthetic anticancer drugs but also for the analysis of natural anticancer compounds present in complicated accompanying organic and inorganic matrices. The same liquid chromatographic techniques were employed for the analysis of synthetic drugs as for the investigation of natural products. Analytical methods included normal phase and reversed phase liquid chromatography (HPLC, RP-HPLC), ultra performance liquid chromatography (UPLC), size exclusion chromatography (SEC), and gel permeation chromatography (GPC), etc.

A new RP-HPLC method was developed and validated for the quantitative analysis of curcuma in encapsulated formulations. Poly(lactic-co-glycolic acid) PLGA and poly-lactic-co-glycolic acid (PLGA-PEG) were included in the investigations. RP-HPLC method employed fluorescence detector, the analytes were separated on a C18 column (250 mm x 4.6 mm, average particle size being 5 μm). Mobile phase consisted of ethanol, water and acetonitrile (80:10:10 v/v/v). Separations were carried out in isocratic mode at the flow-rate of 0.8 mL min⁻¹. Fluorescence detection used 365 nm excitation wavelength and 512 nm emission wavelength. The selectivity, linearity, precision, accuracy, robustness, limit of detection and limit of quantitation of the method were determined. The correlation between the detector response and the concentration was linear in the range of 1 - 50 $\mu\text{g mL}^{-1}$. The limits of detection and quantitation were 9.65 and 50 ng mL⁻¹ respectively. The mean recovery of curcumin was 101.14 \pm 2.8 % ($n = 9$). The inter- and intra-day variation was lower than 3.73 %. It was stated that the method can be used successfully for the investigation of the encapsulation efficacy of curcumin in PLGA and PLGA-PEG nanoparticles.¹

Poly(β -amino ester urethane)-based multiblock copolymers were synthesized and their employment as injectable, biodegradable and pH/temperature-sensitive

hydrogel system was investigated in detail. Polymers were composed from polyethylene glycol and poly(β -amino ester urethane). The characteristics of the new copolymers were measured by applying nuclear magnetic resonance spectroscopy, Fourier transform infrared spectroscopy and gel-permeation chromatography. It was established that the aqueous solution of new co-polymers showed a sol-gel phase transition with increasing pH and a gel-to sol phase transition with the increase of temperature. It was further established that the new gels showed no toxicity. The controlled release of the model anticancer drug doxorubicin occurred in 7 days. The use of hydrogels was proposed for biomedical applications and drug/protein-delivery systems.²

The application of crocetin for the prevention and therapy of cancer has been investigated in detail. Crocetin is present in the dry stigma of the plant *Crocus sativus L.* It has been frequently used as anticancer agent alone or in combination with other natural and synthetic antitumor remedies. It was assumed that crocetin affects the growth of tumor cells by inhibiting nucleic acid synthesis, enhancing anti-oxidant system inducing apoptosis and hindering growth factor. Both high performance liquid chromatography and gas chromatography found application in the investigation of chemistry and biochemistry of crocetin.³

The occurrence of two anti-proliferative peptides active against tumor cells in the skin secretion of the South American tree frog (*Phyllomedusa bicolor*) was established. The crude exudate was further separated by size exclusion gel chromatography followed by reversed phase HPLC. Sequence analysis established that two α -helical cationic peptides was responsive for the antimicrobial activity. It was further established that the bioactive peptides belonged to the dermaseptin peptide family. Synthetic dermaseptins (dermaseptins B₂ and B₃) showed similar anticancer activity. It was concluded that these the data can be used for the development of a new class of antitumor agents.⁴

A pharmacokinetic study was applied for the investigation of the behavior of nanoparticle curcumin. Plasma curcumin levels were determined by using HPLC. It was concluded from the data that nanoparticle curcumin increased safely plasma curcumin levels in a dose-dependent manner. The preparation increased bioavailability in human subjects. It was assumed that the method can be applied as a promising tool for the study of the testing of the anticancer effect of curcumin in clinical trials.⁵

Catharantus roseus (L.) G. Don is well known plant species producing a wide variety of terpenoid indole alkaloids with marked biological activity. A new method was developed for producing catharine and other metabolites from *C. roseus* using hairy root cultures. The cultures were genetically transformed by *Agrobacterium rhizogenes* A4. Catharine was separated by HPLC. It was stated that hairy root cultures can be applied in the future metabolic engineering of terpenoid indole alkaloids in plants.⁶

It was established that fluorinated 2-aryl-benzothiazol antitumor molecules can be bioactivated by human cytochrom P450s 1A1 and 2W1 and can be deactivated by cytochrome P450 2S1. It was further found that both 2-(4-amino-3-methylphenyl)-5-fluorobenzothiazol and 5-fluoro-2-(3,4-dimethoxyphenyl)benzothiazol contain benzothiazole pharmacophore. It was assumed that the biological activity markedly depended on the involvement of 1A1 and 2W1 in the biological procedures.⁷

Radiolabeling of bleomycin-glucuronide (BLMG) was carried out by using I-131 and the efficacy of the radiolabeling was investigated by thin-layer radiochromatography and HPLC. The yield of radiolabeling was about 65 %. It was further established that the tumor uptakes was high in the first 30 min after injection. The procedure was proposed as a therapeutic agent, especially for colon cancer in nuclear medical applications.⁸

Electrospray ionization Fourier transform ion cyclotron resonance mass spectrometry (FTICR MS) has been applied for the investigation of the interaction of platinum drug cisplatin with cytochrome *c*. The results indicated that the primary monoadduct of the cisplatin–cytochrome interaction is $c\text{-Pt}(\text{NH}_3)\text{Cl}$. It was further established that the ratio of cisplatin and cytochrome influence considerably the composition of the complex. It was proposed that the procedure can be successfully applied for the study of metallodrug/protein complexes. The measurements indicated the presence of four binding sites for cisplatin on cytochrome (Met65, Met80, His18, His33).⁹

A quercetin-based polymer was developed to enhance its short half-life in buffered solution. Quercetin was covalently bonded to polymethacrylic acid backbone. The biological activity of the complex was investigated using various biological and chemical methods such as FT-IR, UV-Vis, (GPC). It was concluded from the data that polymer conjugation enhanced considerably the stability of quercetin resulting in the sustained activity of the flavonoid.¹⁰

Bioactive peptides has also been found in various marine organisms. The results obtained in this very interesting field of research has been previously reviewed. Bioactive peptides belonging to different phyla (Ponifera, Crideria, Nemertina, Crustacea, Mollusca, Echinodermata, and Cranata) have been investigated for bioactive components. Bioactive molecules were isolated by traditional chromatographic methods such as gel filtration, ion exchange, and RP-HPLC.¹¹

Sanguisorba minor was extracted with ethanol, the ethanol soluble components were separated by reversed-phase HPLC and the most abundant analytes were identified by

multiple stage mass spectrometry. Kinetic and equilibrium parameters were calculated by a concerted spectrophotometric and biosensor-based method. It was established that quercetin-3-glucuronide was the responsive analyte showing in vitro plasmin inhibition, cell-based assays proved that this analyte was effective in suppressing plasma-induced loss of cancer cell adhesion. It was assumed that these data may help the rational design of new anticancer drugs.¹²

Three-dimensional cell bioreactor combined with HPLC-MS was developed for the affinity screening of bioactive components of herb medicine. Paclitaxel, resveratrol, ketoprofen, and penicillin G were selected as model compounds. It was established that after 30 min incubation time the binding degrees of paclitaxel and resveratrol were 82.2 ± 7.2 % and 66.1 ± 4.1 % while the binding of non-anticancer drugs was lower than 3 %. The method was employed for the analysis of the bioactive component in Polygonum cillinerve (Nakai) Ohwi (PCO) extract. The method separated two main components of the extract: aristolochic acid A (63.0 ± 5.1 %) and aristolochic acid B (18.8 ± 0.9 %). It was stated that the procedure is highly specific, efficace, and suitable for affinity screening of bioactive compounds.¹³

It was reported that a new polypeptide was extracted and purified from the ascidian *Ciona savignyi*. The polypeptide with high antitumor activity was purified by acetone fractionation, ultra filtration, ion exchange chromatography, gel chromatography and HPLC. It was found that the polypeptide shows considerable antitumor activity and its molecular mass is 5931. The preliminary results suggest that the new polypeptides is a promising candidate for the treatment of cancer.¹⁴

The composition of the acetone extract of the lichens *Parmelia caperata*, *P. saxatilis*, *P. sulcata* was investigated by HPLC and the antioxidant, antimicrobial and anticancer of the main fractions were determined by applying various physicochemical methods. It was established that the main fractions were protocetraric acid, usnic acid and depsidone salazinic acid. Besides of these compounds the presence of atranosin and chloroatranorin was also verified. The results indicated that lichens can be applied as new sources of antimicrobial, antioxidant and anticancer compounds.¹⁵

Liquid chromatography coupled with tandem mass spectrometry has been employed for the characterization the intratumoral pharmacokinetic (PK) and pharmacodynamics (PD) of the anticancer agent gefinitib. The measurements suggested that the methods applied can be successfully employed for the determination of PKs and KD values of other experimental models.¹⁶

TLC and HPLC methods were employed for the study and accumulation of the lipophilic deoxynucleoside analogs elacytarabine and CP-4126. Cytarabine (ara-C), gemcitabine (dFdC). To bypass transport-related drug resistance elacitarabine (CP40055), ara-5'-elaidic-acid ester and CP-4526 (CO 1.01), gemcitabine-5'-elaidic-acid-ester were included in the investigations. The results indicated that the metabolism and accumulation of the target compounds depended considerably on their chemical structure and lipophilicity.¹⁷

Nonventional gas-chromatography mass-spectrometry (GC-MS) was applied for the determination of 5-fluorouracil (5-FU) in blood samples and the results were compared with those obtained by a new immunoassay method. It was concluded from the results that the results obtained by the two methods are commensurable and can be applied for the analysis of 5-FU in serum from patients with gastric cancer.¹⁸

Novel 2-cyanoazidines were synthesized and their immunomodulating effect and anticancer activity were investigated in detail. Chiral chromatography was employed for the investigation of enantiomers. It was established that azimexon and ciamexon showed marked anticancer activity.¹⁹

The combination of metallomics and proteomics was applied for the investigation of the impact of the metallodrug RAPTA-T on human cancer cells. Size exclusion chromatography was employed for the determination of the distribution profile of the metallodrug within the cancer cells. It was stated that the metallomics treatment exerts a marked influence on the composition of cellular proteomics.²⁰

Differential gel electrophoresis and peptide mass fingerprinting carried out by HPLC were employed for the proteome analysis of the impact of sorafenib a multi-target oral anticancer drug. It was established that the results may help the better understanding of the exact mechanism of sorafenib.²¹

Hydrophilic interaction high performance liquid chromatography (HILIC) was employed for the investigation of the epigenic modulation of the HeLa cell membrane N-glycome. The results indicated that the composition of HeLa cell membrane depended considerably on the epigenic inhibitors.²²

The antibiotic and anticancer activity of actinobacteria found in Gulf of California has been investigated in detail. It was established that the marine sediment contained 235 actinobacterial strains. The antibacterial strains were classified according to their morphology, seawater requirement, 16S RNA sequencing as *Streptomyces*, *Microspora*, and *Salinospora*. Bioactive compounds were extracted using liquid-liquid extraction with ethyl acetate and the samples were control for biological activities. It was established that some extract showed marked anticancer activity against breast cancer and cervical cancer cells. It was concluded from the results that this method can be successfully applied for the discovery of bioactive marine actinobacteria. Molecular weights were determined by HPLC-MS. It was further assumed that the procedure can be employed for the separation of actinobacteria strains important for human health.²³

The application of various electrically driven systems in the separation and quantitative determination of anticancer drugs has been previously investigated in detail. The use of these methodologies was motivated by their capacity to determine impurity profiles, to quality control of pharmaceutical preparations, lipophylicity determination, investigation of the interaction between metallodrugs and

proteins or nucleotides, characterization and quantification of metabolites in biological matrices and real-word samples.²⁴

SPME-GC-MS method was developed and applied for the study of the breath composition before and after anticancer therapy. Analytes were concentrated on different sorbents the best results were achieved by carboxen-polydimethylsiloxane. It was further established that cytostatic drugs increase the concentration of acetone and isoprene in the breath. Volatile metabolites were not identified in expired air.²⁵

The interaction of ellipticine (5,11-dimethyl-6H-pyrido[4,3-b]carbazole) with DNA was studied by capillary electrophoresis combined with laser induced fluorescence detection (CE-LIF). The background electrolyte was 50 mM sodium acetate, pH 4.5. The limit of detection for ellipticine was 5x10 nm. Optimal solvent contained 20 % dimethyl sulfoxide. It was concluded from the data that the method can be employed in vitro studied of ellipticine-DNA complexes.²⁶

Gas chromatography-ion trap mass spectrometry (GC-IT-MS) was employed for the investigation of the metabolite profile of the aqueous extract obtained from *Dracaene draco* L. leaf and fruit. It was established that leaf extract contained several amino acids, palmitic, linolenic and stearic acid while fruit extract contained only proline, oleic and stearic acid. Anticancer activities of the extracts were tested against human colon (Caco-2), kidney (A-498) and liver (HepG2) cancer cell lines. It was found that *D. draco* extracts inhibited proliferation of human colon and tumor cells. It was assumed that *D. draco* extracts can be applied as a chemopreventive agent for colon and kidney cancers.²⁷

Polypeptide-based star-block quadripolymers were synthesized as unimolecular nanocarriers for the simultaneous encapsulation of hydrophobic and hydrophilic guest molecules. The synthesis was controlled with ¹H NMR, GPC, and laser light dynamic scattering. The investigations indicated that these star-block quadripolymers can be successfully applied in the drug delivery systems.²⁸

A new type of alendronate (ALE)-conjugated amphiphilic copolymer was synthesized and employed for the formation micelles in aqueous solution. The results indicated that H-40-star-PEG/ALE micelles are highly promising bone-targeted drug carriers for skeletal metastases.²⁹

The characterization of the novel ruthenium-based anticancer drug (RAPTA-T) was carried out by employing various biochemical and biophysical investigation methods such as size exclusion chromatography, inductively coupled mass spectrometry combined with subcellular fractionation procedures, and multidimensional protein identification technology (MudPIT). The investigation revealed marked differences in the intracellular behaviour between cisplatin sensitive and cisplatin resistant cell lines. It was assumed that the results may help the elucidation of the mechanism of action of RAPTA-T and help the better understanding of the cellular response mechanisms to metallodrug treatment.³⁰

TLC and GC/MS were applied for the study of the antimicrobial effect of essential oils against *Streptococcus mutans*. Samples were prepared by hydrodistillation and the minimum inhibitory concentrations (MIC) were determined. Biofilm formation was followed by using electron scanning electron microscopy. The presence of terpenes in the samples was determined by chemical analysis. It was established that essential oils showed marked biological activity against biofilm formed by *S. mutans* and human tumor cell lines.³¹

Various HPLC methods were employed for the separation and quantitative determination of proteins and the results were compared. High performance size exclusive (HP-SEC), strong anion exchange (SAX), weak cation exchange (WCX) and RP-HPLC were included in the measurements. The chromatographic technologies were compared also with electrophoretic analytical methods using the following criteria: precision, high selectivity, low quantitation limit, analysis time and sample preparation conditions.³²

Fluorinated and pegylated polyaspartamide derivatives were synthesized to increase the solubility and efficacy of Flutamide. The new polymers were characterized by spectroscopic analyses, SEC, pyrene colorimetric assay, light scattering analysis and scanning electron microscopy. It was established that the activity of the flutamide was higher in the presence of copolymers.³³

Poly(L-glutamic acid)-based star-block copolymers were synthesized as possible pH-responsive nanocarriers for cationic drugs. The copolymers were characterized by ¹H-NMR, GPC, dynamic light scattering (DLS), and transmission electron microscopy (TEM). It was found that the model compounds (crystal violet, doxorubicin hydrochloride) were efficiently entrapped at physiological pH. The sustained release of the drugs were also observed.³⁴

The synthesis of new dendron-like PEO block copolymers was also carried out. The new copolymer was characterized by ¹H NMR, FTIR, GPC, differential scanning calorimetry, polarized optical microscopy, and wide angle X ray diffraction.³⁵

Novel molecularly imprinted polymers (MIPs), based on acrylonitrile methacryl acid matrix were synthesized and characterized with elemental analysis, attenuated total reflectance infrared spectroscopy (ATR-FTIR), RAMAN spectroscopy, SEC, thermogravimetric analysis (TGA), and differential scanning calorimetry (DSC). It was established that the imprinting process depended considerably on the structure of polymer.³⁶

Cyclodextrin-overhanging hyperbranched core-double-shell was synthesized and characterized. The polymers were characterized by heteronuclear multiple bond correlation (HMBC), SEC/multiple laser light scattering (SEC/MALLS), UV-vis spectrophotometry and dynamic light scattering (DLS).³⁷

The biological activities of the extract of fenugreek was studied in detail. The investigation was motivated by the anti-diabetic, antitumor and immunestimulating activity of the extract. Active ingredients were extracted with 50 % ethanol and the composition of the extract was investigated

by GC-MS. The presence of some bioactive compounds in the extract was established such as gingerol (4.82 %), cedrene (2.91 %), zingerone (16.5 %), vanillin (1.52 %), and eugenol (1.25 %). It was established that fenugreek is an inducer of autophagy in human cells.³⁸

Solid-phase microextraction followed by GC/MS method was employed for the analysis of breath profile before and after anticancer therapy. The extraction efficiency of eight sorbent was compared. The results indicated that the highest efficacy was achieved using carboxen-polydimethylsiloxane fiber. It was further found that cytostatic drugs increased the concentration of acetone and isoprene in the breath.³⁹

Capillary electrophoresis combined with laser induced fluorescence (LIF) detection was applied for the investigation of DNA aptamers as inhibitors of 2-oxoglutarate-dependent oxygenases. It was further stated that the results may stimulate the development of oligonucleotide aptamers for human homologues.⁴⁰

Capillary electrophoretic (CE) technologies have been extensively employed in the development of metal-based therapeutics and diagnostics. The newest results on this rapidly developing field has been earlier discussed. The applications include impurity profiling, quality control of pharmaceutical formulations, determination of molecular hydrophobicity, interaction between metallodrugs and proteins or nucleotides, and characterization and quantitative determination of metabolites in various biological and real-world samples.⁴¹

CE-LIF has also been employed for the investigation of the bioactivity of magnetically immunisolated peroxisomes. It was established that the combination of magnetic immunisolation and CE-LIF can be successfully applied for the investigation subcellular-specific biotransformations of xenobiotics occurring at immunisolated subcellular compartments.⁴²

The subcellular localization of doxorubicin (DOX) in free and in encapsulation form was investigated using MEKC-LIF (micellar electrokinetic chromatography, laser induced fluorescence). The MEKC migration buffer consisted of 10 mM borate, and 100 mM sodium dodecylsulphate. The limit of quantitation (LOQ) and the limit of detection (LOD) were 43.1 ng mL⁻¹ and 3.36 ng mL⁻¹. It was established that MEKC-LIF can be successfully applied for cytotoxicity studies of anthracycline-type anticancer drugs.⁴³

Capillary gel electrophoresis combined with LIF was employed for the study of the mode of action of bleomycin in human cells. It was concluded from the results that the MEKC-LIF procedure may help the better understanding of the mode of action of bleomycin.⁴⁴

CE combined with fluorescence resonance energy transfer (FRET) has been successfully applied for the investigation of the caspase activation in tumor cells and for the evaluation of the anticancer drugs that target apoptotic pathways. It was further found that the FRET-based CE system is a useful tool for the investigation of the mechanisms of anticancer drugs and anticancer drug screening.⁴⁵

Capillary zone electrophoresis combined with laser induced electrospray ionization mass spectrometry (CZE-ESI-MS) was employed for the investigation of the behavior of anticancer cis- and trans[dihalidobis(2-propanone oxime)platinum(II)] complexes in aqueous solutions. The measurements indicated that the degradation of trans isomers was considerably faster than those of cis counterparts. The decomposition products of the isomers were also markedly different.⁴⁶

TLC and GC/MS methods were employed for the investigation of the presence and concentration of swainsonine an indolizidine alkaloid in *Oxtropis glabra*. The measurements indicated that swainsonine causes diffuse vacuolation of neurons, epithelial cells of renal tubules by electron microscope. It was concluded from the data that the main toxic ingredient of *O. glabra* is swainsonine.⁴⁷

The amino acid and fatty acid composition as well as the antitumoral activity of the aqueous extracts of *Dracaena draco* L. leaf and fruit was measured. The anticancer potential of *Dracaena draco* leaf and fruit extracts was also determined. Metabolic profiles were analysed by gas chromatography-ion-trap-mass spectrometry (GC-IT-MS). It was established that the leaf extract contained several amino acids, palmitic, linolenic and stearic acid, while only proline, oleic and stearic acid were present in the fruit extract. It has been further found that the extracts show marked antiproliferative effects against human colon and renal tumor cells, their effect was weak against HepG2 cells. The results suggested that the extracts of *D. draco* can be successfully used as cancer chemopreventives and/or chemotherapeutic agent for colon and kidney cancers.⁴⁸

A new type of folic acid (FA)-conjugated amphiphilic 4-arm star-shaped PLGA-PEG-NH₂(4s-PLGA-PEG-NH₂) micelles was synthesized and applied as nanocarrier for tumor targeted drug delivery. The micelles were prepared by the solvent evaporation method. The structure of the polymer was investigated by H-1 NMR, GPC, dynamic light scattering, UV spectra, and confocal laser scanning microscopy (CLSM). DOX was employed as model compound. The investigations indicated that the FA-DOX micelles have a higher cellular uptake, consequently, higher cytotoxicity to tumor cells.⁴⁹

A new class of drug delivery systems (DDSs) were synthesized and their capacity was compared. Some parameters of the products were determined by various physicochemical methods such as molecular weight, nuclear magnetic resonance, GPC, critical micelle concentration (CMC), sizes, and drug loading capacity (DLC). The results indicated that these polymers can be successfully applied as drug delivery systems.⁵⁰

Another series of block copolymer micelles were synthesized and employed for the study of the interaction between polymers and DOX. The structure of the block copolymers was verified by H-1 NMR and GPC. The investigations indicated that the new polymers are suitable for anticancer drug delivery.⁵¹

New amphiphilic graft polymers were prepared and applied as drug carriers. The products were characterized by proton, nuclear magnetic resonance spectra (H-1 NMR),

Fourier transform spectroscopy (FTIR) and GPC. The critical micelle concentrations were also determined. Transmission electronic microscopy (TEM) and dynamic light scattering (DLS) methods have also been employed for the investigations. The results suggested that PLGG-g-mPEG micelles are promising potential carriers for delivering anticancer drugs.⁵²

Bioreducible and core-crosslinked hybrid micelles were prepared from biodegradable and biocompatible trimethoxysilyl-terminated and disulfide-bond linked block copolymers poly(e-caprolactone)-S-S-poly(ethylene oxide). It was stated that the procedure can be employed for the preparation of bioreducible and core-crosslinked hybrid micelles for anticancer drug delivery systems.⁵³

A multiarm poly(acrylic acid) star polymer was prepared and investigated by NMR and SEC. It was established that the product shows excellent water solubility, and low viscosity making the polymer suitable for the delivery of chemotherapeutics.⁵⁴

The preparation and in vitro evaluation of doxorubicin-loaded Fe₃O₄ magnetic nanoparticles modified with biocompatible copolymers was reported. The copolymers were characterized by H-1 NMR, GPC, X-ray powder diffraction, scanning electron microscopy and vibrating sample magnetometry. It was established that magnetic nanoparticles can find therapeutical application in the near future.⁵⁵

Poly(β -amino ester urethane (PEU)-based-multiblock copolymers containing poly(ethylene glycol) (PEG) were synthesized and their characteristic were investigated by various physicochemical methods such as nuclear magnetic resonance spectroscopy, FTIR, and GPC. The measurements suggested that the new synthetic copolymers can be applied as a potential candidate for biomedical application and drug-delivery systems.⁵⁶

Abbreviations

AIRFT-IR	attenuated total reflectance infrared spectroscopy
BLMG	bleomycin glucuronide
CLSM	confocal laser scanning microscopy
CMC	critical micelle concentration
CZE-ESI-MS	capillary zone electrophoresis electrospray ionization mass spectrometry
CE-LIF	capillary electrophoresis with laser-induced fluorescence detection
DES	dynamic light scattering
DOX	doxorubicin
DLC	drug loading capacity
DLS	dynamic light scattering
DSC	differential scanning calorimetry
FA	folic acid
FTIR	Fourier transform infrared spectroscopy

FRET	fluorescence resonance energy transfer
FTICR MS	Fourier transform ion cyclotron resonance mass spectrometry
5-FU	5-Fluorouracil
GC-IT-MS	gas chromatography-ion-trap-mass spectrometry
GPC	gel permeation chromatography
HILIC	hydrophobic interaction high performance liquid chromatography
HP-SEC	high performance size exclusion chromatography
HPLC	high performance liquid chromatography
LIF	laser induced fluorescence
LOD	limit of detection
LOQ	limit of quantitation
MEKC	micellar electrokinetic chromatography
MudPIT	multidimensional protein identification technology
PD	pharmacodynamics
PEG	polyethylene glycol
PEU	poly(β -amino ester urethane)
PK	pharmacokinetics
PLGA	poly(lactic-co-glycolic acid)
PLGA-PEG	poly(lactic-co-glycolic acid)-polyethylene-glycol
SAX	strong cation exchange chromatography
SEM	scanning electron microscopy
SDS	sodium dodecyl sulfate
SEC	size exclusion chromatography
SPME	solid phase microextraction
TEM	transmission electron microscopy
TGA	thermogravimetric analysis
WCX	weak cation exchange chromatography

References

- ¹do Nascimento, T. C. F., Casa, D. M., Dalmolin, L. F., de Mattos, A. C., Khalil, N. M., Mainardes, R. M., *Curr. Pharm. Anal.* **2012**, 8, 324-333.
- ²Huynh, C. T., Nguyen, M. K., Jeong, I. K., Kim, S. W., Lee, D. S., *J. Biomat. Sci.-Polym.Ed.*, **2012**, 23, 1091-1106.
- ³Gutheil, W. G., Reed, G., Ray, A., Ansnt, S., Dhar, A., *Curr. Pharm. Biotechnol.*, **2012**, 13, 173-179.
- ⁴van Zoggel, H., Hamma-Kourbali, Y., Galanth, C., Ladram, A., Nicolas, P., Courty, J., Amiche, M., Deibe, J., *Amino Acids*, **2012**, 42, 385-395.
- ⁵Kanai, M., Imaizumi, A., Otsuka, Y., Sasaki, H., Hashiguchi, M., Tsujiko, K., Matsumoto, S., Ishiguro, H., Chiba, T., *Cancer Chemother. Pharmacol.*, **2012**, 69, 65-70.
- ⁶Zhou, M. L., Zhu, X. M., Shao, J. R., Wu, Y. M., Tang, Y., *Appl. Biochem. Biotechnol.*, **2012**, 166, 1674-1684.
- ⁷Wang, K., Guengerich, F. P., *Chem. Res. Toxicol.*, **2012**, 25, 1740-1751.
- ⁸Demiroglu, H., Avobasi, U., Muftuler, F. Z. B., Ichedef, C. A., Gumuser, F. G., Sakarya, S., *Cancer Biother. Radiopharm.*, **2012**, 27, 371-383.
- ⁹Zhang, N., Du, Y. Cui, N., Xing, J., Liu, Z. Liu, S., *Anal. Chem.*, **2012**, 84, 6206-12.
- ¹⁰Puoci, F., Morelli, C., Cirillo, G., Curcio, M., Parisi, O. I., Maris, P., Sisci, D., Picci, N., *Anticanc. Res.*, **2012**, 32, 2843-2847.
- ¹¹Lazcano-Perez, F., Roman-Gonzalez, S. A., Sanchez-Puig, N., Arreguin-Espinosa, R., *Prot. Pept. Lett.* **2012**, 19, 700-707.
- ¹²Cuoccioloni, M., Bonfili, L., Mozicalfredo, M., Cecarini, V., Eleuteri, A. M., Angeletti, M., *Biochim. Biophys. Acta. General Subj.*, **2012**, 1820, 1027-1034.
- ¹³Mou, Z. L., Qi, X. N., Liu, R. L., Zhang, J., Zhang, Z. Q., *J. Chromatogr.*, **2012**, 1243, 33-38.
- ¹⁴Cheng, L. Y., Wang C. G., Liu, H. Z., Wang, F. X., Zheng, L. H: Zha, J., Chu, E., Lin, X. K., *Clin. Colorectal Cancer*, **2012**, 11, 207-214.
- ¹⁵Manojlovic, N., Rankovic, B., Kosanic, M., Vasiljevic, P., Stanojkovic, T., *Phytomedicine*, **2012**, 19, 1166-1172.
- ¹⁶Sharma, J., Lv, H, Gallo, J. M., *J. Pharm. Sci.*, **2012**, 101, 4100-4106.
- ¹⁷Adema, A. D., Smid, K., Losekoot, N., Honeywell, R. J., Verheul, H. M., Myhren, F., Sandvold, M. L., Peters, G. J., *Invest. New Drugs*, **2013**, 30, 1908-1916.
- ¹⁸Matsumoto, H., Higashida, M., Kubota, H., Murakami, H., Tsutsumi, K., Nakashima, H., Oka, Y., Okumura, H., Nakamura, M., Hirai, T., *Anticancer Res.*, **2012**, 32, 5111-5114.
- ¹⁹Remers, W., Dorr, R. T., *Current Med. Chem.*, **2012**, 19, 5745-5753.
- ²⁰Wolters, D. A., Stefanopoulpu, M., Dyson, P. J., Grossi, M. *Metallomics*, **2012**, 4, 1185-1196.
- ²¹Suo, A. L., Zhang, M. X., Yao, Y., Zhang, L. M., Huang, C., Nan, K. J., Zhang, W. G., *Med. Oncol.*, **2012**, 29, 1827-1836.
- ²²Horvat, T., Muzinic., A., Bansic., D., Bosnar, M. H., Zoldos, V., *Biochem., Biophys. Acta-Gen. Subj.*, **2012**, 1820, 1412-1419.
- ²³Soria-Mercado, I. E., Torres-Beltran, M., Cardoso-Martinez, F., Millán-Aquinaga, N., Becerril-Espinosa, A., *Cienc. Marinas*, **2012**, 38, 609-624.
- ²⁴Bytze, A. K., Hartinger, C. G., *Electrophoresis*, **2012**, 33, 622-634.
- ²⁵Ulanowska, A., Trawinska, E., Sawricki, P., Buszewski, B., *J. Sep. Sci.*, **2012**, 35, 2908-2913.
- ²⁶Ryvolova, M., Adam, V., Eykschlager, T., Stiborova, M., Kizek, R., *Electrophoresis*, **2012**, 33, 1545 -1549.
- ²⁷Valente, M. J., de Pinho, P. G., Henrique, R., Pereira, J. A., Carvalho, M., *Food Chem. Toxicol.*, **2012**, 50, 3847-3852.
- ²⁸Li, J. Y., Xu, S. Q., Zheng, J. H., Pan, Y., Wang, J. Z., Zhang, L. M., He, X. Y., Liu, D., *Eur. Polym. J.*, **2012**, 48, 1696-1708.
- ²⁹Chen, H., Li, G. L., Chi, H. R., Wang, D. L., Tu, C. L., Pan, L. J., Zhu, L. J., Qiu, F., Guo, F. L. Zhu, X. Y., *Bioconjugate Chem.*, **2012**, 23, 1915-1924.
- ³⁰Wolters, D. A., Stefanopoulou, M., Dyson, P. J., Groessl, M., *Metallomics*, **2012**, 4, 1185-1196.
- ³¹Galvao, L. C. D., Furrett, V. F., Bersan, S. M. F., da Cunha, M. G., Ruiz, A. L. T. G., de Carvalho, J. E., Sartoratto, A., Rehder, V. I. G., Figueira, G. M., Duarte, M. C. T., Ikegaki, M., de Alencar, S. M., Rosalen P. L., *Evid.-Based Compl. Altern. Med.*, **2012**, 751435.
- ³²Groetefend, S., Kaminski, L., Wroblewitz, S., El Deeb, S., Kuhn, N., Reichl, S., Limberger, M., Watt, S., Watzig, H., *J. Pharm. Biomed. Anal.*, **2012**, 71, 127-138.
- ³³Piccioneello, A. P., Pitaressi, G., Pace, A., Triolo, D., Picone, P., Buscemi, S., Giammona, G., *J. Drug Targ.*, **2012**, 20, 433-444.
- ³⁴Huang, H. H., Li, J. Y., Liao, L. H., Li, J. H., Wu, L. X., Dong, C. K., Lai, P. P., Liu, D. J., *Eur. Polym. J.*, **2012**, 48, 696-704.

- ³⁵Xu, Y. C., Dong, C. M., *J. Polym. Sci. Part A-Polym. Chem.*, **2012**, 50, 1216-1225.
- ³⁶Dima, S. O., Sarbu, A., Dobre, T., Purcar, V., Nicolae, C. A., *Materiale Plastice*, **2012**, 49, 106-113.
- ³⁷Tian, W., Lv, X. Y., Mu, C. G., Zhang, W. H., Kong, J., Liu, Y., Y. Fan, X. D., *J. Polym. Sci. Part A-Polym. Chem.*, **2012**, 50, 759-771.
- ³⁸Al-Daghri, N. M., Alokail, M. S., Alkharfy, K. M., Mohammed, A. K., Abd-Alrahman, S.H., Yakout, S. M., Amer, O. E., Krishnawarmi, S., *BMC Compl. Alt. Med.*, **2012**, 12, 202.
- ³⁹Ulanowska, A., Trawinska, E., Sawricky, P., Buszewski, B., *J. Sep. Sci.*, **2012**, 35, 2908-2913.
- ⁴⁰Krylowa, S. M., Koshkin, V., Bagg, E., Schfield, C. J., Krylow, S. N., *J. Med. Chem.*, **2012**, 55, 3546-3552.
- ⁴¹Bytzeck, A. K., Hartinger, C. G., *Electrophoresis*, **2012**, 33, 622-634.
- ⁴²Wang, Y. H., Taylor, T. H., Arriaga, E. A., *Anal. Bioanal. Chem.*, **2012**, 402, 41-49.
- ⁴³Ho, J. A. A., Fan, N. C., Jou, A. F. J., Wu, L. C. Sun, T. P., *Talanta*, **2012**, 99, 683-688.
- ⁴⁴Nguyen, H. T. Q., Murray, V., *J. Biol. Inorg. Chem.*, **2012**, 17, 1209-1205.
- ⁴⁵Sha, S., Jin, H. L., Li, X., Yang, J., Ai, R. T. Lu, J. L., *Protein Cell.*, **2012**, 3, 392-399.
- ⁴⁶Grabmann, G., Meier, S. M. Scaffidi-Domianello, Y. Y. Galanski, M., Keppler, B. K., Hartinger, C. G., *J. Chromy. A*, **2012**, 1267, 156-161.
- ⁴⁷Lu, H., Wang, S. S., Zhao, B. Y., *Asian J. Anim. Vet. Adv.*, **2012**, 7, 822-831.
- ⁴⁸Valente, M. J., de Pinho, P. G., Henrique, R., Pereira, J. A., Carvalh, M., *Food Chem. Techn.*, **2012**, 50, 3847-3852.
- ⁴⁹Ma, G. L., Zhao, S. X., Jin, X., Chen, M. M., Zhang Z. P., Song, C. X., *Chem J. Chinese Univ.*, **2012**, 33, 1854-1859 (in Chinese, Abstract in English).
- ⁵⁰Yun, J. M., Park, S. Y., Lee, E. S. Youn, Y. S., Park, G. Y., Lim, C., Lee, B. J., Song, H. T., *Macromol. Res.*, **2012**, 20, 944-953
- ⁵¹Zhang, C. Y., Yang, Y. Q., Huang, T. X., Zhao, B., Guo, X. D., Wang, J. F., Zhang, L. J., *Biomaterials*, **2012**, 33, 6273-6283.
- ⁵²Yu, Z. X., He, B., Long, C. Y., Liu, R., Sheng, M. M., Wang, G., Tang, J. Z., Gu, Z. W., *Macromol. Res.*, **2012**, 20, 250-258.
- ⁵³Wang, Y. J., Dong, C. M., *J. Polym. Sci., Part A-Polym. Chem.*, **2012**, 50, 1645-1656.
- ⁵⁴Duan, S. F., Cai, S., Xie, Y. M., Bagby, T., Ren, S. Q., Forest, M. L., *J. Polym. Sci. Part A-Polym. Chem.*, **2012**, 50, 2715-2724.
- ⁵⁵Akbarzadeh, A., Mikaeli, H., Zarghami, N., Mohammad, R., Barkhordary, A., Davaran, S., *Int. J. Nanomed.*, **2012**, 7, 511-526.
- ⁵⁶Huynh, C. T., Nguyen, M. K., Jeong, I. K., Kim, S. W., Lee, D. S., *J. Biomat. Sci. Polym. Ed.*, **2012**, 23, 1091-1106.

Received: 09.02.2014.
Accepted: 15.02.2014.



GREEN SYNTHESIS OF SILVER NANOPARTICLES BY THE ACTION OF BLACK OR GREEN TEA INFUSIONS ON SILVER IONS

Franco Cataldo^{[a]*}

Key Words: Green synthesis; Black tea infusion; Green tea infusion; Tea polyphenols; Silver nanoparticles; Colloidal silver; Particle size distribution; Z-potential; antibacterial properties.

Silver nanoparticles were obtained by the reduction of Ag^+ ions through the action of black tea or green tea infusions. Also decaffeinated tea infusion is able to produce silver nanoparticles. The tea polyphenols present in the black and green tea are able not only to reduce silver ions but also to stabilize the resulting nanoparticles acting as “capping agents”. The surface plasmon resonance characteristic absorption band of silver nanoparticles was used to monitor the reduction kinetics of silver in black and green tea infusions respectively. It was found a faster reduction kinetics in green tea infusion. Dynamic light scattering (DLS) was used for the determination of the average diameter of the silver nanoparticles which were found of 20.8 nm in green tea infusion and 78.7 nm in black tea infusion. For comparison the average diameter of silver nanoparticles obtained in tannin was found at 55.7 nm. DLS was also used for the determination of the Z-potential of the silver colloidal dispersions in black and in green tea infusions. The results show that stable suspension are obtained since the tea polyphenols act also as capping and stabilizing agents of the nanoparticles. The bactericidal properties of silver nanoparticles in both black and green tea infusions were confirmed on the Gram(-) bacterium *P. Aeruginosa*. Instead, the silver nanoparticles in both black and green tea infusions are not effective against the spores of *B. Subtilis*.

* Corresponding Authors

E-Mail: franco.cataldo@fastwebnet.it

[a] Actinium Chemical Research srl, Via Casilina, 1626A, 00133 Rome, Italy

instead of the conventional chemical reducing agents¹⁻⁴ and other approaches like photon irradiation, electrosputtering, electrochemical reduction, sonication, laser ablation.^{1-4,12}

The successful use of plant extracts as reducing and capping agents of silver colloidal solutions is covered by recent reviews⁴⁻¹¹ and by several recent papers.¹²⁻²⁵

Introduction

The synthesis of metal nanoparticles in general and silver nanoparticles in particular represents a promise with potential applications in dermatology, cosmetics, pharmacology but also in catalysis and nanotechnology in general.¹⁻³ The interest on silver nanoparticles has its roots on the antibacterial and antiviral properties of colloidal silver which is also effective against fungi and protozoa.¹⁻³ A number of papers were dedicated to different synthetic approaches and to the characterization of different types of silver nanoparticles and numerous reviews are available summarizing the most relevant progresses and potential applications.⁴⁻¹¹

Particularly innovative and under great expansion is the topic of green synthesis of silver nanoparticles using readily available reducing agents and capping agents taken from plants and hence from renewable sources. In view of the potential and safe application of silver nanoparticles it is necessary to have a green approach in their synthesis which means that it is fundamental to use solvents, reducing and capping agents which are completely safe for the mammals and for the environment. Other aspects of a green synthesis require that the selected reagents are easily accessible (possibly from renewable sources), widely distributed, safe to handle and able to minimize the waste and energy costs. More in detail, the green synthesis of silver nanoparticles involves the utilization of biological systems such as yeast, fungi, bacteria and plant extracts⁴⁻¹¹

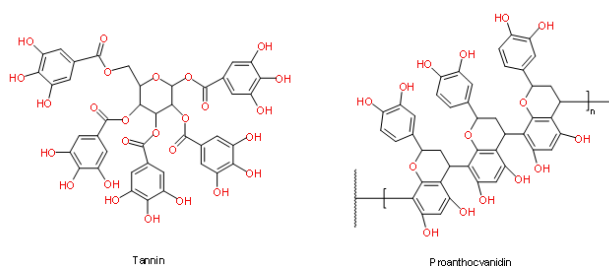


Chart 1. Examples of tannin structures. Gallic acid ester (left) and proanthocyanidin (right)

In a recent paper we have shown that tannin (see Chart 1 for the chemical structure of tannin) is an effective reducing and capping agent for the production of silver nanoparticles in agreement with the green synthetic approach.¹² Tannin, known also as “gallotannic acid” and as “tannic acid” is extracted from different plant sources or from plant galls and its chemical structure is a mixture of molecules of pentagalloylglucose, pentagalloylglucose and proanthocyanidins (Chart 1).^{26,27} It forms colloidal solutions in water and it is a reducing agent used to treat leather and also in medicine as astringent.^{26,27} Tannic acid is not toxic and could be suitably combined with colloidal silver to stabilize the resulting lyosol, thus acting simultaneously as

reducing and capping agent.¹² After the work on tannic acid,¹² it was a logical consequence for us to study both the black and green tea tannins as reducing and stabilizing agents of silver nanoparticles and the present work represent a full account of such work. Black tea polyphenols were already reported in literature as effective reducing agents for the synthesis of silver nanoparticles²⁸⁻⁴³ but in the current work we will present a very simple and effective synthetic approach using a simple black tea beverage as reducing agent. Furthermore, we will show that decaffeinated black tea is still an effective reducing and capping agent for the production of colloidal silver solutions. Finally, we will show also the effectiveness in silver nanoparticles production of the green tea beverage. In all cases the resulting colloidal silver solutions can be prepared at high concentration and are stable.

Experimental

Materials and equipment

The black tea used in the present work was a commercially available black tea from Ati a subsidiary of Unilever Italia (Rome, Italy). Similarly, the green tea used in the present work was from Lipton another subsidiary of Unilever Italia (Rome, Italy). The decaffeinated tea adopted in this work was instead from Star spa (Milan, Italy). The electronic absorption spectra were studied using a Shimadzu UV 2450 spectrophotometer using thermostatically controlled quartz cuvettes kept at 20 °C. The reference cuvette was always filled with distilled water. The colloidal silver particle size diameter and the relative Z-potential were measured on a dynamic light scattering: Zetasizer-7 from Malvern. The bactericidal properties of the colloidal solutions of silver nanoparticles in black and in green tea were tested following UNI EN 1040 test method on *P. Aeruginosa*. The sporicidal properties of the colloidal solutions of silver nanoparticles in black and in green tea were tested following UNI EN 13704 test method on spores of *B. Subtilis*.

Reduction of Ag⁺ with black tea infusion (50 mg L⁻¹ Ag)

A black tea bag of 1.5 g was left for 20 min in 250 ml of distilled boiling water. After cooling to room temperature, 60 ml of the infusion were taken with a pipette and diluted to 500 ml in a volumetric flask and hand-shaken to homogenize the dilution. The pH of the resulting solution was neutral and was made alkaline by adding a very small portion of potassium carbonate (K₂CO₃) until a pH = 10 was reached. Separately a stock solution of 54 mg of AgNO₃ in 200 ml of distilled water was prepared.

Two experiments were performed. The first experiment was designed to illustrate the reduction of Ag⁺ with black tea tannins. From the alkalized 500 ml stock solution at pH = 10 were taken 80 ml which were transferred in a magnetically stirred flask. Stirring was set at the minimum possible speed. The stock solution of AgNO₃ was added in portions of 5 ml per time. After each addition the solution was stirred and then the resulting electronic absorption

spectrum was recorded. The progress of silver nanoparticles production was followed with the progressive addition of the AgNO₃ solution.

The other experiment was aimed at measuring the reduction kinetics according to the following approach. From the alkalized 500 ml stock solution at pH = 10 were taken 50 ml which were transferred in a magnetically stirred flask. Then 20 ml of the AgNO₃ stock solution were added in a single shot. The growth of the surface plasmon resonance band of the separated silver nanoparticles was monitored spectrophotometrically as function of time.

Reduction of Ag⁺ with black tea infusion (85 mg L⁻¹ Ag)

A black tea bag of 1.5 g was left for 20 min in 500 ml of distilled boiling water. After cooling to room temperature the pH was adjusted to 10 by adding a small amount (≈ 500 mg) of K₂CO₃. Then AgNO₃ (67 mg) were added directly into the tea infusion, dissolved completely and left in the dark overnight. The solution was very dark and for the spectrophotometric measurements a samples taken from the solution were diluted 1:100, 1:10, 1:5 and 1:2.5 with distilled water and the resulting spectra were measured with the purpose of the determination of the molar extinction coefficient.

Reduction of Ag⁺ with black tea infusion (234 mg L⁻¹ Ag)

The same procedure described in the preceding paragraph was followed. The unique difference is the amount of AgNO₃ added directly into the black tea infusion: 184 mg corresponding to 234 mg L⁻¹ of Ag.

Reduction of Ag⁺ with decaffeinated black tea infusion (286 mg L⁻¹ Ag)

The same procedure described in the preceding paragraph was followed. The unique differences are the use of a 1.5 g of decaffeinated tea bag instead of black tea bag and the amount of AgNO₃ added directly into the decaffeinated black tea infusion: 225 mg corresponding to 286 mg L⁻¹ of Ag. The absence of caffeine and other xanthines in the infusion does not impair reducing power of the tea infusion.

Reduction of Ag⁺ with green tea infusion

A green tea bag of 1.3 g was left for 20 min in 200 ml of distilled boiling water. After cooling to room temperature, 60 ml of the infusion were taken with a pipette and diluted to 500 ml in a volumetric flask and hand-shaken to homogenize the dilution. The pH of the resulting solution was 6 and was made alkaline by adding a very small portion of potassium carbonate (K₂CO₃) until a pH=10 was reached. Separately a stock solution of 54 mg of AgNO₃ in 200 ml of distilled water was prepared.

The reduction speed of Ag⁺ caused by the green tea infusion was studied spectrophotometrically by adding known volumes of AgNO₃ stock solution into the alkalized green tea stock solution.

Reduction of Ag⁺ with green tea infusion (186 mg L⁻¹ Ag)

A green tea bag of 1.3 g was left for 20 min in 500 ml of distilled boiling water. After cooling to room temperature the pH was adjusted to 10 by adding a small amount (≈ 500 mg) of K_2CO_3 . Then $AgNO_3$ (147 mg) were added directly into the tea infusion, dissolved completely. The solution turned from yellow-amber color into dark-brown and was left in the dark overnight. The solution was very dark and for the spectrophotometric measurements a samples taken from the solution were diluted 1:100, 1:40, 1:25, 1:10 and 1:6.6 with distilled water and the resulting spectra were measured with the purpose of the determination of the molar extinction coefficient.

Reduction of Ag⁺ with green tea infusion (286 mg L⁻¹ Ag)

The same procedure described in the preceding paragraph was followed. The unique difference are the amount of green tea (2.6 g instead of 1.3) and the amount of AgNO₃ added directly into the black tea infusion: 225 mg corresponding to 286 mg L⁻¹ of Ag.

Results and Discussion

Colloidal silver production with black tea infusion

The components of black tea beverage are reported in Table 1^{44,45} and consist of a mixture of different type of molecules.

Table 1. Composition of black tea beverage

Components	Extracted solids (weight %)
Thearubigins	35.8
Theaflavins	2.6
Catechins	11.2
Gallic acid	1.1
Chlorogenic acid	0.2
Caffeine	7.5
Theobromine	0.7
Oxalic acid	1.5
Mixture of aliphatic acids	1.2
Lipids and waxes	4.8
Sugars	6.9
Polysaccharides	4.2
Pectin	0.2
Peptides	6.0
Theanine	3.5
Amino acids	3.0
Potassium cation	4.8
Other minerals	4.7
Aroma components	0.1

The main component (about 36%) is represented by thearubigins (see Chart 2) whose chemical structure is polyphenolic in nature, very complex and not yet fully understood.⁴⁵⁻⁴⁷

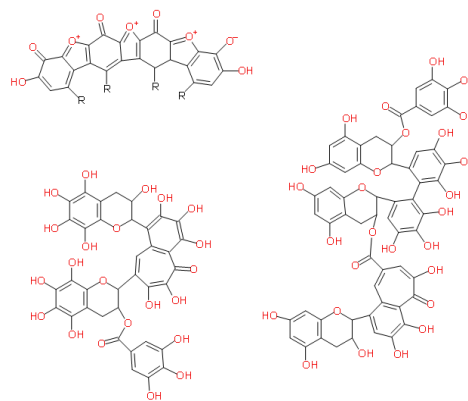


Chart 2. Proposed structures for thearubigins present in black tea⁴⁵⁻⁴⁸

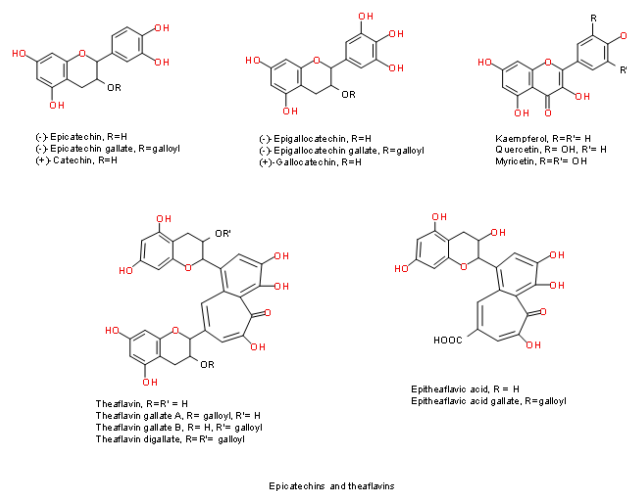


Chart 3. Epicatechins and Teaflavins present in black and green tea⁴⁴

Initially it was thought that thearubigins were characterized by a high molecular weight, instead recent investigations⁴⁵⁻⁴⁷ have clarified that thearubigins consist of a rich mixture of oligomers with molecular weight around 2×10^3 Da derived from the oxidation of tea catechins and theaflavins (see Chart 3). The other important component of black tea beverage (see Table 1) are the catechins like for example catechin, galocatechin, epicatechin and epigallocatechin (the last two also esterified with gallic acid) and the flavanols (see Chart 3).

All these substances are reducing agents but also the minor components of black tea beverage like gallic acid and chlorogenic acid, the sugars and polysaccharides, the lipids, the peptides and amino acids may act as reducing agents for the silver ion into silver lyosol and especially as capping agents which means that these substances are able to coordinate and coat the silver nanoparticles stabilizing them in the colloidal state. Indeed the standard electrochemical potential (vs Standard Hydrogen Electrode) for epigallocatechin is +430 mV while epicatechin exhibits a potential of +560 mV and theaflavin +510 mV.⁴⁸ Such electrochemical potentials should be compared with that of silver $E_{\text{Ag}^+/\text{Ag}} = +799.6$ mV and it is immediately evident that the catechins and the flavins present in tea are effective reducing agent of silver ions.

Furthermore the antioxidant properties of green and black tea leaf and extracts were studied by electron spin resonance (EPR) technique putting in evidence an higher content of semiquinone radicals in black tea in agreement with its preparation through an oxidative enzymatic process.⁴⁹ Another EPR study has evidenced that the antioxidant power (thus, its reducing power) of green tea is higher than that of black tea as expected.⁵⁰ The antioxidant activity of black and green tea was also studied with a fluorescence assay and has confirmed the greatest antioxidant activity for green tea.⁵¹ Among the black teas a distinction was made between Orthodox black tea which is hand-processed and the CTC black tea which is the common machinery processed tea used in tea bags. At the fluorescence assay the Orthodox black tea gives the same antioxidant response as the green tea while the CTC black tea gives about 50% lower antioxidant activity.⁵¹ Another interesting aspect studied by Carloni and colleagues⁵¹ regard the tea chelating activity for ferrous ions. It was found that the highest chelating activity is offered by Orthodox black tea followed by the CTC black tea while the lowest chelating activity was found in the case of green tea. The chelating activity is related to the ability of a given tea to stabilize the silver nanoparticles: higher chelating activity means better colloid stabilization.

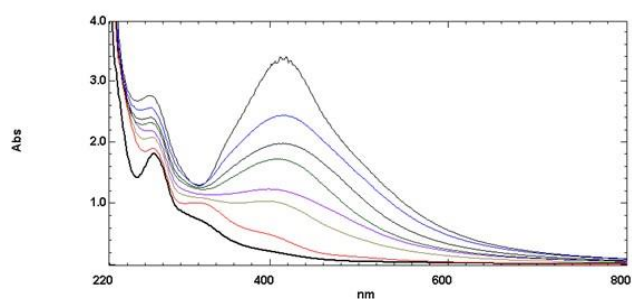


Figure 1. Electronic absorption spectra (curves from bottom to top): diluted black tea infusion as detailed in the experimental section (black thick line); after K_2CO_3 addition to pH=10 (red line); after addition of 5, 7, 10, 15, 20 and 25 ml of $AgNO_3$ respectively, there is the growth of the silver nanoparticle absorption band at about 414 nm.

With all the above premises it was not a surprise to observe the reduction of silver nitrate by black tea infusion as shown in Fig. 1. It was performed as detailed in the experimental section by adding $AgNO_3$ solution to an alkalized tea infusion. It is important to note that it was necessary to bring the pH of the tea infusion to 10 by the addition of small amounts of K_2CO_3 to observe the Ag^+ reduction. In neutral conditions the addition of $AgNO_3$ does not lead to any separation of Ag nanoparticles. The evidence of the synthesis of silver nanoparticles is offered by the development of the absorption band at 393.7 nm which grows in intensity as function of the $AgNO_3$ added and which is shifted toward 408.6 nm and then to 414.4 nm. The band at 394-414 nm is due exclusively to the formation of silver nanoparticles in the solution and is attributed to collective excitation of the electron gas in each particle due to the periodic change of the electron density at the surface modulated by the electromagnetic field of the incident radiation. Such absorption band is known as surface plasmon resonance absorption band.^{1,3,4,6,12} Fig 2 shows the linear growth of the surface plasmon resonance of silver nanoparticles as function of the amount of silver ions added

to the black tea infusion. To each silver ions addition corresponds an increment in the intensity of the absorption band due to silver nanoparticles. This implies a reduction of silver ions according to the reaction $Ag^+ + e^- \rightarrow Ag^0$ such reaction is promoted by the polyphenols, the catechins and the flavonols present in the black tea infusion.

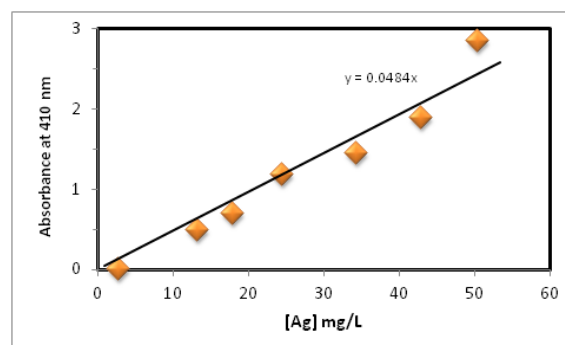


Figure 2. Linear growth of the surface plasmon resonance band at about 410 nm due to the formation and accumulation of colloidal Ag nanoparticles reduced by black tea infusion. In the abscissa the silver concentration added to the stock tea solution. The absorbance values are those of Fig. 1 corrected for the absorption of the starting solution without silver.

To measure the reduction kinetics of silver ions to silver nanoparticles the experiment reported in the experimental section (second part) was designed. It consisted in the addition of a known amount of silver nitrate into the alkalized black tea infusion measuring the time needed for the growth of the band at about 414 nm associated to the formation of silver nanoparticles. The data of this experiment are shown in Fig. 3 in a graph where the \ln of the absorbance ratio at about 410 nm measured at any time A_t and at the beginning of the experiment A_0 are plotted against the reaction time t (in s). All the experimental data are fitted by the logarithm equation

$$\ln \frac{A}{A_0} = 0.4646 \ln t - 2.3546 \quad (1)$$

where

A_0 = initial absorbance

A_t = absorbance at the t moment

Suggesting a more complex kinetic law than the pseudofirst order. However, it is possible to consider only the first tract of the curve where the data are reasonably linear as shown by the red line in Fig. 3. For these early stages of reaction the pseudofirst reaction kinetics principle can be applied so that:

$$\ln \frac{A}{A_0} = 9.44 \cdot 10^{-4} t \quad (2)$$

where A_0 and A_t are the same as in Eqn.1.

Consequently the rate constant of this tract is $k_{black} = 9.44 \times 10^{-4} s^{-1}$.

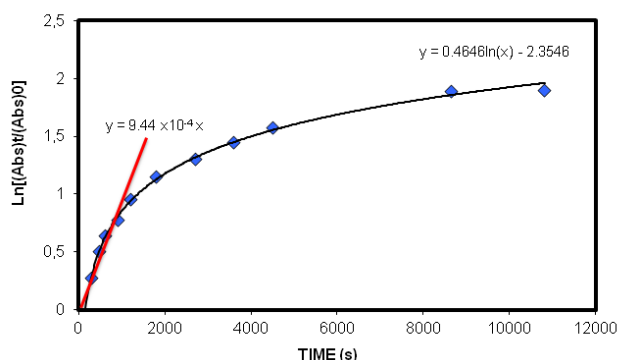


Figure 3. Kinetics of the reduction of Ag^+ by alkalized black tea infusion. The entire process does not conform to the pseudofirst reaction kinetics law unless one considers only the first stages of the reaction as shown in the figure.

Colloidal silver production with green tea infusion

As already discussed in the experimental section the reducing power of green tea is higher than that of the common CTC black tea and only the Orthodox black tea may be comparable in reducing power to the green tea.⁴⁹⁻⁵¹ The reason of the higher reducing power of the green tea is very simple: its catechins and flavanols components (see Chart 3) have not undergone the enzymatic oxidation process which is instead subjected the black tea components.⁴⁴ In Table 2 are summarized the main green tea components present in a green tea infusion^{44, 52} and it is evident the absence of the polyphenolic fraction known as thearubigins which are instead present in the black tea infusion. Consequently it is plain to expect that green tea is able to reduce Ag^+ ions, but again, it is recommended to alkalize also green tea infusion to pH=10 prior to add a silver salt for the reduction. It has been found that the green tea infusions are slightly more acidic than the black tea infusions since the typical pH of the former is about 6 against 7 found in the black tea infusion.

Table 2. Composition of green tea beverage

Component	Weight % of the extracted solids
Epigallocatechin gallate	20.3
Epicatechin gallate	5.2
Epigallocatechin	8.4
Epicatechin	2.0
Flavanols	2.2
Caffeine	7.4
Theanine	4.7
Glutamic acid	0.5
Aspartic acid	0.5
Arginine	0.7
Other amino acids	0.8
Sugars	6.7
Alcohol insolubles	12.2
Potassium cation	4.0
Aroma components	0.1

Fig. 4 shows the electronic absorption spectra of green tea infusion at the dilution reported in a previous. In these conditions the green tea infusion shows only a shoulder at 325 nm.

When the pH of the green tea infusion is brought to 10, the shoulder at 325 nm becomes a peak. The subsequent addition of AgNO_3 solution in portions of 2.5 ml per time or 5 ml per time leads to the development of the absorption band associated to the formation of silver nanoparticles, the surface plasmon resonance band. Initially the peak of such band was found at 410 nm but gradually the peak shifted to longer wavelengths as the concentration of silver nanoparticles was increased reaching the final value of 416 nm.

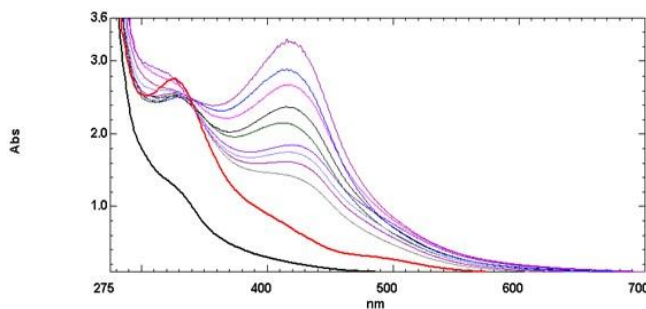


Figure 4. Electronic absorption spectra (curves from bottom to top): diluted green tea infusion as detailed in the experimental section (black thick line); after K_2CO_3 addition to pH=10 (red line); after addition of known volumes of AgNO_3 there is the growth of the silver nanoparticle absorption band at about 415 nm.

The kinetics of Ag^+ ions reduction to silver nanoparticles exerted by the green tea infusion is described in the experimental section. Also in the case of green tea infusion the pseudofirst kinetic law is followed only in the first stages of the reduction and graphs similar to that shown in Fig. 3 can be obtained. The pseudofirst order kinetic rate constant for green tea infusion reduction of Ag^+ ions was found about one order of magnitude larger than that measured previously on black tea: $k_{\text{green}} = 8.9 \times 10^{-3} \text{ s}^{-1}$.

Molar extinction coefficient of the silver nanoparticles produced under different conditions

The appearance of the surface plasmon resonance absorption band is the result of the interaction of the incident light on the silver nanoparticle surface with the conduction electrons of the metal. According to the Mie theory, the total cross-section of light absorption of a particle is directly related to the particle radius.¹ Thus, the increase in the intensity of the surface plasmon resonance band is directly related to the diameter of the particles but applying the Lambert-Beer law, the cross-section or molar extinction coefficient is also related to the concentration of the suspended particles. Thus, contrary to common molecules where the molar extinction coefficient is due only to their concentration in the case of colloidal nanoparticle suspension such cross section value is regulated by the particle dimensions other than their concentration. In other words, it is possible to affirm that each family of particles with a given diameter possesses a peculiar and unique molar extinction coefficient. Experimental data have shown that in addition to increase in absorption, the growth of silver particles is accompanied by the surface plasmon resonance broadening and red shifting of its absorption maximum.¹

Table 3. Molar extinction coefficients (ϵ) of the Ag nanoparticles

Colloidal solution	Original concn. [Ag] mg L ⁻¹	Measured concn., [Ag] mg L ⁻¹	Wavelength λ_{\max} , nm	ϵ , L cm ⁻¹ mol ⁻¹	Notes
Tannic Acid	15	26	404-414	15886	ref. ¹²
Black tea pH = 10	85	0.85-17	409.7-413.4	14541	This work
Black tea pH = 5	85	2.6-17	418-424	12018	This work
Black tea pH = 10	234	2.3-23.4	410.8-413.4	12244	This work
Decaffeinated black tea pH = 10	286	2.9-11.4	406-408	13474	This work
Green tea pH=10	186	1.9-27.9	406-411	12041	This work
Double green tea pH=10	286	2.9-21.5	405.6-408.0	13576	This work
Silver proteinate (*)	1500	7.5-30	402-403	9083	Commercial sample

(*) Absorption max at 402 nm

This explains why the surface plasmon resonance band of silver nanoparticles reduced with green tea infusion shows an initial band at 410 nm and then, with further Ag⁺ reduction the band is red shifted to 416 nm. Similarly, in the black tea infusion the silver nanoparticles start from a surface plasmon resonance band at 394 nm which reaches 414 nm at the completion of the reduction.

The measurement of the molar extinction coefficient of silver nanoparticles was performed as detailed in the experimental section for black tea, for decaffeinated black tea and for green tea. The procedure involved the preparation of a tea infusion in 500 ml of distilled water, the alkalization of the infusion to pH=10 through the addition of K₂CO₃ and then by the addition of AgNO₃ in the desired amounts as specified in the mentioned experimental sections and as summarized in Table 3. Under these conditions the solutions were too dark for any spectrophotometric measurements and therefore known volumes of the colloidal solutions were diluted with distilled water and the absorbance at about 410-415 nm was determined. In general three different dilutions were performed and the average molar extinction coefficient was taken and reported in Table 3 using the Lambert-Beer law:

$$\epsilon = Ab^{-1}c^{-1} \quad (3)$$

The molar extinction coefficient ϵ (in L cm⁻¹ mol⁻¹) of silver nanoparticles was determined assuming the complete reduction of the Ag⁺ ions added and being b (expressed in cm) the path length of the quartz cuvette used for the measurement and c (in mol L⁻¹) the silver concentration.

In the measurement range comprised in the interval of 0.5-30 mg L⁻¹ of Ag the ϵ value of each sample studied was found practically constant and the average measured value is reported in Table 3. The highest $\epsilon = 15886$ L cm⁻¹ mol⁻¹ was measured on the silver nanoparticles reduced with tannic acid in a previous work but the wavelength range of the surface plasmon resonance is comparable to that found on the silver nanoparticles reduced in black and green tea.¹² As a general comment, the Ag nanoparticles in black tea infusion tend to have the surface plasmon resonance band slightly red shifted in comparison to the analogous samples prepared in green tea infusion. This fact combined with a general trend to slight higher molar extinction coefficient ϵ values for the Ag nanoparticles in black tea infusion, already

anticipates that the average diameter of the silver nanoparticles in black tea infusion should be larger than that of the Ag nanoparticled in green tea infusion (see next section).

As shown in Table 3, in one case we have changed the pH of the silver/black tea colloidal solution bringing it from 10 down to 5. No precipitations or phase separations were observed in the colloidal suspension upon acidification, however the spectrophotometric analysis revealed red shift of the silver nanoparticles absorption band from 410-414 nm at pH=10 to 418-424 nm at pH=5 this red shift is consistent with the phenomenon of silver particles aggregation and growth.¹ The molar extinction coefficient dropped from an initial value of $\epsilon = 14541$ L cm⁻¹ mol⁻¹ in the basic lysol to $\epsilon = 12018$ L cm⁻¹ mol⁻¹ in the acidified solution suggesting a light etching of the surface of the silver nanoparticles.

Decaffeinated black tea is able to reduce Ag⁺ ions in the same way as the normal black tea (see Table 3). This implies that the silver reduction is due to the polyphenols, catechins and flavanols and not by caffeine and theobromin. The molar extinction coefficient of the silver nanoparticles in decaffeinated black tea is $\epsilon = 13474$ L cm⁻¹ mol⁻¹, a value completely inside the ϵ values range measured in different black tea samples.

For comparison Table 3 reports also the molar extinction coefficient measured on a commercial sample of silver proteinate, a commercial antiseptic where silver is reduced and stabilized to nanoparticles by the action of egg albumin protein. Silver proteinate shows an $\epsilon = 9083$ L cm⁻¹ mol⁻¹, a value significantly lower than the ϵ values measured on all silver colloidal solutions prepared in black and green tea. Furthermore, the λ_{\max} value of the surface plasmon resonance band of silver proteinate was found at only 402 nm. The combined data of ϵ and λ_{\max} suggest a smaller particle size for silver proteinate than the silver nanoparticles prepared by black or green tea infusions.

Another information which can be gained from the electronic absorption spectra of silver nanoparticles is the shape of the particles. Krutyakov et al.¹ discuss in detail this aspect considering different forms of silver nanoparticles (spheroidal, cylindrical, polyhedral) and presenting the corresponding electronic absorption spectrum. The spherical silver nanoparticles display the simplest electronic absorption spectrum with the a single surface plasmon resonance band as those shown in Fig. 1 and Fig. 4.

Table 4. Average diameter, polydispersion index and zeta potential of Ag nanoparticles

Colloidal solution	Average diameter, nm	Polydispersion index	Z-potential in mV	Notes
Tannic Acid	55.7	0.303	-33.0	ref. ¹²
Black tea pH = 10	78.7	0.560	-31.0	This work
Green tea pH = 10	20.8	0.370	-29.8	This work

All the other silver nanoparticles forms display a more complex spectrum with additional bands and sub-bands or with the main peak shifted at longer wavelengths. Based on the spectra recorded on the silver nanoparticles reduced with tannic acid, black and green tea infusions it can be concluded that in all cases considered in the present work, spherical particles were produced.

Particle size of silver nanoparticles

The Dynamic Light Scattering (DLS) analytical technique measures the Brownian motion of nanoparticles whose speed of motion (or diffusion constant), is linked to particle size through the Stokes–Einstein equation. Using the Malvern Zetasizer the silver colloidal suspensions were analyzed both in the black tea and in the green tea infusions as detailed in the experimental section. The results of such analysis are shown in Fig. 5.

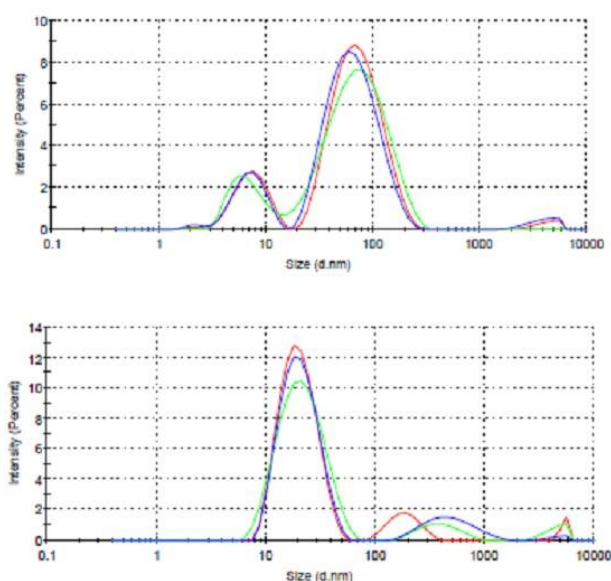


Figure 5. Dynamic light scattering analysis of the particle size distribution of the silver nanoparticles produced in black tea and in green tea infusion as detailed in the experimental section.

The particle size distribution is broader (polydispersion index 0.560) and centered at about 78 nm in the case of the silver colloidal nanoparticles in black tea while the distribution is narrower (polydispersion index 0.370) in the case of silver colloidal nanoparticles in green tea with the average size at about 20.8 nm. All the data are summarized in Table 4.

For comparison are reported also the polydispersion index (0.303) and the average size distribution of the silver nanoparticles produced in tannic acid in a previous work.¹²

The catechins and flavanols in green tea are able to produce smaller silver nanoparticles and with a narrower distribution than the thearubigins polyphenols present in the black tea which instead give higher average diameter and broader particle size distribution. Of course these data are more direct and precise than the analysis made with the electronic absorption spectroscopy which indeed suggested smaller particle size for the Ag nanoparticles in green tea ($\lambda = 406\text{--}410\text{ nm}$ and $\epsilon = 13576\text{ L cm}^{-1}\text{ mol}^{-1}$) than in black tea ($\lambda = 410\text{--}413\text{ nm}$ and $\epsilon = 14541\text{ L cm}^{-1}\text{ mol}^{-1}$).

Stability of the colloidal silver in black and green tea

Zeta (ζ) potential is the potential difference between the medium where the particles are dispersed and the stationary layer of fluid attached to the surface of each particle by mean of electrostatic interactions, dispersion forces, hydrogen bond [53,54]. The zeta potential indicates the degree of repulsion between adjacent, similarly charged particles in a dispersion. A high Z-potential will confer stability to the colloidal dispersion. This means that the dispersion will resist aggregation of its particles.^{53,54} When the Z-potential is low, attraction exceeds repulsion and the dispersion will break and flocculate. So, colloids with high Z-potential (negative or positive) are electrically stabilized while colloids with low Z-potentials tend to coagulate or flocculate.^{53,54} Using the Malvern Zetasizer we have measured also the Z-potential of the silver colloidal nanoparticles in black tea, green tea and those obtained with tannic acid in a previous work¹² for comparison. All the results are reported in Table 4. A colloidal suspension is considered stable if the Z-potential $\geq |25|\text{ mV}$. Of course this limit is a convention and $\pm 25\text{ mV}$ is the limit that arbitrary separates low-charged surfaces from highly charged surfaces. Table 4 shows that the Z-potential of Ag nanoparticles in black tea have $\zeta = -31\text{ mV}$ while such value is slightly lower in the case of Ag nanoparticles in green tea have $\zeta = -29.8\text{ mV}$ probably for the lower coordination ability of green tea catechins and flavanols in comparison to the higher coordination ability of thearubigins present only in the black tea. Anyway both silver colloidal dispersion either in black or in green tea exhibit more than satisfactory stability. Silver nanoparticles in tannic acid are even slightly better stabilized since $\zeta = -33\text{ mV}$ and this could be again attributed to a better ability of tannins to coat or to act as capping agents of the silver nanoparticles preventing the undesired aggregation and flocculation.

Evaluation of bactericidal and sporicidal effect of silver nanoparticles in black and in green tea

The bactericidal effect of silver is known since ancient times. The bactericidal effect of colloidal silver is firstly due to the production and release of Ag^+ ions which exert an oligodynamic effect on bacteria and protozoa.^{1,4,6,9,10,55}

Table 5. Evaluation of bactericidal activity according to UNI EN1040 on *P. Aeruginosa*

Colloidal Ag in Black Tea [Ag] = 186 mg L ⁻¹	Contact time 5 min	Contact time 10 min	Contact time 15 min
[Ag] = 186 mg L ⁻¹	270 cfu R=5log	250 cfu R=5log	<10 cfu R>5log
[Ag] = 3.72 mg L ⁻¹	>300 cfu R<5log	200 cfu R>5log	<10 cfu R>5log
[Ag] = 1.86 mg L ⁻¹	>300 cfu R<5log	250 cfu R=5log	<10 cfu R>5log
Colloidal Ag in Green Tea [Ag] = 233 mg L⁻¹			
[Ag] = 233 mg L ⁻¹	370 cfu R<5log	230 cfu R=5log	<10 cfu R>5log
[Ag] = 4.66 mg L ⁻¹	400 cfu R<5log	200 cfu R=5log	<10 cfu R>5log
[Ag] = 2.33 mg L ⁻¹	410 cfu R<5log	250 cfu R=5log	<10 cfu R>5log

Note: cfu = colony forming unit

Table 6. Evaluation of sporicidal activity according to UNI EN 13704 on spores of *B. Subtilis*

Colloidal Ag in Black Tea [Ag] = 186 mg L ⁻¹	Contact time 5 min	Contact time 10 min	Contact time 15 min
[Ag] = 186 mg L ⁻¹ (Neat)	>300 cfu	>300 cfu	>300 cfu
[Ag] = 3.72 mg L ⁻¹ (Diluted 1:50)	No reduction	No reduction	No reduction
[Ag] = 1.86 mg L ⁻¹ (Diluted 1:100)	No reduction	No reduction	No reduction
Colloidal Ag in Green Tea [Ag] = 233 mg L⁻¹			
[Ag] = 233 mg L ⁻¹ (Neat)	>300 cfu	>300 cfu	>300 cfu
[Ag] = 4.66 mg L ⁻¹ (Diluted 1:50)	No reduction	No reduction	No reduction
[Ag] = 2.33 mg L ⁻¹ (Diluted 1:100)	No reduction	No reduction	No reduction

Note: cfu = colony forming unit

Even at high dilution the Ag⁺ ions bind to the –SH groups of enzymes inhibiting their activity and also causing the denaturation of proteins.⁵⁵ Silver also reacts with the amino-, carboxyl-, phosphate-, and imidazole-groups and diminish the activities of lactate dehydrogenase and glutathione peroxidase.⁵⁵ Furthermore, silver nanoparticles may attach to the surface of membrane cell disturbing permeability and respiration function of the cell. Smaller Ag nanoparticles are more effective bactericidal than the larger nanoparticles since they can penetrate the bacterial cells and causing the disruption of the cell walls thereby causing the production of free radicals including ROS (reactive oxygen species).^{1,4,6,9,10,55} The oligodynamic effect has been observed in living cells, algae, molds, spores, fungi, viruses, prokaryotic and eukaryotic microorganisms however silver nanoparticles are not very effective against viruses and especially against spores.⁵⁵

In the present work, we have evaluated the silver nanoparticles solutions both in black and in green tea against the Gram-negative bacterium *Pseudomonas Aeruginosa*. The test was conducted following the standard procedure UNI EN 1040 and the test results are summarized in Table 5. As expected, both silver nanoparticles solutions in black and in green tea infusion are effective toward *P. Aeruginosa*: even at the highest dilution adopted 1:100 the ufc was <10 with 15 min contact time. It is important also to emphasize that tea polyphenols are recognized antimicrobial agents.⁵⁶ In particular epigallocatechin gallate and epicatechin gallate are reported to be the most effective agents.⁵⁶ Synergistic effects of tea polyphenols with antibiotics were also reported.⁵⁶ In our specific case it possible synergistic effects between the silver nanoparticles and the tea polyphenols could be expected. Tea polyphenols are also effective antiviral agents⁵⁶ and may compensate the lower activity of

silver against viruses when combination of silver nanoparticles and tea infusion are used. Finally, it has also been demonstrated that tea polyphenols are effective against fungi and molds and their combination with silver should be certainly synergistic.⁵⁶

Particularly interesting is the activity of tea polyphenols against *Clostridium* and *Bacillus* spores. Spores are known to be extremely resistant toward antimicrobial and disinfecting agents and indeed silver is not effective against them. After incubation with tea polyphenols, *C. Botulinum* and *C. Butyricum* spores were decreased in number while no effect was shown in *Bacillus Cereus* spores.⁵⁶ As shown in Table 6, our silver nanoparticles solutions in black and green tea infusions were tested against the *Bacillus Subtilis* spores. Notwithstanding the good premises the experimental data show that silver nanoparticles either in black tea infusion or in green tea infusion are not effective together with tea polyphenols against the *Bacillus Subtilis* spores. Even the neat silver nanoparticles solutions and 15 min contact time are not effective against the spores.

Conclusions

Simple tea infusions from black tea, green tea and even from decaffeinated tea are able to reduce silver ions into silver nanoparticles which remain suspended into the infusions because the tea polyphenols act both as reducing agents and capping agents of the resulting colloidal silver.

The kinetics of silver reduction in black tea and in green tea was determined spectrophotometrically by monitoring the growth in intensity of the surface plasmon resonance band of silver nanoparticles. A pseudofirst order rate

constant of $k_{\text{black}} = 9.44 \times 10^{-4} \text{ s}^{-1}$ was determined on black tea infusion and of $k_{\text{green}} = 8.9 \times 10^{-3} \text{ s}^{-1}$ in the case of green tea infusion. The molar extinction coefficient of the surface plasmon resonance band of silver nanoparticles was also determined in black and green tea infusions and compared with that determined on silver nanoparticles in tannin and on commercial silver proteinate for comparison.

A direct determination of the particle size distribution and the average diameter of the silver nanoparticles both in black and in green tea infusions was obtained by dynamic light scattering (DLS) measurements. Silver nanoparticles show a narrower distribution in green tea with an average diameter of 20.8 nm. The distribution of the silver particles size results broader in black tea with an average diameter of 78.7 nm. For comparison the silver nanoparticles in tannin exhibit an average diameter of 55.7 nm.

The stability of silver nanoparticles colloidal dispersions in both black and green tea infusions was determined with DLS measurements through the Z-potential value. The experimental results show that the silver nanoparticles in tea infusions exhibit a more than satisfactory long term stability and in any case comparable to Z-potential value measurable on silver nanoparticles produced with tannin. This result confirms that the tea polyphenols act simultaneously as reducing agents of silver ions and as capping agent of the resulting nanoparticles stabilizing the resulting colloidal suspension.

The bactericidal properties of silver nanoparticles in both black and green tea infusions were confirmed on the Gram(-) bacterium *P. Aeruginosa*. Instead, the silver nanoparticles in both black and green tea infusions are not effective against the spores of *B. Subtilis*.

References

- Krutyakov, Y.A., Kudrinskiy, A. A., Olenin, A.Y., Lisichkin, G. V. *Russian Chem. Rev.* **2008**, 77, 233.
- Nath, D., Banerjee, P., *Environ. Toxicol. Pharmacol.* **2013**, 36, 997.
- Ravindran, A., Chandran, P., Khan, S.S., *Colloids Surf.B: Biointerfaces* **2013**, 105, 342.
- Sharma, V.K., Yngard, R.A., Lin, Y., *Adv. Colloid Interface Sci.* **2009**, 145, 83.
- Abou El-Nour, K.M..M., Eftaiha, A., Al-Warthan, A., Ammar, R.A.A., *Arabian J. Chem.* **2010**, 3, 135.
- Tolaymat, T.M., El Badawy, A.M., Genaidy, A., Scheckel, K.G., Luxton, T.P., Suidan, M., *Sci. Total Environ.* **2010**, 408, 999.
- Moritz, M. Geszke-Moritz, M. *Chem. Engin. J.* **2013**, 228, 596.
- Mittal, A. K., Chisti, Y., Banerjee, U.C., *Biotechnology Adv.* **2013**, 31, 346.
- Sharma, T. K., Chopra, A., Sapra, M., Kumawat, D., Patil, S.D., Pathania, R., Navani, N.K., *Int. J. Green Nanotech.*, **2012**, 4, 1.
- Roy, N., Gaur, A., Jain, A., Bhattacharya, S., Rani, V., *Environ. Toxicol. Pharmacol.*, **2013**, 36, 807.
- Kharisova, O.V., Dias, H.V.R., Kharisov, B.I., Olvera Perez, B., Perez, V.M.J., *Trends in Biotechnology*, **2012**, 31, 240.
- Cataldo, F., Ursini, O., Angelini, G., *European Chemical Bulletin* **2013**, 2, 700.
- Jha, A.K., Prasad, K., *Int. J. Green Nanotech.: Phys. Chem.*, **2010**, 1, 110.
- Guidelli, E.J., Ramos, A.P., Zanicuelli, M.E.D., Baffa, O., *Spectrochim. Acta Part A* **2011**, 82, 140.
- Ghaseminezhad, S.M., Hamed, S., Shojaosadati, S.A. *Carbohydrate Polym.* **2012**, 89, 467.
- Dipankar, C., Murugan, S., *Colloids Surfaces B: Biointerfaces* **2012**, 98, 112.
- Bankura, K.P., Maity, D., Mollick, M.M.R, Mondal, D., Bhowmick, B., Bain, M.K., Chakraborty, A., Sarkar, J., Acharya, K., Chattopadhyay, D., *Carbohydrate Polym.* **2012**, 89, 1159.
- Pandey, S., Goswami, G.K., Nanda, K.K., *Int. J. Biol. Macromol.*, **2012**, 51, 583.
- El-Rafie, H.M., El-Rafie, M.H., Zahran, M.K., *Carbohydrate Polym.* **2013**, 96, 403.
- Prakash, P., Gnanaprakasam, P., Emmanuel, R., Arokiyaraj, S., Saravanan, M., *Colloids Surfaces B: Biointerfaces* **2013**, 108, 255.
- Rao, Y.S., Kotakadi, V.S., Prasad, T.N.V.K.V., Reddy, A.V., Sai Gopal, D.V.R. *Spectrochim. Acta Part A* **2013**, 103, 156.
- Kanmani, P., Lim, S.T., *Carbohydrate Polym.* **2013**, 97, 421.
- Barua, S., Konwarh, R., Bhattacharya, S.S., Das, P., Devi, K.S.P., Maiti, T.K., Mandal, M., Karak, N., *Colloids Surfaces B: Biointerfaces* **2013**, 105, 37.
- Sen, I.K., Mandal, A.K., Chakraborty, S., Dey, B., Chakraborty, R., Islam, S.S., *Int. J. Biol. Macromol.*, **2013**, 62, 439.
- Bharali, P., Saikia, J.P., Paul, S., Konwar, B.K. *Int. J. Biol. Macromol.*, **2013**, 61, 238.
- Steglich, W, Fugmann, B., Lang-Fugmann, S.(eds.) "Rompp Encyclopedia of Natural Products", Georg Thieme Verlag, Stuttgart **2000**, 630.
- Budavari, S. (ed.) "The Merck Index", 12th Ed. Merck Research Laboratories, Whitehouse Station, **1996**, 9221.
- Ajitha, B., Reddy, Y. A. K., Reddy, P.S., *Spectrochim. Acta Part A* **2014**, 121, 164.
- Ashokkumar, S., Ravi, S., Kathiravan, V., Velmurugan, S., *Spectrochim. Acta Part A* **2014**, 121, 88.
- Xu, W., Jin, W., Lin, L., Zhang, C., Li, Z., Li, Y., Song, R., Li, B., *Carbohydrate Polym.* **2014**, 101, 961.
- Reddy, N.J., Vali, D.N., Rani, M., Rani, S.S., *Mater. Sci. Engin. C* **2014**, 34, 115.
- Vimala, K., Varaprasad, K., Sadiku, R., Ramam, K., Kanny, K., *Int. J. Biol. Macromol.*, **2014**, 63, 75.
- Vilchis-Nestor, A.R., Sánchez-Mendieta, V., Camacho-López, M.A., Gómez-Espinosa, R.M., Arenas Alatorre, J.A., *Mater. Lett.* **2008**, 62, 3103.
- Moulton, M.C., Braydich-Stolle, L.K., Nadagouda, M.N., Kunzelman, S., Hussain, S.M., Varma, R.S. *Nanoscale* **2010**, 2, 763.
- Vaseeharan, B., Ramasamy, P., Chen, J.C., *Lett. Appl. Microbiol.* **2010**, 50, 352.
- Kamal, S. S. K., Sahoo, P.K., Vimala, J., Premkumar, M., Ram, S., Durai, L., *Acta Chim. Slov.* **2010**, 57, 808.
- Moulton, M.C., Braydich-Stolle, L.K., Nadagoud, M.N., Kunzelman, S., Hussain, S.M., Varma, S.R., *Nanoscale*, **2010**, 2, 763.
- Loo, Y.Y., Chieng, B.W., Nishibuchi, M., Radu, S., *Int. J. Nanomedicine* **2012**, 7, 4263.
- Uddin, M.J., Chaudhuri, B., Pramanik, K., Middyac, T.R., Chaudhuri, B., *Mater. Sci. Engin. B* **2012**, 177, 1741.

- ⁴⁰Özyürek, M., Güngör, N., Baki, S., Güçlü, K., Apak, R., *Anal. Chem.* **2012**, *84*, 8052.
- ⁴¹Chandra, G.K., Tripathy, D.R., Dasgupta, S., Roy, A. *Appl. Spectrosc.* **2012**, *66*, 744.
- ⁴²Yu. A. Mirgorod, V. G. Borodina, *Inorg. Mater.* **2013**, *49*, 980.
- ⁴³M. Zou, M. Du, H. Zhu, C. Xu, N. Li, Y. Fu, *Polym. Engin. Sci.* **2013**, *53*, 1099.
- ⁴⁴Y. H. Hui, "Encyclopedia of Food Science and Technology", Wiley, New York, **1992**, 2292.
- ⁴⁵Sang, S., Lambert, J.D., Ho, C.T., Yang, C.S., *Pharmacol. Research* **2011**, *64*, 87.
- ⁴⁶Stodt, U., Engelhardt, U.H., *Food Research Int.*, **2013**, *53*, 636.
- ⁴⁷Kuhnert, N., *Archives Biochem. Biophys.* **2010**, *501*, 37.
- ⁴⁸Luczaj, W., Skrzydlewska, E., *Preventive Medicine* **2005**, *40*, 910.
- ⁴⁹Polovka, M., Brezova, V., Stasko, A., *Biophysical Chem.* **2003**, *106*, 39.
- ⁵⁰Morsy, M.A., Khaled, M.M., *Spectrochimica Acta Part A* **2002**, *58*, 1271.
- ⁵¹Carlioni, P., Tiano, L., Padella, L., Bacchetti, T., Customu, C., Kay, A., Damiani, E., *Food Research Int.* **2013**, *53*, 900.
- ⁵²Ananingsih, V.K., Sharma, A., Zhou, W., *Food Research Int.* **2013**, *50*, 469.
- ⁵³Greenwood, R., Kendall, K., *J. Eur. Ceramic Soc.* **1999**, *19*, 479.
- ⁵⁴Hanaor, D.A.H., Michelazzi, M., Leonelli, C., Sorrell, C.C., *J. Eur. Ceramic Soc.* **2012**, *32*, 235.
- ⁵⁵Wikipedia: http://en.wikipedia.org/wiki/Oligodynamic_effect
- ⁵⁶Bansal, S., Choudhary, S., Sharma, M., Kumar, S.S., Lohan, S., Bhardwaj, V., Syan, N., Jyoti, S., *Food Research Int.* **2013**, *53*, 568.

Received: 16.01.2014.

Accepted: 18.02.2014.



PYRIDAZINE AND ITS RELATED COMPOUNDS. PART 16.¹
SYNTHESIS AND SOME REACTIONS OF 3-HYDRAZINO-1*H*-
PYRAZOLO[3,4-*c*]PYRIDAZINE

Ali Deeb,^{[a]*} Mohamed Fouad Zayed,^[b] Atef Amer^[a] and Ahmed Ali^[b]

Keywords: 3-Hydrazino-1*H*-pyrazolo[3,4-*c*]pyridazine derivatives; biological activity; 1,2,4-triazole and triazine derivatives;

The reaction of 3-hydrazino derivative **1** with phenyl isothiocyanate afforded the corresponding thiocarbamoylhydrazine. Subsequent ring closure in basic medium yielded the 1,2,4-triazolo derivative **3**. Condensation of **1** with ethyl chloroformate produced N'-diethoxycarbonyl derivative **4**. Condensation with *p*-nitrobenzaldehyde, with a number of monosaccharides and with pyruvic acid, compound **1** afforded the respective hydrazones **5a-g**. Cyclodehydration of **5a** and **5e** gave the corresponding triazolo and triazine derivatives **6** and **7** respectively. Heating **1** and α -dicarbonyl compounds gave the tricyclic pyridazinopyrazolotriazines **8a-c**. Reaction of **1** with diethyl oxalate gave triazinedione **9**. The hydrazine **1** cyclized with active methylene compounds to produce the corresponding pyrazolyl derivatives and some related compounds are described.

* Corresponding Authors

E-Mail: dralideeb@hotmail.com

[a] Department of Chemistry, Faculty of Science, Zagazig University, Egypt.

[b] Laboratory of Photochemistry, National Research Center,
Dokki, Giza, Egypt.

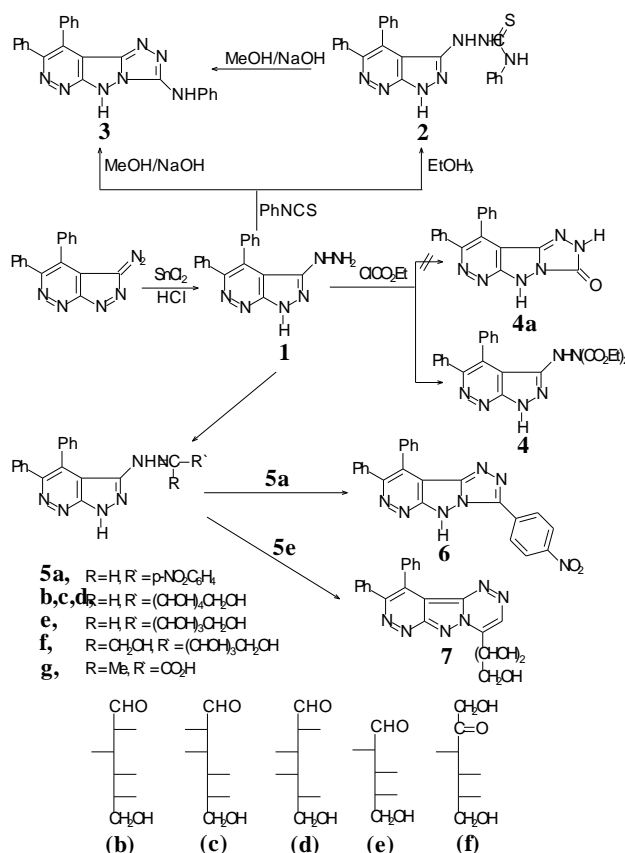
INTRODUCTION

Pyridazine and related compounds find wide application in different biological and medicinal fields.²⁻⁴ Also a good deal of important is being given to pyrazole, triazole, triazine and their derivatives due to their wide use in medicinal chemistry.⁵⁻⁷ Hence, it was thought that the incorporation of the latter heterocyclic moieties into pyridazines moiety might modify their biological activity.

RESULTS AND DISCUSSION

The present investigation which is in continuation of our previous work on 3-diazopyrazolo[3,4-*c*]pyridazine, deals with the synthesis of different 3-substituted heterocycles pyridazines.⁸ For this purpose 3-hydrazino-4,5-diphenyl-1*H* pyrazolo[3,4-*c*]pyridazine **1** was prepared in 54 % yield as white crystals (m.p. 162-163 °C) by addition of stannous chloride in portion-wise to a solution of 3-diazo-4,5-diphenylpyrazolo[3,4-*c*]pyridazine⁹ in conc. HCl at room temperature. The process is quick and is readily carried out in a beaker or open flask. The reaction progress was completed until no diazo compound could be detected by t.l.c. as well as no coupling colour with β-naphthol, its structure was assigned on the basis of analytical and spectral data. The infrared spectrum revealed the presence of NH₂ group at 3420, 3325, NH group at 3260, 1630 (C=N) and 1550 cm⁻¹ (C=C), and no absorption referred to diazo group. ¹H-NMR spectrum showed the presence of broad singlet at □ 4.00 (NH), broad singlet at 6.00 (NH₂), broad singlet at 12.6 attributed to the NH pyrazole and multiplet at 7.00-7.40 ppm for 10 H (2 Ph).

The reaction of the hydrazine **1** with phenyl isothiocyanate in boiling ethanol afforded the corresponding thiocarbamoylhydrazine (**2**) in 68.2% yield, while in boiling 2*N* methanolic sodium hydroxide afforded, unexpectedly a single product. The isolated product was proven to be identical with N,8,9-triphenyl-5*H*-[1,2,4]triazolo[4',3':1,5]pyrazolo[3,4-*c*]pyridazin-3-amine **3**.



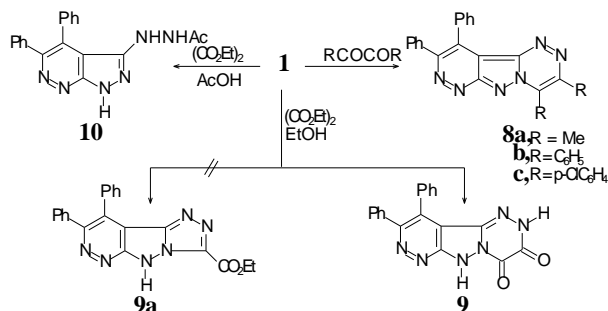
Scheme 1.

Mechanistically, the formation of **3** from **1** involves the initial formation of **2** which undergoes immediate intramolecular nucleophilic attack of ring-2 nitrogen on the thione group with elimination of H₂S. This mechanism was proved by converting **2** to **3** upon boiling in methanolic sodium hydroxide. However, the isolation of **2** from the reaction of **1** and phenyl isothiocyanate in boiling ethanol indicates that **2** is thermostable at the boiling point of ethanol. The structures of compounds **2** and **3** were inferred from analytical and spectral data.

Compound **1** reacted with ethyl chloroformate at refluxed temperature produced 2-(4,5-diphenyl-1*H*-pyrazolo[3,4-*c*]pyridazin-3-yl)hydrazine-1,1-dicarboxylate **4** instead of anticipated product triazolopyrazolopyridazine **4a**. The structure of **4** is supported by its elemental analysis and spectral data. The infrared spectrum showed NH groups at 3428, 3310, and C=O ester at 1749 cm⁻¹, the mass spectrum showed molecular ion peaks at *m/z*: 446.

Treatment of compound **1** with *p*-nitrobenzaldehyde in refluxed ethanol gave the corresponding hydrazones **5a**, also the condensation with aldoses namely D-glucose, D-mannose, D-galactose and D-arabinose gave the corresponding hydrazone **5b-e** in a good yield. Similarly, the reaction of **1** with D-fructose gave the hydrazone **5f**. The hydrazones **5a** and **5e** subsequently undergo oxidative cyclization to give the corresponding triazolopyrazolopyridazine **6** and pyridazinopyrazolotriazine **7**, respectively. Condensation of compound **1** with pyruvic acid in refluxing acetic acid gave 2-(4,5-diphenyl-1*H*-pyrazolo[3,4-*c*]pyridazin-3-yl)hydrazonopropionic acid **5g** (Scheme 1).

The reaction of **1** with α -dicarbonyl compounds was assumed to involve one or both of the carbonyl groups in the condensation. Thus, heating equimolar amounts of **1** and diacetyl, benzil and/or *p,p'*-dichlorobenzil in ethanol undergo cyclodehydration to give the tricyclic pyridazinopyrazolotriazines **8a-c**. Mechanistically the formation of the tricyclic compounds **8a-c** involves, the initial formation the corresponding monohydrazone which undergo immediate intramolecular nucleophilic attack of ring-2 nitrogen on the other carbonyl group with elimination of water molecule. Attempts to isolate acyclic monohydrazone intermediate for these reactions were unsuccessful.



Scheme 2

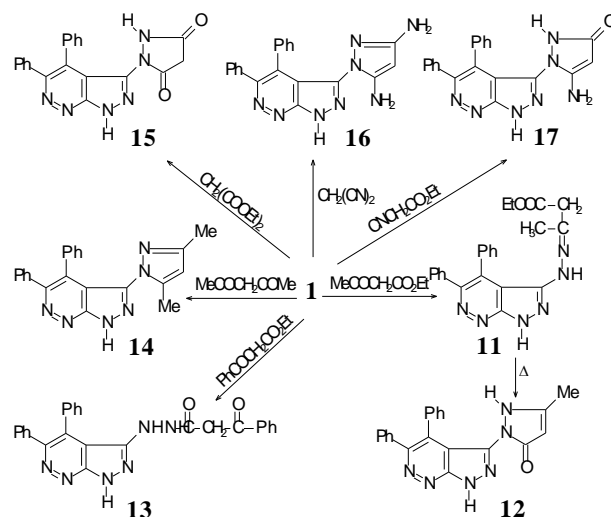
Treatment of compound **1** with diethyl oxalate in refluxing glacial acetic acid, the product isolated in 58 % yield was not the expected pyridazinopyrazolotriazinedione **9** nor triazolopyrazolopyridazine carboxylic ester **9a**, but

instead N'-(4,5-diphenyl-1*H*-pyrazolo[3,4-*c*]pyridazin-3-yl)acetohydrazide **10** as evidenced by the analytical and spectral data.

In order to confirm the effect of the solvent on the nature of the product, an attempt was made to react with the hydrazino compound **1** with glacial acetic acid at refluxed temperature. The isolated product was proved to be identical in every respect with **10**. On the other hand, reacting **1** with diethyl oxalate in boiling ethanol yielded the corresponding 9,10-diphenylpyridazino[3',4':3,4]pyrazolo[5,1-*c*][1,2,4]triazine-3,4(2*H*,6*H*)-dione **9** instead of anticipated product triazolopyrazolopyridazine carboxylic ester **9a**. The assignment of structure **9** was based on analytical and spectral data.

Among the reactions of hydrazinopyrazolopyridazine **1**, the reaction with active methylene reagents is the most useful for synthetic purposes.

Condensation of compound **1** with ethyl acetoacetate in refluxing ethanol gave ethyl 3-(2-(4,5-diphenyl-1*H*-pyrazolo[3,4-*c*]pyridazin-3-yl)hydrazono)butanoate **11**, which when heated in glacial acetic acid, undergoes cyclohydration to give pyrazolone derivative **12** (Scheme 3).

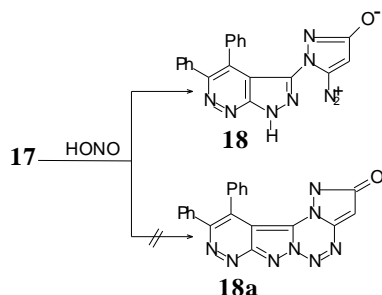


Scheme 3

The structure of **11** and **12** are supported by their analytical and spectral data. We have found that compound **1** reacts with ethyl benzoylacetate in glacial acetic acid at refluxed temperature gave benzoylacetate acid hydrazide derivative **13** in 47 % yield, all attempts for cyclization of compound **11** were unsuccessful. In the same manner an ethanolic solution of **1**, when treated with acetylacetone formed easily the corresponding pyrazole derivative **14**.

Reaction of hydrazine **1** with diethyl malonate, the isolated product was proven to be 1-(4,5-diphenyl-1*H*-pyrazolo[3,4-*c*]pyridazin-3-yl)pyrazolidine-3,5-dione, **15**. Similarly, treatment of compound **1** with malononitrile in ethanol at reflux temperature gave the corresponding diaminopyrazole derivative **16**. lastly treatment of **1** with ethyl cyanoacetate in glacial acetic acid gave the corresponding aminopyrazolone derivative **17**. The formation of **17** is supported by its infrared, mass and

elemental analyses. The diazotization of aminopyrazolone derivative **17** with sodium nitrite in acetic acid at room temperature, yellow crystals deposited during the reaction time, as a single product. The isolated product was proven to be 1-(4,5-diphenyl-1H-pyrazolo[3,4-c]pyridazin-3-yl)pyrazole-5-diazonium-3-olate **18** instead of the tetracyclic condensed system **18a**. The data used to characterize of all the compounds prepared are given under experimental.



Scheme 4

EXPERIMENTALS

Melting points were determined on a Büchi 510 apparatus and are reported uncorrected. IR spectra were recorded as potassium bromide disks on a Perkin-Elmer 383 spectrophotometer. ¹H-NMR spectra were obtained on a Bruker Ac 200 F instrument. Mass spectra were obtained at 70eV by using a AEI MS: 30 mass spectrometer. All reactions were monitored by thin layer chromatography, carried out on 0.2 mm silica gel 60 F-254 (Merck) plates using U.V. light (254 and 366 nm).

3-Hydrazino-4,5-diphenyl-1H-pyrazolo[3,4-c]pyridazine, 1

To a stirred solution of 3-diazo-4,5-diphenylpyrazolo[3,4-c]pyridazine (0.6 g, 2 mmol) in concd. hydrochloric acid (5 mL), stannous chloride (2 g, 10 mmol) was added in portions. The reaction mixture was left over night and the solution was neutralized with 10 % aq. Na₂CO₃ followed by extracted with chloroform (3×20 mL). The extracts were collected, dried (MgSO₄) and evaporated under reduced pressure. The solid residue was recrystallized from ethanol, (0.33g, 54 %), m.p. 162-163 °C. IR: 3420, 3325 (NH₂), 3260 (NH), 1630, 1550 cm⁻¹; ¹H-NMR (DMSO-d₆): δ 12.6 (br s, 1H, NH, pyrazole), 7.00-7.40 (m, 10H, 2Ph), 6.00 (br s, 2H, NH₂) and 4.00 (br s, 1H, NH). Anal. Calcd for C₁₇H₁₄N₆: C, 67.53; H, 4.67; N, 27.80. Found: C, 67.40; H, 4.50; N, 27.70.

2-(4,5-Diphenyl-1H-pyrazolo[3,4-c]pyridazin-3-yl)-N-phenylhydrazinecarbothioamide, 2

To a solution of compound **1** (0.5 g, 1.7 mmol) in ethanol (15 mL) phenyl isothiocyanate (0.25 g, 1.9 mmol) was added. The reaction mixture was refluxed for 20 h. The solvent was evaporated under reduced pressure; the residue was washed with pet. ether 40-60 °C. A light yellow product was obtained recrystallized from methanol gave pure product in a yield (0.2 g, 68.2 %), m.p. 285-286 °C; IR: 3440, 3198 (NH), 3058 (CH, aromatic), 2922, 2852 (CH, aliphatic), 1599 (C=N) and 1447, 1321, 1229, 1178 cm⁻¹; MS: *m/z*: 438 (M⁺+ 1, 13.2 %), 313 (M⁺- S, NHPh, 4.4 %), 286 (M⁺- NH(C=S)NHPh, 3.3 %), 271 (M⁺-

NHNH(C=S)NHPh, 7.2 %). Anal. Calcd for C₂₄H₁₉N₇S: C, 65.88; H, 4.37; N, 22.42. Found: C, 65.70; H, 4.20; N, 22.50.

N,8,9-Triphenyl-5H-[1,2,4]triazolo[4',3':1,5]pyrazolo[3,4-c]pyridazin-3-amine, 3

Method A: A solution of compound **1** (0.5 g, 1.7 mmol) and phenyl isothiocyanate (0.25 g, 1.9 mmol) in methanolic sodium hydroxide (30 mL, 20%) was refluxed for 6 h. The cooled reaction mixture was filtered and the filtrate was evaporated, the residue was dissolve in water (25 mL) and acidification with 3N hydrochloric acid. The precipitate was filtered, washed with water, dried and recrystallized from methanol, (0.15 g, 54.2%), m.p. 175-176 °C. IR: 3425, 3190 (NH), 3057 (CH, aromatic), 1635 (C=N), and 1459, 1446, 1379, 1237 cm⁻¹; MS: *m/z*: 405 (M⁺+2, 15.7%), 286 (M⁺- N=CNPh, 88.7%, ion A), 256 (ion A-N₂H₂, 10.7%). Anal. Calcd for C₂₄H₁₇N₇: C, 71.45; H, 4.25; N, 24.31. Found: C, 71.30; H, 4.10; N, 24.20.

Method B: A solution of compound **2** (0.5 g, 1.1 mmol) in methanolic sodium hydroxide (30 mL, 20 %) was refluxed for 6 h., the same work-up as in method A, gave (0.15 g, 54.2 %) of **3**. It was identical with that prepared by method A.

2-(4,5-Diphenyl-1H-pyrazolo[3,4-c]pyridazin-3-yl)hydrazine-1,1-dicarboxylate, 4

A mixture of compound **1** (0.5 g, 1.7 mmol) and ethyl chloroformate (5 mL) was refluxed for 3 h. The cooled reaction mixture was poured onto water (50 mL). The separated solid product was filtered, dried and recrystallized from ethanol, (0.4 g, 64.5%), m.p. 130-131 °C; IR: 3428, 3310 (NH), 3060 (CH, aromatic), 2983, 2930 (CH, aliphatic), 1749 (C=O ester), 1633 (C=N) and 1445, 1406, 1307, 1257 cm⁻¹; MS: *m/z*: 446 (M⁺, 16.6 %), 401 (M⁺- OEt, 3.6 %), 374 (M⁺- COOEt, 8.2%), 287 (M⁺-N(COOEt)₂, 100 %), 271 (M⁺- NHN(COOEt)₂, 49.6%). Anal.: Calcd for C₂₃H₂₂N₆O₄: C, 61.87; H, 4.98; N, 18.83. Found: C, 61.70; H, 5.00; N, 18.70.

2-(4-Nitrobenzylidene)hydrazinyl-4,5-diphenyl-1H-pyrazolo[3,4-c]pyridazine 5a

To a solution of compound **1** (0.2 g, 0.66 mmol) in ethanol (15 mL), *p*-nitrobenzaldehyde (0.1 g, 0.66 mmol) was added. The reaction mixture was refluxed for 5 h. Upon cooling the solid product was filtered and recrystallized from ethanol, (0.2 g, 69.4 %), m.p. 252-253 °C; IR: 3322, 3151 (NH), 3083 (CH, aromatic), 2971, 2848 (CH, aliphatic), 1604 (C=N), 1516, 1340 (NO₂), and 1155, 1107 cm⁻¹; MS: *m/z*: 435 (M⁺, 30.4 %), 419 (M⁺- O, 6.1 %), 403 (M⁺-O₂, 2.4 %), 286 (M⁺- N=CH-C₆H₄NO₂, 100 %), 271 (M⁺-NHN=CH-C₆H₄-NO₂, 14.1 %). Anal. Calcd for C₂₄H₁₇N₇O₂: C, 66.19; H, 3.94; N, 22.52. Found: C, 66.00; H, 4.00; N, 22.60.

3-(Aldosehydrazono)-4,5-diphenyl-1H-pyrazolo[3,4-c]pyridazine

General procedure: A mixture of compound **1** (0.5 g, 1.7 mmol) and aldose namely: D-glucose, D-mannose, D-

galactose, and D-arabinose (1.8 mmol) was refluxed in absolute ethanol (10 ml) contain few drops of acetic acid for 3 h. Upon cooling, the precipitated product was filtered off, dried and recrystallized from ethanol.

3-(D-Glucosehydrazono)-4,5-diphenyl-1H-pyrazolo[3,4-c]pyridazine, 5b.

Yield: 69.1 %; m.p. 170-171 °C; IR: 3375 (OH), 3209 (NH), 3060 (CH, aromatic), 2922, 2854 (CH, aliphatic), 1564 (C=N) and 1449, 1397, 1312 cm⁻¹. Anal. Calcd for C₂₃H₂₄N₆O₅: C, 59.47; H, 5.21; N, 18.09. Found: C, 59.30; H, 5.00; N, 17.90.

3-(D-Mannosehydrazono)-4,5-diphenyl-1H-pyrazolo[3,4-c]pyridazine, 5c.

Yield 71 %; m.p. 168-169 °C; IR: 3450 (OH), 3204 (NH), 3060 (CH, aliphatic), 2922 (CH, aliphatic), 1565 (C=N) and 1487, 1426, 1396, 1316 cm⁻¹. Anal. Calcd for C₂₃H₂₄N₆O₅: C, 59.47; H, 5.21; N, 18.09. Found: C, 59.60; H, 5.10; N, 17.80.

3-(D-Galactosehydrazono)-4,5-diphenyl-1H-pyrazolo[3,4-c]pyridazine, 5d.

Yield 69.1 %; m.p. 185-186 °C; IR: 3374 (OH), 3208 (NH), 3060 (CH, aliphatic), 2922, 2854 (CH, aliphatic), 1564 (C=N), and 1487, 1427, 1397, 1115 cm⁻¹. Anal. Calcd for C₂₃H₂₄N₆O₅: C, 59.47; H, 5.21; N, 18.09. Found: C, 59.10; H, 4.90; N, 17.80.

3-(D-Arabinosehydrazono)-4,5-diphenyl-1H-pyrazolo[3,4-c]pyridazine, 5e.

Yield 65.1 %; m.p. 220-221 °C, IR: 3350 (OH), 3195 (NH), 3050 (CH, aromatic), 2922, 2850 (CH, aliphatic), 1560 (C=N) and 1490, 1443, 1315 cm⁻¹. Anal. Calcd for C₂₂H₂₂N₆O₄: C, 60.81; H, 5.10; N, 19.34. Found: C, 60.70; H, 4.90; N, 19.50.

3-(D-Fructosehydrazono)-4,5-diphenyl-1H-pyrazolo[3,4-c]pyridazine, 5f.

To a solution of compound **1** (0.5 g, 1.7 mmol) in absolute ethanol (15 mL), D-fructose (0.3 g, 1.7 mmol) and few drops of acetic acid were added. The reaction mixture was refluxed for 5 h., the solvent was evaporated under reduced pressure. The residue was washed with water several times, dried and recrystallized from ethanol, (0.21 g, 76.9 %), m.p. 229-230 °C; IR: 3382 (OH), 3150 (NH), 3059 (CH, aromatic), 2918, 2849 (CH, aliphatic), 1618 (C=N) and 1547, 1471, 1445, 1378, 1337 cm⁻¹. Anal. Calcd for C₂₃H₂₄N₆O₅: C, 59.47; H, 5.21; N, 18.09. Found: C, 59.20; H, 5.30; N, 18.30.

3-(4-Nitrophenyl)-8,9-diphenyl-5H-[1,2,4]-triazolo[4',5':5,1]pyrazolo-[3,4-c]pyridazine, 6

A solution of compound **5a** (0.5 g, 1.5 mmol) in glacial acetic acid (10 mL), was treated with bromine (0.1 g, 6.3

mmol) in glacial acetic acid (1 mL) and stirred at room temperature for 30 minutes. The reaction mixture was poured into water (100 mL), the precipitated product was filtered, dried and recrystallized from ethanol, (0.3 g, 60.3 %), m.p. 283-284 °C; IR: 3410 (NH), 3092 (CH aromatic), 1599 (C=N), 1513, 1341 (NO₂) and 1478, 1443, 1388, 1202 cm⁻¹. Anal. Calcd for C₂₄H₁₅N₇O₂: C, 66.50; H, 3.49; N, 22.63. Found: C, 66.60; H, 3.30; N, 22.70.

1-(9,10-Diphenylpyridazino[3',4':3,4]pyrazolo[5,1-c][1,2,4]triazin-4-yl)propane-1,2,3-triole, 7

A solution of compound **5e** (0.2 g, 0.46 mmol) in glacial acetic acid (15 mL), was treated with bromine (0.1 g, 6.3 mmol) in glacial acetic acid (1 mL). The reaction mixture was refluxed for 5 h. The solid product, which separated out on cooling was filtered off, washed with water, dried and recrystallized from ethanol, (0.15 g, 55.6 %), m.p. 180-181 °C; IR: 3350 (OH), 2195 (NH), 3050 (CH, aromatic), 2922, 2850 (CH, aliphatic), 1660 (C=N) and 1490, 1443, 1315 cm⁻¹; MS: *m/z* 413 (M⁺- 1, 1 %), 412 (M⁺- 2, 1.8 %), 287 (M⁺- NCH=C(CHOH)-CH₂OH, 100 %), 271 (M⁺- N=NCH=C(CHOH)CH₂OH, 69.1 %). Anal. Calcd for C₂₂H₁₈N₆O₃: C, 63.76; H, 4.38; N, 20.28. Found: C, 63.80; H, 4.40; N, 20.00.

2-(4,5-Diphenyl-1H-pyrazolo[3,4-c]pyridazin-3-yl)hydrazono-propionic acid, 5g

A solution of compound **1** (0.5 g, 1.7 mmol) in glacial acetic acid (25 mL) was treated with pyruvic acid (0.15 g, 1.7 mmol). The reaction mixture was refluxed for 6 h. Upon cooling the precipitated product was filtered off and recrystallized from ethanol, (0.4 g, 64.9 %), m.p. > 300 °C; IR: 3333, 3202 (NH), 3060 (CH, aromatic), 2922, 2852 (CH, aliphatic), 1671 (C=O), 1622 (C=N) and 1568, 1446, 1379, 1323, 1212 cm⁻¹; MS: *m/z*: 372 (M⁺, 3.6%), 371 (M⁺-1, 3.6 %), 287 (M⁺-N=C(Me)CO₂H, 13.2 %), 286 (M⁺-(1+N=C(Me)CO₂H), 10.4 %), 271 (M⁺- NHN=C(Me)CO₂H, 100 %). Anal. Calcd for C₂₀H₁₆N₆O₂: C, 64.50; H, 4.33; N, 22.57. Found: C, 64.40; H, 4.40; N, 22.60.

Reaction of 3-Hydrazino-4,5-diphenyl-1H-pyrazolo[3,4-c]pyridazine **1 with α-Dicarbonyl compounds**

General procedure: A solution of compound **1** (0.5 g, 1.7 mmol) in absolute ethanol (20 ml) was treated with α-dicarbonyl compounds (1.7 mmol) namely diacetyl, benzil and/or *p,p'*-dichlorobenzil. The reaction mixture was refluxed for 8 h, 5 h and 5 h respectively. Upon cooling the precipitated product was filtered off and recrystallized from ethanol.

3,4-Dimethyl-9,10-diphenylpyridazino[3',4':3,4]pyrazolo[5,1-c]-1,2,4-triazine, 8a.

Yield (0.5 g, 42.8 %); m.p. > 300 °C; IR: 3090 (CH, aromatic), 2924, 2853 (CH, aliphatic), 1600 (C=N) and 1444, 1310, 1129, 1024 cm⁻¹; MS: *m/z*: 352 (M⁺, 47.9 %), 351 (M⁺-1, 29.9 %), 271 (M⁺- N=N-C(Me)=C(Me), 12.4 %). Anal. Calcd for C₂₁H₁₆N₆: C, 71.57; H, 4.58; N, 23.85. Found: C, 71.70; H, 4.00; N, 23.70.

3,4,9,10-Tetraphenylpyridazino[3',4':3,4]pyrazolo[5,1-c]-1,2,4-triazine, 8b.

Yield (0.3 g, 33.3 %); m.p. > 300 °C; IR: 3092 (CH, aromatic), 1645 (C=N), and 1449, 1380, 1112 cm⁻¹. MS: *m/z* 476 (M⁺, 100 %), 475 (M⁺-1, 35.8 %), 447 (M⁺-N₂, 7.3 %), 270 (M⁺-N=NC(Ph)=C(Ph), 10.8 %). Anal. Calcd for C₃₁H₂₀N₆: C, 78.13; H, 4.23; N, 17.64. Found: C, 78.00; H, 4.10; N, 17.50.

3,4-Bis(4-chlorophenyl)-9,10-diphenylpyridazino[3',4':3,4]pyrazolo[5,1-c][1,2,4]triazine, 8c.

Yield (0.5 g, 55.4 %), m.p. > 300 °C; IR: 3082 (CH, aromatic), 1640 (C=N) and 1444, 1380, 1240, 1128 cm⁻¹; MS: *m/z* 545 (M⁺, 41.1%), 544 (M⁺-1, 72.5), 517 (M⁺-N₂, 6.6 % ion A), 406 (ion A - ClC₆H₄, 4.6 %), 271 (M⁺-N=N-C(Ar)=C(Ar), 8.4%). Anal. Calcd for C₃₁H₁₈Cl₂N₆: C, 68.27; H, 3.33; N, 15.41. Found: C, 68.10; H, 3.20; N, 15.30.

N'-(4,5-Diphenyl-1H-pyrazolo[3,4-c]pyridazin-3-yl)acetohydrazide, 10

A solution of compound **1** (0.5 g, 1.7 mmol) in glacial acetic acid (15 mL) was refluxed for 8 h. The cooled reaction mixture was poured onto water (100 mL). The separated solid product was filtered off, dried and recrystallized from ethanol, (0.34 g, 57.9 %), m.p. 198-199 °C; IR: 3410, 3176 (NH), 3087, 3060 (CH, aromatic), 2996, 2854 (CH, aliphatic), 1669 (C=O), 1618 (C=N) and 1565, 1439, 1314, 1127 cm⁻¹; MS: *m/z* : 344 (M⁺, 21.5 %), 329 (M - Me, 6 %), 301 (M⁺-COMe, 17.2 %), 28.6 (M⁺-NHCOMe, 100 %), 271 (M⁺-NHNHCOMe, 17.2 %). Anal. Calcd for C₁₉H₁₆N₆O: C, 66.26; H, 4.69; N, 24.41. Found: C, 66.30; H, 4.50; N, 24.50.

9,10-Diphenyl-6H-pyridazino[3',4':3,4]pyrazolo[5,1-c][1,2,4]-triazine-3,4(2H,6H)-dione, 9

To a solution of compound **1** (0.5 g, 1.7 mmol) in absolute ethanol (25 mL), diethyl oxalate (0.2 g, 1.7 mmol) was added. The reaction mixture was refluxed for 1 h., then hydrochloric acid (5 mL) was added and the heating was prolonged for 4 h. Upon cooling the precipitated product was filtered off, dried and recrystallized from ethanol, (0.3 g, 57.9 %), m.p. > 300 °C; IR: 3374 (NH), 3091 (CH, aromatic), 1706 (C=O), 1678 (C=O), 1621 (C=N), and 1462, 1376, 1243 cm⁻¹. Anal. Calcd for C₁₉H₁₂N₆O₂: C, 64.04; H, 3.39; N, 23.59. Found: C, 63.90; H, 3.20; N, 23.40.

Ethyl 3-(2-(4,5-diphenyl-1H-pyrazolo[3,4-c]pyridazin-3-yl)hydrazono)butanoate, 11

A mixture of compound **1** (1.0 g, 3.3 mmol) and ethyl acetoacetate (0.4 g, 3.3 mmol) was refluxed in absolute ethanol (20 mL) for 4h. The solvent was then evaporated under reduced pressure and the residue was washed with diethyl ether. The solid product was recrystallized from ethanol, (0.7 g, 56.2 %), m.p. 252-253 °C; IR: 3416, 3133 (NH), 3058 (CH, aromatic), 2920, 2853 (CH, aliphatic), 1703 (C=O), 1585 (C=N), and 1464, 1323, 1138, 1030 cm⁻¹; MS: *m/z*: 413 (M⁺-1, 1.9 %), 412 (M⁺-2, 6.2 % ion A), 396 (ion A - CH₄, 42.9%), 368 (M⁺-OEt, 9.6 %), 271 (M⁺-NHN=C(Me)-CH₂COOEt, 50.6%). Anal. Calcd for

C₂₃H₂₂N₆O₂: C, 66.65; H, 5.35; N, 20.28. Found: C, 66.50; H, 5.20; N, 20.10.

2-(4,5-Diphenyl-1H-pyrazolo[3,4-c]pyridazin-3-yl)-5-methyl-1H-pyrazol-3(2H)-one, 12

Compound **11** (0.4 g, 0.97 mmol) was heated under reflux in glacial acetic acid (10 mL) for 10 h. The cooled reaction mixture was poured onto cold water (100 mL). The white precipitates was filtered off, washed with water, dried, and recrystallized from ethanol, (0.3 g, 84.3 %), m.p. 210-211 °C; IR: 3138 (NH), 3059 (CH, aromatic), 2923, 2854 (CH, aliphatic), 1674 (C=O), 1572 (C=N), and 1464, 1422, 1395, 1134 cm⁻¹; MS: *m/z*: 368 (M⁺, 12.1 %), 367 (M⁺-1, 8.7 %), 353 (M⁺-Me, 4.9 %), 285 (M⁺-N=C(Me)CH₂CO, 8.9 % ion A), 271 (ion A - N, 7.0 %). Anal. Calcd for C₂₁H₁₆N₆O: C, 68.46; H, 4.37; N, 22.81. Found: C, 68.30; H, 4.10; N, 22.70.

N'-(4,5-Diphenyl-1H-pyrazolo[3,4-c]pyridazin-3-yl)-3-oxo-3-phenylpropanehydrazide, 13

A mixture of compound **1** (1.0 g, 3.3 mmol) and ethyl benzoylacetate (0.6 g, 3.3 mmol) was refluxed in glacial acetic acid (15 mL) for 24 h. The cooled reaction mixture was poured onto water (100 mL). The yellow precipitates was filtered off, dried and recrystallized from ethanol, (0.4 g, 47.1 %), m.p. > 300 °C; IR: 3422, 3159 (NH), 3061 (CH, aromatic), 2922, 2853 (CH, aliphatic), 1738 (C=O, ketone), 1677 (C=O, amide), 1618 (C=N) and 1565, 1462, 1248, 1131 cm⁻¹; MS: *m/z*: 447 (M⁺-1, 11.1 %), 446 (M⁺-2, 28.9 %), 415 (M⁺-O₂, 14.3 %), 371 (M⁺-Ph, 7.0 %), 287 (M⁺-NH(C=O)CH₂(C=O)C₆H₅, 9.7 %, ion A), 271 (ion A - NH, 12.5 %). Anal. Calcd for C₁₆H₂₀N₆O₂: C, 69.63; H, 4.49; N, 18.74. Found: C, 69.50; H, 4.20; N, 18.60.

3-(3,5-Dimethyl-1H-pyrazol-1-yl)-4,5-diphenyl-1H-pyrazolo[3,4-c]pyridazine, 14

To a solution of compound **1** (1.0 g, 3.3 mmol) in absolute ethanol (20 mL), acetylacetone (0.33 g, 3.3 mmol) was added. The reaction mixture was refluxed for 5 h. The solvent was then evaporated under reduced pressure and the residue was washed with pet. ether 40-60 °C dried and recrystallized from ethanol, (0.69g, 57.7 %), m.p. 243-244 °C; IR: 3139 (NH), 3100, 3060 (CH, aromatic), 2957, 2854 (CH, aliphatic), 1567 (C=N) and 1532, 1421, 1355, 1133, 1029 cm⁻¹; MS: *m/z*: 366 (M⁺, 88.6%), 365 (M⁺-1, 100 %), 351 (M⁺-Me, 28.1 %), 271 (M⁺-NN=C(Me)CH=C(Me), 23.5 %). Anal. Calcd for C₂₂H₁₈N₆: C, 72.11; H, 4.96; N, 22.94. Found: C, 72.00; H, 4.80; N, 22.80.

1-(4,5-Diphenyl-1H-pyrazolo[3,4-c]pyridazin-3-yl)pyrazolidine-3,5-dione, 15

A mixture of compound **1** (1.0 g, 3.3 mmol) and diethyl malonate (10 mL) was heated under reflux for 4 h. Upon cooling the solid product was filtered off, washed with pet. ether 40-60 °C and recrystallized from ethanol, (0.5 g, 81.6%), m.p. > 300 °C; IR: 3392, 3150 (NH), 3061 (CH, aromatic), 1732 (C=O), 1603 (C=N), and 1444, 1372, 1298, 1151 cm⁻¹; MS: *m/z*: 370 (M⁺, 1.7 %), 369 (M⁺-1, 4.5 %), 368 (M⁺-2, 10.7 %), 354 (M⁺-O, 1.9 %), 338 (M⁺-O₂, 1.9 %), 271 (M⁺-NNH(C=O)CH₂(C=O), 1.5%). Anal. Calcd for C₂₀H₁₄N₆O₂: C, 64.85; H, 3.80; N, 22.69. Found: C, 64.70; H, 3.70; N, 22.50.

1-(4,5-Diphenyl-1H-pyrazolo[3,4-c]pyridazin-3-yl)-1H-pyrazole-3,5-diamine, 16

To a solution of compound **1** (1.0 g, 3.3 mmol) in absolute ethanol (20 mL), malononitrile (0.2 g, 3.3 mmol) was added. The reaction mixture was refluxed for 20 h. The solvent was then evaporated to its half, upon cooling the solid product was filtered off, dried and recrystallized from ethanol, (0.4 g, 65.6 %), m.p. > 300 °C; IR: 3318 (NH₂), 3190 (NH), 3060 (CH, aromatic), 1633 (C=N) and 1577, 1462, 1376, 1308, 1151 cm⁻¹; MS: *m/z*: 369 (M⁺+1, 1.5 %), 368 (M⁺, 2.7 %), 257 (M⁺-(N+N-N=C(NH₂)-CH=C(NH₂), 70.2 %, ion A), 256 (ion A-1, 2.0 %. Anal. Calcd for C₂₀H₁₆N₈: C, 65.20; 4.38; N, 30.42. Found: C, 65.00; H, 4.10; N, 30.00.

5-Amino-1-(4,5-diphenyl-1H-pyrazolo[3,4-c]pyridazin-3-yl)-1H-pyrazol-3(2H)-one, 17

To a solution of compound **1** (1.0 g, 3.3 mmol) in glacial acetic acid (20 mL) ethyl cyanoacetate (0.4 g, 3.3 mmol) was added. The reaction mixture was refluxed for 10 h. The cooled reaction mixture was poured onto water (100 mL) and the precipitate was filtered off, dried and recrystallized from ethanol, (0.62 g, 50.6 %), m.p. 134-135 °C; IR: 3444 (NH₂), 3150 (NH), 3059 (CH, aromatic), 1672 (C=O), 1620 (C=N), and 1566, 1441, 1357, 1305 cm⁻¹; MS: *m/z*: 368 (M⁺-1, 0.1 %), 271 (M⁺-NNH(C=O)CH=C(NH₂), 100 %). Anal. Calcd for C₂₀H₁₅N₇O: C, 65.03; H, 4.09; N, 26.55. Found: C, 64.90; H, 3.90; N, 26.40.

1-(4,5-Diphenyl-1H-pyrazolo[3,4-c]pyridazin-3-yl)pyrazole-5-di-azonium-3-olate, 18

At room temperature a solution of sodium nitrite (0.4 g, 5.9 mmol) in H₂O (2 mL) was added in portion-wise to a stirred solution of compound **17** (0.3 g, 0.81 mmol) in acetic acid (5 mL).

The reaction mixture was stirred for 1 h. A yellow solid product was filtered off, dried and recrystallized from ethanol, (0.17 g, 54.4 %), m.p. 153-154 °C; IR: 3148 (NH), 3059 (CH, aromatic), 2135 (-N≡N), 1672 (C=O), 1635 (C=N), and 1564, 1441, 1305, 1134, 1031 cm⁻¹. Anal. Calcd for C₂₀H₁₂N₈O: C, 63.15; H, 3.18; N, 29.46. Found: C, 63.00; H, 3.00; N, 29.30.

REFERENCES

- ¹Part 15, *Eur. Chem. Bull.*, **2014**, 3(2), 115-118.
- ²Heinisch, G., Kopelent, H., In: Ellis, G. P., West, G. B. (eds) *Progress in Medicinal Chemistry*, **1992**, vol. 29, Elsevier, Amsterdam.
- ³Dal Piaz, V., Paolo Giovannoni, M.; Castellana, C.; Palacios, J. M., Beleta, J. M. Domenech, Segarra, V., *J. Med. Chem.*, **1997**, 40, 1417-21.
- ⁴Matyus, P., *J. Heterocycl. Chem.*, **1998**, 35, 1075-1089.
- ⁵Bistochi, G. A., Ricci, A., Jacquignon, P., *Farmaco Ed. Sci.*, **1981**, 36, 315-33.
- ⁶Prasad, A. R., Ramalingam, J., Rao, A. B., Diawan, P. W., Sattur, P. B., *J. Med. Chem.*, **1989**, 24, 199-201.
- ⁷O'Reilly, S. M., Newlands, E. S., Gloser, M. G., Brampton, M., Rice-Edwards, J. M., Illingworth, R. D., Richards, P. G., Kennard, C., Colguhoum, I. R., Lewis, P., Stevens, M. F. G. *Eur. J. Cancer*, **1993**, 29, 940-2.
- ⁸Deeb, A., Bayoumy, B., Hataba, A., Fikry, R., *Heterocycles*, **1991**, 32, 901-904.
- ⁹Deeb, A., Kotb, M., *Heterocycles*, **2004**, 63, 1143-50.

Received: 04.01.2014.

Accepted: 24.02.2014.



SYNTHESIS AND CRYSTAL STRUCTURE OF 2-AMINO-7,7-DIMETHYL-4-(4-NITROPHENYL)-5-OXO-1,4,5,6,7,8-HEXAHYDROQUINOLINE-3-CARBONITRILE

Rajni Kant^{[a]*}, Vivek K. Gupta^[a], Sumati Anthal^[a], Preetika Sharma^[a], D. R. Patil^[b], A. G. Mulik^[b] and M. B. Deshmukh^[b]

Keywords: Multicomponent synthesis; Dihydropyridine; Crystal structure; Direct methods; N-H...O hydrogen bonding.

The title molecule, 2-amino-7, 7-dimethyl-4-(4-nitrophenyl)-5-oxo-1,4,5,6,7,8- hexahydroquinoline-3-carbonitrile, C₂₁ H₂₅ N₅ O₄, was synthesized by multicomponent synthesis and characterized by IR, ¹H NMR, Elemental and Single-crystal analysis. The compound crystallizes in the triclinic space group P-1 with unit cell parameters, a = 7.5762(2), b = 9.9019(4), c = 14.1138(5) Å, α = 89.708(3), β = 90.249(3), γ = 102.124(3)°, Z=2. The crystal structure was solved by direct methods using single-crystal X-ray diffraction data collected at room temperature and refined by full-matrix least-squares procedures to a final R-value of 0.1183 for 3090 observed reflections. The dihydropyridine and cyclohexene rings both adopt *sofa* conformations. The five essentially planar atoms of the dihydropyridine ring form a dihedral angle of 82.13(6)° with the benzene ring. In the crystal, N-H...O hydrogen bonds link molecules into a two-dimensional network.

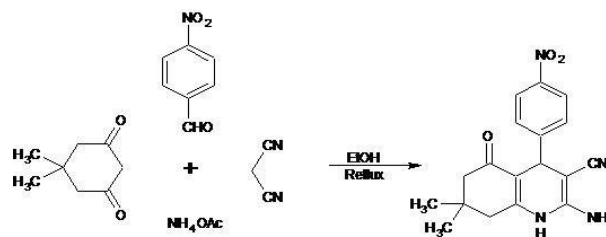
* Corresponding Authors

Fax: +91 191 243 2051

E-Mail: rkvk.paper11@gmail.com

[a] X-ray Crystallography Laboratory, Post-Graduate Department of Physics & Electronics, University of Jammu, Jammu Tawi - 180 006, India

[b] Department of Chemistry, Shivaji University, Kolhapur - 416 004 (MS), India



Scheme 1. Synthesis of title compound

Introduction

A multicomponent reaction provides powerful tool for the synthesis of complex molecules. Multicomponent transformations combine classical concerns such as selectivity, efficiency, molecular complexity and are important in combinatorial, organic and medicinal chemistry.^{1,2}

Many heterocyclic compounds containing 1,4-dihydropyridine (DHP) nucleus act as a versatile intermediate for the synthesis of several pharmaceuticals together with those of cardiovascular drugs, antidiabetic agents, neuroprotectant and as a calcium channel modulators, laser dyes and photo initiators.³⁻⁸ The design and synthesis of 1,4-dihydropyridines has attracted much attention over the past thirty years due to the calcium antagonist effect they display.⁹ The establishment of the pharmacological action as drugs for the treatment of cardiovascular diseases such as angina, hypertension or arrhythmia was mainly based on the structural studies carried out by X-ray diffraction on differently substituted 1,4-dihydropyridines.¹⁰ Generally, 1, 4- dihydropyridine compounds are synthesized by Hantsch method by condensation of aldehydes, active methylene compounds and ammonia or primary amines.⁹⁻¹¹

In continuation of our on-going work on multicomponent reactions, we explain here the synthesis and structure of compound 2-amino-7, 7-dimethyl-4-(4-nitrophenyl)-5-oxo-1,4,5,6,7,8- hexahydroquinoline-3-carbonitrile (Scheme 1).

Methods

Materials and methods

All the chemicals were purchased from S D Fine Chem Limited and used as received without further purification. Melting point was determined on Labstar melting apparatus was uncorrected. The IR spectra was run on a Perkin-Elmer, FTIR-1600 spectrophotometer and expressed in cm⁻¹(KBr). ¹H NMR spectra was recorded on Bruker Avance (300 MHz) spectrometer in DMSO-d₆ using TMS as the internal standard. Elemental analysis was performed on a EURO - EA elemental analyzer.

Synthesis

In a 50 ml round bottom flask 5, 5-dimethylcyclohexane-1,3-dione (1 mmol), ammonium acetate (3.5 mmol), malononitrile (1 mmole) and 4-nitrobenzaldehyde (1 mmol) were charged in ethanol (7 ml). Then reaction mixture was stirred at reflux condition till completion of reaction (monitored by TLC), the reaction mixture was stirred at RT for 15 min. Separated solid was then filtered off and recrystallized from ethanol to afford pure product. The product was characterized by IR, ¹H NMR, Elemental and Single crystal analysis. M.P.: 292 – 294 °C, Yield: 81%.

IR (KBr): 3393, 3325, 3222, 2959, 2177, 1654, 1517 cm^{-1} . ^1H NMR (300 MHz, $\text{DMSO}-d_6$): δ 0.88(s, 3H, CH_3), 1.00 (s, 3H, CH_3), 1.95 – 2.19(m, 2H, CH_2), 2.35– 2.49 (m, 2H, CH_2), 4.45(s, 1H, CH), 5.95(s, 2H, NH_2), 7.36 – 7.39(d, 2H, $J = 9$ Hz, Ar- H), 8.11 – 8.14(d, 2H, $J = 9$ Hz, Ar- H), 9.02(bs, 1H, NH). Analysis: Calculated for $\text{C}_{18}\text{H}_{18}\text{N}_4\text{O}_3$ (338.36): C, 63.89%; H, 5.36%; N, 16.56%; Found: C, 63.84%; H, 5.32%; N, 16.60%.

X-ray Data Collection, Crystal Structure Determination and Refinement

X-ray intensity data of 16144 reflections (of which 4055 unique) were collected on *X'calibur* CCD area-detector diffractometer equipped with graphite monochromated MoK α radiation ($\lambda = 0.71073$ Å).¹² The crystal used for data collection was of dimensions 0.30 x 0.20 x 0.20 mm. The cell dimensions were determined by least-squares fit of angular settings of 8011 reflections in the θ range 4.06 to 29.26 °. The intensities were measured by ω scan mode for θ ranges 3.57 to 26.00 °. 3090 reflections were treated as observed ($I > 2\sigma(I)$). Data were corrected for Lorentz, polarisation and absorption factors. The structure was solved by direct methods using SHELXS97.¹³ All non-hydrogen atoms of the molecule were located in the best E-map. All the hydrogen atoms (except N1 and N19 H atoms) were geometrically fixed and allowed to ride on the corresponding non-hydrogen atoms with C-H = 0.93-0.98 Å, and $U_{iso} = 1.5U_{eq}$ of the attached C atom for methyl H atoms and 1.2 U_{eq} for other H atoms. Full-matrix least-squares refinement was carried out using SHELXL97.¹³ The final refinement cycles converged to an $R = 0.0485$ and $wR(F^2) = 0.1183$ for the observed data. Residual electron densities ranged from -0.191 to 0.261 eÅ⁻³. Atomic scattering factors were taken from International Tables for X-ray Crystallography (1992, Vol. C, Tables 4.2.6.8 and 6.1.1.4). The crystallographic data are summarized in Table 1. CCDC-958413 contains the supplementary crystallographic data for this paper. These data can be obtained free of charge from The Cambridge Crystallographic Data Centre via www.ccdc.cam.ac.uk/data_request/cif.

Results and discussion

An ORTEP view of the title compound with atomic labeling is shown in Figure 1.¹⁴ The geometry of the molecule was calculated using the PLATON¹⁵ and PARST¹⁶ software.

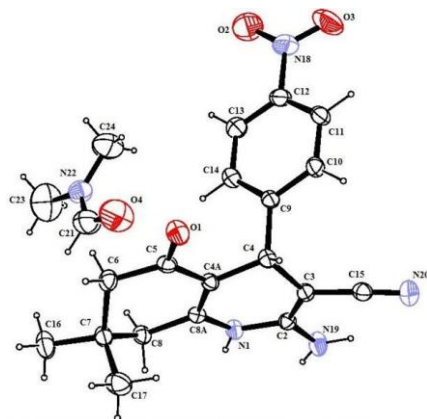


Figure 1. Ortep view of the molecule with displacements ellipsoids drawn at the 50 % probability level. H atoms are shown as small spheres of arbitrary radii.

Table 1. Crystallographic data and other experimental details of **I**.

CCDC Number	958413
Crystal colour	Yellow
Crystal description	rectangular
Crystal size	0.30x0.20x0.20 mm
Empirical formula	C ₂₁ H ₂₅ N ₅ O ₄
Formula weight	411.46
Radiation, wavelength	Mo K α , 0.71073 Å
Unit cell dimensions	$a=7.5762(2)$ Å $b=9.9019(4)$ Å $c=14.1138(5)$ Å $\alpha=89.708(3)^\circ$ $\beta=90.249(3)^\circ$ $\gamma=102.124(3)^\circ$
Crystal system	Triclinic
Temperature, K	293(2) K
Space group	P-1
Unit cell volume	1035.16(6) Å ³
No. of molecules per unit cell,	Z=2
Absorption coefficient	0.094 mm ⁻¹
F(000)	436
θ range for entire data collection	3.57 < θ < 26.00
Reflections collected/unique	16144 / 4055
Reflections observed ($I > 2\sigma(I)$)	3090
Range of indices	$h=-9$ to 9 $k=-12$ to 12 $l=-17$ to 17
Completeness, %	99.7
Final R -factor	0.0485
$wR(F^2)$	0.1183
R_{int}	0.0338
R_{sigma}	0.0302
Goodness-of-fit	1.036
$(\Delta / \sigma)_{\text{max}}$	-0.001 (for tors H24A)
Final residual electron density	-0.191 < $\Delta\rho$ < 0.261 eÅ ⁻³

Crystal data, along with data collection and structure refinement details are summarized in Table 1. Selected bond lengths and angles are given in Table 2, while hydrogen bonds are presented in Table 3.

In (I) (Fig.1), all bond lengths and angles are normal and correspond to those observed in related structures.¹⁷⁻¹⁹ Phenyl ring (C9-C14) is perfectly planar with a maximum deviation of 0.004(2) for C14 atom. The (N1/C2/C3/C4/C4A/C8A) and (C4A/C5/C6/C7/C8/C8A) rings adopt sofa conformations with best mirror plane passing through C4 and C7 atoms [asymmetry parameters = $\Delta C_s(C4) = 6.39$ & $\Delta C_s(C7) = 6.68$], respectively²⁰ with atoms C4 and C7 forming the flaps in each ring. The five essentially planar atoms (N1/C2/C3/C4A/C8A) of the dihydropyridine ring form a dihedral angle of 82.13(6)° with the benzene ring. The bond length and bond angle of (C15-N20) = 1.148(2) Å and (C3-C15-N20) = 177.48(19)° show linear character of the cyano group, a feature observed in carbonitrile compounds. The double bond C5=O1 bond distance is confirmed by its respective distance of 1.239(2) Å. The length of the double bond C5=O1 is larger than the standard value for carbonyl group (1.192 Å) and lengthening of this double bond is due to the reason that O1 involves in inter-molecular interactions.

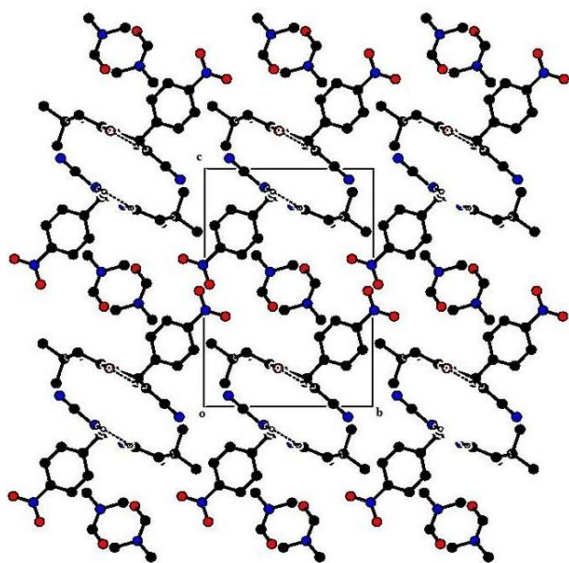
Table 2. Selected bond lengths (Å) and angles (°) for **I**.

Bond lengths, Å		Bond angles, °		Bond angles, °	
N1-C8A	1.372(2)	C8A-N1-C2	121.5(1)	N19-C2-C3	124.8(2)
O1-C5	1.239(2)	N19-C2-N1	115.2(2)	C3-C2-N1	120.1(2)
O3-N18	1.220(2)	O1-C5-C4A	120.7(2)	O1-C5-C6	120.2(2)
C2-N19	1.350(2)	C4A-C8A-N1	120.7(2)	N1-C8A-C8	115.5(1)
C15-N20	1.148(2)	C11-C12-N18	118.7(2)	C13-C12-N18	119.2(2)
N22-C23	1.438(3)	N20-C15-C3	177.5(2)	O2-N18-O3	123.3(2)
N1-C2	1.380(2)	O2-N18-C12	118.5(2)	O3-N18-C12	118.3(2)
O2-N18	1.215(3)	O4-C21-N22	125.9(3)	C21-N22-C23	122.4(3)
O4-C21	1.214(3)	C21-N22-C24	119.7(2)	C23-N22-C24	117.9(3)
C12-N18	1.470(2)				
C21-N22	1.313(3)				
N22-C24	1.447(3)				

Table 3. Hydrogen bonding parameters (Å, °) for **I**.

Bond	D-H, Å	H...A, Å	D...A, Å	D-H ...A angle, °	Symmetry Code
C8-H8B...O4	0.97	3.331(3)	2.56	103	
C24-H24B...O4	0.96	2.756(3)	2.38	136	
C14-H14 ...O4	0.93	3.349(3)	2.475	157	
N19-H19A...O1	0.87(2)	2.840(2)	2.02(2)	156(2)	$x-1, +y, +z$
N1-H1...O1	0.86(2)	2.911(2)	2.13(2)	150.2(2)	$x-1, +y, +z$

Packing view of the molecules in the unit cell viewed down the a-axis is shown (see Figure 2). The title molecule is stabilized by intramolecular interactions and intermolecular interactions are responsible for the stability of crystal structure. The molecules are linked into infinite chains by N-H...O inter-molecular hydrogen bonds. Details of intra- and intermolecular hydrogen bonds are given (see Table 3).

**Figure 3.** The crystal packing viewed down the a-axis is shown

Acknowledgements

One of the authors (Rajni Kant) acknowledges the Department of Science & Technology for single crystal X-ray diffractometer as a National Facility under Project No. SR/S2/CMP-47/2003.

References

- Chen, D., Zhu, Q., Su, W., *Tetrahedron Lett.* **2011**, 52, 2601.
- Nielsen, T. E., Schreiber, S. L., *Angew. Chem. Int. Ed.*, **2008**, 47, 48.
- Tu, S., Miao, C., Gao, Y., Fang, F., Zhuang, Q., Feng, Y., Shi, D. *Synlett.*, **2004**, 2, 255.
- Fan, X., Li, Y., Zhang, X., Qu, G., Wang, *HeteroatomChem.* **2007**, 18, 7.
- Leon, R., Rios, C., Contelles, J. M., Lopez, G. M., Garcia, A. G., Villarroya, M., *Eur. J. Med. Chem.*, **2008**, 43, 668.
- Safari, J., Banitata, H. S., Khalili, S. D., *J. Mol. Catal. A.*, **2011**, 335, 46.
- Kumar, S., Sharma, P., Kapoor, K. K., Hundal, M. S., *Tetrahedron*, **2008**, 64, 536.
- Leon, R., Rios, C., Marco-Contelles, J., Huertas, O., Barril, X., Luque, F. J., Lopez, M. G., Garcia, A. G., Villarroya, M., *Bioorg. Med. Chem.*, **2008**, 16, 7759.
- Mayler, W. G., In: *Calcium Antagonist*. London: Academic Press **1989**.
- Triggle, D. J., Langs, D. A., Jamis, R. A., *Med. Res. Rev.*, **1989**, 9, 123.

- ¹¹Hantsch, A., *J. Liebigs Ann. Chem.* **1882**, 1, 215.
- ¹²Oxford Diffraction **2010**, CrysAlis PRO. Oxford Diffraction Ltd, Yarnton, Oxfordshire, England.
- ¹³Sheldrick, G. M., *Acta Cryst.*, **2008**, A64, 112.
- ¹⁴Farrugia, L. J., *J. Appl. Cryst.*, **2012**, 45, 849.
- ¹⁵Spek, A. L., *Acta Cryst.*, **2009**, D65, 148.
- ¹⁶Nardelli, M., *J. Appl. Cryst.*, **1995**, 28, 659.
- ¹⁷Jiang, H., Wang, X. S., Zhang, M.-M., Li, Y. L., Shi, D.-Q., *Acta Cryst.*, **2006**, E62, o1184–o1186.
- ¹⁸Tu, S., Zhang, J., Zhu, X., Xu, J., Wang, Q., *Acta Cryst.*, **2005**, E61, o983.
- ¹⁹Rajni Kant, Gupta, V. K., Kapoor, K., Patil, D. R., Mulik, A. G., Deshmukh, M. B., *Acta Cryst.*, **2013**, E69, o105.
- ²⁰Duax, W. L., Norton, D. A., *In Atlas of Steroid Structures*, Vol. 1. New York: Plenum Press, **1975**.

Received: 26.12.2013.

Accepted: 24.02.2014.



CORROSION PROBLEMS IN PETROLEUM INDUSTRY AND THEIR SOLUTION

S. Santhana Prabha,^[a] R. Joseph Rathish,^[b] R. Dorothy,^[b] G.Brindha,^[c] M. Pandiarajan,^[d] Abdulameed Al-Hashem,^[e] and S.Rajendran^{[c,d]*}

Keywords: Corrosion inhibitors, Petroleum industry, oil wells, green inhibitors, biocidal inhibitors

Corrosion costs the oil industry billions of dollars a year. Corrosion affects every aspect of exploration and production, from offshore rigs to casing, and reviews the role of corrosion agents such as drilling and production fluids. Methods of control and techniques to monitor corrosion, along with an explanation of the chemical causes of corrosion are discussed.

Corresponding Authors

E-Mail: srmjoany@sify.com

- [a] TCS, Chennai, India,
- [b] PSNA College of Engineering and Technology,
- [c] Corrosion Research Centre, RVS School of Engineering and Technology, Dindigul-624005, India.
- [d] Corrosion Research Centre, PG and Research, Department of Chemistry, GTN Arts College, Dindigul- 624005.
- [e] Petroleum Research Centre, Kuwait Institute for Scientific Research, Kuwait-24885

INTRODUCTION

Corrosion costs of the oil industry are billions of dollars in a year. Corrosion affects every aspect of exploration and production, from offshore rigs to casing. Methods of control and techniques to monitor corrosion, along with an explanation of the chemical causes of corrosion are discussed.

DISCUSSION

Corrosion in petroleum industry¹⁻³

The Petroleum industry contains a wide variety of corrosive environments. Some of these are unique to this industry. Thus it is convenient to group all these environments together. Corrosion problems occur in the petroleum industry in at least three general areas: (1) production, (2) transportation and storage, and (3) refinery operations.

Production

Oil and gas fields consume a tremendous amount of iron and steel pipe, tubing, pumps, valves, and sucker rods. Leaks cause loss of oil and gas and also permit infiltration of water and silt, thus increasing corrosion damage. Saline water and sulphides are often present in oil and gas wells. Corrosion in wells occurs inside and outside the casing. Surface equipment is subject to atmospheric corrosion. In secondary recovery operations, water is pumped into the well to force up the oil.

Condensate wells

Condensate wells handle fluids (gas containing dissolved hydrocarbons) at pressures up to 1,751,300 Nm. Depths run up to 4572 m Carbon dioxide is the chief corrosive agent, with organic acids contributing to the attack. Approximately 90 % of the corrosive condensate wells encounter conditions as follows: (1) depth greater than 1524 m, (2) bottom hole temperature above 71° C and pressure above 262,695 Nm (3) a carbon dioxide partial pressure above 2,626.95 Nm, and (4) a wellhead pH of less than 5.4.

Corrosion characteristics of a well are determined by (1) inspection of surface equipment, (2) analysis for carbon dioxide, organic acid, and iron, (3) coupon exposure tests, and (4) tubing-caliper surveys. Determination of iron content and tubing-caliper surveys are used to measure the effectiveness of inhibitor treatment.

Earlier practices involved addition of neutralizers such as ammonia, sodium carbonate, sodium hydroxide, and sodium silicate, but these were replaced in many cases by organic inhibitors, available in oil-soluble, water-dispersible, or water-soluble forms. In some applications, alloy steels have replaced the medium-carbon manganese steels (J-55 and N-80) previously used. Straight chromium and nickel on corrosion of steel by condensate-well fluid. Straight chromium stainless steels, Stellite, Monel, and copper-base alloys are commonly used for valves and other wellhead parts. Galvanic corrosion is apparently not a factor because substantial amounts of high-conductivity water are not present.

Sweet oil wells

It appears that corrosion in high-pressure flowing wells that produce pipeline oil has become almost commonplace in many areas. Three methods are used to combat this corrosion – coated tubing, inhibitors, and alloys. Coated tubing has found most favor, and until recently, backed-on phenolics have been used for almost all coating installations. Air-dried and baked epoxy resins are now being used in increasing amounts.

Sour oil wells these wells handle oil with higher sulfur contents than sweet wells and represent a more corrosive environment. In high H₂S wells there may be severe attack on the casing in the upper part of the well where the space is filled with gas. Water vapor condenses in this area and picks up H₂S and CO₂.

Corrosion is reduced by inhibitors which are injected continuously or periodically depending on the well corrosivity. Offshore drilling presents many interesting corrosion problems. Platforms are built over the water and supported by beam piles driven into the ocean floor. Each beam is surrounded by a pipe casing or protection. Similar platforms are used far out at sea for radar towers.

A variety of corrosion prevention methods are used in such structures. These include: (1) Adding inhibitors to the stagnant seawater between beams and casings, (2) Cathodic protection, with sacrificial anodes or impressed currents, of underwater structures, (3) Paints and other organic coatings to protect exposed structures above the splash zone, (4) Monel sheathing at the casing splash zone. This portion of offshore structures is the most susceptible to rapid corrosion.

Transportation and storage

Petroleum products are transported by tankers, pipelines, railway tank cars, and tank trucks. The outside submerged surfaces of tanks on the outside surface of underground pipelines are protected with coatings and by using cathodic protection. Cathodic protection is also applied to the inside of tankers to prevent corrosion by seawater used for washing or ballast. Gasoline-carrying tankers present a more severe internal corrosion problem than oil tanks because the gasoline keeps the metal too clean. Oil leaves a film that affords some protection. Tank cars and tank trucks are coated on the outside for atmospheric corrosion.

The main reason for internal corrosion of storage tanks is the presence of water which settles and remains on the bottom. Coatings and cathodic protection are used. Alkaline sodium chromate (or sodium nitrate) has been found to be an effective inhibitor for corrosion of domestic fuel oil tanks.

Internal corrosion of product pipelines can be controlled with coatings and inhibitors (a few parts per million) such as amines and nitrites. Ingenious methods for coating pipelines in place underground have also been developed.

Refinery operations

Most of the corrosion difficulties in refineries are due to inorganics such as water, H₂S, CO₂, sulfuric acid, and sodium chloride, and not to the organics themselves. For this reason, the petroleum industry has much in common with the chemical industry.

Corrosive agents may be classified into two general categories: (1) those present in feedstock or crude oil, and (2) those associated with processes or control.

Water is usually present in crude oils, and complete removal is difficult. Water acts as an electrolyte and causes

corrosion. It also tends to hydrolyze other materials, particularly chlorides, and thus forms an acidic environment.

Carbon dioxide has, in recent years, come to be recognized as one of the most important corrosive agents, especially in operations where gas is the feedstock, or raw material. Many gas wells produce large quantities of carbon dioxide.

Salt water is produced in most oil wells, and relatively large quantities of it get into the refinery, either in the water emulsified in the crude or in the crystalline form dispersed in the crude. The salts are calcium chloride, magnesium chloride, and sodium chloride. Desalting methods include washing and settling, addition of chemicals such as sulfonates to break the emulsion, centrifuging, and filtering. Salts and water are usually removed as quickly as possible, but the operations are frequently incomplete. If they are not removed, or only partially removed, hydrochloric acid often forms. Magnesium chloride is readily hydrolyzed. In this case, ammonia may be needed in amounts equivalent to three times the stoichiometric equivalent of sulphide and chloride ions.

Hydrogen sulphides, mercaptans, and other sulphur compounds are present in many of the crudes and gases processed by refineries. These are removed by reaction with sodium hydroxide, lime, iron oxide, or sodium carbonate, but for various reasons they are frequently not removed until the final operation is approached. Corrosion problems are associated with the refining process itself or with processes utilized to remove sulfur compounds.

Nitrogen is becoming an important consideration in some of the newer processes. Nitrogen is present in some crudes, but a more important source is the nitrogen in air. Large quantities of air are used in some of the burning operations associated with catalytic cracking processes. Ammonia and cyanides will form under certain conditions when nitrogen is present. The former can damage heat exchangers made of copper-bearing alloys. Cyanides are an important factor controlling the diffusion of hydrogen into steel.

Oxygen (or air) is drawn into tanks and other equipment as they are emptied, or enters during shutdown periods. It could also be drawn into the system by pumps. Oxygen can also be present as result of reactions of other compounds, such as water and carbon dioxide. The water used in the system often contains oxygen in solution.

Sulphuric acid is used in large quantities in many refinery operations such as alkylation and polymerization. The acid becomes contaminated and its corrosion characteristics may change. Utilization of this acid and its recovery or concentration presents corrosion problems that are extremely important to the refinery. For example, sludges often contain large quantities of carbon or carbonaceous material which make the acid strongly reducing in nature. These may attack stainless steels, and under the same conditions the copper-base alloys will give better performance.

Ammonia is used to control the pH of water and to reduce chloride acidity in the process streams. This procedure works well if the pH is 7, but is damaging to copper-bearing

alloys if the pH is 8 or above. Ammonia is added to vapors in the process and also to condensers to neutralize acid condensate. It is desirable to add ammonia just before the aqueous phase forms.

Hydrochloric acid forms because of hydrolysis as described earlier. Sometimes it is an intentional addition to the process stream. This is fairly volatile acid so it is often present in distillation columns and also in the condensed petroleum fractions (hydrofluoric acid is used in one alkylation process).

Caustic (sodium hydroxide) and lime are sometimes added for hydrogen sulphide removal and for neutralization. Lime and caustic additions to the crude reduces the amount of HCl present in the overhead vapors. These chemical are dispersed in oil before adding to the stream for better mixing. Less than the theoretical additions are made to avoid an excess of alkali. Caustic sometimes causes deposits (and clogging) that are difficult to remove. It also causes stress corrosion.

Naphthenic acid, when present in oils, can be quite corrosive at 221 to 399 ° C, and type 316 stainless is sometimes required as a constructional material. Substantial amounts of this acid are present in some oils. For less severe conditions 5 % Cr steel is satisfactory. Monel is used when temperatures are below 260 ° C.

Polythionic acid causes rapid intergranular SCC of sensitized austenitic stainless steels in some refinery operations. Type 304 is susceptible. This attack is minimized if properly heat-treated (not sensitized) 304 or the low-carbon or stabilized types are used.

Refinery corrosion is sometimes separated into two classifications: (1) low-temperature corrosion and (2) high-temperature corrosion. The dividing point is usually 260 ° C. Presumably, water can exist below 260 ° C, and the mechanism of aqueous corrosion apply. The high-temperature mechanism takes over above 260 ° C. Perhaps another reason for the division at 260 ° C is that ordinary carbon steel is economical for handling most crudes and naphthas up to this temperature, but alloy steels and other materials must be used at higher temperature. This is a general classification and should not be regarded as a strict division.

Such a classification is not entirely satisfactory, even if it applies directly for actual operating conditions at temperature. For example, high-temperature equipment is generally affected by water and other condensates that form when the equipment is shut down, when it is purged with steam or water, or when it is started up again. Many fail to recognize the effect of the conditions that exist when the equipment is not in operation – not only in refineries but in many other process industries as well.

Alloy used in refinery operations Ordinary carbon steel is by far the most important alloy, since it accounts for over 98 % of the construction materials used in the industry. As a general rule, every attempt should be made to use steel. This can be done by modifying the process in some manner such as lowering the temperature or adding inhibitors. Steel is the least expensive engineering metal aside from cast iron. In

some cases, alloy steels are more economical because they have a longer service life, and they should be judiciously selected, where applicable.

Carbon steel is often unsuitable for heat-exchanger tubes because of corrosion by the cooling water. Brass, arsenical Admiralty Metal, red brass, and cupronickels are widely used. Austenitic stainless steels are expensive and may crack in chloride-containing waters. These steels, however, are used for tubing in stills and gas-cracking tubes. In some cases, a single tower is lined with two or three different materials to take care of the changing corrosiveness from the top to the bottom of the tower.

Corrosion by sour crudes increases with temperature (increases rapidly around 800 F) and with increasing sulfur content. Chromium is the most beneficial alloying element in steel for resistance to sulfur compounds. Accordingly, the chromium content of steel is increased with increasing sulfur and temperature starting as low as 1% Cr. Experience indicates that 2.25% Cr, 1% Mo steel is generally adequate for less than 0.2% H₂S in the gas stream. High sulphide contents require 5% Cr or higher. The Cr-Mo steel mentioned above and 4 to 6% Cr, 0.5% Mo steel are widely used in refineries.

In addition to the “naturally occurring” carbon dioxide, some severe problems have been encountered because of CO₂ injection or flooding to enhance recovery of oil. Two basic components of the mechanism are consistent with actual experiment: (1) The main cathodic reaction is the reduction of undissociated carbonic acid or hydrogen ion, and (2) the expected high corrosion rates from the latter reaction are not achieved many systems because of the inhibiting effect of ferrous carbonate scale. The severe corrosion in amine-gas-treating systems occurs because the cathodic reaction involves carbonic acid, which comes from thermal decomposition of bicarbonate ion on heating surfaces.

Various inhibitors are used in petroleum industries in various stages. They are discussed in the following section.

A) Green Inhibitors

Green inhibitors in acid medium⁴

During acidizing stimulation or cleanup operations, metal tubulars, down hole tools/valves, surface lines, etc. are exposed to acidic fluids and are prone to corrosion. Because corrosion rates drastically increase in high-temperature wells, controlling corrosion is critical and must be dealt with carefully. In addition, corrosion protection is important for maintaining the integrity and long life of down hole tools installed in a well. Several corrosion inhibitors, such as quaternary ammonium compounds, propargyl alcohol-based compounds, etc., have been effectively used in the industry. However, because of stringent environmental regulations, attention has focused on the development of new corrosion inhibitors that are environmentally benign. Food-grade products that are considered “green” chemicals have significant potential as corrosion inhibitors in the oil and gas industry. Chicory has been used as a corrosion inhibitor for high-temperature

and strong-acidic conditions. Chicory is a perennial bush plant available in many parts of the world. The root of the chicory plant can be roasted and ground for use as a coffee substitute or additive. Chicory is environmentally acceptable and, being of plant origin, is widely recognized as biodegradable in nature. It has been found that chicory can provide corrosion protection for alloys, such as N-80, 13Cr-L80, and 1010 steel, in the presence of either inorganic or organic acids at temperatures up to 121 °C. Considering its good performance, low price, and no toxicity issues, chicory has significant potential for acid corrosion-inhibition applications. The mixing procedure for preparing the blend, experimental setup and test procedure, and laboratory results of high-pressure/high-temperature (HP/HT) corrosion tests are well established.

Medicinal plants as green corrosion inhibitors⁵

Pipelines are the safest and most economical means of transporting oil and gas in offshore and onshore production facilities. Corrosion inhibitors continue to play a significant role in protecting the pipelines from internal corrosion. A number of corrosion inhibitors have been developed with low environmental impact without compromising on their inhibitor efficiency. Recently geographical location specific-regulations for several regions have been implemented. The most prominent of these are the environmental regulations for the North Sea (UK, Norway, Denmark, The Netherlands), US Gulf Coast, Eastern Canada etc. Taj et al., describe the investigations using aqueous extracts of leaves of medicinal plants A, B and C; and root of plant D as environmentally friendly corrosion inhibitors of mild steel in synthetic ocean water by weight loss method. These natural products were designed for application in Indian oil and gas industry and other environmentally sensitive platforms; exploiting their low toxicity-as medicinal plants and ease of biodegradation-as water soluble extracts. Aqueous extracts of plant materials A, B, C and D were investigated for Bioaccumulation. All the extracts exhibited low bioaccumulation and good corrosion protection. These preliminary investigations conducted to select green inhibitors revealed that aqueous extracts of C and D exhibited better corrosion performance than A and B. Weight loss studies results at 50ppm and 100 ppm in the absence and presence of Hydrogen sulphide further support this fact. Taj et al., also give a brief overview of the principal criteria the inhibitor developers must follow to determine whether a given corrosion inhibitor is environmentally acceptable in a given region.

Polyglucosides as green corrosion inhibitors⁶

The chemical application of corrosion inhibitors is a widely adopted practice in production and processing operations in the oil and gas industry. Particularly challenging is the development of new chemistries, which maintain good protection of materials under a variety of conditions while being environmentally acceptable. Craddock et al., illustrate patented work in the chemistry of alkyl polyglucosides (APGs) and their synergistic effect with polyaspartates. They outline the development of this inhibitor class, which demonstrates good general inhibitor performance in a number of oilfield brines,

shows good filming characteristics under conditions of shear, and also has an excellent environmental profile. The base chemistry of alkyl polyglucosides is explained. The effect of inhibitors in a number of sweet and sour conditions as well as under various temperature conditions in a variety of oilfield waters has been illustrated. The results of laboratory tests under these conditions, such as linear polarization resistivity (LPR) the so-called "bubble test," and the rotating cylinder electrode (RCE), are presented and discussed.

B) Biocidal Inhibitors

Microbial control strategies and treatments⁷

Worldwide, the production of natural gas and now oil from shale basins (source rock) has been embraced as a commercially viable way of producing unconventional energy resources leading to a revolution in gas production in the US. Developments to invest in and tap into this alternative way of gas production are taking off in Europe and Asia. Hydraulic fracturing is a proven technology, used for many years to develop hydrocarbon resources. Successful strategies with hydraulic fracturing include the safe and effective use of chemical additives, proper well casing and robust water management programs. During the exploitation of hydrocarbons from shales, chemical additives such as corrosion inhibitors, gelling agents, biocides etc, have to be used in the fracturing of wells. Sustainable chemistries and effective product stewardship programs are required to minimize environmental and human exposure hazards. The addition of water with organic molecules to the actual fractured wells makes these environments subject to unwanted growth of microorganisms and biofilm development, which has detrimental effects on hydrocarbon flow and leads to pipeline/equipment corrosion. Often the presence of sulfate reducing microorganisms leads to unwanted H₂S production and subsequently souring. Due to this, water cycle management and properly designed microbial control programs for all water sources including injected water or produced water, are required. Because the microbial challenges and environmental parameters of these water sources vary, different microbial control strategies and treatments are required for each source. New formulations of biocides and control programs aimed at the needs of the gas and oil industry have been developed, e.g. improved heat stability and the reduction in biocide levels to achieve the same level of microbial control.

Bactericidal inhibitor in oil wells of Azerbaijan⁸

At present, Caspian Sea water is injected for reservoir pressure maintenance for oil production in Azerbaijan. There are different groups of bacteria, sulfate ions and organic matter in this water. This leads to corrosion and the destruction of oil-gas field equipment. The injection of bactericidal inhibitor in wells is used for protecting oil-gas field equipment from corrosion and microbiological wear in offshore conditions. Results of sulfonated and neutralized products of catalytic cracking of gasoil fraction are known. These were investigated under both laboratory and field conditions. SNQF reagent is a mixture with properties of bactericidal inhibitor which efficiently resists anode and

cathode reaction of steel. Also the SNGF reagent efficiency persists over 7 day later. Results of field testing and the availability of raw bactericidal inhibitor ensure recommending of the SNQF reagent for a wide range of application. Structures of the active species have been confirmed by analytical data. The synergistic corrosion inhibition by these species has been proved.

Estimation of onshore plant effluent concentrations⁹

When assessing environmental risks from industrial discharges it is a prerequisite to properly estimate concentrations of many chemicals in the discharge effluent. For many chemicals (e.g. hydrocarbons, metals) analytical methods are available and effluent concentrations can directly be measured. However, for many man-added, process chemicals (e.g. biocides, corrosion inhibitors) no analytical methods are available and concentrations need to be estimated based on the amounts used and physical chemical behavior of the components. For this purpose a designated model has been developed to be applied to oil refineries and terminals. The Onshore Plant Effluent Model (OPEM) estimates the annual average effluent volume and concentrations of chemical components in the discharged water from upstream oil plants. OPEM can be tailored to a specific facility by using a generic process diagram in which all relevant parts of the process can be included; creating a system that represents the facility that the model will be run for. To be able to run and provide accurate output, the model needs information including composition of each process chemical, physico-chemical properties, effect thresholds (i.e. PNECs) and basic toxicity data. This data is stored in databases that form an integrated part of OPEM. Another input for the model is the characterization of the inflows. Here a selection can be made from flows of oil with traces of water and chemicals from a specific field, flows of chemicals that are applied directly to the system and additional water flows like rain and drainage water. Finally, mass balance data must be entered, which represents a quantification of the inflows or chemicals used. OPEM uses dilution and mass balance equations to calculate the effluent concentration of each component in any part of the facility including the discharged effluent. For every chemical component OPEM produces a pie-chart presenting the origin of the component (where is it used and in which process chemicals). Even though developed for upstream oil industry, OPEM is a generic model that can be used for complex effluent concentration calculations for any process facility. Estimated effluent concentrations of chemical components together with the information on the origin of the components are an important input for environmental risk management.

Potential of *Bacillus* strain B21 as a biocontrol agent to fight corrosion in the oil industry¹⁰

The role of the antagonistic potential of nonpathogenic strain B21 against sulfate-reducing bacteria (SRB) consortium has been enlightened. The inhibitor effects of strain B21 were compared with those of the chemical biocide tetrakis(hydroxymethyl)phosphonium sulfate (THPS), generally used in the petroleum industry. The biological inhibitor exhibited much better and effective performance. Growth of SRB in coculture with bacteria strain B21 antagonist exhibited decline in SRB growth,

reduction in production of sulphides, with consumption of sulfate. The observed effect seems more important in comparison with the effect caused by the tested biocide (THPS). Strain B21, a dominant facultative aerobic species, has salt growth requirement always above 5% (w/v) salts with optimal concentration of 10-15%. Phylogenetic analysis based on partial 16S rRNA gene sequences showed that strain B21 is a member of the genus *Bacillus*, being most closely related to *Bacillus qingdaonensis* DQ115802 (94.0% sequence similarity), *Bacillus ainingensis* DQ504377 (94.0%), and *Bacillus salarius* AY667494 (92.2%). Comparative analysis of partial 16S rRNA gene sequence data plus physiological, biochemical, and phenotypic features of the novel isolate and related species of *Bacillus* indicated that strain B21 may represent a novel species within the genus *Bacillus*, named *Bacillus* sp. (EMBL, FR671419). The application potential of *Bacillus* strain B21 as a biocontrol agent to fight corrosion in the oil industry has been established.

Sulphite-reducing bacteria corrosion risk in oil fields¹¹

Sulphite-reducing bacteria are generally considered to have a profound impact on the petroleum industry as their sulphide production activity contributes to reservoir souring and pipeline corrosion. SRB can be controlled by injecting biocides into pipelines and above-ground facilities. A recent "green" alternative for controlling reservoir souring is to inject nitrate, as nitrate is relatively harmless and is ultimately reduced to nitrogen gas. Resident nitrate-reducing bacteria (NRB) reduce nitrate to nitrite, which is a strong inhibitor of SRB, thereby inhibiting sulphide production. However, NRB-mediated oxidation of sulphide with nitrate and/or chemical reaction between nitrite and sulphide can generate sulphur-polysulphide (S-PS), which can expedite corrosion. S-PS is also rapidly formed by chemical reactions, when sour produced waters, containing substantial sulphide concentrations, are exposed to air. Once formed, S-PS can be removed by either of two alternative routes, which may thus reduce corrosion risk. In the presence of (i) excess electron acceptor (e.g. nitrate), NRB may further oxidize the S-PS to sulphite, whereas in the presence of (ii) excess electron donor (oil organics, e.g. acetate) the S-PS may be reduced back to sulphide. A specialized group of sulphur-reducing bacteria catalyzes this reaction. A representative of this group, *Desulfuromonas acetoxidans*, derives energy for growth from the reaction: 4 sulphur + acetate = 4 sulphide + 2CO₂. Because oil field waters tend to be electron donor rich and electron acceptor poor, one would expect S-PS to be removed by the second route. A survey of the microbial community in produced waters from an oil field with low bottom hole temperatures indicated *Desulfuromonas* species to be common. Hence, once S-PS is formed by reaction of excess sulphide with a limiting concentration of nitrate or oxygen, it may subsequently be effectively removed through the activity of sulfur-reducing bacteria such as *Desulfuromonas*.

Fouling of pipelines¹²

Naphthenic acids (NAs) are partially uncharacterised complex mixtures of carboxylic acids, resulting from the microbial oxidation of petroleum hydrocarbons. They are associated with the fouling of pipelines and process

equipment in oil production and with corrosion in oil refineries. As byproducts of the rapidly expanding oil (tar) sands industries, NAs are also pollutants and have proved to be toxic to a range of organisms. They also have important beneficial uses as fungicides, tyre additives and, paradoxically, also in the manufacture of corrosion inhibitors. These features make the characterization of NAs an important goal for analytical chemists. Here we describe the synthesis of amide derivatives of NAs for characterization by liquid chromatography/ electrospray ionization multistage mass spectrometry (LC/ESI-MS-*n*). The method was applied to commercially available carboxylic acids, novel synthetic NAs, commercial NAs refined from crude oils, crude oil NAs and Athabasca oil sands NAs. In addition to confirming the number of alicyclic rings and length of alkyl side chain substituents (confirming information from existing methods), the MS *n* results provided further structural information. Most important of these was the finding that bi- to polycyclic acids containing ethanoate side chains, in addition to alkyl substituents, were widespread amongst the oil and oil sands NAs. The latter NAs are known end members of the β -oxidation of NAs with even carbon number alkananoate chains. Since such NA mixtures are toxic, they should be targets for bioremediation. Bioremediation of NAs can also be monitored better by application of the methods described herein.

C) Inhibitors for biological corrosion¹³

The sulfate-reducing bacteria growth kinetics and the biotransformation of sulfate into hydrogen sulphide were studied under laboratory conditions, using batch and continuous assays to determine the effect of molybdate and nitrate as metabolic inhibitors. The microorganisms were isolated from water coming from a natural gas dehydration plant, where they were associated with Microbiologically Influenced Corrosion (MIC) processes, and later cultured in plank tonic and sessile states. The addition of 5 mM molybdate showed a growth reduction to levels of non-detectable floating cells and a six order of magnitude reduction in biofilms, concomitant with a sulphide decrease of around 100% in all cultures inhibited by this compound. The addition of 75 mM nitrate showed a four order of magnitude reduction in free bacterial cells and a two order of magnitude reduction in adhered bacterial cells, respectively, as well as a sulphide decrease of around 80%. The decreased corrosion rate detected suggests that these inorganic salts could be nonconventional biocides for an effective and environmentally non contaminant way of controlling and mitigating internal biocorrosion processes in storage tanks and pipelines in natural gas and petroleum industrial systems.

D) Others

Inhibition of corrosion of carbon steel in H₂S containing medium¹⁴

Understanding and controlling hydrogen sulphide (H₂S) corrosion becomes increasingly important in the petroleum industry. Iron sulphide is formed on the internal pipeline surface as a corrosion product of carbon steel in an

environment containing H₂S. Some of the iron sulphide particles are suspended in the liquid phase or deposited at the bottom of a pipeline. Iron sulphide decreases the corrosion inhibition efficiency due to the adsorption of corrosion inhibitor on the surface of iron sulphide particles. The effect of iron sulphide on the efficiency of a corrosion inhibitor in a highly sour environment and to explore effective technical methodologies to study H₂S corrosion and inhibition has been investigated. Experiments have been performed in a series of autoclaves with a total pressure of 896 kPa (538 kPa CO₂ 290 kPa H₂S, and 69 kPa water vapor). Iron sulphide effects were studied separately in two different cases: directly deposited on the steel surface or suspended in the test solution. In the experiments, weight loss was applied to study the corrosion inhibition efficiency. Corrosion product films/scales formed on the surface of the steel were analyzed by Scanning Electron Microscopy (SEM) and Energy Dispersive X-ray analysis (EDX).

Carbon steel wet gas pipeline in Thailand¹⁵

As a primary energy source, natural gas continues to play a major role in meeting Thailand's energy requirements and is preferred for generating the country's electricity. As energy demand increases, a fully integrated pipeline integrity program for wet gas pipelines becomes necessary to ensure safe production from Thailand's gas fields. Corrosion mitigation and monitoring strategies implemented on a 63.5 km (40 mile) long, 385 mm (15.2 in) maximum internal diameter, carbon steel wet gas pipeline. The pipeline is in Khon Kaen Province, located northeast of central Thailand. Extensive pre-startup analysis was conducted, such as pipeline dynamic flow modeling and corrosion prediction modeling, from which the final corrosion management strategy was derived. Advanced corrosion measurement tools have been developed for continuous data collection, such as high-resolution metal loss probes and high-sensitivity ultrasonic wall thickness transducers. Performance data have been collected. Key performance indicators for corrosion control, including hydrogen sulphide measurements, iron counts, corrosion inhibitor residuals, and sulfate reducing bacteria, along with pipe wall corrosion measurements and cathodic protection potentials, are also considered. Recent in-line inspection data has been used to correlate the continuous monitoring data collected over the last several years with the recorded pipeline condition to evaluate the effectiveness of the corrosion management program.

Polyacrylamide based polymers as efficient corrosion inhibitors for carbon steel¹⁶

Owing to superior properties such as temperature resistance and salt tolerance etc., modified polyacrylamide (PAM) as one of the main injected polymers has been widely investigated to enhance oil production in reservoirs. A novel poly(AM-co-A- β -CD-co-AE) polymer was synthesized by utilizing β -CD and AE to copolymerize with AM and characterized by FT-IR and SEM. Furthermore, the temperature resistance and salt tolerance of poly(AM-co-A- β -CD-co-AE) polymer were explored. It is observed that the presence of the poly(AM-co-A- β -CD-co-AE) polymer better achieved temperature resistance and salt tolerance properties

than is the case with PAM, which has potential application for enhancing oil recovery in the high-temperature and high-mineralization oilfield. On the other hand, the inhibition performance of poly(AM-co-A- β -CD-co-AE) polymer as corrosion inhibitor was evaluated by SEM and electrochemical techniques. SEM observations of the carbon steel surface confirmed the protective role of the corrosion inhibitor. The results of potentiodynamic polarization and EIS measurements on the corrosion inhibition of carbon steel samples in 0.5 M sulfuric acid solutions revealed that the highest inhibition efficiency of it over 90 % was obtained, indicating poly(AM-co-A- β -CD-co-AE) polymer acts as a more efficient corrosion inhibitor for carbon steel.

Nontoxic corrosion inhibitors for N80 steel in hydrochloric acid¹⁷

The protective ability of 1-(2-aminoethyl)-2-oleylimidazoline (AEOI) and 1-(2-oleylamidoethyl)-2-oleylimidazoline (OAEIO) as corrosion inhibitors for N80 steel in 15% hydrochloric acid has been evaluated. This may find application as eco-friendly corrosion inhibitors in acidizing processes in petroleum industry. Different concentrations of synthesized inhibitors AEOI and OAEIO were added to the test solution (15 % HCl) and the corrosion inhibition of N80 steel in hydrochloric acid medium containing inhibitors was tested by weight loss, potentiodynamic polarization and AC impedance measurements. Influence of temperature (298-323 K) on the inhibition behavior was studied. Surface studies were performed by using FTIR spectra and SEM. Both the inhibitors, AEOI and OAEIO at 150 ppm concentration show maximum efficiency 90.26% and 96.23 %, respectively at 298 K in 15 % HCl solution. Both the inhibitors act as mixed corrosion inhibitors. The adsorption of the corrosion inhibitors at the surface of N80 steel is the root cause of corrosion inhibition.

Environmentally friendly calcium carbonate scale inhibitor for high temperature and high pressure (HTHP) wells¹⁸

The formation of calcium carbonate mineral scale is a persistent and expensive problem in oil and gas production, especially in the high temperature and high pressure (HTHP) wells. Scaling of metallic or insulating walls in contact with hard water may cause unscheduled equipment shutdown and loss of production. Environmentally friendly calcium carbonate scale inhibitors have been developed for HTHP squeeze application in the oil and gas field water treatment. Typical commercial scale inhibitors, including several phosphonate based squeeze scale inhibitors and patented environmentally friendly polyacrylic copolymers have been tested based on thermally stability test, formation water compatibility test, dynamic scale loop test and core flood test. In this paper, an environmentally friendly calcium carbonate scale inhibitor has been developed to inhibit calcium carbonate scale deposition effectively under HTHP conditions. The characteristics of this product are as following:

- Thermally stable at high temperature.
- Excellent calcium tolerance at high temperature.

•Good inhibition performance on CaCO₃ deposition at high temperature.

•Long squeeze life and no formation damage based on core flood test.

•Environmentally friendly.

•Easy residual analysis by ICP, HPLC and hyamine methods.

This paper will gives a comprehensive study of developing environmentally friendly calcium carbonate scale inhibitors for squeeze application for HTHP wells in the oil and gas fields, which includes thermally stability, dynamic scale loop performance, adsorption and desorption performance, compatibility, residual analysis and environmental regulation.

Corrosion inhibitor and kinetic hydrate inhibitor for the pearl GTL project¹⁹

PEARL GTL (Gas to Liquids) project is a fully integrated project that will take 1.6 billion cubic feet per day of unprocessed gas from Qatar's North field into onshore gas processing plants, producing 140,000 barrels per day of GTL products and 120,000 barrels per day of natural gas liquids. There will be no processing facilities on the two offshore platforms - all produced fluids will be transported to shore via the main pipelines for treatment. The gas contains H₂S and CO₂ and is consequently corrosive so continuous injection of corrosion inhibitor into the pipelines is necessary. Sea bottom temperatures can be below hydrate formation temperature so it is necessary for part of the year to also inject kinetic hydrate inhibitor into the inlet of the pipeline to avoid hydrate formation. The challenging combination of highly corrosive conditions, minimal offshore intervention and very high plant uptime requirements means that corrosion control and flow assurance of the highest effectiveness is required.

CONCLUSION

Corrosion cost of the oil industry is very high. Oil industry faces corrosion problems at various stages, including oil wells, transportation, storage and refinery operations. Various inhibitors- organic and inorganic have been used to prevent corrosion in petroleum industry. Recently, green inhibitors and biocidal inhibitors have gained momentum in this area.

REFERENCES

¹https://www.google.co.in/search?q=corrosion+in+petroleum+industry&oeq=corrosion+in+petroleum+industry&aqs=chrome..69j57j015.8972j0j8&sourceid=chrome&espv=210&es_sm=93&ie=UTF-8

²<http://corrosion-malaysiapetroleum.blogspot.in/2008/06/corrosion-in-petroleum-industry.html>.

- ³<http://www.onepetro.org/mslib/servlet/onepetropreview?id=00029784>.
- ⁴Choudhary, Y. K., Sabhapondit, A., Kumar, A., *Soc. Petrol. Eng. – SPE Int. Conf. Exhib. Oilfield Corros.*, **2012**, 264-273.
- ⁵Taj, S., Siddekha, A., Papavinasam, S., Revie, R.W., *NACE – Int. Corros. Conf. Ser.*, **2007**, 076301-0763013.
- ⁶Craddock, H. A., Caird, S., Wilkinson, H., Guzmann, M. *SPE Projects, Facilities Construct.*, **2007**, 2(4).
- ⁷Van Der Kraan, G. M., Keene, P. A., James, M., Yin, B., Williams, T. M., Van Ruiten, O. P. J., Love, D.J. *Soc. Petrol. Eng. - SPE/EAGE Eur. Unconvent. Resources Conf. Exhibit.*, **2012**, 569-578.
- ⁸Hamidova, N. S., Azimov, N. A., Veliyeva, R. G. *SOCAR Proc.*, **2011**, 62-66.
- ⁹Binay, N. P., Smit, M. G. D., Frost, T. K., Stone, K., Firth, S. *Soc. Petrol. Eng. - SPE Int. Conf. Health, Safety Environ. Oil Gas Explorat. Product.* **2011**, 313-320.
- ¹⁰Gana, M. L., Kebbouche-Gana, S., Touzi, A., Zorgani, M. A., Pauss, A., Lounici, H., Mameri, N., *J. Ind. Microbiol. Biotechnol.*, **2011**, 38(3), 391-404.
- ¹¹Johnston, S. L., Cunningham, G., Voordouw, G., Jack, T. R. *NACE – Int. Corros. Conf. Ser.*, **2010**.
- ¹²Smith, B. E., Rowland, S. J. *Rapid Commun. Mass Spectrom.*, **2008**, 22(23), 3909-3927.
- ¹³Torrado Rincón, J. R., Calixto Gómez, D. M., Sarmiento Caraballo, A. E., Panqueva Álvarez, J. H. *Rev. Argent. Microbiol.*, **2008**, 40(1), 52-62.
- ¹⁴Sun, H., Fang, H., Davis, J., Hudgins, R., *NACE – Int. Corros. Conf. Ser.*, **2012**, 5088-5102.
- ¹⁵Cenegy, L. M., McAfee, C. A., Engchanil, R., Thatsana, A., *Soc. Petrol. Eng. – Int. Petrol. Technol. Conf. 2012, IPTC 2012*, **2012**, 1364-1380.
- ¹⁶Zou, C., Tang, Q., Tan, N., Xiao, P., Hu, X. *Starch/Staerke*, **2012**, 64(4), 281-289.
- ¹⁷Yadav, M., Behera, D., Sharma, U., *Arab. J. Chem*, (Article in Press), **2012**.
- ¹⁸Chen, T., Chen, P., Montgomerie, H., Hagen, T., Ekpeni, H. *NACE – Int. Corros. Conf. Ser.*, **2011**.
- ¹⁹Pit, H., Ünsal, R., McFarland, S., *Int. Petrol. Technol. Conf., IPTC 2008*, **2008**, 1520-1526.

Received: 02.02.2014.

Accepted: 27.02.2014.